Study of Void Growth in Commercially Pure Titanium

by

Marina Pushkareva

Thesis

Submitted to the Faculty of Graduate and Postdoctoral Studies

in Partial Fulfillment of the Requirements for the Degree of

Doctor of Philosophy

in Advanced Materials and Manufacturing

Ottawa-Carleton Institute for Mechanical and Aerospace Engineering

University of Ottawa

TITLE: Study of Void Growth in Commercially Pure Titanium

AUTHOR: Marina Pushkareva

SUPERVISOR: Arnaud Weck

NUMBER OF PAGES: x, 169

ABSTRACT

The ductile fracture process, which consists of the nucleation, growth and coalescence of microvoids, was extensively studied for materials deforming homogeneously. For materials with a non-homogeneous deformation behavior, such as those having hexagonal closed packed (HCP) crystal structure, experimental and numerical data is lacking. Therefore, the fracture properties of materials with such HCP structure, like titanium (used in aerospace and biomedical applications), zirconium (nuclear industry) and magnesium (manufacturing industry) are not well understood.

The main research objective of this Ph.D. thesis is to better understand the mechanisms governing fracture in commercially pure (CP) titanium. In particular, the effect of grain orientation on void growth is investigated. The fracture process of CP titanium was visualized in model materials containing artificial holes. These model materials were fabricated using a femtosecond laser coupled with a diffusion bonding technique to obtain voids in the interior of titanium samples. Diffusion bonding was carried out either above or below the phase transformation temperature resulting in different microstructures. Changes in void dimensions during in-situ straining were recorded in three dimensions using x-ray computed tomography. Void growth obtained experimentally was compared with the Rice and Tracey model which predicted well the average void growth. However, a large scatter in void growth was observed experimentally and was explained in terms of differences in grain orientation which was confirmed by crystal plasticity simulations. It was also shown that grain orientation has a stronger effect on void growth than intervoid spacing and material strength. Intervoid spacing, however, appears to control whether the intervoid ligament failure is ductile or brittle. While this study showed a good agreement between experiments and simulations on average, there is no direct void growth comparison for particular grain orientations. In a follow-up study, an experimental approach was developed to directly relate the growth of a void to its underlying grain orientation. This is achieved by first annealing CP titanium samples below the α-β phase transformation temperature, then performing electron backscatter diffraction

(EBSD) and finally diffusion bonding the samples together. Samples were then tested in x-ray tomography. This study showed the importance of the local state of strain on void growth. Crystal plasticity simulations that take into account the particular grain orientation and the local state of strain were found to predict well experimental void growth. Crystal plasticity simulations confirmed that the orientation of the void-containing grain is more important than the orientation of surrounding grains and more important than the volume fraction of voids, in order to determine void growth.

This thesis on the growth and coalescence of voids is important to validate and improve the predictions of ductile fracture models and to design new materials with improved fracture properties.

PREFACE

The work presented in this Ph.D. thesis was performed at the University of Ottawa unless otherwise stated. Sample polishing and etching, microstructutal characterisation using optical microscope, microhardness testing, laser void drilling, sample annealing, diffusion bonding, fractography analysis using SEM was performed by the author. Dr. Mohammed Yandouzi is acknowledged for acquiring EBSD maps. Machine shop of the Mechanical Engineering Department is acknowledged for cutting the tensile coupons.

X-Ray tomography experiments from Chapter 3 were performed by the author during her research stay at INSA de Lyon in France.

X-Ray tomography experiments from Chapter 5 were performed by the author during her research stay at IMDEA Materiales in Spain.

Crystal plasticity simulations were performed by the author using the UMAT (user material) subroutine developed at IMDEA Materiales by Prof. Javier Segurado and Prof. Javier LLorca.

Some parts of this work have been or will be published as follows:

- Chapters 3 and 4 have been published as: **Marina Pushkareva**, Jérôme Adrien, Eric Maire, Javier Segurado, Javier Llorca, Arnaud Weck, "Three-dimensional investigation of grain orientation effects on void growth in commercially pure titanium", Materials Science and Engineering: A, 671 (2016) 221-232.
- Chapters 5 and 6 will be published as: **Marina Pushkareva**, Federico Sket, Javier Segurado, Javier Llorca, Mohammed Yandouzi, Arnaud Weck, "Grain orientation effects on void growth in CP titanium: a direct comparison between 3D experiments and crystal plasticity simulations".

ACKNOWLEDGEMENTS

I would like to thank my supervisor Prof. Arnaud Weck for his guidance throughout my PhD and for giving me the opportunity to perform X-Ray tomography experiments at INSA de Lyon in France and the opportunity to perform X-Ray tomography experiments and crystal plasticity simulations at IMDEA Materiales in Spain.

I am grateful for my research stay at INSA de Lyon in France and for letting me use the X-ray tomography to: Prof. Eric Maire, Jérome Adrien and all the members of MATEIS group.

I express my gratitude for my research stay at IMDEA Materiales in Spain to: Prof. Javier LLorca, Prof. Javier Segurado, Dr. Federico Sket, Anton Cristian Jormescu, Daniel Rodriguez and all the members of IMDEA Materiales.

I would like to thank Dr. Mohammed Yandouzi for EBSD maps.

I would like to acknowledge the help mechanical engineering technical officers John Perrins, Léo Denner and Paul Burberry.

I express my gratitude to my research colleagues: the members of our FROG group (Fracture and Femtosecond Research Ottawa Group), in particular Elisa Cantergiani, Mishaal Azhar, Emily Bradley, Trevor Meunier and Yusha Lan; and students of Materials Characterisation Laboratory, in particular, Rubén Fernández Urrutia and Leon Guo.

Lastly, I thank my family and Simon for their support.

Table of Contents

Page

LIST OF ABBREVIATIONS/ACRONYMS

BCC	body-centered cubic
CNC	computer numerical control
CP	commercially pure
CRSS	critical resolved shear stress
DIC	digital interference contrast
EBSD	electron backscatter diffraction
EYT	equal yield in tension
FCC	face centered cubic
FEA	finite element analysis
FIB	focused ion beam
GNDs	geometrically necessary dislocations
HCP	hexagonal close-packed
IPF	inverse pole figure
RT	Rice and Tracey (model)
SEM	scanning electron microscope
TEM	transmission electron microscope
UTS	ultimate tensile stress

Chapter 1 INTRODUCTION

1.1 BACKGROUND

In contrast to brittle fracture where failure is sudden and catastrophic, ductile fracture results in progressive failure due to plastic deformation. This leads to a time-dependent fracture where damage can be monitored throughout the life of the material. Damage assessment is highly useful because it enables the replacement or repair of materials prior to critical failure, preventing collateral damage to neighbouring systems that could lead to higher repair cost or more importantly that could jeopardize the safety of people. Hence, from an economical and safety standpoint, it is critical to understand what affects the ductile fracture of materials. The ductile fracture process consists of three stages: void nucleation, void growth and void coalescence. The study of void growth and coalescence is important in order to predict when materials will break, to create new materials with improved properties, and to validate and improve the predictions of ductile fracture models.

Ductile fracture was extensively studied both experimentally and numerically mainly in homogeneous materials. However there is a lack of both experimental and numerical data on anisotropic materials such as those having hexagonal closed packed (HCP) crystal structure even though they are extensively used in industry. Fracture properties of materials with such HCP structure, including titanium (used in aerospace and biomedical applications), zirconium (nuclear industry) and magnesium (manufacturing industry) are not well understood.

1.2 AIM AND SCOPE

The main research objective of this Ph.D. project is to better understand the failure of a material deforming heterogeneously. More specifically, the effects of grain orientation on void growth will be investigated in commercially pure (CP) titanium. In order to achieve this goal, both experimental and numerical approaches will be combined to get a better understanding of the fracture processes active in this material. Model materials will be used in order to simplify the analysis of fracture where the

voids geometry (void size, shape, orientation, and spacing) will be controlled. Study of void growth and coalescence will be addressed by:

i) Fabricating model materials by diffusion bonding titanium sheets in which holes are artificially introduced using a femtosecond laser;

ii) Tensile testing these model materials in-situ in an X-Ray Computed Tomography system to relate void growth to the grain matrix orientation

iii) Modelling using crystal plasticity models in a finite element scheme to predict the experimentally observed behavior.

1.3 Organization of the thesis

The work is organized as follows:

Chapter 1: Introduction.

Chapter 2: Review of ductile and brittle fracture processes with an emphasis on the microstructure and mechanical properties of CP titanium alloy.

Chapter 3: Results on the indirect investigation of grain orientation effects on void growth in CP titanium.

Chapter 4: Crystal plasticity simulations results on the indirect observations of grain orientation effects on void growth in CP titanium.

Chapter 5: Results on the direct investigation on grain orientation effects on void growth in CP titanium.

Chapter 6: Crystal plasticity simulations results on the direct observations of grain orientation effects on void growth in CP titanium.

Chapter 7: Conclusions and future work.

Chapter 2 LITERATURE REVIEW

2.1 FUNDAMENTAL ASPECTS OF TITANIUM ALLOYS

2.1.1 TITANIUM BASIC PROPERTIES AND APPLICATIONS

Titanium has the highest specific strength (strength to density ratio) compared to Fe, Ni and Al (Table 2.1). Titanium has a very high reactivity with oxygen which results in: (i) stable oxide layer formation and thus very high corrosion resistance; (ii) its high price (need of inert atmosphere to produce Ti); (iii) the maximum use temperature of about 600°C as above this temperature oxygen diffusion becomes too fast and crosses the protective barrier resulting in embrittlement [1]. The high melting temperature of titanium, compared to Al, makes Ti a good choice for light weight structural applications where temperatures are above 150°C. Titanium also has good biocompatibility.

Table 2.1: Some important characteristics of titanium as compared to other structural metallic materials based on Fe, Ni, and Al [1].

	Ti	Fe	Ni	Al
Melting Temperature (°C)	1670	1538	1455	660
Allotropic Transformation (°C)	$\beta \overset{882}{\longrightarrow} \alpha$	$\gamma \overset{912}{\longrightarrow} \alpha$	-	-
Crystal Structure	bcc → hcp	fcc → bcc	fcc	fcc
Room Temperature *E* (GPa)	115	215	200	72
Yield Stress Level (MPa)	1000	1000	1000	500
Density (g/cm^3)	4.5	7.9	8.9	2.7
Comparative Corrosion Resistance	Very High	Low	Medium	High
Comparative Reactivity with Oxygen	Very High	Low	Low	High
Comparative Price of Metal	Very High	Low	High	Medium

Titanium alloys have various applications in: (i) aerospace industry (airframes and aeroengines); (ii) biomedical field (implant material); (iii) chemical and power industries (corrosion resistant material, offshore structures); (iv) building applications (exterior walls, roofing material); (v) consumer products (spectacle frames, cameras,

watches, jewelry, sporting goods including golf club heads, tennis rackets, bicycle frames, spikes in sprinters' running shoes); (vi) mass-produced automobiles (valves, valve spring, connecting rods, suspension springs, bolts, fasteners, exhaust system) and high performance vehicles (Formula-One racing cars) [1].

Titanium alloys are classified by their microstructure into three categories: α, α+β, and β alloys according to their position in a pseudo-binary section through a β isomorphous phase diagram (Figure 2.1) [1].

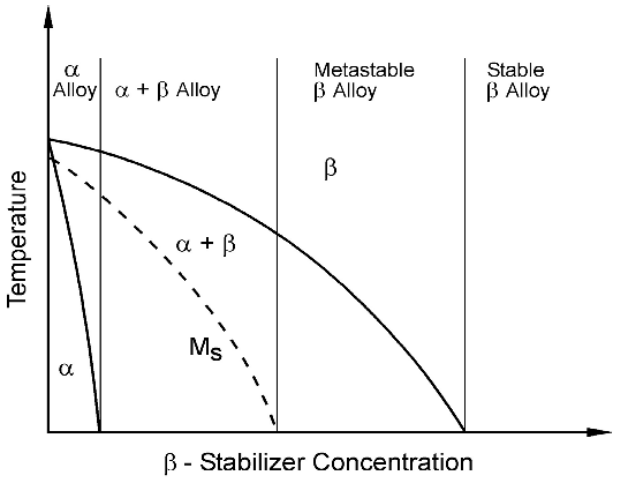

Figure 2.1: Pseudo-binary section through a–β isomorphous phase diagram (schematically) [1].

2.1.2 Crystal structure and deformation modes

2.1.2.1 Crystal structure

Pure titanium has two allotropic structures (Table 2.1): a hexagonal close-packed crystal structure α at lower temperatures and a body-centered cubic crystal structure β at higher temperatures. The allotropic phase transformation temperature is 882°C for pure titanium but the exact value depends on the purity of the metal [1].

Figure 2.2(a) illustrates the hexagonal unit cell of the Ti α phase. Its room temperature lattice parameters are *a* (0.295 nm) and *c* (0.468 nm). Thus *c/a* ratio for pure α titanium is 1.587, smaller than the ideal ratio of 1.633 for the hexagonal close-packed crystal structure. The *c/a* ratio can be correlated with different mechanical properties and explains different (either ductile or brittle) behaviour of HCP metals [2]. Figure 2.2(a) shows the three most densely packed types of lattice planes, the (0002)

plane, also called basal plane, one of the three {0101} planes, also called prismatic planes, and one of the six {1110} planes, also called pyramidal planes as well as the three close-packed directions a_1, a_2, and a_3 with the indices <0211> [1].

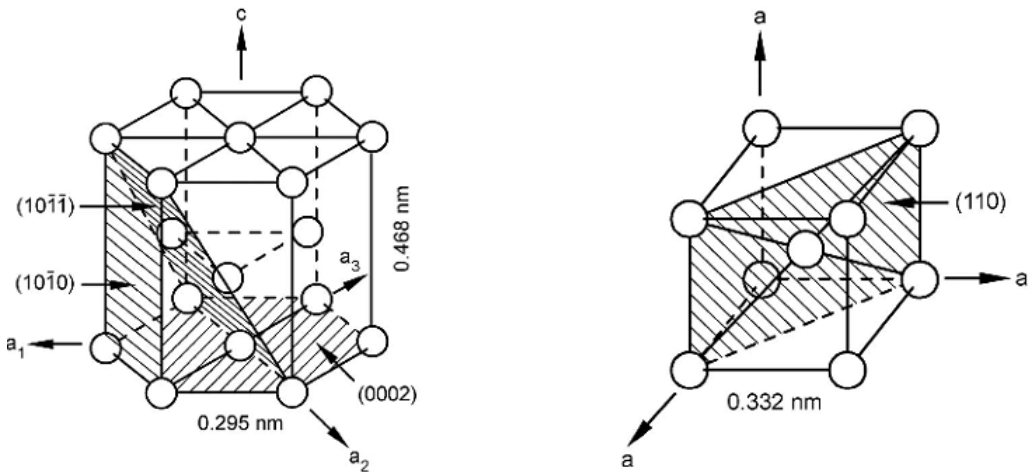

(a) (b)

Figure 2.2: Unit cell of Ti (a) α phase; (b) β phase [1].

The α phase, due to its hexagonal crystal structure, has anisotropic character which means that the elastic properties of titanium and its alloys will vary significantly with crystal orientation as shown in Figure 2.3 [1].

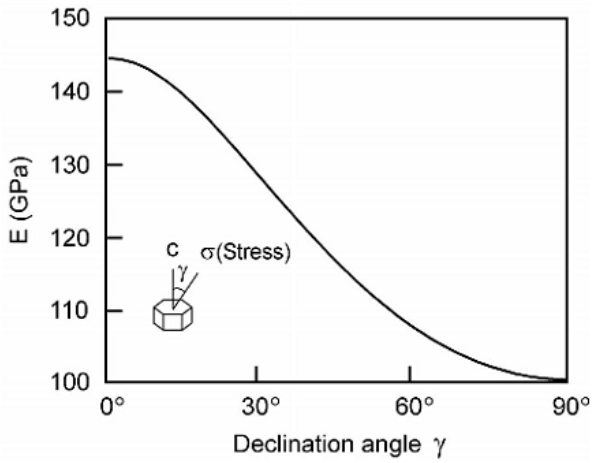

Figure 2.3: Modulus of elasticity *E* of α titanium single crystals as a function of declination angle γ [3].

Figure 2.2(b) illustrates the body-centered cubic (BCC) unit cell of the β phase along with one variant of the six most densely packed {110} lattice planes and one of the four close-packed directions <111>. Lattice parameter at 900°C is 0.332 nm [1].

2.1.2.2 SLIP SYSTEMS

Figure 2.4 illustrates the various possible slip planes and slip directions for α titanium. Table 2.2 shows slip systems in α Ti. During deformation the activation of slip systems depends on the crystal orientation [4,5]. For example, if a grain in a polycrystalline material is orientated such that the applied stress is parallel to the c-axis, the slip systems with the lowest critical resolved shear stresses (CRSS) are first activated. Values of the CRSS are dependent on alloy chemical composition and on test temperature. An example of temperature influence on CRSS in single crystals of Ti-6.6Al is shown in Figure 2.5. Critical resolved shear stresses for Ti for some slip systems are presented in [6]. Gong and Wilkinson [7] determined critical resolved shear stresses of 181 MPa for $\langle a \rangle$ on the prismatic, 474 MPa for $\langle c + a \rangle$ on the pyramidal and 209 MPa for $\langle a \rangle$ on the basal planes for CP Ti via the reverse process of fitting the model load–displacement curves to experimental ones.

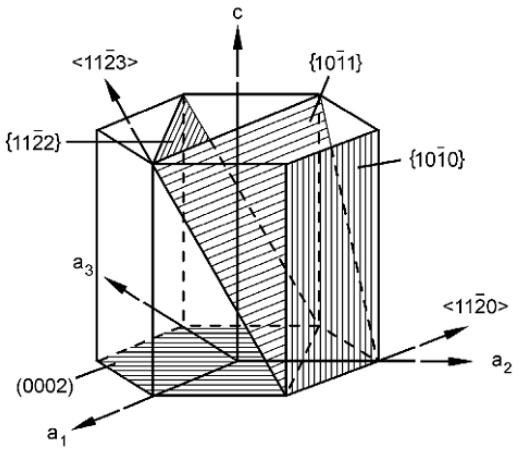

Figure 2.4: Slip planes and slip directions in the hexagonal α Ti phase [1].

Table 2.2: Slip systems in the hexagonal α phase Ti [2,6].

Slip system type	Burgers vector type	Slip direction	Slip plane	Number of slip systems	
				Total	Independent
1	$\bar{a}$	$\langle 11\bar{2}0 \rangle$	(0002)	3	2
2	$\bar{a}$	$\langle 11\bar{2}0 \rangle$	$\{10\bar{1}0\}$	3	2
3	$\bar{a}$	$\langle 11\bar{2}0 \rangle$	$\{10\bar{1}1\}$	6	4
4	$\bar{c} + \bar{a}$	$\langle 11\bar{2}3 \rangle$	$\{11\bar{2}2\}$	6	5

Viswanathan et al. [8] studied the effect of crystal orientation on the indentation hardness of Ti alloy using TEM. They noted an increase in hardness near the [0001] indentation axis (Figure 2.6) and attributed the hardening to a high density of $\langle c + a \rangle$ type geometrically necessary dislocations (GNDs) directly below the indentation. Merson et al. [9] reported similar trends.

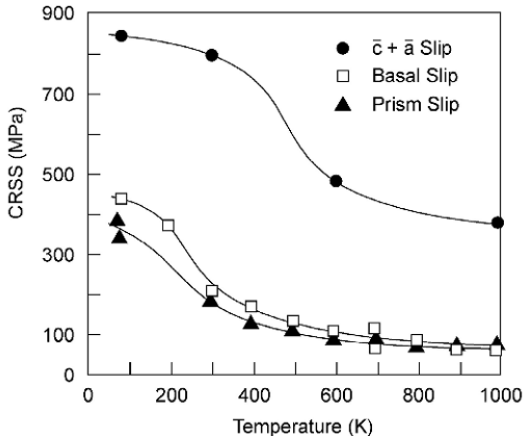

Figure 2.5: Temperature dependence of CRSS for slip with $\bar{a}$ and $\bar{c} + \bar{a}$ Burgers vectors in single crystals of Ti-6.6Al [10].

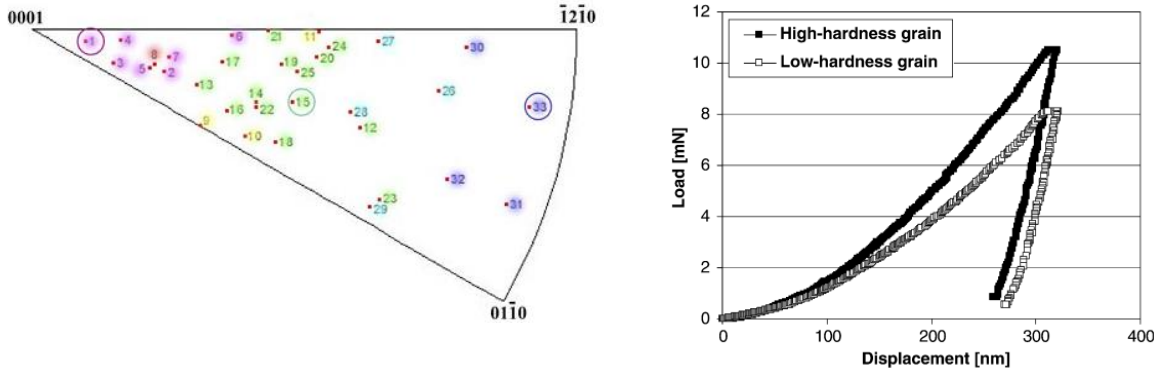

(a) (b)

Figure 2.6: (a) Inverse pole figure showing the orientations of the α grains of Ti alloy that were selected for the study: each orientation has an associated hardness value which is numbered 1–33 in decreasing magnitude of hardness; (b) typical load versus displacement plots are shown for grains exhibiting high-hardness and low-hardness values, i.e., #1 and #33, respectively [8].

Britton and al. [11] reported that both indentation modulus and hardness of CP Ti decrease significantly as the indentation axis is inclined further from the c-axis (Figure 2.7); the plastic response showing the more marked anisotropy. Indentation

modulus is the elastic modulus of the specimen determined from the slope of the unloading of the load-displacement response [12]. The results are explained in terms of different slip systems activated at different orientations. $\langle a \rangle$ type slip can only deform material parallel to the basal plane, thus as the crystal is rotated, $\langle c + a \rangle$ type slip will be required more for plastic deformation. In the extreme case where the load is applied directly parallel to the c direction, only the motion of $\langle c + a \rangle$ dislocations can accommodate the indentation. $\langle c + a \rangle$ type slip is approximately three times as difficult to initiate as $\langle a \rangle$ type slip [8], resulting in higher hardness at 0 declination angle.

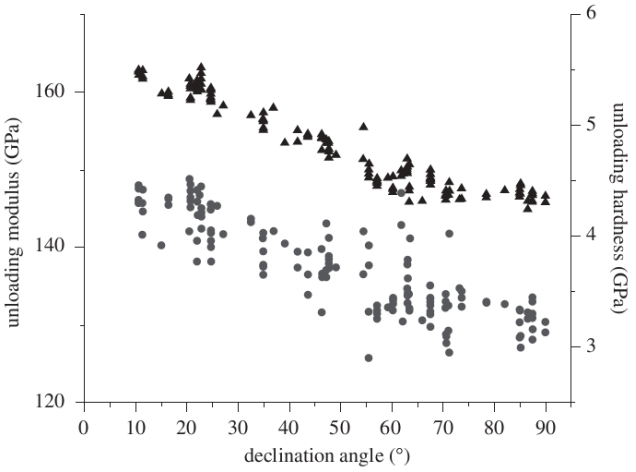

Figure 2.7: Variations in the unloading modulus and hardness with declination angle in CP Ti. Filled grey circles stand for unloading modules; filled black triangles stand for unloading hardness [11].

The stresses required to activate the deformation modes in HCP metals are very dependent on the orientation of the stress axis and are determined by the Schmid factor [6]:

$$\frac{\sigma_s}{\sigma_n} = \cos\varphi\cos\lambda$$

where σ_s is shear stress resolved on the slip or twin plane in the slip or twinning direction,

σ_n is applied stress,

φ and λ are, respectively, the angle between the stress axis and the slip or twin plane normal and slip or twinning direction (Figure 2.8(a)).

Variation of the Schmid factor with angle φ between the c-axis and the tensile-stress axis for some slip and twinning modes in titanium is plotted in Figure 2.8(b) and (c) [6]. The unit stereographic triangle from the basal projection of the hexagonal lattice is formed by great circles through (0001), $(11\bar{2}0)$, and $(10\bar{1}0)$ poles (Figure 2.8(b)). Areas $(01\bar{1}0)[2\bar{1}\bar{1}0]$ and $(0001)[2\bar{1}\bar{1}0]$ represent resolved shear stress for the most highly stresses prism-and-basal slip systems respectively. Area $\{10\bar{1}2\}$ represents the variation of resolved shear stress for some $\{10\bar{1}2\}$ planes. Curves for $(11\bar{2}1)$ and $(11\bar{2}2)$ correspond to a stress axis that moves in a $(1\bar{1}00)$ plane, and indicates the variation in the resolved shear stress for twinning on these planes.

In some metals (Cd, Zn, Mg, Be) basal slip is only slightly temperature-dependent below room temperature [13], in others (titanium) it is temperature-dependent (Figure 2.9).

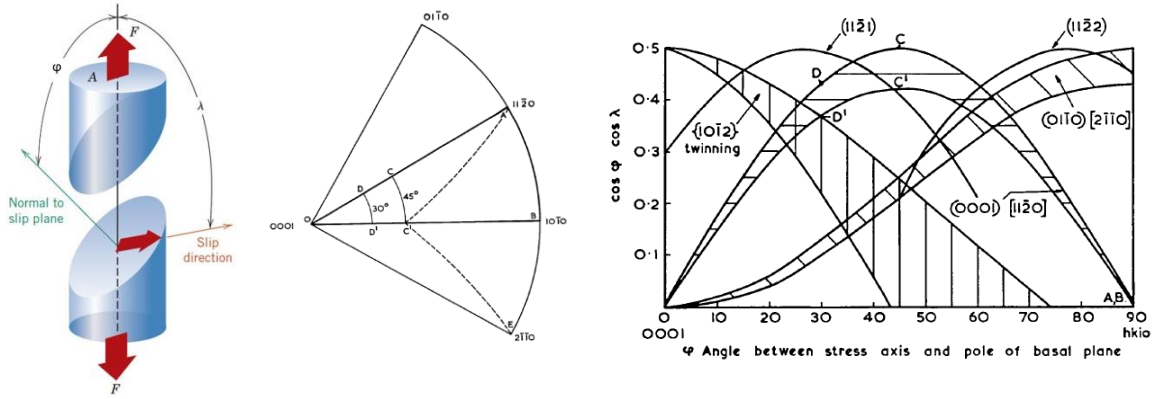

(a) (b) (c)

Figure 2.8: (a) Geometrical relationships between the tensile axis, slip plane, and slip direction used in calculating the Schmid factor [14];(b) standard stereographic triangle $(0001) - (10\bar{1}0) - (11\bar{2}0)$ for a HCP metal; (c) orientation-dependence of the resolved shear stress for slip and twinning within the stereographic triangle AOB [6].

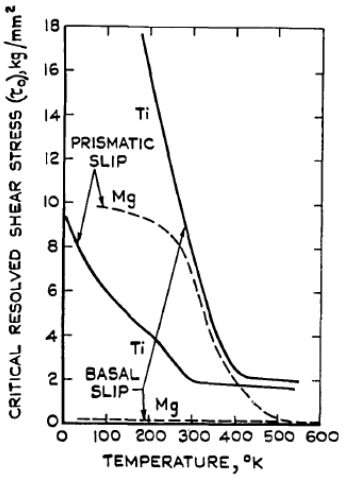

Figure 2.9: Temperature–dependence of the critical resolved shear stresses for basal and prismatic slip in Mg and Ti [6].

In addition to conventional slip by dislocations hexagonal α titanium shows activation of twinning deformation modes which explains the ductile behavior of Ti especially at low temperatures. The bcc β phase also shows twinning in addition to slip. Twinning occurs in the single phase state and decreases with increasing solute content [1].

2.1.2.3 TWINNING MODES

Twinning is a significant deformation mechanism in HCP titanium [6,15–20]. One contributing effect of twinning to general plastic flow is that unfavorably oriented grains for slip and twinning are reoriented into a more favorable position upon twinning [2]. Given the strong influence of texture in anisotropic materials such as hexagonal close-packed metals, the occurrence of twinning drastically changes the crystallographic texture and the misorientation distribution in a polycrystalline material and thus controls macroscopic properties [15]. The misorientation distribution may also be a predominant factor when dealing with properties that depend on the grain-boundary network, e.g. fatigue life, corrosion behavior [15]. Twinning alters the microstructure and the texture evolution through deformation and also influences the recrystallization mechanisms [21–23].

Twinning elements in α titanium are presented in Table 2.3. These twinning modes are active if all of three conditions are satisfied:

(i) plastic deformation is along c-axis, so that the dislocations with a basal Burgers vector cannot move;

(ii) deformation occurs at low temperature;

(iii) titanium does not contain critical amounts of solute atoms because solute atoms (O, Al) suppress twinning [24].

Table 2.3: Twinning elements in α titanium [6].

Twinning plane (1^{st} undeformed plane) (K_1)	Twinning shear direction (η_1)	Second undeformed plane (K_2)	Direction of intersection of plane of shear with K_2 (η_2)	Plane of shear perpendicular to K_1 and K_2	Magnitude of twinning shear
$\{10\bar{1}2\}$	$\langle 10\bar{1}\bar{1}\rangle$	$\{\bar{1}012\}$	$\langle 10\bar{1}1\rangle$	$\{1\bar{2}10\}$	0.167
$\{11\bar{2}1\}$	$\langle 11\bar{2}\bar{6}\rangle$	(0002)	$\langle 11\bar{2}0\rangle$	$\{\bar{1}100\}$	0.638
$\{11\bar{2}2\}$	$\langle 11\bar{2}\bar{3}\rangle$	$\{11\bar{2}\bar{4}\}$	$\langle 22\bar{4}3\rangle$	$\{\bar{1}100\}$	0.225

Under tension, twins of the most frequent $\{10\bar{1}2\}$ type and $\{11\bar{2}1\}$ type are activated. Under compression, $\{11\bar{2}2\}$ twins are activated. However $\{10\bar{1}1\}$ were also observed under compression at temperatures higher than 400°C [25]. The designation ‘‘tensile” twin indicates that the twin accommodates c-axis elongation, whereas a ‘‘compressive” twin accommodates c-axis contraction [2]. Metals that exhibit extensive ductility (e.g., Ti, Re, Zr) twin profusely by both tension and compression types while those with limited ductility (e.g., Zn and Be) twin only by the most common type, the $\{10\bar{1}2\}$ twin [2].

Depending on crystal orientation, i.e. slip and twinning systems activated, the mechanical properties change (Figure 2.10, Figure 2.11) [18,26,27]. Figure 2.10 illustrates yield stress and plastic strain ratio as a function of cutting angle with respect to rolling direction. Figure 2.11 shows equivalent stress-equivalent strain curves for different sample orientations. Zaeffer [20] reported that in T60, the high oxygen content completely suppresses twinning which contradicts [18]. Battaini et al. [26]

reported that higher flow stresses were primarily due to an unfavourable orientation for prism-$\langle a \rangle$ slip and secondly due to a greater proportion of $\{11\bar{2}2\}$ to $\{10\bar{1}2\}$ twinning (samples NR and NT, Figure 2.11).

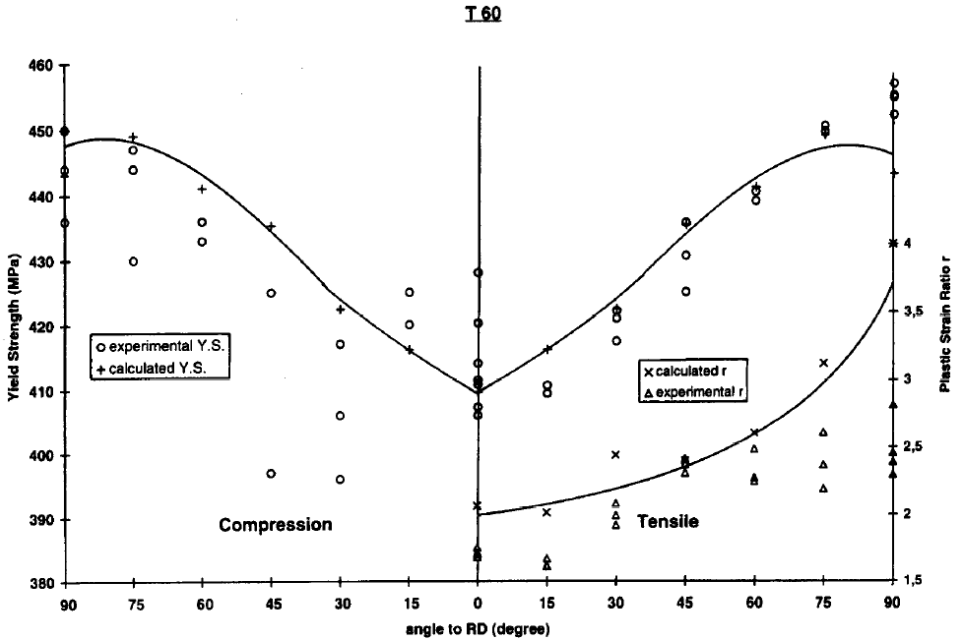

Figure 2.10: Yield stress and plastic strain ratio vs cutting angle with respect to RD (rolling direction) for titanium T60 alloy (Ti + 2000 ppm O). Comparison between measurements and predictions [18].

Farrell et al. [28] reported that the stress-strain curve of Nb that exhibits twinning has the load drops at -196°C (Figure 2.12(a)). Similar results were reported for α Ti [29]. Irregularities in the curves for specimens which exhibited $\{10\bar{1}2\}$ twins only occur at the higher temperatures 423-773°K (Figure 2.12(b)). However, for specimens which exhibited $\{11\bar{2}1\}$ twins in tension, irregularities in the stress-strain curves occurred at temperatures as low as 78K (Figure 2.12(c)). Pronounced yield drops seen in Figure 2.12(c) indicate that the stress for the nucleation of $\{11\bar{2}1\}$ twins is higher than that for their propagation. Yield drops were also observed during the c-axis compression of specimens which exhibited $\{11\bar{2}2\}$ twins [25], the amount of the drop increasing with increase in test temperature. However no yield drops existed for specimens similarly loaded at temperatures where $\{10\bar{1}1\}$ twinning occurred [25].

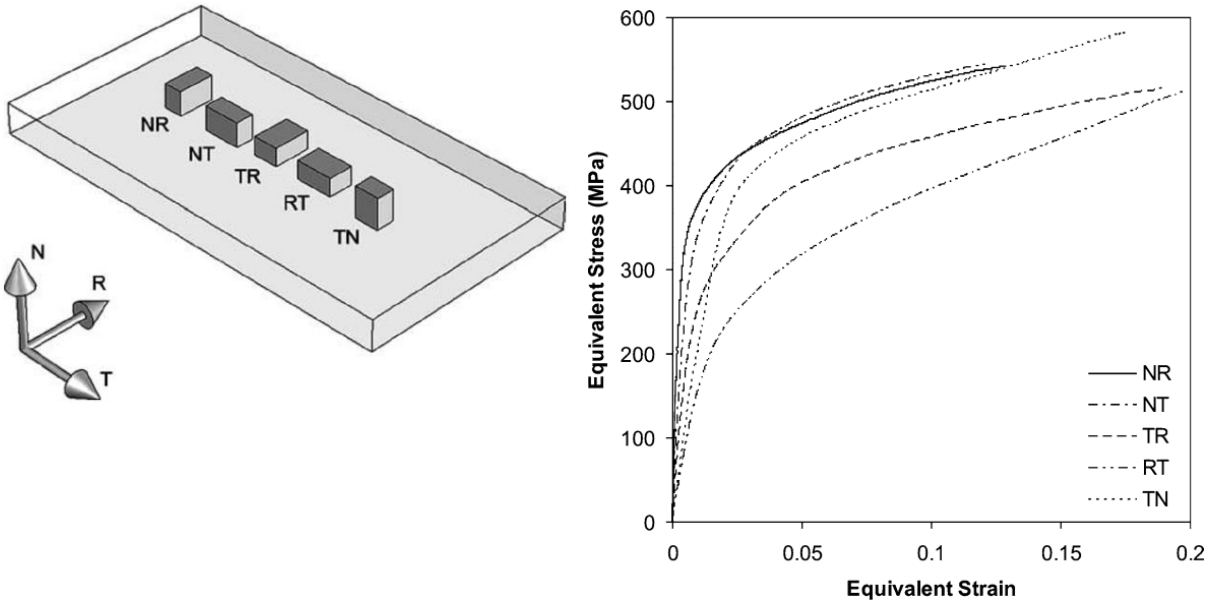

(a) (b)

Figure 2.11: (a) Orientation and names of plane strain compression samples cut from plate of CP Ti. The first letter in the name of the sample indicates the compression direction and the second letter indicates the extension direction, where R is rolling direction, T is transverse direction, and N is normal direction; (b) modulus-corrected flow curves for plane strain compression of samples of different orientations [26].

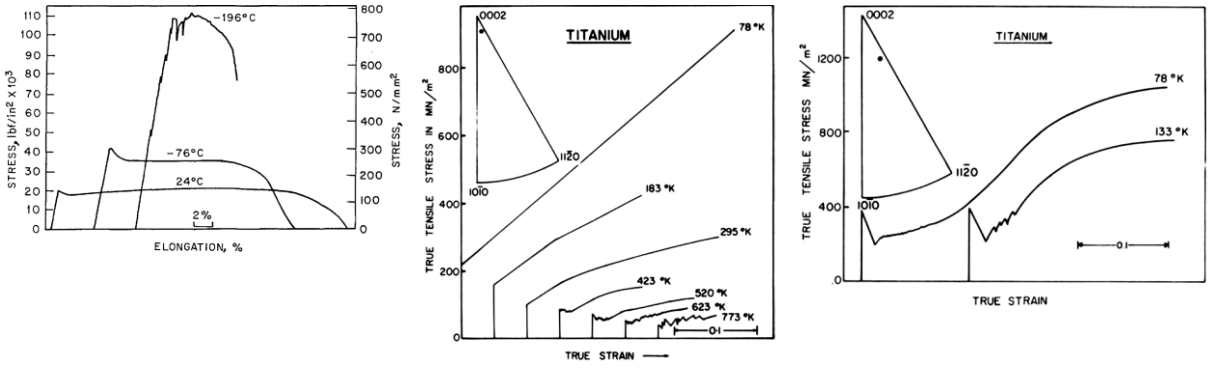

(a) (b) (c)

Figure 2.12: Typical stress-strain curves for: (a) annealed polycrystalline Nb deformed at various temperatures [28]; (b) Ti single crystals which exhibited $\{10\bar{1}2\}$ twins [29]; (c) Ti single crystals which exhibited $\{11\bar{2}1\}$ twins [29].

2.1.3 PHASE TRANSFORMATIONS

Alloying elements have a strong effect on α→β transformation in titanium. The elements with respect to α→β transformation are classified into [1]:

(i) α stabilizers such as Al, O, N, C, B;

(ii) β stabilizers such as V, Mo, Nb, Cr, Fe, Si;

(iii) neutral elements such as Zr, Hf, Sn.

Depending on cooling rate (Figure 2.13) and alloy composition of CP titanium and titanium alloys, the phase transformation β→α can occur martensitically or by a diffusion controlled nucleation and growth process [1]. In both cases the crystallographic orientation relationship between α and β obey the Burgers relationship [30,31]:

$$(110)_\beta \parallel (0002)_\alpha$$

$$[1\bar{1}1]_\beta \parallel [11\bar{2}0]_\alpha$$

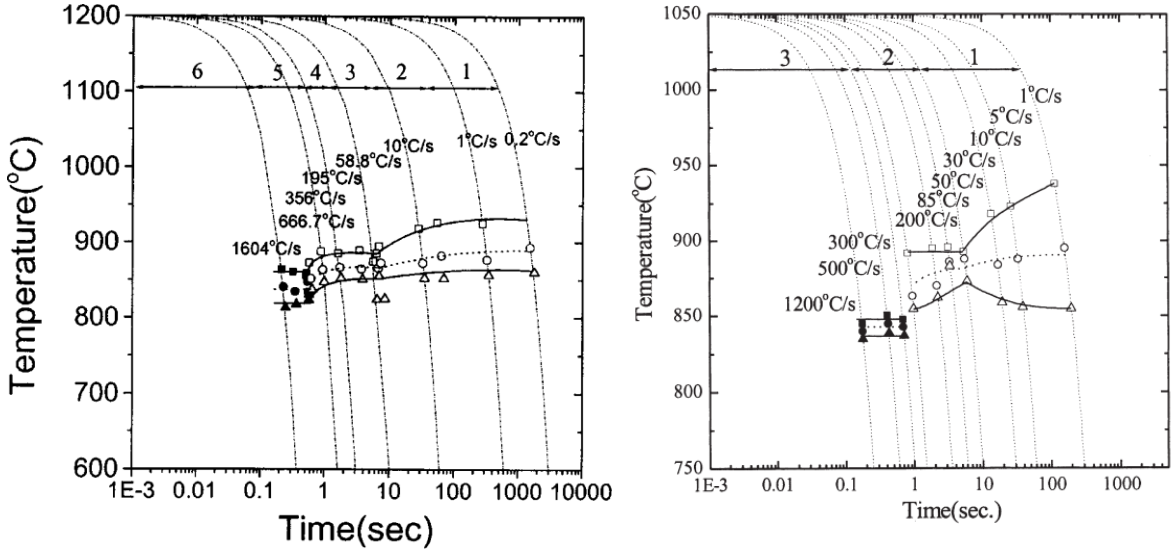

(a) (b)

Figure 2.13: Continuous cooling transformation curve: (a) grade 2 CP Ti: 1: platelike alpha, 2: serrated alpha, 3: acicular alpha, 4: acicular alpha + massive alpha, 5: acicular alpha + basketweave alpha + massive alpha, and 6: martensite [32]; and (b) grade 4 CP Ti: 1: platelike alpha + acicular alpha, 2: acicular alpha + massive alpha, and 3: lath type martensite [33].

Slow cooling rate (range 1 in Figure 2.13) gives rise platelike alpha (Figure 2.14) [32].

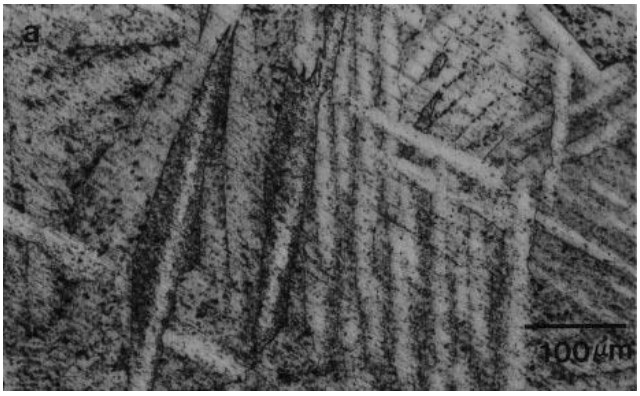

Figure 2.14: Optical micrograph of a grade 2 CP Ti at cooling rate 1 °C/s, showing platelike alpha [32].

2.1.4 Oxidation and diffusion bonding

2.1.4.1 Oxidation

When Ti is exposed to air, the oxidation product TiO_2 having tetragonal rutile crystal structure forms on its surface [1,34]. This oxide layer is often called scale or α-case. The high chemical affinity of titanium to oxygen which is higher than for titanium to nitrogen is the driving force for the rapid oxidation of titanium. Increased oxygen level strengthens the α phase and changes the deformation behavior of α titanium from a wavy to a planar slip mode [35]. Thus, less ductile α-case can result in the formation of surface cracks under tension loading and can cause low overall ductility of Ti or early crack nucleation under fatigue loading conditions.

High diffusion rates of oxygen at temperatures higher than 550°C leads to high oxidation rate of Ti which limits the practical application of titanium to 550°C. Various alloying elements such as Al, Si, Cr (> 10%), Nb, Ta, W, and Mo decrease the diffusion rate of oxygen through the scale [36].

Oxygen solubility in β-phase is lower (Figure 2.15, [37]).

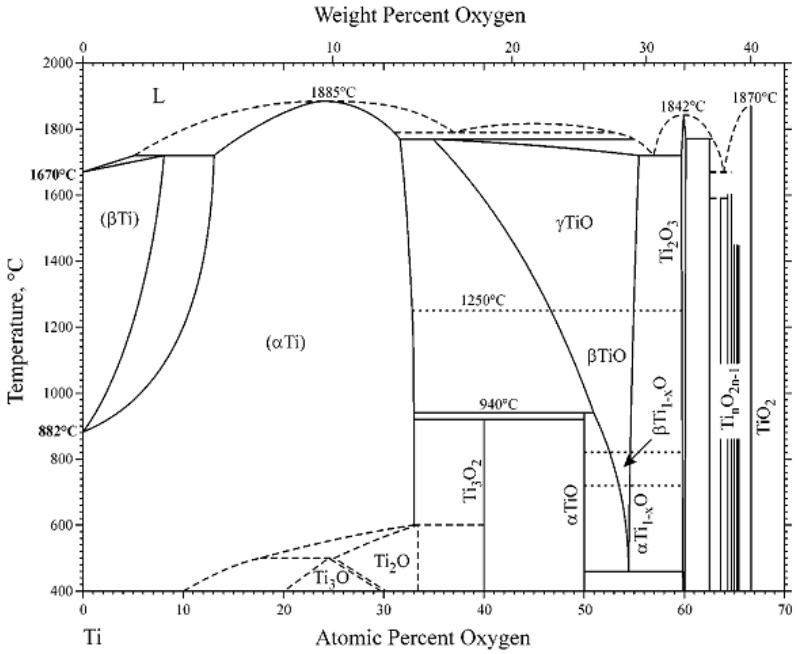

Figure 2.15: Ti-O phase diagram assessed by [38].

2.1.4.2 DIFFUSION BONDING

When two sheets of titanium alloy are placed in direct contact under a modest pressure and are heated to about 600°C or higher, the TiO_2 on the surface of the sheets dissolves, leaving pure surfaces in contact. Due to inter-diffusion two sheets bond together resulting in a bond that is imperceptible even during metallographic examination. This method of joining is called diffusion bonding. The capability of titanium for diffusion bonding is due to its propensity to dissolve its own surface oxide when heated to ≥ 550°C in vacuum or high purity inert gas (i.e. a nonoxidizing environment) [1]. However according to [39] CP titanium does not have clean faying surfaces because they have oxide films that prevent true metal-to-metal contact at the bonding interface. Only at temperatures higher than 900°C the electric resistance across bonding interface for CP titanium approaches that of the base metal [39]. In fact the metal-to-metal contact forms at temperature higher than 320°C and increases upon the increase of temperature [39].

Temperature is an important parameter of the diffusion bonding. Diffusion bonding at temperatures in the (α+β) phase field does not perturb the equiaxed microstructure of the pieces being joined. However the bonding process develops more rapidly at

temperatures in β phase region than those in α phase region [40] and the bonding process is accelerated by the α→β transformation [39].

Surface roughness of the pieces to be joined is another important parameter of the diffusion bonding. Tensile strength is higher when final surface grinding is performed with 1500 grade emery paper than with 600 grade emery paper. Even though roughening the faying surface leads to disruption of the oxide film (which facilitates diffusion bonding), it also leads to formation of voids at the bonding interface [41].

During diffusion bonding it is important to shield the bonding surfaces from air because pure titanium and titanium alloys are extremely reactive above 540°C [41]. The material can become embrittled by the interstitial absorption of hydrogen, nitrogen and oxygen gases, and it is advised to perform diffusion bonding in vacuum at a pressure of 10^{-5} to 10^{-4} torr [42].

In summary, diffusion bonding process requires heat, pressure, clean surfaces, and an inert environment [43]. The quality and ductility of the joint improves with increasing treatment temperature (the most important parameter), applied pressure, treatment time, and with decreasing roughness of the surfaces [44].

2.2 Ductile versus brittle fracture in HCP metals

This section discusses first which parameters ductility depends on, then the deformation modes and finally presents parameters that control ductile vs. brittle fracture in HCP metals.

In general the ductility of a metal is a function of grain size, temperature and strain rate. Ductility increases when:

(i) the grain size is decreased (however not valid for both very large grain and extremely fine grain polyscrystalline materials) [14];

(ii) the test temperature is increased;

(iii) the strain rate is decreased.

Fracture of titanium changes from ductile in the fine grained (1 and 20 μm) CP Ti [45] to brittle in coarse-grained CP Ti (~ 1mm) [46]. Salishchev and Mironov [47] reported a slight tendency for a decrease in the total plasticity of CP Ti when average crystallite size is refined from >10 μm to <1μm (Figure 2.16). At temperatures below 0.1 T_m (~ -100°C) CP Ti fails in brittle manner (cleavage) whereas at temperatures greater than 0.1 T_m additional slip modes become activated and failure occurs by ductile fracture [48]. Melting temperature for Ti is equal to 1670°C (Table 2.1).

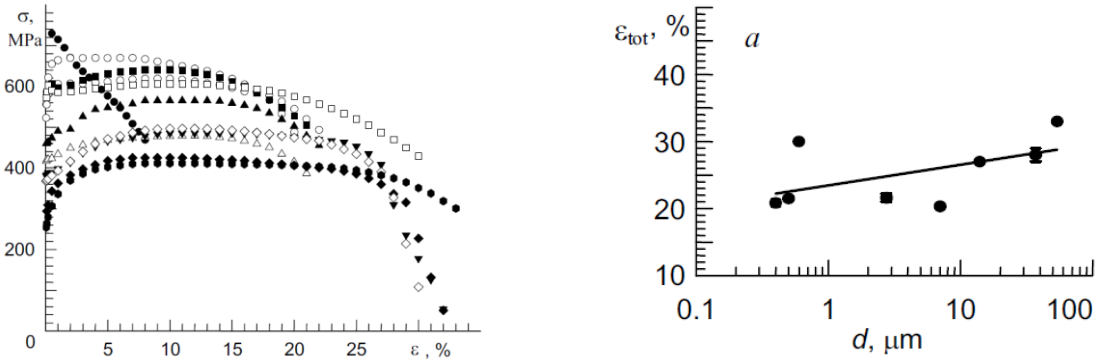

(a) (b)

Figure 2.16: (a) tensile stress-strain diagrams of CP Ti specimens with different grain size, d, μm: ~ 0.4 in the as-forged state (●), ~ 0.4 in the annealed state (○), ~ 0.5 (■), ~ 0.6 (□), ~ 2.5 (▲), ~ 3 (△), ~ 14 (▼), ~ 35 (◆), ~ 39 (◇), and ~ 54 (⬢) [47]; (b) effect of the average crystalline size on the total plasticity before fracture of CP Ti [47].

Ductility of CP Ti at room temperature was observed to decrease with increasing interstitial content [49]. Elevated oxygen concentrations (due to exposure to laboratory air at 650 °C for 420 h) negatively impact ductility and resistance to fatigue crack initiation of near-α titanium alloys [50]. Locally elevated concentrations of oxygen near the surfaces of air exposed samples changed the fracture mode from ductile, microvoid coalescence (Figure 2.17(a)) to brittle facet formation and grain boundary separation (Figure 2.17(b)) at stresses below the macroscopic yield point during quasi-static loading of material. During cyclic loading of air exposed samples similar features and an increased propensity for facet formation were observed.

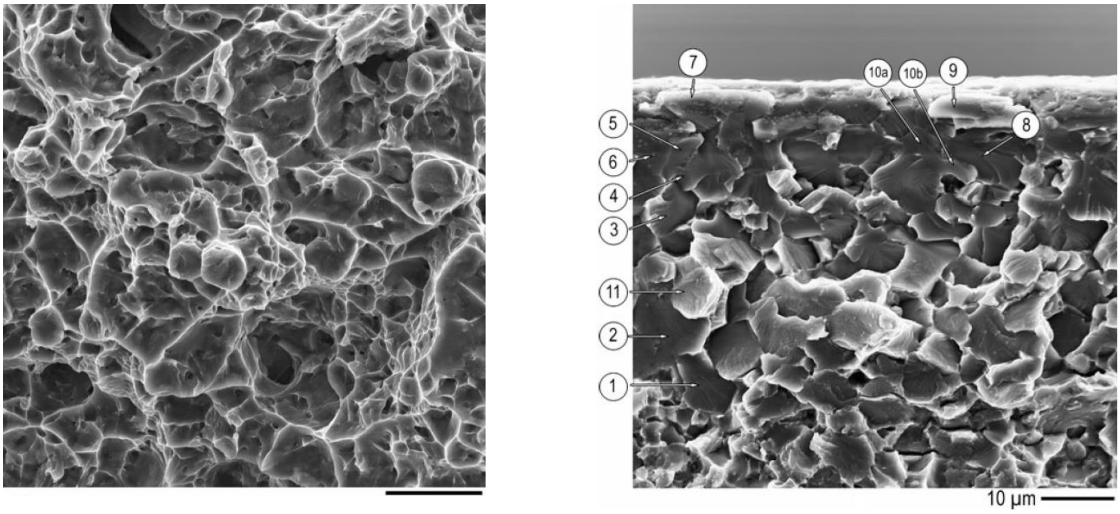

(a) (b)

Figure 2.17: SEM secondary electron images of near-α titanium alloy showing: (a) ductile microvoid coalescence in the as-received sample; (b) faceted fracture in the oxygen-rich, near-surface region of the sample [50].

With the embrittlement of titanium alloys exposed to air at high temperatures arises a need to reduce this embrittlement. Hansen et al. [51] invented a heat treatment to reduce the embrittlement of Ti alloys that become brittle after operating above 454 °C for extended periods of time because of alpha phase precipitates as a film in grain boundaries. The invented heat treatment cycle consists of: (i) heating the alloy above the alpha solvus temperature for a period of time sufficient to produce a fully beta phase microstructure, (ii) heating the alloy at a temperature about 150 °C below the alpha solvus temperature and holding for a period of time; (iii) cooling at a controlled rate to produce precipitates consisting of coarse, stable alpha phase particles generally situated in the grain boundaries. These alpha particles are much less harmful to the material than the grain boundary films of alpha phase discussed above. The decrease in dissolved oxygen content in the beta phase, thanks to its precipitation as alpha phase, or TiO_2, particles, increases the ductility of the alloy.

In addition to air embrittlement, several authors report the embrittlement of Ti caused by hydrogen [52–55].

2.2.1 Effect of deformation modes

There are two deformation modes in metals: slip and twinning. Their activation depends on temperature, environment and strain rate. Thus ductility also depends on these parameters. Fracture mechanisms maps identify the dominant fracture mechanism as a function of applied stress and test temperature. Fracture mechanisms map for titanium is presented in Figure 2.18 [48], and for some HCP metals in [56]. Figure 2.18 illustrates that depending on the test temperature and applied stress CP Ti fractures during monotonic tensile loading in any of the following ways: by cleavage, by ductile fracture, by intergranular creep fracture and by rupture.

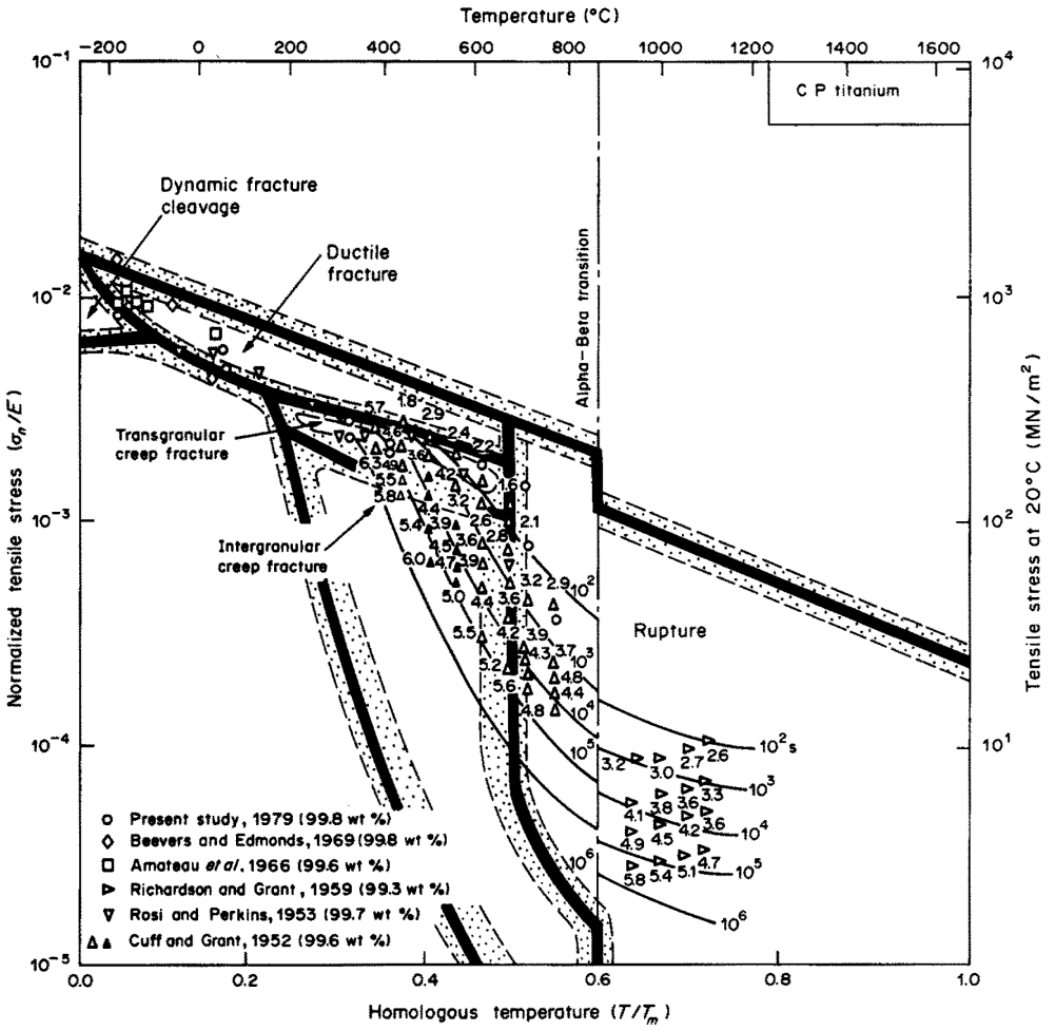

Figure 2.18: Fracture mechanism map of normalized tensile stress vs homologous temperature for CP titanium (references listed on the map, in order, are [46,57–60]) [48].

2.2.2 Parameters controlling ductile vs. brittle fracture in HCP metals.

Yoo [2] correlated the strength of HCP metals with cohesive energy ΔH_0^0:

(i) weak metals (Mg, Zn, Cd) have low cohesive energy (< 36 kcal/g-at.);

(ii) strong metals (all transitional metals – Ti, Co, Zr, Tc, Ru, Hf, Re and Os) have high cohesive energy (> 100 kcal/g-at.).

Indeed the lattice parameter decreases when more d-electrons are added in transition metal, meaning that the density, the cohesive energy and the elastic bulk modulus increase.

The plastic range of pure metal is correlated with the ratio of elastic bulk modulus to shear modulus *K/G*: a high value of *K/G* is associated with ductility, and a low value of *K/G* with brittleness [2].

Another ductility correlation study was made by Rice and Thomason [61]. They showed that crystals with wide cores of dislocations and small value of the parameter Ga/Γ ($\leq$ 7.5 to 10) are ductile, while crystals with narrow cores and large values of Ga/Γ are brittle (where G is the shear modulus, a is the lattice parameter and Γ is the surface energy). This is because the dislocations with larger core widths are more mobile and thus the plastic flow is easier.

Ductile fracture of HCP metals depends on the number of slip and twinning planes available [48]. Titanium, unlike other HCP metals like Mg, Be and Re exhibits ductile fracture at low temperatures (< 0.3 T_m) thanks to a large number of slip and twinning planes available. Brittleness of Cd-Mg alloy in which twinning is eliminated by making $c/a = \sqrt{3}$ confirms the importance of twinning [62].

Ductility of HCP metals is related to twinning:

(i) metals that exhibit extensive ductility (for example, Re, Zr and Ti) twin by both tension and compression types;

(ii) metals with limited ductility (for example, Zn and Be) twin only by the most common type, the $\{10\bar{1}2\}$ twin, which is a compression twin for Cd and Zn as $c/a > \sqrt{3}$ and a tensile twin for the rest of HCP metals [2].

Thanks to twinning the unfavorably oriented grains for slip and twinning are reoriented into a more favorable position upon twinning, thus the total plastic strain may be increased considerably.

In conclusion in hexagonal metals with reasonably high surface energies, the greater the number of operative twin modes, the larger the overall ductility is.

2.3 THE DUCTILE FRACTURE PROCESS

2.3.1 EXPERIMENTAL FACTS ON TI AND OTHER MATERIALS

Ductile fracture process consists of three stages: void nucleation, growth and coalescence [63–65]. While different macroscopic modes may be observed, all ductile fracture surfaces reveal a dimpled character which is a result of a set of generic micromechanisms of damage initiation and accumulation. These mechanisms are addressed next.

2.3.1.1 VOID NUCLEATION

Void nucleation occurs by decohesion at the particle-matrix interface or by particle cracking (Figure 2.19) [66–68]. For elongated inclusions loaded along their length, particle fragmentation is reported. In multiphase material systems damage can initiate in a brittle phase [69,70] or at interfaces. Table 2.4 summarizes factors favoring one mode of nucleation over the other.

Ductile fracture in CP Ti takes place by nucleation of voids and by their growth and coalescence [50] (Figure 2.17(a)). Commercial Ti alloys generally do not contain hard second phases or non-metallic inclusions, so voids are nucleated at slip band intersections with interfaces, including grain and phase boundaries, or because of plastic incompatibility at these locations [71,72].

Table 2.4: Key parameters in void nucleation and relative trends upon increasing the parameter for the microscopic mechanism [64].

Parameter	Type	Trend	
		Decohesion	Cracking
Matrix yield strength		↘	↗
Matrix hardening exponent		↘	↗
Particle elongation		↘	↗
Particle stiffness		↗	↗
Load orientation	Axial	↘	↗
	Transverse	↗	↘
Load triaxiality		↗	↘

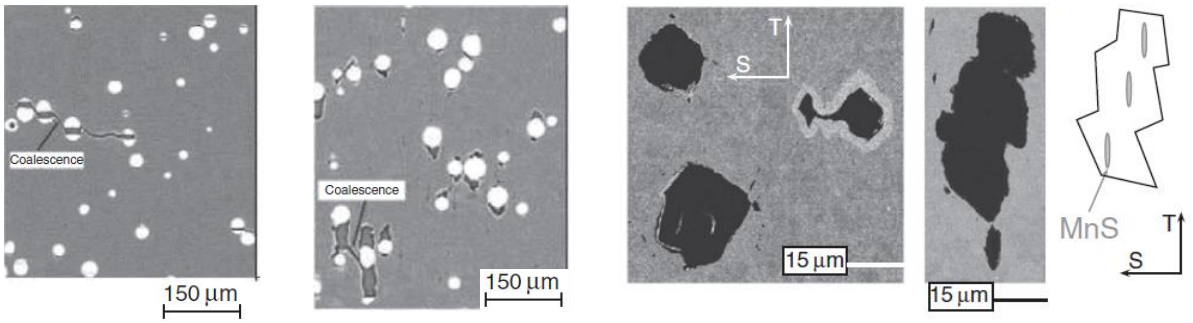

(a) (b) (c)

Figure 2.19: Micromechanisms of ductile fracture: (a) particle cracking, formation of penny-shaped cracks and void coalescence in a model metal matrix composite (hard matrix) [73]; (b) Particle–matrix decohesion and void growth to coalescence in a model MMC (soft matrix) [73]; (c) Void growth and coalescence in a C–Mn steel [74]. The Ni plating around the coalescing voids indicates that they are connected to the main crack.

Xue et al. [75] reported that shear bands are the preferred sites for nucleation, growth, and coalescence of voids in CP Ti and Ti–6Al–4V alloy (Figure 2.20) under high-strain-rate deformation ($\sim 10^4$ s^{-1}). The nucleation of micro-voids is considered as a result of the tensile stress inside shear bands. During nucleation stage of voids three voids with circular or elliptical shape are initiated within shear band, completely inside the band (Figure 2.20(a)). Most of the voids first grow to the width of the band and then are elongated to elliptical shape along the direction of the shear band

(Figure 2.20(b)). Further growth of these voids is accompanied with void elongation and rotation along the shear direction (Figure 2.20(c)). The third stage of void development is coalescence of voids and crack generation (Figure 2.20(d)). These elliptical voids tilt their long axis to a certain angle coalescence of a group of voids inside shear band. It was observed in experiments that growing shear bands form an approximately periodical pattern. This is called a self-organization phenomenon. The position of the shear band is determined by the location of geometrical imperfections or structural discontinuities (second phase particles, inclusions and grain boundary triple points) [76].

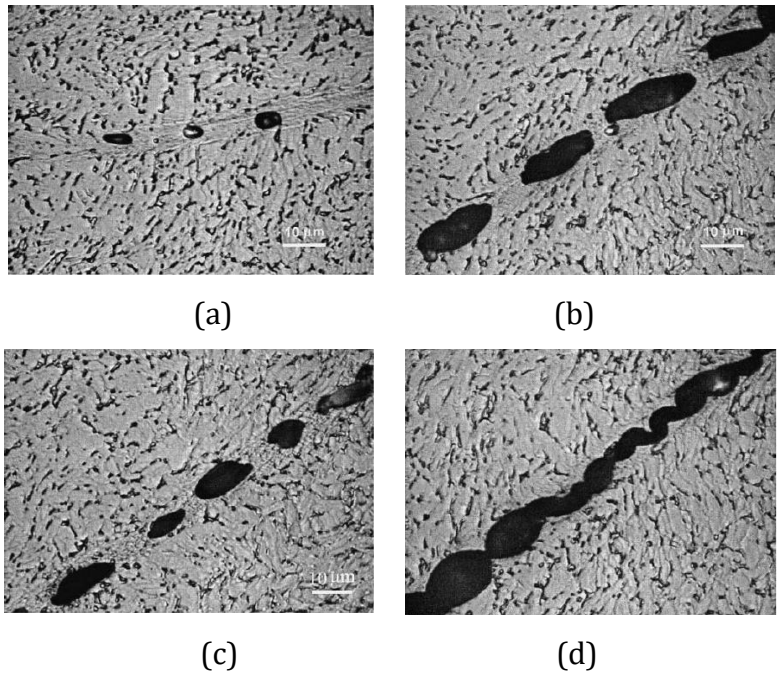

Figure 2.20: Void nucleation and growth inside a shear band in Ti–6Al-4V alloy: (a) nucleation of voids within a shear band; (b) growth of voids; (c) elongation and rotation of voids; (d) coalescence [75].

2.3.1.2 VOID GROWTH

Several techniques have been used to obtain information on void growth rate during plastic deformation including density measurements, interrupted tests, and x-ray tomography.

Marini et al. [77] and Garrison and Moody [78] used interrupted tests to measure void growth rates. The main results of these studies are that voids generally grow

exponentially with strain and that the stress triaxiality has an important effect on void growth. Mudry [79] performed measurements of the same kind on structural steel, but the void growth ratio was not measured in the direction of loading.

Pardoen and Delannay [80] assessed void growth rate via density measurements in copper bars containing copper oxide particles as main nucleation sites. Two main findings are: (i) overall porosity levels of about 0.01–0.015 were reached near failure and (ii) the rate of growth of porosity was found to be lower in the annealed material with higher hardening capacity.

Koss and coworkers [81,82] and Benzerga [74] measured void dimensions on metallographically polished sections of notched round bars using interrupted tests. Chae and Koss [81] used the general methodology of Beremin [67] and Marini et al. [77] combining local measurements with finite-element calculations. They mapped the local strains and stress triaxialities to the local porosities determined from void dimensions. They found that the value of local void area fraction at incipient coalescence is equal to 0.005±0.001.

Benzerga et al. [83] used interrupted tests to measure void size and porosity in a steel similar to the materials used by Beremin [67], Mudry [79], and Jablokov et al. [82] in terms of their inclusion content. The main void nucleation sites were elongated MnS sulfides and Al oxides. Main conclusions from this work are: (i) in the central region of the bars where void growth is maximum, void growth ratios varied between 3 and 10 under longitudinal loading and between 2 and 50 under transverse loading, depending on triaxiality level and growth direction, which is in contrast with [77]; (ii) void growth ratios larger than 10 are only realized for elongated voids in the short-transverse direction; (iii) the critical porosity was found to be about 0.02 under longitudinal loading and a little below 0.01 under transverse loading.

Margolin and Mahajan found that void length as a function of true strain for Ti-6Al-4V alloy is linear (Figure 2.21) [84]. They used a sectioning technique to measure the void length. For an equiaxed α microstructure, void growth depended on martensite plate lengths for a given aging treatment. For a mixed Widmanstatten plus

grain boundary α microstructure, void growth depended on prior β grain size and grain boundary α thickness. Same linear void growth behaviour was found in [85].

X-ray tomography allows in situ real-time examination of microscale ductile damage processes in three dimensions [64]. This technique helps to avoid destructive, often tedious cross-sectioning of test specimens. Babout et al. [86] assessed the ceramic particle growth in aluminium matrices along with damage mechanisms. Weck et al. [87] visualised void growth and coalescence in model samples made of high purity copper and Glidcop. Maire et al. [88] clearly visualised the damage steps (initiation, growth and coalescence) in aluminium alloys during interrupted and continuous in situ tensile tests in synchrotron X-ray tomography.

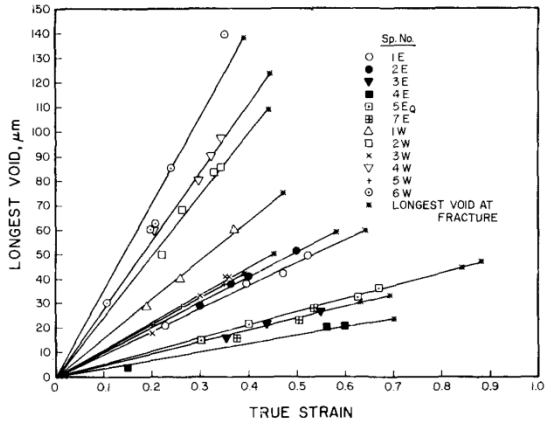

Figure 2.21: Longest void as a function of true strain in Ti-6Al-4V alloy [84].

Xue et al. [75] reported the void growth in CP Ti and Ti–6Al–4V under high-strain-rate deformation takes place inside shear bands (Figure 2.20(b) and (c)) (see Subsection 2.3.1.1 for more details).

2.3.1.3 VOID COALESCENCE

Void growth is usually terminated by void linking or coalescence. There are three modes of void coalescence: (i) internal necking, (ii) void coalescence in a microshear band or 'void-sheet' coalecence; and (iii) formation of voided columns or "necklace" coalescence. The mode of void coalescence depends on microstructural factors, loading conditions, and matrix plastic flow properties [74]. Internal necking is the most commonly observed mode [89] (Figure 2.22(a)). Void coalescence in a microshear

band, also known as “void-sheet” coalescence is the second most commonly observed mode [90] (Figure 2.22(b)). In this mode the stable void growth is suddenly terminated when voids are still quite apart, thus resulting in decrease in local and perhaps global ductility. Coalescence in a shear band depends on configuration and the inclination of the microshear band depends on the relative positions of the voids. A third mode of void coalescence is the formation of voided columns or “necklace” coalescence [74] (Figure 2.22(c)). This type of void coalescence is quite prominent in steels containing elongated MnS inclusions loaded along the rolling direction. It is favored at low stress triaxialities. Even though coalescence in columns has little effect on macroscopic ductility, it may lead to microdelaminations.

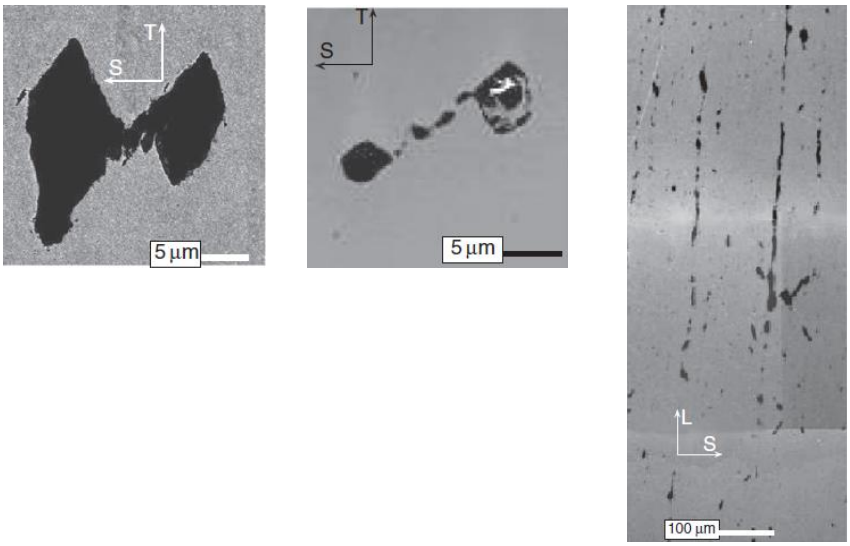

(a) (b) (c)

Figure 2.22: Modes of void coalescence: (a) internal necking [91]; (b) coalescence in a microshear band [74]; (c) “Necklace” coalescence or coalescence in columns [74]. Loading is axisymmetric in (a) and (b) and plane strain in (d). Major loading axis is vertical for all figures.

Figure 2.23 depicts how the above fundamental mechanisms affect the macroscopic load–displacement response in a typical notched bar experiment. Void nucleation and growth (as well as a few isolated and inconsequential void-coalescence events) contribute to damage accumulation prior to point (c) in Figure 2.23. The onset of a macroscopic crack via the coalescence of the two or three largest voids results in the change in slope of the load–displacement curve at point (c). The descending part of the

curve after point (c) corresponds to the stage of crack propagation inside the bar. The faster load drop in the latter stages is associated with the formation of shear lips. Although the two pieces seem separated in the two-dimensional (2D) view (Figure 2.23), they are in fact still connected in 3D by ligaments that are not visible. Final point (f) depicts fracture of the sample.

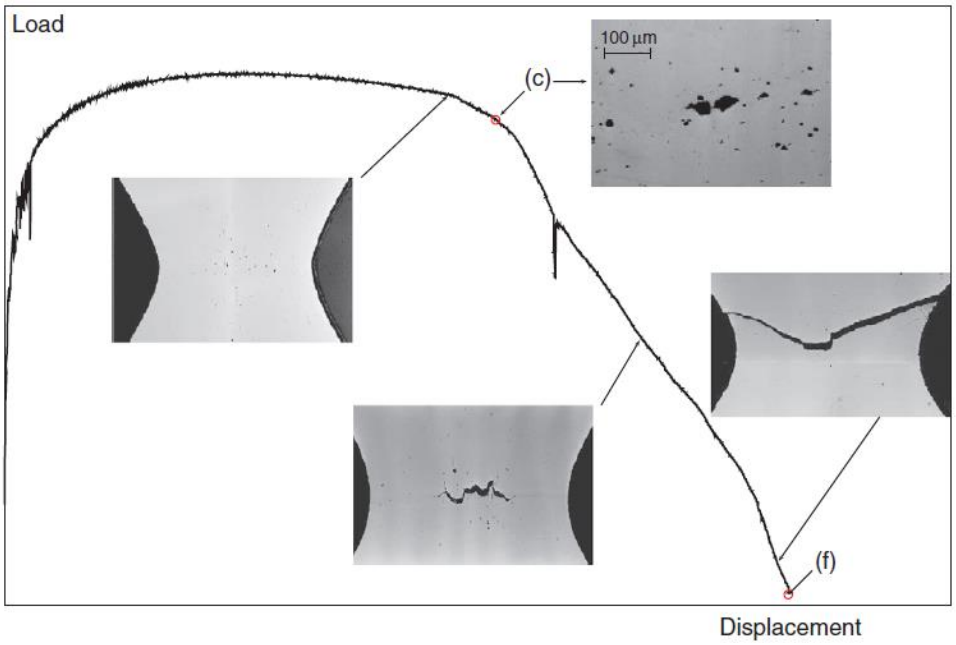

Figure 2.23: Phenomenology of ductile fracture in round notched bars of high-strength steel: damage accumulation, initiation of macroscopic crack, crack growth, and shear lip formation [74].

Weck and Wilkinson [92,93] investigated modes of ductile fracture using "model" systems in which holes were laser drilled into plates. Figure 2.24 clearly shows that the failure modes (internal necking or shear) depend strongly on the arrangement of the holes. Hosokawa et al. [94] used similar approach but by means of continuous X-ray tomography. They measured the plastic strain at the onset of void coalescence (instead of simple linkage) for the first time.

Margolin and Mahajan found that the coalescence of voids in Ti-6Al-4V alloy occurs as a result of local growth of independently formed voids, rather than as a result of voids forming ahead of a major void and later joining the leading voids [84]. The latter mechanism of void growth would cause accelerating growth [85] rather than linear behaviour found in their study.

Xue et al. [75] reported the void coalescence in CP Ti and Ti–6Al–4V under high-strain-rate deformation takes place inside shear bands (Figure 2.20(d)) (see Subsection 2.3.1.1 for more details).

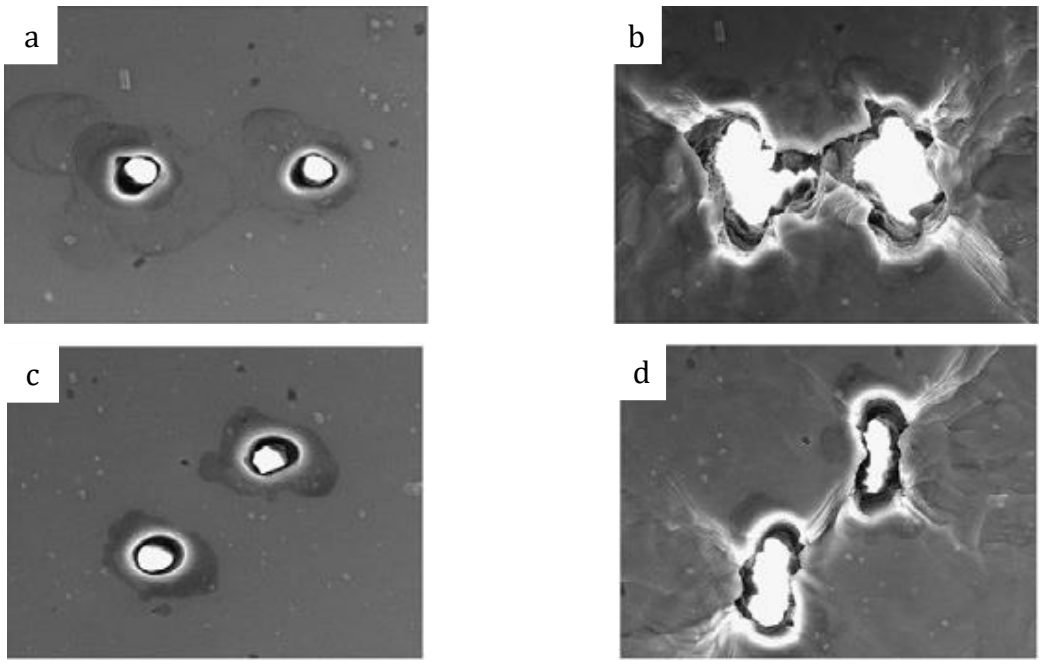

Figure 2.24: In situ SEM images of the deformation sequence of aluminum alloy 5052 containing various hole configurations and taken at various far field true strains. Two holes oriented at 90° with respect to the tensile direction (vertical): (a), (b) 0.220. Two holes oriented at 45° with respect to the tensile direction (vertical): (c) 0, (d) 0.233. Initial void diameter was 10 μm [92].

2.3.2 Parameters affecting ductile fracture

2.3.2.1 The effect of hydrostatic pressure on the nucleation and growth of microvoids.

A highly compressive pressure P increases the microvoid nucleation strain and possibly even eliminates the microvoid nucleation if P is sufficiently high. Experimental results (Figure 2.25(a)) confirm that microvoid nucleation is suppressed by the effects of a large P and is virtually eliminated prior to fracture when P reaches a magnitude of the order of the uniaxial yield stress σ_y [95–99].

Regarding void growth the effects of P are as follows: (i) for an effective mean-normal stress of zero ($P = -\sigma_m$) the extensional void growth a/a_0 is considerably lower and the compressive growth $b/b_0=c/c_0$ is considerably higher than without P; (ii)

changing the effective mean-normal stress level ($\sigma_m + P$) to $-0.5\sigma_y$ and then to $-\sigma_y$ reduces the extensional growth a/a_0 and increases the transverse compressive growth $b/b_0=c/c_0$; this effect is more pronounced for non-hardening plasticity in comparison to linear-hardening plasticity.

Figure 2.25(b) shows that an increase in hydrostatic pressure P from zero to 300 MPa increases the microvoid nucleation strain from ~0.5 to ~0.9.

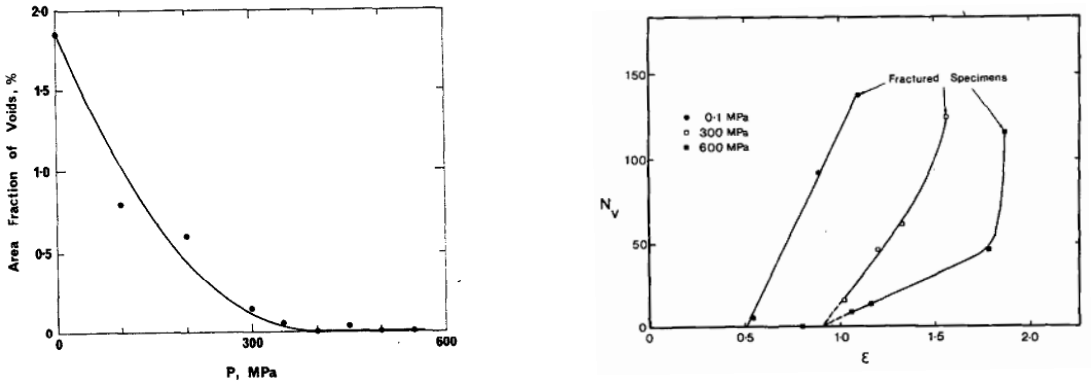

(a) (b)

Figure 2.25: (a) variation of area fraction of voids in α brass tension specimens with pressure [96]; (b) variation in the number of voids in the centre of the necked region of steel with strain [100].

2.3.2.2 THE EFFECTS OF TEMPERATURE AND STRAIN RATE ON THE NUCLEATION, GROWTH AND CRITICAL CONDITIONS FOR COALESCENCE OF MICROVOIDS.

In the temperature range 0.1 to ~ 0.7 T_m, temperature and strain rate have an approximate inverse effect on material flow stress: i.e. the effects on flow stress of an increase in strain rate are broadly equivalent to a reduction in test temperature [101–103].

Experimental results [104–106] show that microvoid nucleation is generally reduced by elevated temperatures and lower strain rates, and can be virtually eliminated at high temperatures [103] to give tensile failure by complete rupture (the 100% reduction in area of an external neck). On the contrary increased strain-rates and reduced test temperature promote microvoid nucleation [104,105].

Once microvoids have been nucleated, subsequent growth of voids is influenced by temperature and strain rate through their effect on the material yield stress and work-

hardening rate. The increased test temperature and reduced strain rate reduce both the material yield stress and work hardening rate, and promote growth of microvoids.

Temperature and strain rate influence the material yield stress and therefore influence microvoid coalescence [107].

For a given test temperature, the stress σ can be related to strain rate $\dot{\epsilon}$ by a simple power law of the form:

$$\sigma = \sigma_0 \dot{\epsilon}^m$$

where σ_0 is a stress related parameter,
m is the strain rate sensitivity index.

Negative values of the strain rate sensitivity index *m* promote ductile fracture at smaller void-growth strains. General effects of changes in the strain rate sensitivity index are as follows: (i) when $m>0$, material flow stress increases with strain rate; (ii) when $m=0$, flow stress is insensitive to strain rate, and (iii) when $m<0$, flow stress decreases with strain rate.

2.3.2.3 THE EFFECT OF GRAIN ORIENTATION ON DUCTILE FRACTURE.

Several studies have focused on the effects of texture and microstructure on mechanical properties anisotropy of different materials [108–110]. The mechanical properties of single-crystal α-Ti are highly anisotropic [111].

A range of different length scales are typically found in titanium alloys, where the behaviour of individual laths, colonies of laths and prior beta grains influence the macroscopic mechanical properties [112]. Crystal orientation was shown to affect the friction characteristics of titanium single crystals in vacuum [113] and the fracture toughness of Ti alloy [114]. Orientation influences mechanical properties and fracture behavior of Ti [26,115]. This is due to the fact that activation of slip and twinning systems depends on crystal orientation (more details are presented in Subsections 2.1.2.2 and 2.1.2.3).

The $\alpha \rightarrow \beta \rightarrow \alpha$ phase transformation can change the microstructure and texture of inherited material and results in significant changes in active slip and twin

systems [116]. Elongation, yield and tensile strength of as-received CP Ti, which had a microstructure of recrystallized α grains and dispersed β phase, were greater in transverse direction than in direction parallel to the rolling. This result was explained in terms of operating slip systems. When the tensile axis is parallel to the rolling direction, deformation must be accommodated by the operation of easier $(1\bar{1}00)\langle 11\bar{2}0\rangle$ prismatic slip systems. However, when the tensile axis is parallel to the transverse direction, the deformation is more difficult $(0002)\langle 12\bar{1}0\rangle$ basal or $\langle c+a\rangle$ pyramidal slips. After allotropic phase transformation, CP Ti consists of a randomly distributed Widmanstatten microstructure, which resulted in lower elongation than as-received CP Ti [116]. Yield strength of a specimen with Widmanstatten microstructure tested in transverse direction was greater than that in rolling direction. This result was explained as follows: (i) most basal planes were aligned with transverse direction; (ii) the prismatic $\langle a\rangle$ slip system which has low critical resolved shear stress, could be an active deformation system in the specimen tested in rolling direction; (iii) in the specimen tested in the transverse direction, the hexagonal c-axis extension caused the restriction of shear and slip deformation systems. Thus because the plastic flow was difficult to proceed, fracture mechanism in the sample tested in tensile direction was intergranular and in rolling direction was a combination of intergranular and dimple fracture.

Bantounas et al. [117] examined the effect of grain orientation on fracture morphology during high-cycle fatigue of Ti alloy (Figure 2.26). They found that facets on fracture surface are due to near-basal plane cracking and observed in grains oriented with their c-axis between 0° and 90° to the principal loading direction. Grains responsible for initiation were limited to orientations between 15° and 40°. The remaining orientations were shown to accommodate faceted crack growth. High-cycle fatigue performance was found inversely proportional to the number of unfavourably oriented grains (grains with its c-axis near to the loading direction). Similar results were reported in [118].

Strong anisotropic behavior of CP Ti was demonstrated in [27,119], Figure 2.27. Figure 2.27 illustrates three curves obtained in simple shear tests. The observed

anisotropic behavior is explained by the influence of the loading orientation on the activation of different families of slip systems and subsequent texture evolution.

Herbig et al. [120] used X-ray diffraction contrast tomography combined with propagation-based phase-contrast tomography to get a full picture description for the analysis of local crack growth rate of short fatigue cracks in three dimensions: the three-dimensional crack morphology at different propagation stages, and the shape and orientation of the grains around the crack in the metastable beta titanium alloy Ti 21S (BCC) (Figure 2.28). An animated 3-D view of Figure 2.28(a) showing the different growth steps of the crack as well as all the grains intersecting the fracture surface can be found in the web version of the paper [120].

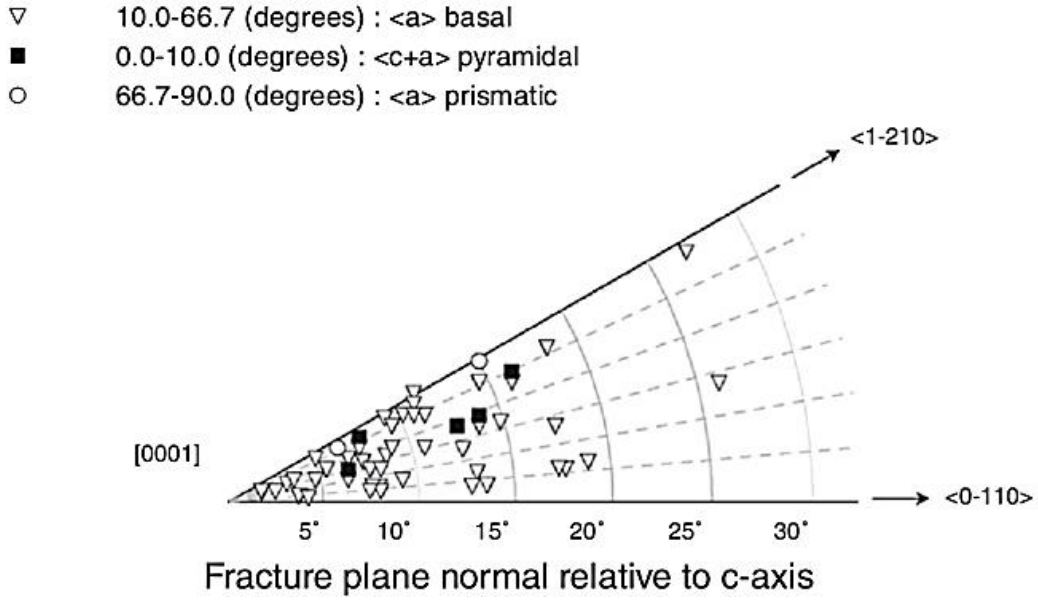

Figure 2.26: An inverse pole figure (IPF) showing the orientation of the facet plane normal relative to the c-axis of each fractured grain [117].

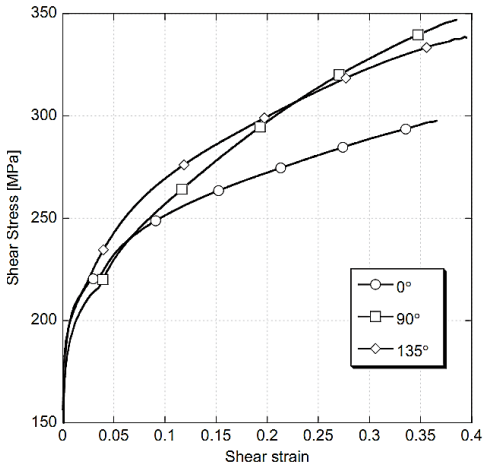

Figure 2.27: Experimental simple shear stress-strain curves for CP Ti deformed at 0°, 90° and 135° from rolling direction [27].

Bieler et al. [121] examined the deformation behavior of a Ti–6Al–4V alloy by orientation imaging microscopy and found that, during hot tension at 815°C, at the stage of prefracture, pores nucleate along the boundaries of grains one of which has a c-axis parallel to the tensile axis.

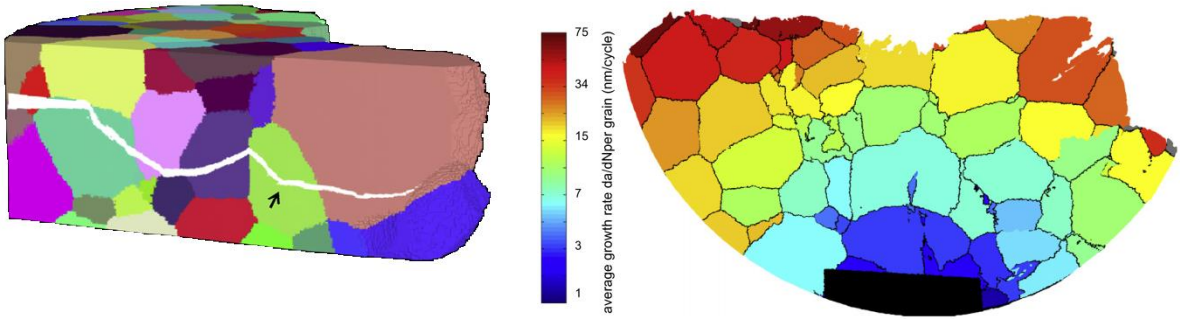

Figure 2.28: (a) Three-dimensional rendition of the fatigue crack after 75.5 K cycles (the fatigue load is applied vertically). 2-D view of the crack path on a plane cut in the bulk of the sample. Changes in the direction of the crack can be correlated with the presence of grain boundaries, but can also be observed within a grain (arrow). (b) Average crack growth rate for each individual grain crossed by the crack [120].

Khasegava et al. [122] studied the effect of texture in CP Ti sheets on the normal anisotropy coefficient $R = d\varepsilon_y/d\varepsilon_z$ and the limiting degree of drawing. They showed that an increase in R from 1.5 for sheets with a prismatic texture to 6.5 for sheets with a basal texture led to an increase in the limiting degree of drawing from 2.4 to 2.8.

Betsofen et al. [123] related the high ductility of the PT3Vkt α titanium alloy to the fact that it has a ratio of critical shear stresses in the operating slip and twinning systems such that the material is virtually isotropic with respect to tensile loads. This specific feature minimizes the effect of the incompatibility of deformation in grains with different orientations during tension, which is the main cause of the fracture of titanium alloys [121].

Bieler et al. [124] distinguished two types of grains in CP Ti: soft and hard grains. Using strains measured with the focused ion beam (FIB) deposited markers, they illustrated that hard grains (with the c-axis toward the tensile axis) generally deformed about half as much as soft grains during 4-point bending. They found a statistically significant correlation between the prismatic dislocation slip in soft oriented grains and nucleation of twins in hard oriented grains. They suggest that twinning plays an important role in nucleation damage in Ti as a result of either the large shear strain for twins, or from subsequent plastic deformation incompatibility at the twin boundary after the twin formation.

Umakoshi et al. [125] investigated anisotropy in fracture behavior and toughness of Ti_3Al single crystals using micro-compact tension specimens with a notch cut along (0001) or along the direction tilted by an angle (ϕ) from (0001). Their results indicated that for specimens with $\phi = 0°$ and 30°, fracture occurred in a brittle manner showing low fracture toughness value, while a high fracture toughness value was obtained for specimens with $\phi = 90°$. In fact there is a great difference in strength and ductility among slip systems in Ti_3Al. Activation of prism, basal and pyramidal slips occurred more easily in this order [126–128]. Prism slip occurred homogeneously under a low applied stress and adequate ductility was obtained. On the contrary, slip on the basal plane showed coarse slip bands resulting in rough steps on the specimen surface, often susceptible to brittle fracture.

2.3.3 DUCTILE FRACTURE MODELLING

Metal plasticity may be viewed and thus modelled at different length scales (Figure 2.29) [129]. With time, research was moving from the right (macroscopic theory) to the left (atomistics) and now is focused on connecting them in both

hierarchical and concurrent ways (multiscale modelling). Ductile fracture models were recently reviewed in [63–65].

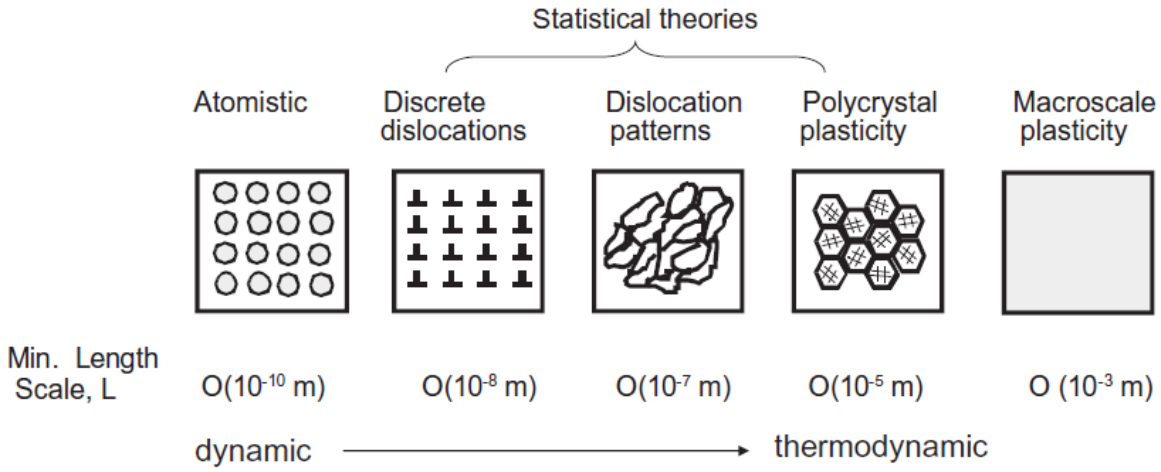

Figure 2.29: Hierarchy of length scales in metal plasticity ranging from atomic (dislocation cores) to patterns of dislocations to multiple grains to macroscopic scale [129].

2.3.3.1 VOID NUCLEATION MODELLING

Void nucleation criteria are based either on dislocation theory for crystalline materials or on pure continuum mechanics. A necessary condition for the nucleation of microvoid is that stress, strain or energy reaches some critical value. The stress criteria is necessary for breaking the bonds and the energy criteria for the creation of new surfaces at the inclusion/matrix interface. The energy criteria is satisfied at the very onset of plastic deformation for particles bigger than 25 nm in diameter [130]. For inclusion sizes under about 1 μm, dislocation models are required to describe the microvoid nucleation process; for inclusions bigger than 1 μm, the plastic continuum models are applicable [107].

Analytical models

Argon et al. [89] suggested that for inclusion larger than 1 μm the critical condition for microvoid nucleation, by decohesion of the particle/matrix interface, is represented by:

$$\overline{\sigma} + \sigma_m = \sigma_c$$

where $\bar{\sigma}$ is the equivalent stress (Von Mises stress), σ_m is the mean normal stress, and σ_c is critical stress for void nucleation.

This equation was developed for a small volume fraction of circular inclusions.

The primary difference between this criterion for microvoid nucleation and that of sub-micron sized particles developed by Goods and Brown [131] is that the parameters in this equation are all independent of particle radius.

Helbert et al. [132] proposed the nucleation criteria corresponding to voids at the α/β interface in α/β titanium alloys. This macroscopic nucleation criterion:

$$\Sigma_m = f(\varepsilon_{peq}) = A + Bexp(-C\varepsilon_{peq}^a)$$

where Σ_m is the hydrostatic stress,
ε_{peq} is the von Mises equivalent plastic strain,
ε_{peq}^a is the nucleation strain,
A, B and C are experimentally determined parameters,

was explained with the help of microscopic observations.

Numerical models

A continuum model for void nucleation by inclusion debonding was proposed (Figure 2.30) [133–135]. Figure 2.31 illustrates predicted modes of void development for various interfacial strength σ_{max}. For debonding to occur both the energy and a maximum load and/or displacement have to be overcome.

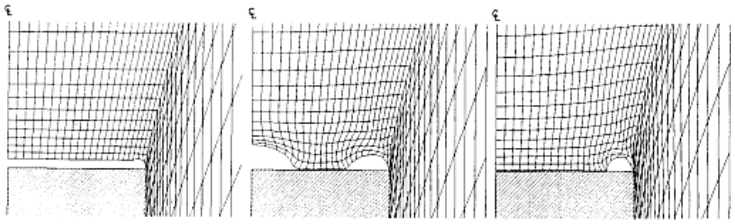

(a) (b) (c)

Figure 2.30: Deformed finite element meshes for different relations between the interface strength σ_{max} and the yield stress of the matrix σ_0: (a) $\sigma_{max}/\sigma_0 = 3$; (b) $\sigma_{max}/\sigma_0 = 5$; (c) $\sigma_{max}/\sigma_0 = 6$ [135].

Segurado and Llorca [136] used cohesive zone models to implement the decohesion event into 3D finite element simulations (Figure 2.31). Figure 2.31 illustrates the effect of the interfacial fracture on the pattern of the accumulated plastic strain in the matrix. The maximum plastic strains were concentrated in a very thin layer surrounding the rigid sphere before decohesion (Figure 2.31(a)), then after decohesion they spread very quickly throughout the cylindrical cell (Figure 2.31(b)).

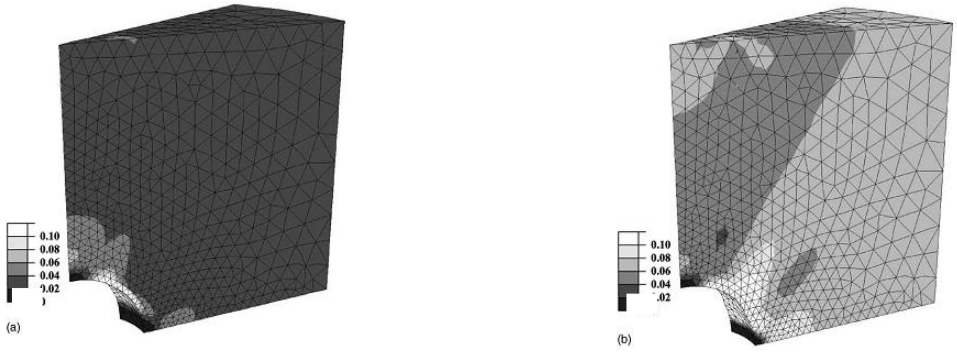

(a) (b)

Figure 2.31: Contour plots of the accumulated plastic strain in the matrix: (a) $\epsilon_z = 3.5\%$ and (b) $\epsilon_z = 8.8\%$ [136].

Katani et al. [137] showed using finite element (FE) model that that void nucleation in Ti-6Al-4V alloy start from low strength and soft phase (α) which is in good agreement with experimental observations [138,139]. They imported a microstructure SEM image with recognised α and β phases into a FE model and represented α phase by the Gurson–Tvegaard–Needleman model and β with elasto-plastic behavior [140].

Dunne and Katramados [141] observed void nucleation, growth and coalescence in two-phase, near-alpha, titanium alloy IM1I834 under hot working conditions. They developed a micro-mechanical model for void nucleation based on a debonding process between primary α particles and β matrix. They developed the FE model and examined the stress sensitivity of void nucleation within the particle-matrix system. Their results are in agreement with other phenomenological approaches for most stress states.

The first stage of ductile fracture still remains very poorly understood due to complexity of chemistry, physics and mechanics of real second-phase particles embedded in a given matrix [65]. However 3-D X-ray tomography should contribute to

a better knowledge of void nucleation as it provides a direct observation of the phenomenon.

2.3.3.2 VOID GROWTH MODELLING

Different models of void growth have been proposed; many of them are based on the Rice and Tracey (RT) [142] model and/or the Gurson model [143].

Rice and Tracey model

Continuum plasticity models of void growth have been developed for an isolated cylindrical void by McClintock [144] and initially spherical void by Rice and Tracey [142]. The case of a spherical void is more realistic and thus will be reviewed in this section. The Rice and Tracy model evaluates the growth of an initially spherical void of radius R in an infinite, rigid, perfectly plastic material subjected to a uniform remote strain field $\dot{\epsilon}_{ij}$ and remote stress field $\sigma_{ij} = S_{ij} + \sigma_m \delta_{ij}$, where S_{ij} is the deviatoric stress tensor, σ_m is the mean normal stress and δ_{ij} is the Kronecker delta. The stress-strain field is characterised in terms of principal components $\dot{\epsilon}_1 \geq \dot{\epsilon}_2 \geq \dot{\epsilon}_3$ by the Lode variable $\nu = -\frac{3\dot{\epsilon}_2}{\dot{\epsilon}_1 - \dot{\epsilon}_3}$. The analytical solution for the rates if growth is in the principal strain rate directions 1, 2, 3 is:

$$\dot{R}_i = \left\{ (1+E)\dot{\epsilon}_i + \left(\frac{2}{3}\dot{\epsilon}_j \dot{\epsilon}_j\right)^{1/2} D \right\} R \qquad (2.1)$$

where $(i, j) = 1, 2, 3$,

$(1 + E) \approx 5/3$ for linear hardening, and low values of σ_m with non-hardening,

$(1 + E) \approx 2$ for high values of σ_m with non-hardening,

$D = 0.75\, \sigma_m / Y$ for linear hardening,

$D = 0.558 \sinh\left(\frac{3}{2}\frac{\sigma_m}{Y}\right) + 0.008\upsilon \cosh\left(\frac{3}{2}\frac{\sigma_m}{Y}\right)$ for non-hardening.

The first term of the equation (2.1) is responsible for the shape-change without a change in volume and is affected by the deviatoric part of the stress tensor. The second term expresses the volume (or dilatational) change of the void without changing its shape and is affected only by the hydrostatic part of the stress tensor.

Thomason [107] integrated the equation (2.1) under the conditions where the void no longer remains spherical and obtained the following general expressions for the three principal radii of the ellipsoidal void:

$$R_1 = \left(A + \frac{3+\nu}{2\sqrt{\nu^2+3}}B\right)R_0 \tag{2.2a}$$

$$R_2 = \left(A - \frac{\nu B}{\sqrt{\nu^2+3}}\right)R_0 \tag{2.2b}$$

$$R_3 = \left(A + \frac{(\nu-3)B}{2\sqrt{\nu^2+3}}\right)R_0 \tag{2.2c}$$

where $A = \exp\left(\frac{2\sqrt{\nu^2+3}}{3+\nu}D\epsilon_1\right)$,

$B = \left(\frac{1+E}{D}\right)(A-1)$,

ϵ_1 is the total logarithmic strain integrated over the total strain path from initial undeformed state to the current void geometry (R_1, R_2, R_3).

Equations (2.2) have been evaluated for a wide range of stress triaxialities (mean-normal stresses σ_m/Y), in both the non-hardening and hardening condition (Figure 2.32). Figure 2.32 illustrates the sensitivity of void growth to both the mean-normal stress level and the state of hardening in the matrix.

The Rice and Tracey model (equations (2.2)) was validated by comparing the present theoretical results with the experimental results by Atkinson [145,146] who observed by TEM the void nucleation at SiO_2 particles in a Cu-SiO_2 alloy system. Further confirmation of the general validity of the Rice and Tracey model has been obtained by Le Roy et al. [68] who found a good agreement between experimental results of area fraction of voids as a function of strain for low-, medium- and high-carbon steels up to a strain $\epsilon_1 \sim 0.6$ and Rice and Tracey model. At higher strains the authors introduced a dual-population model of void nucleation assuming that damage results from the superimposed effect of two nucleating population of particles (spherical and elongated).

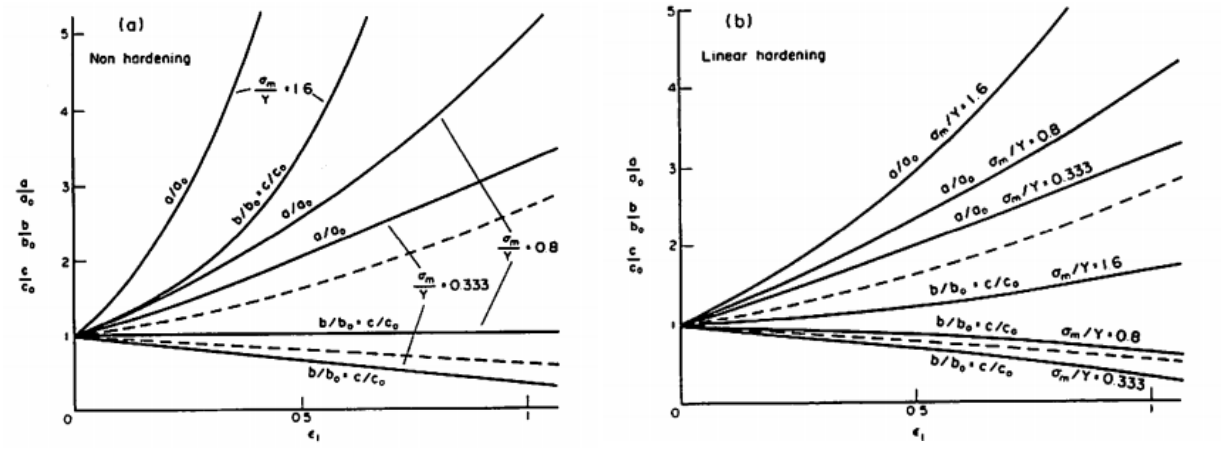

Figure 2.32: The effect of increasing plastic strain on the principal radii (a, b, c) of an initially spherical void ($a_0=b_0=c_0$) in uniaxial tension (ν=+1) at various mean normal stresses σ_m/Y. (a) Non-hardening and (b) linear hardening material. The dotted lines show the change in void dimension that would occur without any amplification of the basic uniform strain field ($\epsilon_1, \epsilon_2, \epsilon_3$) [107].

A version of RT model accounting for the shape change has also been developed [107,142]. These models have been extended by subsequent studies in order to take into account interaction between neighboring voids [77,147] or strain hardening [80,148,149].

The Rice and Tracey expression for the average rate of growth

$$\frac{dR}{R} = \alpha_{RT} \exp\left(\frac{3}{2}T\right) d\varepsilon$$

where R is the actual radius of the cavity,

ε is the equivalent plastic strain,

T is triaxiality,

α_{RT} is a constant equal to 0.283,

was revised by Huang using additional velocity fields [150]. Huang obtained similar results but with:

$$\alpha = 0.427 \text{ for } T > 1$$

$$\alpha = 0.427T^{1/4} \text{ for } 1/3 \leq T \leq 1$$

Marini [77] found higher values for α when calibrating the Rice and Tracey model using experimental measurements because the porosity is finite. Budiansky and al.

[148] generalized the RT model to deal with a Norton-Hoff viscosity law $\sigma = \sigma_0 \dot{\varepsilon}^m$, which applies equally to work-hardenable material.

Gurson model

A second broad family of more complex void growth models consists of constitutive models for porous elastoplastic or viscoplastic media. The most used of these models is the Gurson approach [143], which has led to various extensions [83,151–156].

Berg [157] proposed a model that was subsequently developed in the work of Gurson [143], Yamamoto [158] and Tvergaard [151]. This model assumes that the void growth can be fully described by the dilational-plastic response of an elastic-plastic continuum (matrix) containing an imaginary distribution of spherical microvoids. The matrix obeys a standard Von Mises yield criterion and associated flow rule. A Von-Mises yield surface is represented, in principal stress space, by a cylinder (Figure 2.33(a)). Two cases are possible: (i) the material deforms elastically if the stress state applied on the material lies inside the cylinder, and (ii) the material deforms plastically if it is on the cylinder. Thus if a tensile hydrostatic stress σ_m is applied onto the Von Mises material, the material will not yield. Figure 2.33(b) shows how the dilational plasticity models presented here transform the cylindrical yield surface into a truncated cylinder. A hydrostatic tension will now lead to plastic deformation as observed experimentally.

Gurson modelled the weak dilational plastic response of a body containing microvoids by a unit spherical cell with a single central void. According to Gurson, the yield surface is given by the following equation:

$$\phi = \frac{\sigma_n^2}{\sigma_{ys}^2} + 2f \cosh\frac{3\sigma_m^2}{2\sigma_{ys}^2} - (1 - f^2) = 0$$

where σ_n, σ_{ys} and σ_m are the Von-Mises equivalent, yield and mean normal stress respectively, and f is the void volume fraction.

As in the Von Mises yield criterion, the condition for plastic flow is met when $\phi = 0$.

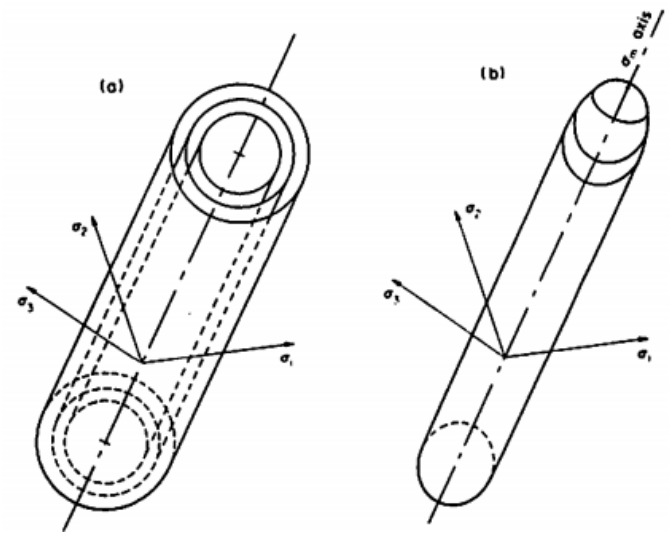

Figure 2.33: (a) The yield and loading cylinders for the case of an assumed isotropic hardening effect; (b) possible truncation of the yield cylinder at high values of mean stress σ_m for a solid containing a volume fraction of microvoids [107].

It was soon recognized that the proposed yield surface was unable to represent fracture and coalescence. In addition, unit cell simulations showed that void growth rates were not accurately predicted. This is why Tvergaard and Needleman [159] modified the expression of the original Gurson yield surface which is presented in Section 2.3.3.3 on void coalescence.

Other extensions of the Gurson model were proposed in the literature [63,64,160]. These modifications take into account several factors including: matrix kinematic hardening, rate dependency and viscoplasticity, plastic anisotropy and void shape effects.

The Benzerga and Besson model is an extension of the Gurson model accounting for plastic anisotropy effects [161]. The rate of growth of porosity associated with this criterion is given by:

$$\frac{\dot{f}}{f(1-f)} = \frac{3}{h}\frac{\sigma_{ys}}{\sigma_n}\sinh\left(\frac{3}{h}\frac{\sigma_m}{\sigma_{ys}}\right)D_{eq}^{p} \tag{2.3}$$

where $\dot{f}$ is the rate of porosity growth,

h is an invariant of the anisotropy tensor in the space of stress deviators,

D_{eq}^{p} is the macroscopic plastic equivalent strain rate.

Therefore, matrix anisotropy affects void growth in two ways: (i) through the scalar h and (ii) the ratio σ_n/D_{eq}^p. Small variations in the anisotropy factor h are significant because of the exponential dependence in Equation (2.3). Different materials will generally have different values of the anisotropy factor h. Values of h less than 2 will increase the porosity rate in comparison to an isotropic porous material. On the other hand, values of h greater than 2 will decrease, in average, the porosity rate. The ratio σ_n/D_{eq}^p will eventually lead to damage anisotropy since the value taken by σ_n depends on the loading orientation.

Analytical (FEA) models

O'Regan et al. [162] analysed void growth in HCP single crystals using finite element analysis and a constitutive theory that implemented a triple slip model. They found that the relative angles between the slip systems are more important in determining the void growth rate than the lattice orientation with respect to the tensile axis. Their simulations were performed under uniaxial straining conditions, thus involving large stress triaxiality.

Potirniche et al. [163] studied the effect of five distinct crystal orientations on void growth in face centered cubic (FCC) single crystals using crystal plasticity by employing unit cells with one and two cylindrical voids. They concluded that voids in certain orientations grow twice as fast as in other orientations under uniaxial tension (Figure 2.34), whereas under biaxial loading the lattice orientations effect on void growth is negligible.

Yerra et al. [164] modeled void growth and coalescence in BCC single crystals with properties typical of ferritic steel using crystal plasticity based 3D finite element calculations. Crystal orientation was shown to strongly affect the void shape evolution, void growth, and strain at the onset of coalescence under low stress triaxiality. While only void growth rate is affected by crystal orientation under high stress triaxiality.

Crepin et al. [165] investigated void growth and rupture of zirconium (HCP) using flat tensile test specimens. The damage voids had hexagonal cross-sections corresponding to the three prismatic slip systems. Based on the experimental

observations, a crystallographic model was developed to explain the stability of the hexagonal shape and rapid void growth rate.

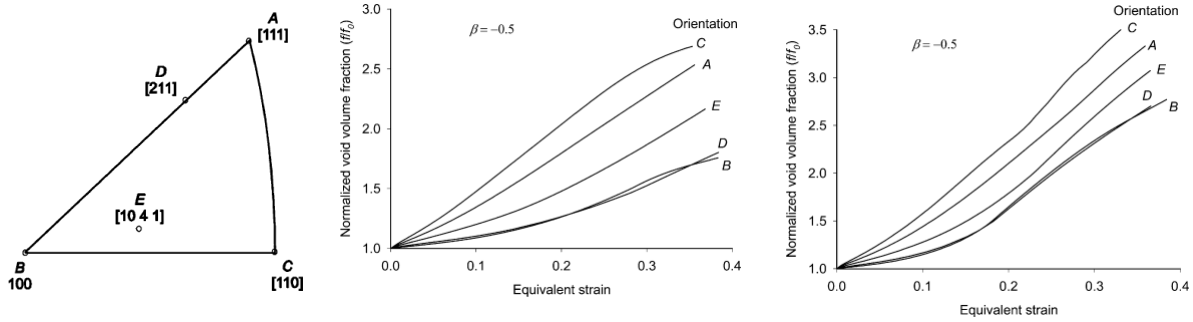

(a) (b) (c)

Figure 2.34: (a) Inverse pole figure showing analysed crystal orientations. Void volume fraction evolution with the applied stress: (b) one-void unit cell; (c) two-void unit cell (β = ratio of biaxial straining; β = -0.5 for the uniaxial loading) [163].

Keralavarma et al. [166] modeled void growth and coalescence in anisotropic plastic solids using FEA. They identified two distinct regimes of behaviour: (i) at high triaxialities, the effect of material anisotropy is found to be persistent, unlike that of initial void shape and (ii) at moderate triaxialities the influence of void shape is found to depend strongly on matrix anisotropy.

2.3.3.3 VOID COALESCENCE

McClintock [144] proposed a criterion for fracture by void growth and coalescence of cylindrical holes in a viscous material and extended it to plastic materials. He found that in plastic materials, there is a strong inverse dependence of fracture strain on hydrostatic tension. This study also outlines the effects of anisotropy and strain-hardening on ductile fracture by the growth of holes and their impingement. This theory overestimates the fracture strain in part because void interactions and localization processes are not taken into account.

Brown and Embury [167] proposed a simple model based on an explicit micromechanical point of view. They modeled coalescence by internal necking. In a perfectly plastic material, internal necking is considered to initiate when it is possible for 45 degrees microshear bands to connect two neighbouring voids (Figure 2.35).

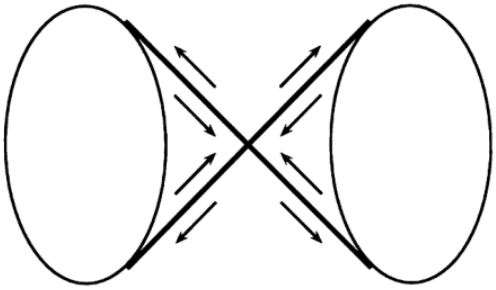

Figure 2.35: Schematic diagram showing the mechanism of cavity coalescence of Brown and Embury [168].

This model generally overestimates the fracture strain. It does not include any triaxiality component and was built for regular array of holes. Later Le Roy et al. [68] modified the model to include the triaxiality component.

Needleman and Tvergaard [169] extended Gurson's model for void growth to account for final material failure. An estimate of the critical void fraction is f_c=0.15 [167]. They modified the expression of the original Gurson yield surface as:

$$\phi = \left(\frac{\sigma_n}{\sigma_{ys}}\right)^2 + 2q_1 f^* \cosh\left(\frac{3q_2}{2}\frac{\sigma_m}{\sigma_{ys}}\right) - 1 - (q_1 f^*)^2 = 0$$

where σ_{ys} is the flow stress of the matrix material,

q_1, q_2 and f^* are new parameters.

The parameters q_1 and q_2 allow describing more accurately void growth rate observed in unit cell calculations. The parameter f^* can be considered as an effective porosity and it depends on the actual porosity f, as indicated in Figure 2.36(a): (i) before void coalescence for $f = f_c$, the void volume fraction and the decrease of load carrying capacity follow the "normal" behavior predicted by the Gurson model; (ii) after the void coalescence process has started, the void volume fraction is accelerated to represent the sudden loss of load carrying capacity (Figure 2.36(b)):

$$f^* = \begin{cases} f, \text{for } f \leq f_c \\ f_c + K(1 - f_c), \text{for } f \geq f_c \end{cases}$$

where K is a constant often called the acceleration factor.

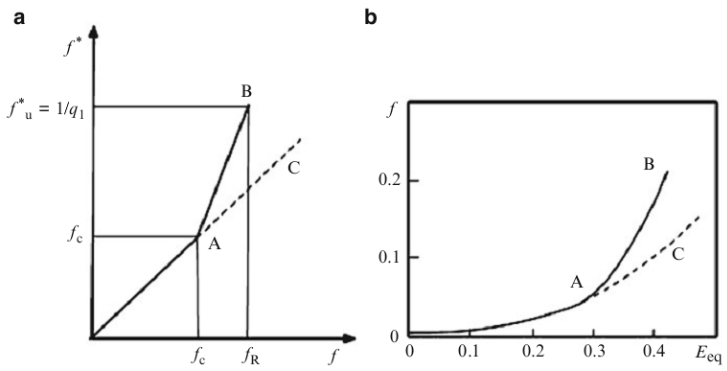

Figure 2.36: (a) Modified Gurson model showing the acceleration in void growth rate when the volume fraction is larger than f_c; (b) response of a finite element FE cell with (curve B) and without (curve C) the introduction of the accelerating function [65].

The critical porosity criterion has been found to not accurately predict coalescence [154,166,170,171]. f_c cannot be taken as a constant - it depends strongly on factors such as void volume fraction, void shape, void spacing, stress triaxiality, strain hardening, etc [154,170,172,173].

Thomason [174] was the first to attempt to model the onset of internal necking by attainment of some plastic limit load in the intervoid ligament. Thomason considers two cases: 2D and 3D. Figure 2.37(a) and (b) respectively show the unit cells containing the two-dimensional prismatic-ellipsoidal void and three-dimensional ellipsoidal void of similar (X_1, X_3) planar geometries. When the diameter of the cavity c is small compared to the distance between the holes e, the mean tensile stress σ_n to cause a necking mode of flow in the internal neck may be much higher than the true yield stress Y, so that internal necking is prevented. Plastic flow will then continue until the cavities have been elongated enough so that the constraint factor σ_n/Y has reached a value low enough for coalescence to begin. The critical condition for microvoid coalescence is given by:

$$\left(\frac{0.3A_{n-2D}}{a/c\,(1-A_{n-2D})}+0.6\right)\left(1-V_f\right)^{-1}=\frac{\sigma_m}{Y}+\frac{1}{2}$$

and for the 3D case and for b = c:

$$\frac{0.1}{\left(\frac{a}{e}\right)^2}+\frac{1.2}{\left(\frac{c}{c+e}\right)^{1/2}}\left(1-V_f\right)^{-1}\left(1-\left(\frac{3\sqrt{\pi}}{4}V_f\right)^{2/3}\left(\frac{b}{b_0}\right)^2 e^{\varepsilon_1}\right)=\frac{\sigma_m}{Y}+\frac{3}{2} \qquad (2.4)$$

Ma Dofang et al. [175] experimentally verified the Thomason's and Brown and Embury's void coalescence criteria. They made a series of tension tests for pure copper sheets. The void coalescence matched the two mentioned criteria to a certain extent.

Pardoen and Hutchinson [154] replaced the constant values of 0.1 and 1.2 in equation (2.4) by two parameters, α and β that incorporate a dependence on the *strain hardening* exponent *n* where β is almost constant and can be taken as 1.24 while α was fitted as a function of the average value of the strain-hardening exponent, *n*:

$$\alpha(n) = 0.1 + 0.217n + 4.83n^2 \qquad (0 \leq n \leq 0.3)$$

Benzerga [176] modified Thomason's model to fit the numerical results at low triaxiality and when the void shape at coalescence is flat.

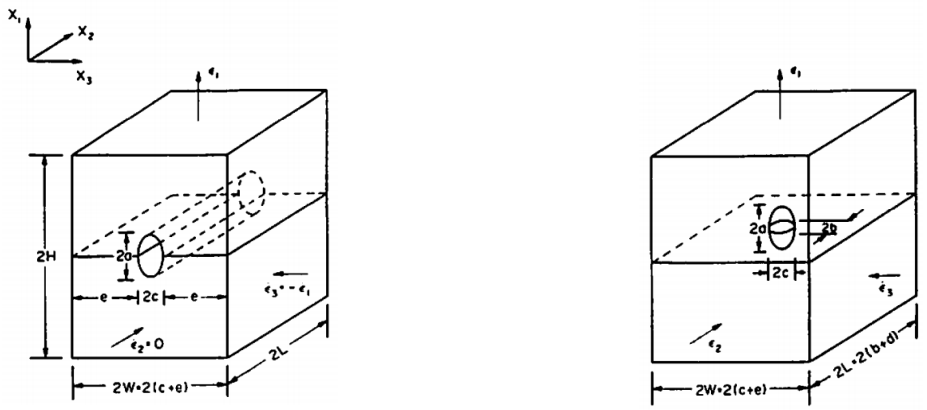

(a) (b)

Figure 2.37: The unit cell of similar (X_1, X_3) planar geometry for (a) two-dimensional models with prismatic elliptical voids and (b) three-dimensional models with ellipsoidal voids [107].

Fabregue and Pardoen [177] introduced the effect of secondary voids on the onset of coalescence by internal necking by multiplying the current mean yield stress of the matrix by (1-f_2), where f_2 is volume fraction of secondary voids.

Keralavarma et al. [166] simulated void growth and coalescence in anisotropic plastic solids using finite element implementation of the voided cell model based on [161]. They represent the microstructure in the voided cell model using hexagonal periodic unit (Figure 2.38(a)), where the hatched bands in the figure schematically represent the texture of the matrix. Figure 2.38(b) shows the effective stress–strain

response for three EYT (equal yield in tension) materials: isotropic, weak in shear material (ib) and shear resistant material (iii). w_0 represents the initial void aspect ratio (ratio of axial to radial semi-axes of the void): w_0=2 (prolate), w_0=1 (spherical), w_0=1/2 (oblate). The onset of coalescence is accompanied by a rapid drop in the stress. The cross mark is referred to as the onset of void coalescence. The stage of microscale localization (past the cross mark) is also accompanied by an accelerated growth of porosity (Figure 2.38(c)) and a rapid drop in the void aspect ratio (Figure 2.38(d)) due to the lateral void expansion during ligament necking. Void coalescence took place by internal necking of the inter-void ligament. They obtained that higher triaxiality results in lower effective strain to coalescence. They found that matrix material anisotropy has a strong effect on void growth and coalescence at all stress triaxiality levels.

Tang et al. [178] investigated void growth and coalescence in magnesium single crystals using one void and two void specimens using molecular dynamics simulations. Their main findings are: (i) the evolution of void shape is greatly affected by the pattern of plastic deformation that developed near the voids, which was strongly dependent on the crystal orientation (Figure 2.39) and specimen size; (ii) the yield strengths of orientation A (see caption under Figure 2.39) were much more sensitive to the strain rate than those of orientation B; (iii) the influence of temperature on yield strengths of orientation B was greater than that of orientation A.

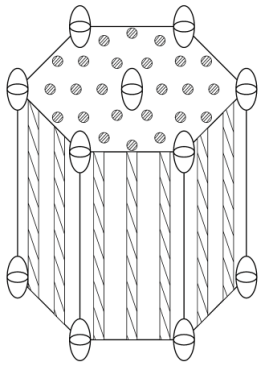

(a)

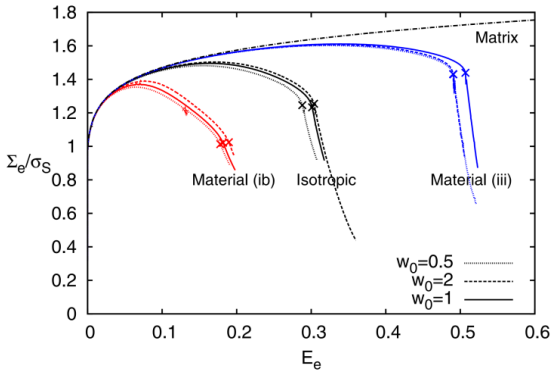

(b)

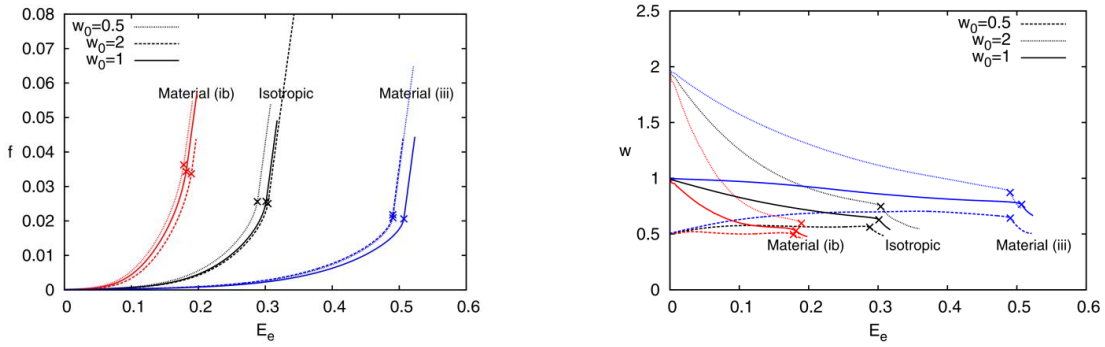

Figure 2.38: (a) Idealized representation of the microstructure in the voided cell model: hexagonal periodic unit. Effect of matrix material anisotropy on the cell model response for initial porosity f_0 = 0.0001, stress triaxiality ratio T = 2 and three values of w_0. Case of EYT (equal yield in tension) materials. (b) Effective stress–strain response, (c) evolution of porosity, (d) evolution of the void aspect ratio [166].

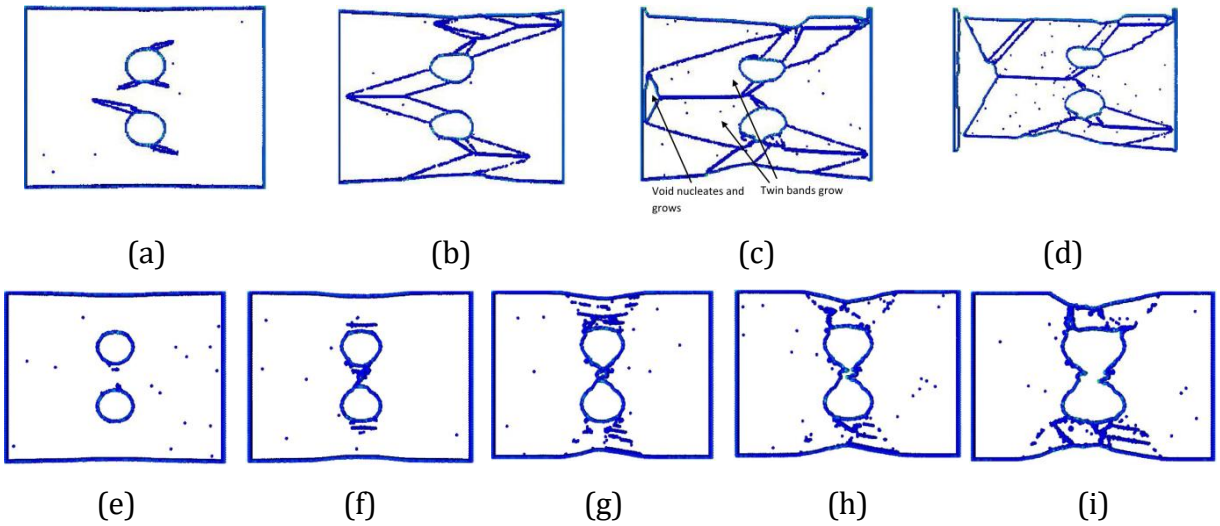

Figure 2.39: Simulation of void coalescence in magnesium single crystals of two orientations. (a)-(d) A – x [0001]–y[1$\bar{2}$10]–z [10$\bar{1}$0] at various applied strains: (a) ε = 0.037; (b) ε = 0.051; (c) ε = 0.151; (d) ε = 0.321. (e)-(i) B – x [1$\bar{2}$10]–y [10$\bar{1}$0]–z[0001] at various applied strains: (e) ε = 0.034; (f) ε = 0.041; (g) ε = 0.057; (h) ε = 0.085; (i) ε = 0.151. Tensile direction is horizontal [178].

2.4 Brittle fracture

Brittle fracture was recently reviewed in [65,179]. In this section experimental observations and modelling of brittle fracture are presented.

2.4.1 Experimental observations of brittle fracture

Brittle fracture modes observed in metals and ceramics are (Figure 2.40): (i) transgranular cleavage fracture, and (ii) intergranular fracture. In crystalline materials,

cleavage fracture occurs preferentially over well–defined crystallographic atomic planes: {0001} in metals with an HCP structure (Ti, Mg, Zn, Be) [168].

Nasiri-Abarbekoh et al. [116] reported a change of fracture mode after phase transformation in CP Ti from ductile (Figure 2.41(a)) to intergranular in transverse direction (Figure 2.41(b)) and a combination of intergranular and dimple fracture in rolling direction (Figure 2.41(c)) due to the activation of different deformation systems.

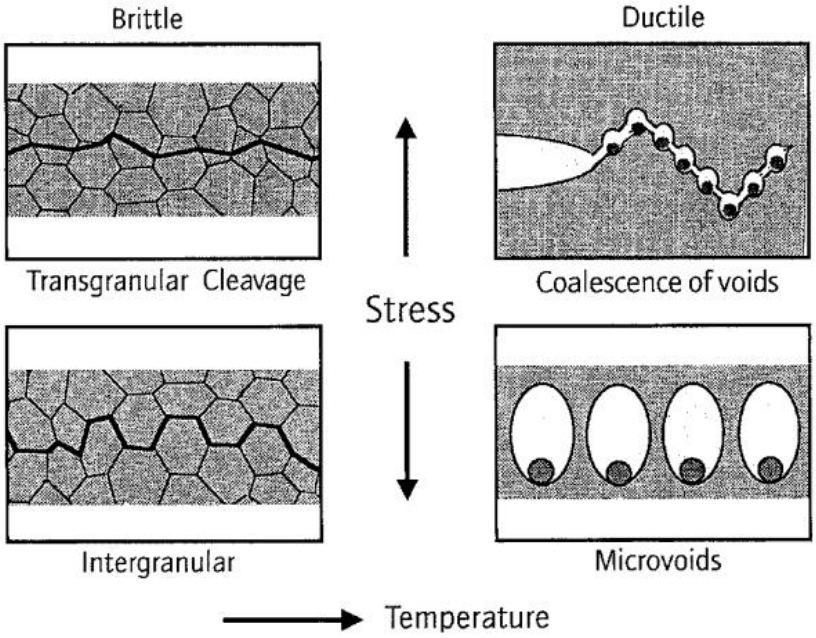

Figure 2.40: Failure mechanisms in metals [180].

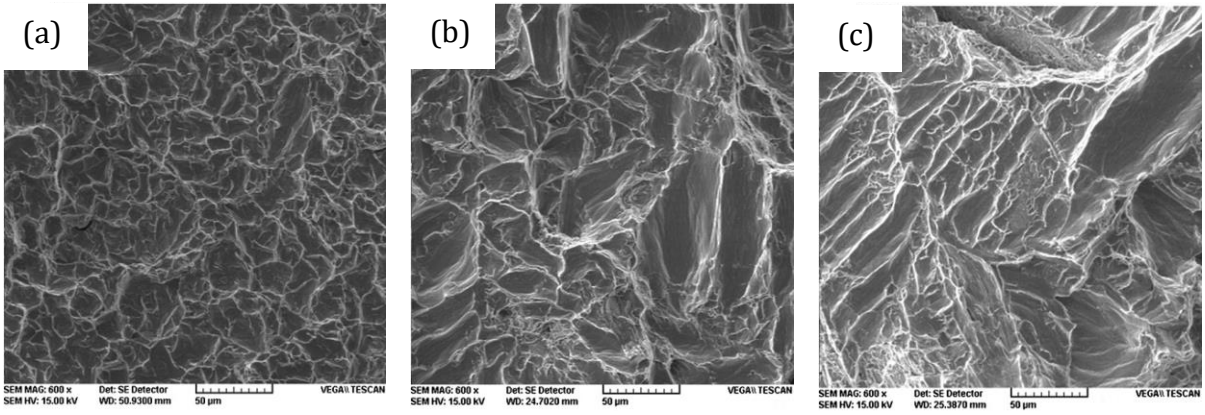

Figure 2.41: SEM micrographs of tear fracture surfaces of CP Ti: (a) before phase transformation in rolling direction; after phase transformation (b) in rolling direction and (c) in transverse direction [116].

Hughes et al. [181] observed the variation of fracture mechanism of polycrystalline zinc with temperature (Figure 2.42). The relative percentage areas of four distinct fracture mechanisms (transgranular, grain boundary, ductile and twin boundary) at each temperature are given in Table 2.5. As the temperature is increased from 77 to 328 K, there is a progressive increase in the intervention of ductile fracture, i.e. the transition from brittle to ductile fracture is encountered.

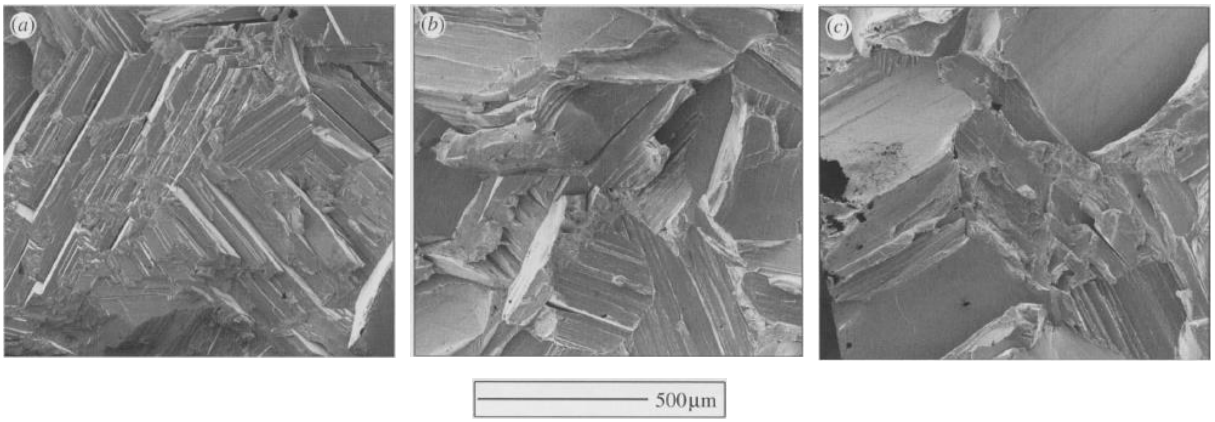

Figure 2.42: Ion-induced secondary-electron images of zinc fracture surfaces, where fracture experiments were carried out at: (a) 77 K; (b) 293 K; (c) 328 K. the scale bar applies to all three images [181].

Table 2.5: The variation of fracture mechanisms with temperature in polycrystalline zinc given as percentages [181].

Temperature	77 K	293 K	328 K
transgranular cleavage	82	65	46
intergranular fracture	4	28	29
ductile fracture	0	7	25
twin boundary fracture	14	0	0

2.4.2 Brittle fracture modelling

In crystalline ceramic materials brittle fracture occurs under purely elastic conditions and the cleavage stress is related to the existence of defects, which are inherently present [65]. In this case the fracture stress is given by the Griffith stress σ_G [65]:

$$\sigma_G = (E\gamma_s/\pi a)^{1/2}$$

where E is Young modulus, γ_s is surface energy, a is the size of the large defects.

Cottrell [182] proposed a theory to explain cleavage in metals. In his theory cleavage cracks are initiated at the intersection between two slip planes or two mechanical twins. In this theory the fracture strength is given by:

$$\sigma_R = K_Y' d^{-1/2}$$

where d is grain size,
K_Y' is a material parameter given by:

$$K_Y' = \frac{E\gamma_s}{\pi(1-\nu^2)k_y}$$

k_y is the material parameter in the Hall-Petch law [183,184].

When cleavage fracture occurs in the ductile-brittle transition regime, cleavage crack may nucleate from microstructural defects, such as inclusions (Figure 2.43). This is observed for example in structural steels [185]. At low temperature, cleavage fracture is essentially nucleation controlled, while, at higher temperature, it is rather growth controlled [186,187].

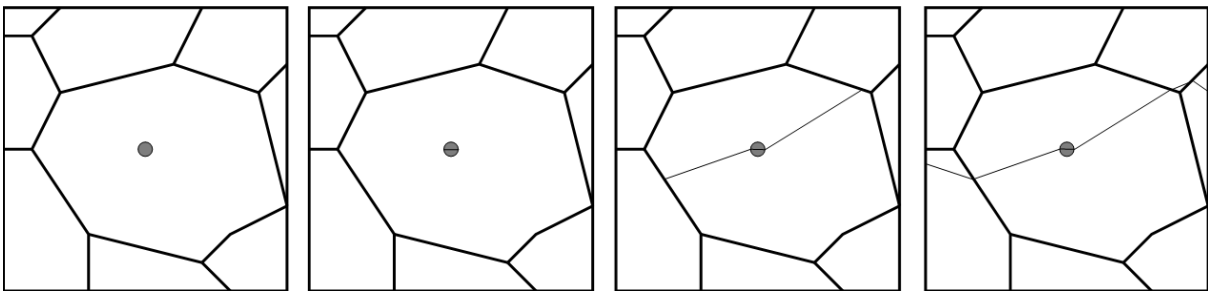

(a) (b) (c) (d)

Figure 2.43: Sketch showing the different steps in the initiation and the propagation of a cleavage crack initiated from an inclusion or a second phase particle (a) and (b), arrested at grain boundaries (c), propagating across the grain boundaries (d) [168].

Beremin [188] proposed the Weibull stress model. He proposed a criterion which is expressed as a probability distribution based on Weibull theory:

$$P_R = 1 - \exp\left(-\left(\frac{\sigma_W}{\sigma_u}\right)^m\right) \tag{2.5}$$

where P_R is the cumulative probability to failure,
m is the Weibull constant,
σ_W is the Weibull stress,
σ_u is the material constant.

In Beremin's model, an implicit threshold Weibull stress is included: there exists a threshold for the stress intensity factor K_{Imin}, below which cleavage cannot occur:

$$K_{Imin} \approx R_p\sqrt{3\pi X_c}$$

where X_c is the critical size of the plastic zone ahead of a crack tip,
R_p is the yield strength.

Some authors [189,190] introduced a threshold stress, σ_{th}, directly into Equation (2.5). Gao et al. [191] proposed a modified form of Equation (2.5):

$$P_R = 1 - \exp\left[-\left(\frac{\sigma_W - \sigma_{W\,min}}{\sigma_u - \sigma_{W\,min}}\right)^m\right]$$

where $\sigma_{W\,min}$ is the minimum value of σ_w at which cleavage fracture becomes possible.

Batdorf and Crose [192] unlike other authors do not assume that all the microcracks are oriented normal to the tensile axis. Thus their theory is more realistic. The theory is based on an effective stress σ_e which causes a crack to propagate as soon as it exceeds a critical value σ_c; σ_e is a function of the normal stress σ_n and shear stress τ that act on the plane of the crack.

The presented "weakest link" theories have some limitations and are not valid in several cases (Figure 2.44). To avoid these difficulties more general theories have been developed in which Weibull's theory appears as a very particular case.

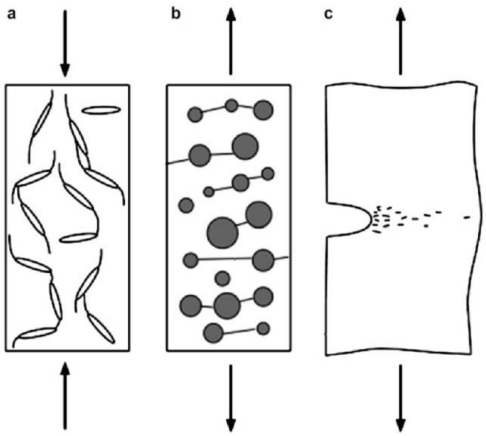

Figure 2.44: Cases where the "weakest link" theory does not apply: (a) compressive loading; (b) cracks stopped by obstacles; (c) high gradients [65].

Hughes et al. [181] developed a pseudo-three-dimensional geometrical model of the brittle fracture of the polycrystalline zinc, assuming that cleavage occurs on (0001) and also on the three variants of the $\{10\bar{1}0\}$ planes, and that twinning plays a major role in the fracture process. Initially in the model, it is assumed that zinc cleaves on the unique basal plane of its HCP structure. The four distinct ways in which cleavage planes in adjacent grains of polycrystal may meet their common grain boundary are schematically shown in Figure 2.45. The proportions of these four mechanisms are deduced using the model shown in Figure 2.46. As a result of the experimental observations of basal plus prismatic cleavage and the formation of twins, this simple model was extended. Thus this model allows: (i) cleavage to occur on a single cleavage plane, either basal or prismatic, in each grain; (ii) cleavage to occur on two or more planes in some or all of the grains; (iii) cleavage crack to interact with a twin boundary.

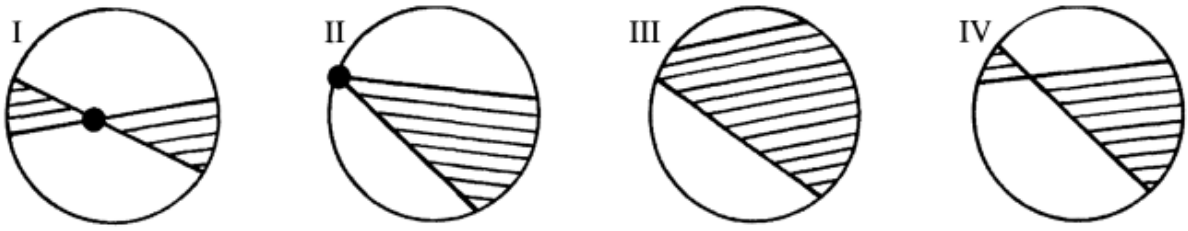

Figure 2.45: The four distinct mechanisms in which grain boundary failure may link cleavage cracks in adjacent grains in Zn. The boundary is shown schematically as a circle and the parts that must fail are indicated by shading. The straight edges of these regions are the traces of the cleavage planes. In mechanisms I and II, the crack crosses the boundary whereas in III and IV, two cracks meet the boundary from opposite sides [181].

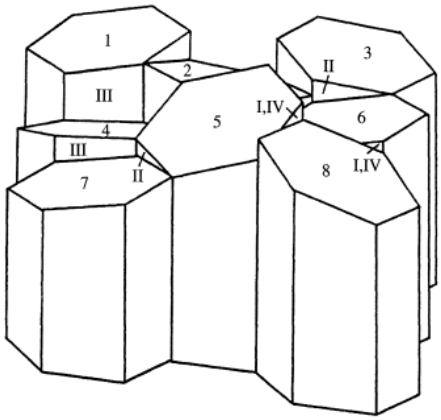

Figure 2.46: Model of a polycrystal consisting of regular hexagonal prisms, used to investigate, topologically, the proportions of crack-propagation mechanisms I-IV that occur in practice in Zn. The cleavage cracks that have formed in the eight grains are labelled 1-8 and examples of mechanisms I-IV are indicated, (I and IV cannot be distinguished) [181].

2.5 RESEARCH OBJECTIVES

The literature review has shown progress in the understanding of the three stages in the ductile fracture process, namely void nucleation, growth and coalescence. Void nucleation was observed in different metals and alloys (including CP Ti) and was shown to occur by decohesion at the particle-matrix interface or by plastic deformation. Void growth rate was measured using different techniques (density measurements, interrupted tests, x-ray tomography). Generally voids grow exponentially with strain and the void growth rate is affected by stress triaxiality. Recent studies have shown the possibility to measure void growth during in-situ tensile tests in x-ray tomography. Void coalescence terminates void growth in one of three modes: internal necking, void coalescence in a microshear band or "necklace" coalescence. Mechanical properties were shown to be affected by crystal orientation because of the dependence of the activation of slip and twinning systems on crystal orientation. This is true for CP Ti which has a HCP crystal structure. Several analytical, FEA and crystal plasticity models were developed for void nucleation, growth and coalescence.

From the literature review it can be concluded that there is a lack of experimental data on void growth in anisotropic materials. Thus the purpose of this work will be to understand how grain orientation affects void growth. The material chosen for this study is CP Ti because it has a hexagonal close packed crystal structure which results in strong anisotropic properties. Furthermore, Ti is fairly ductile which will allow for a detailed investigation of the effect of crystal orientation on void growth. The accuracy of ductile fracture models in the literature will be assessed and crystal orientation dependent models will be validated.

Chapter 3 INDIRECT INVESTIGATION OF GRAIN ORIENTATION EFFECTS ON VOID GROWTH IN CP TITANIUM

This chapter describes the material studied, the experimental methods that have been used in the present study and experimental results on the effect of grain orientation on the growth of voids in CP titanium.

3.1 EXPERIMENTAL PROCEDURES

Fabrication of a model material with controlled parameters simplifies the study of ductile fracture by excluding effects of size, shape and distribution of sites of void nucleation. In this study titanium laser-drilled model materials similar to those of Weck et al. [87] were produced and tested. The experimental approach is summarized in Figure 3.1.

3.1.1 MATERIALS

The material used in the present study was CP titanium alloys (Grade 1). The material was purchased from: (i) NewMet company in the form of thick 0.25 mm titanium foil (99.8% Ti); (ii) AlfaAesar company in the form of thin 0.032 mm titanium foil (99.7% Ti). The chemical composition is presented in Table 3.1.

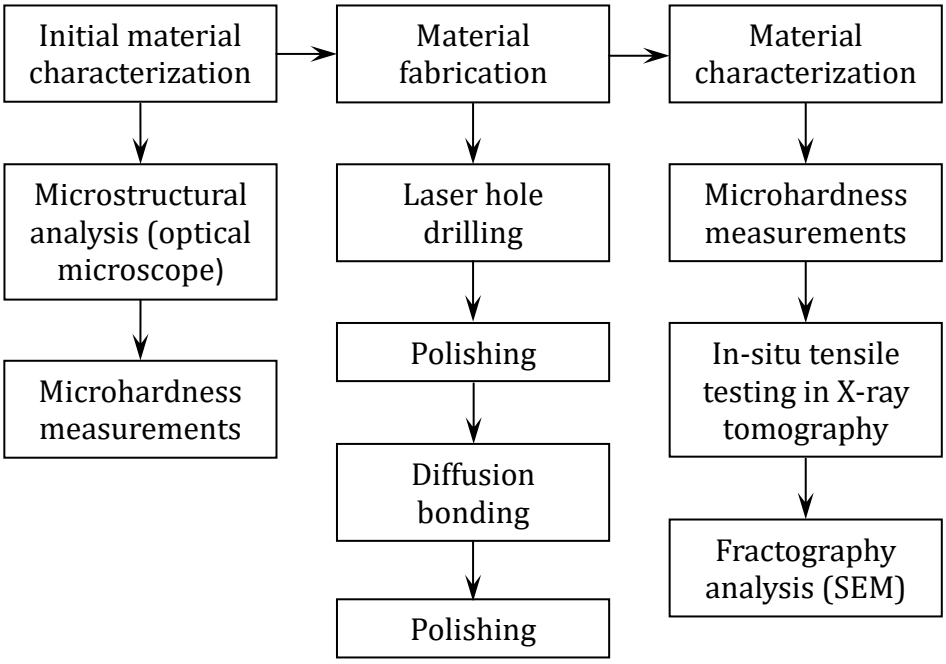

Figure 3.1: Flowchart of the experimental approach.

Table 3.1: Chemical composition in ppm of CP Ti alloys used in the present study. Values are given in ppm.

Alloy	C	Fe	H	N	O
CP titanium alloy (99.8% Ti)	30	200-300	15-17	30-40	300-400
CP titanium alloy (99.96% Ti)	50	400	16	20	500

3.1.2 Material fabrication

Dog-bone-shaped samples (Figure 3.2(a)) were precisely cut from these foils using a computer numerical control (CNC) mill. Arrays of voids were introduced in the thinner titanium foils using femtosecond laser micromachining (Figure 3.3), a technique which allows precise manufacturing of voids without the formation of a heat affected zone. This technique has already been successfully implemented to create model material out of copper and aluminum [87,92,193].

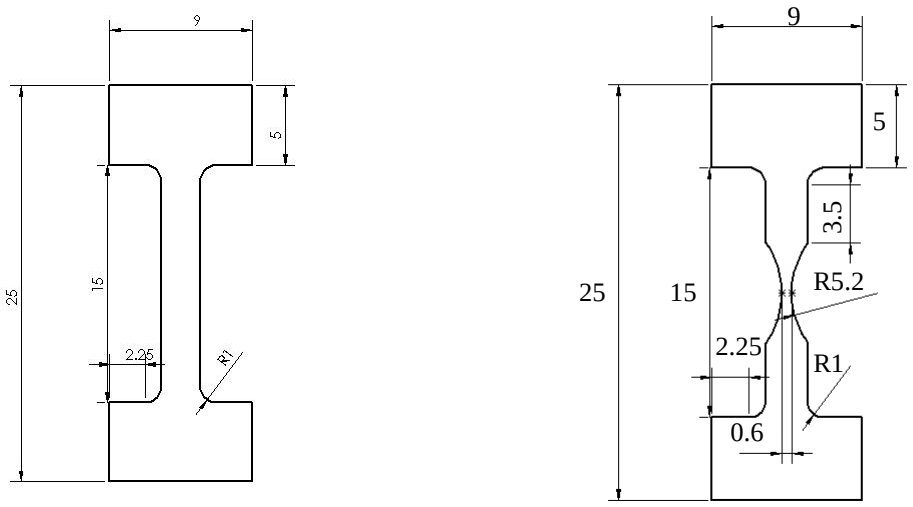

(a) (b)

Figure 3.2: Tensile dog-bone-shaped samples: (a) without necking; (b) with necking. Dimensions are in mm.

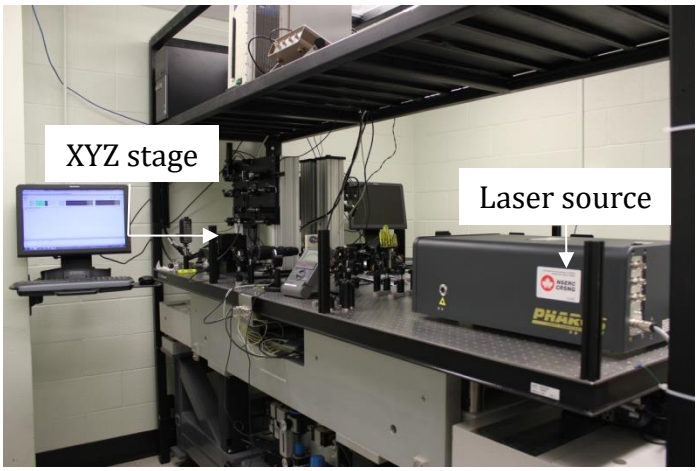

Figure 3.3: Femtosecond laser set-up.

As previously mentioned, model materials are used to simplify the study of the ductile fracture process and exclude the nucleation event from the fracture analysis. Main factors affecting the fracture process locally include the void geometry (size, shape, orientation, and spacing), the materials properties (work hardening rate) and the stress stress (stress triaxiality) [107]. Void orientation and spacing were varied in order to see their influence on void growth and coalescence. Different hole configurations were used (Figure 3.4): (i) rectangular array with intervoid spacings of

70 μm, 100 μm and 120 μm; (ii) holes at 45° with intervoid spacings of 70 μm, 100 μm and 130 μm. The initial void size was 35 μm.

In order to choose the initial void diameter, different considerations were taken into account. First, the resolution of the X-ray tomograph used in the present study to visualize the voids is 1.5 μm (voxel size). To obtain the minimum void diameter that may be tracked with this technique, the resolution is multiplied by 20 (to ensure a good possibility to track changes of void dimensions). Second, the void diameter was chosen (35 μm) and then a thickness close to that diameter was chosen in order to have as spherical voids as possible. The thickness of titanium sheet in which holes are drilled was 0.032 mm. A void diameter of around 35 μm was obtained with a pulse length of 350 fs, an energy of 20 μJ and 1000 pulses (equivalent to 1 s per hole). It is important to note that laser drilling gives holes that have a conical shape. After polishing holes become smaller and finally after diffusion bonding, become quasi-spherical. This reproduces well the microstructural features found in real materials, where the void size range from 1 to 50 μm [144].

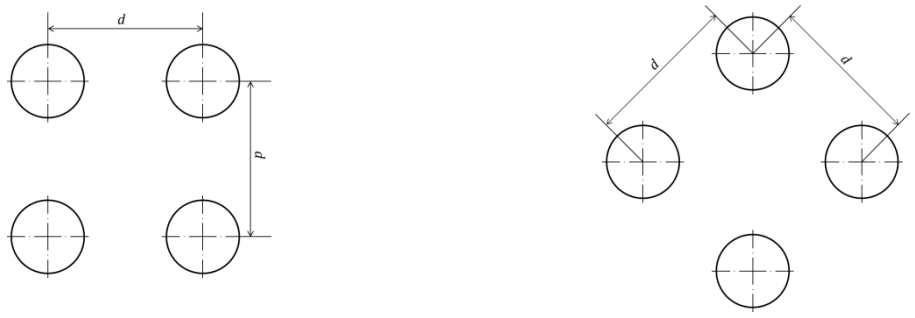

(a) (b)

Figure 3.4: Schematic representation of two void configurations: (a) rectangular array with intervoid spacing *d*; (b) voids at 45° with intervoid spacing *d*.

After laser drilling, 0.25 mm thick titanium sheets were first ground using SiC paper, then polished using a 9 μm diamond spray on an ultrapolishing cloth and finally polished down to a mirror finish using a 0.05 μm colloidal silica suspension. Sheets containing holes were then diffusion bonded to sheets without holes (Figure 3.5) in a vacuum furnace (Figure 3.6(a)) using a diffusion bonding mold (Figure 3.6(b)) at 10^{-7} torr. Typical diffusion bonding temperatures and times were in the range 960-

1000 °C during 2-3 hours. A typical thermal treatment curve obtained from diffusion bonding experiments is shown in Figure 3.7. The step during diffusion bonding (30 minutes at 800 °C) ensures that good vacuum is maintained throughout the test. The cooling rate at the allotropic phase transformation temperature (882 °C) was about 0.40-0.46 °C/s. Two types of samples were obtained: one with a 2-dimensional array of voids (Figure 3.5(a)) inside the material and one with a 3-dimensional array of voids (Figure 3.5(b)) to obtain a more realistic void configuration. After diffusion bonding the samples were cut to introduce the necking (Figure 3.2(b)).

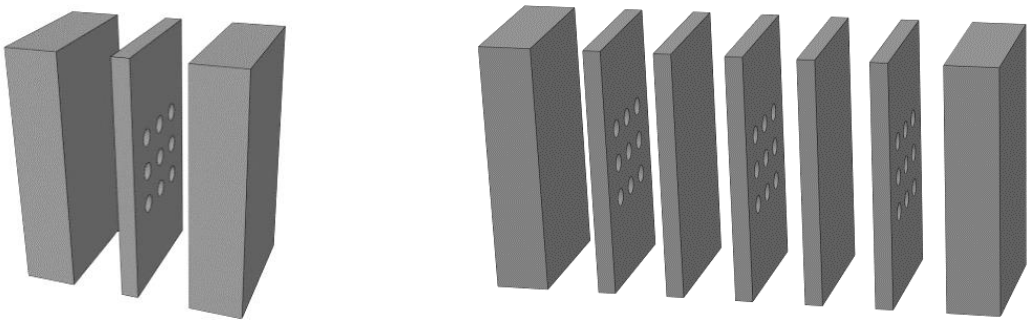

(a) (b)

Figure 3.5: Schematic drawing of 3D model material: (a) 2-dimensional array of voids; (b) 3-dimensional array of voids.

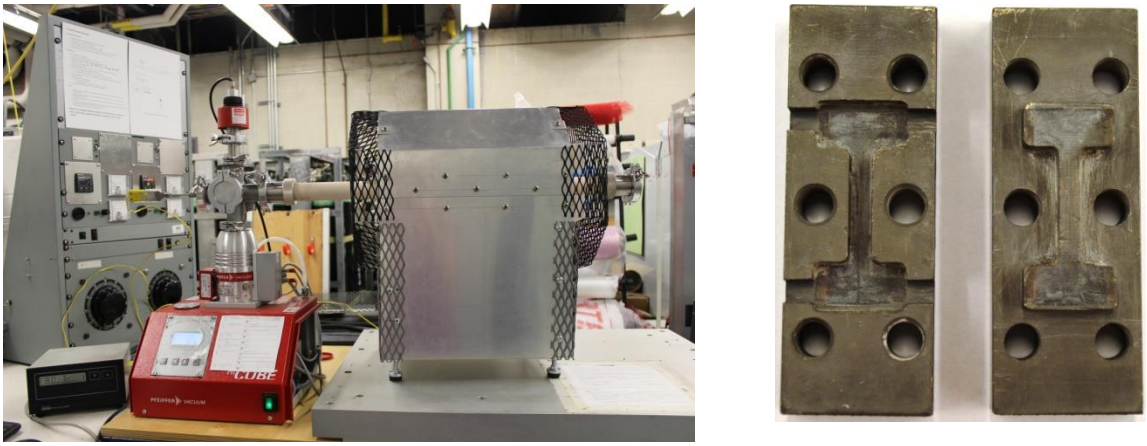

(a) (b)

Figure 3.6: (a) Vacuum furnace used for annealing and diffusion bonding; (b) diffusion bonding mold used for this study.

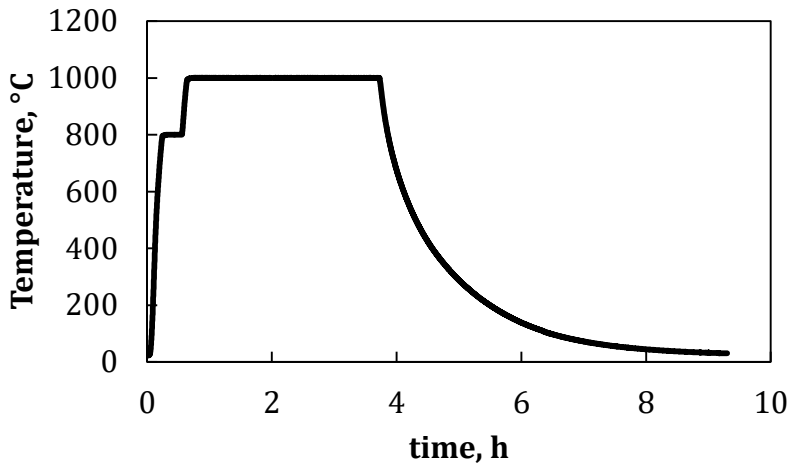

Figure 3.7: A typical thermal treatment curve obtained from diffusion bonding experiments.

3.1.3 Microstructural Characterization

The chemical composition and the thermo-mechanical processing determine the microstructure and the corresponding mechanical properties of titanium alloys. Metallographic preparation and subsequent microstructural characterization were carried out in order to correlate the mechanical properties with the microstructure.

3.1.3.1 Metallographic preparation

After diffusion bonding samples were prepared metallographically by mechanical polishing in order to observe microstructure and prepare sample surface for tomography. This involves planar grinding and polishing in a plane parallel to the diffusion bonding plane using a Buehler Metaserv 2000 grinding/polishing machine. The samples were first ground using SiC paper with a continuous water flow until the oxide layer formed during diffusion bonding was removed. Then the samples were polished using a 9 μm diamond spray on an ultrapolishing cloth. Final polishing was performed with 0.05 μm Struers OP-S suspension on Microcloth/Buehler cloth with an attack polishing agent (1:1 of hydrogen peroxide and colloidal silica). The polished specimens were either analyzed as is or subsequently etched using an etching reagent (1 pct hydrofluoric acid, 5 pct nitric acid, and 15 pct lactic acid [32]) to reveal the microstructure.

3.1.3.2 MICROSTRUCTURAL EXAMINATION

A Nikon OPTIPHOT-100 optical microscope with digital interference contrast (DIC) was used for microstructure examination after etching at different magnifications.

3.1.3.3 QUANTITATIVE MICROSTRUCTURAL ANALYSIS

The line-intercept method [194] was employed to ascertain an average platelike α (α_p) width and all measurements were made using optical microscope images at 100× magnification. First, the number N of grain boundary intersections with randomly placed lines of length L at different angles is measured. Second, the average dimension of a feature is given by the average of all L/N values.

3.1.3.4 MICROHARDNESS TESTING

The resistance to localized plastic deformation was measured through Vickers microhardness. A Vickers diamond indenter was pressed into the test specimen surface by an accurately controlled applied force using a Leitz Wetzlar test machine. The size of the indentation was measured using a light microscope. The Vickers hardness number, in terms of gf and μm, is calculated as follows (3.1) [195]:

$$\mathrm{HV} = 1854.4 \times P/d^2 \tag{3.1}$$

where P is force, gf,
d is mean diagonal length of the indentation, μm.

The loads are typically in grams-force (gf) and indentation diagonals are in micrometers (μm). The used load was 200 gf.

3.1.3.5 FRACTOGRAPHY

Fracture surfaces of titanium samples tested in tomography were observed in a low vacuum scanning electron microscope (SEM) JEOL JSM-5300. The fracture surfaces were characterized using secondary electrons (SE) to identify the fracture topography. Afterwards fracture areas were measured using open source image analysis software ImageJ [196].

3.1.4 In-situ Tensile Testing (X-Ray tomograms)

Tensile testing is the most common mechanical test performed on materials. In this test the sample is subjected to a continuously increasing uniaxial tensile load at a constant strain rate while simultaneously measuring the elongation of the specimen until failure [197]. Titanium samples were pulled in-situ in an x-ray tomography system (Figure 3.8) available at Mateis lab, INSA de Lyon, France, and described in [198]. X-ray tomographs were acquired on a CCD camera with 960 x 768 sensitive elements with a 1.5 μm voxel size. An x-ray energy of 80 keV was used. The number of projections used was 720 initially and was then decreased to 180 in order to decrease time of acquisition while maintaining acceptable image quality. The acquisition time was 500 ms per rotation angle with a total rotation of 180°. Tensile tests were performed at room temperature on a specially designed in situ tensile testing machine. The testing speed was 1 μm/s at the beginning of the test and was decreased to 0.5 μm/s close to the end of the test in order to capture void linkage. High strain rate was employed to reach a void growth stage. During the void growth stage lower strain rate permits acquisition of high amount of data points. The machine was used in tension with a load cell of 2 kN and both load and displacement were recorded during the test. During the in-situ tomography experiments, the samples were deformed in tension and the test was stopped at various levels of deformation in order to acquire tomograms. Depending on how quickly the sample failed and on the number of interesting events occurring during the test, the number of tomograms acquired varied between samples (5 to 10 tomograms).

Figure 3.8: X-ray tomography system used in this study.

3.2 Experimental results

3.2.1 Microstructural examination and microhardness testing

The initial microstructure of as-received CP Ti consisted of equiaxed grain (Figure 3.9).

Metallographic examination of all samples diffusion bonded at temperatures higher than phase transformation temperature reveals fine features (Figure 3.10). These fine features were determined to be platelike α as those obtained by Kim and Park [32] (Figure 2.14). It was found that upon cooling CP Ti grade 2 at rates slower than about 3°C/s [32], platelike alpha appears; while platelike and acicular alpha appear when cooling CP Ti grade 4, which contains more O and Fe, at a rate slower than approximately 30°C/s [33] (Figure 2.13). In this study CP Ti grade 1 is continuously cooled down with a cooling rate at phase transformation temperature (882 °C) of about 0.40-0.46 °C/s. Thus the microstructure represent platelike α due to its characteristic features. The chemical composition of CP Ti (Grade 1) is similar to CP Ti (Grade 2) studied by Kim and Park. Thus all samples consist of platelike α lamellae, formed during the cooling inside the parent β grains. The line-intercept method [194] was employed to ascertain an average platelike α width (Figure 3.11). First, the number N of grain boundary intersections with randomly placed lines of length L at different angles is measured. Second, the average dimension of a feature is given by the average of all L/N values.

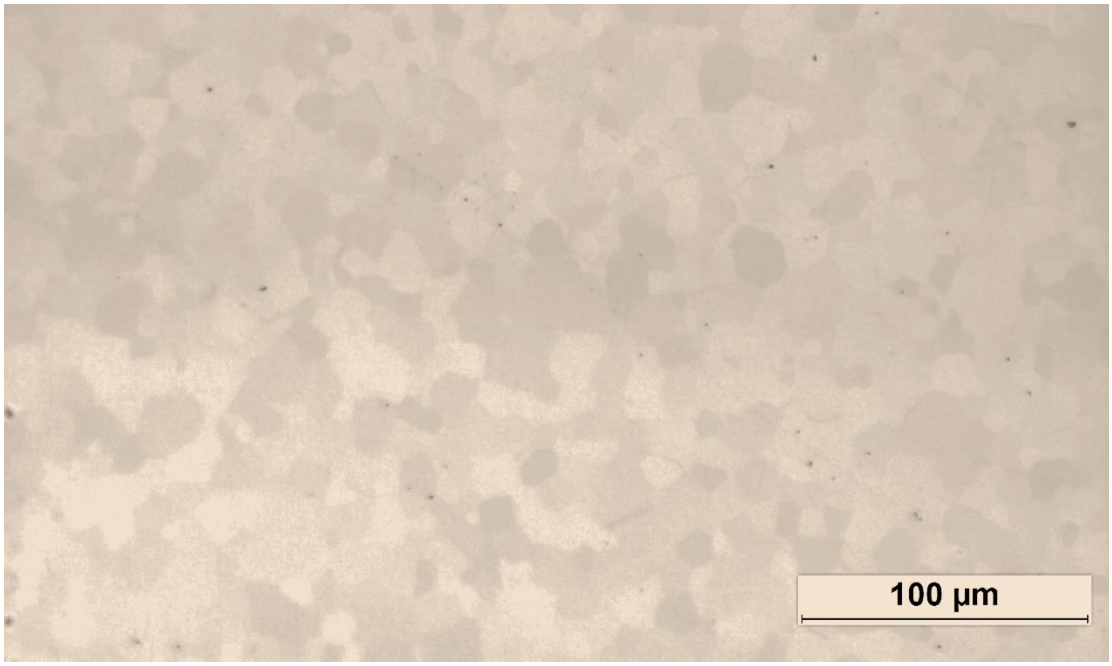

Figure 3.9: Optical micrographs with digital interference contrast of CP Ti showing the initial microstructure.

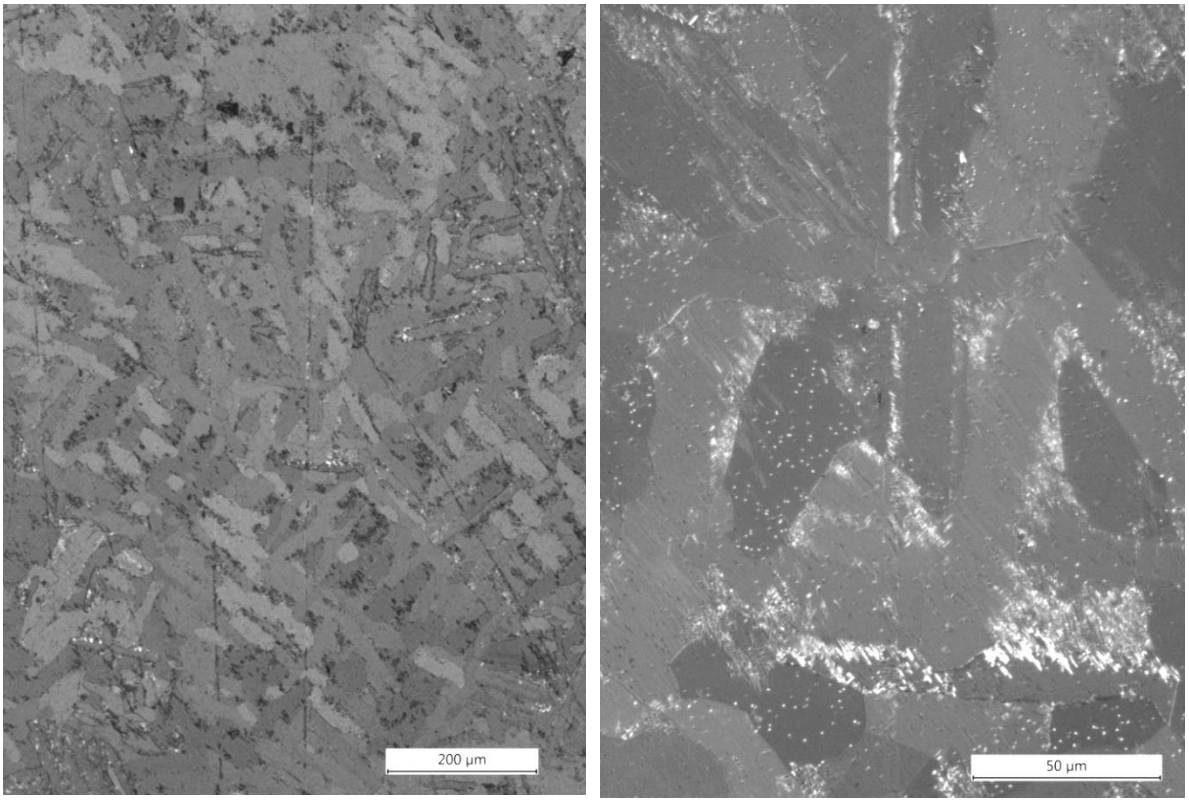

(a) (b)

Figure 3.10: Optical micrographs with digital interference contrast of CP Ti showing platelike α at two magnifications: (a) ×100, (b) × 500.

The width of the α plates was found to slightly increase with decreasing diffusion bonding temperature and time (

Table 3.2, Figure 3.12). It is important to note here that the microstructure consists of colonies of α-plates (or α-lamellae) which form grains. This means that inside each grain, α-plates have the same orientation [121]. Thus the microstructural unit of deformation is the grain (which is larger than the void) whose dimensions are reported in

Table 3.2.

Values of microhardness measured on samples annealed at different temperatures are presented in

Table 3.2. Longer annealing results in slightly smaller α width and in significantly higher values of microhardness. While the α plates width could contribute to the increase in strength, the small change in plate width cannot explain the large change in hardness observed experimentally. The increase in hardness is therefore deduced to be a result of oxidation of the titanium samples during heat treatment. Higher annealing temperature and time result in higher oxygen content in titanium thus higher microhardness, as already demonstrated in [199]. Indeed, oxygen addition leads to solid solution strengthening by asymmetric lattice distortion [200]. The range of oxygen calculated based on the data provided in [199] was found to be ranging from 0.035 at % for sample S2 to 0.044 at % for sample S6.

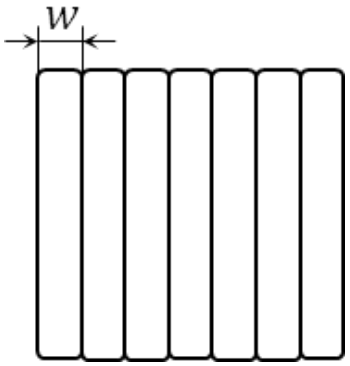

Figure 3.11: A schematic representation of α lamellae where *w* is α width.

Table 3.2: Width of platelike α and microhardness of samples before and after diffusion bonding.

Diffusion bonding parameters		α width,	Δα width,	α colony size	Δα colony size	HV	ΔHV
Temperature, °C	Time, hours	µm	µm	*grain size, µm	*Δgrain size, µm	0.2	0.2
1000	3	16	3	104	10	252	32
1000	2	17	4	92	10	238	28
960	2	18	4	86	10	228	17
as-received		N/A	N/A	*10	*4	178	11

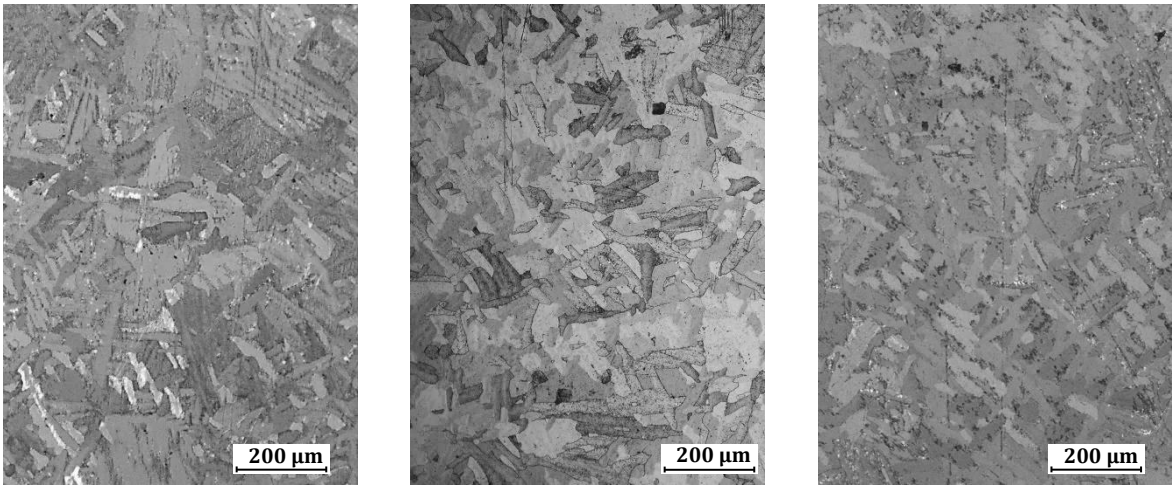

(a) (b) (c)

Figure 3.12: Typical sequence of microstructures (×100) versus diffusion bonding temperature and time: (a) 960 °C, 2 hours, (b) 1000 °C, 2 hours, (c) 1000 °C, 3 hours.

3.2.2 In-situ Tensile Test Results

Using the force registered during the tensile test and the smallest cross sectional area extracted from tomographic reconstructions, true stress-strain curves were constructed for all samples.

To obtain the smallest cross sectional area of the samples in the neck region, the area of each section was calculated automatically using the open source image analysis software ImageJ [196]; then the data was sorted numerically to extract the smallest cross sectional area. True stress-strain curves were calculated using the following equations:

$$\sigma = \frac{L}{A} \tag{3.2}$$

$$\varepsilon = \ln\left(\frac{A_0}{A}\right) \tag{3.3}$$

where L is the load,

A is cross sectional area at a given load,

A_0 is the initial cross sectional area.

True stress-strain curves are represented in Figure 3.13.

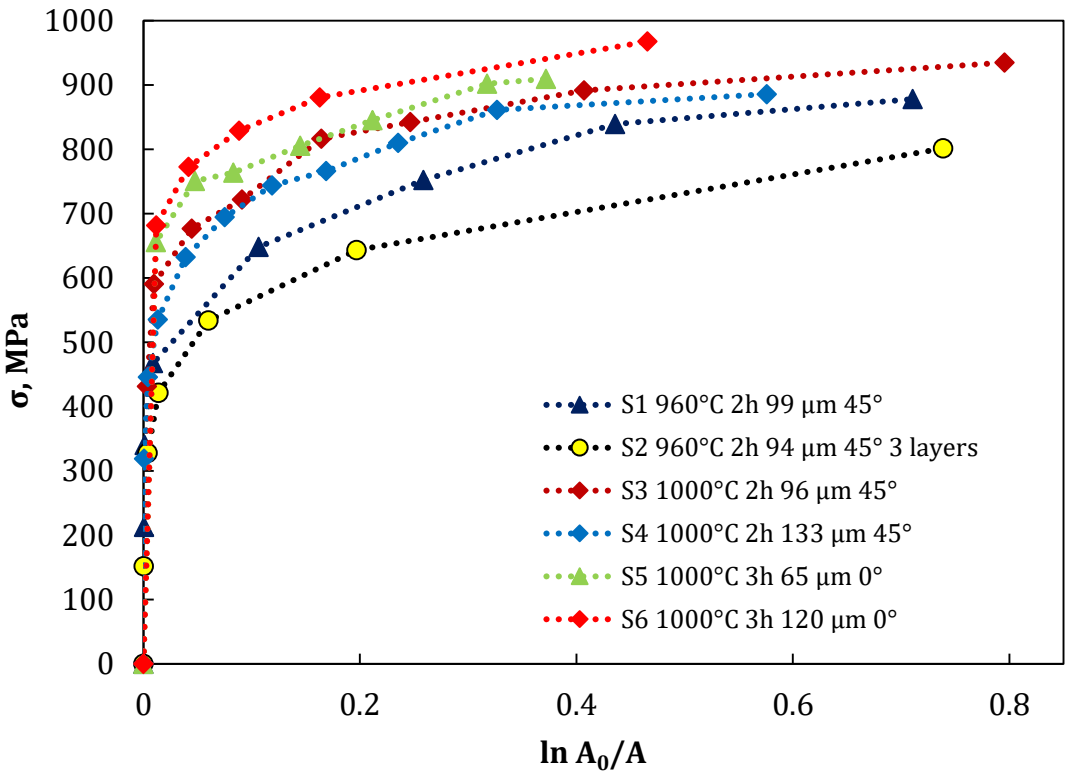

Figure 3.13: True stress-strain curves of CP titanium samples tested in tomography. In the legend, the name of the sample is followed by diffusion bonding temperature and time, and by the void configuration parameters (intervoid spacing and angle of the voids with respect to the tensile axis).

The hardening exponents (n) were obtained from fitting the stress strain curves with the following equation:

$$\sigma - \sigma_y = K\varepsilon_p^n$$

where σ_y is yield stress,

K is strength coefficient,

ε_p is plastic strain.

Hardening exponents ranging from 0.25 to 0.46 were extracted from the stress strain curves (Table 3.3, Figure 3.14).

One can note (Figure 3.13, Table 3.4) that the yield stress of samples annealed at 960 °C is lower than that of samples annealed at 1000 °C. This correlates with the

microhardness results presented in section 3.2.1 which were explained in terms of sample oxidation during annealing.

Table 3.3. Hardening exponent *n* of different samples.

Sample	Diffusion bonding parameters		Void configuration		Number of layers	*n*
	Temperature, [°C]	Time, [hours]	Void interspacing, [μm]	Angle, [°]		
S1	960	2	99	45	1	0.33
S2	960	2	94	45	3	0.38
S3	1000	2	96	45	1	0.25
S4	1000	2	133	45	1	0.39
S5	1000	3	65	0	1	0.46
S6	1000	3	120	0	1	0.42

Table 3.4. Yield stress and ultimate stress of different samples.

Sample	yield stress, MPa	ultimate stress, MPa
S1	340	878
S2	328	802
S3	431	935
S4	446	886
S5	656	910
S6	682	968

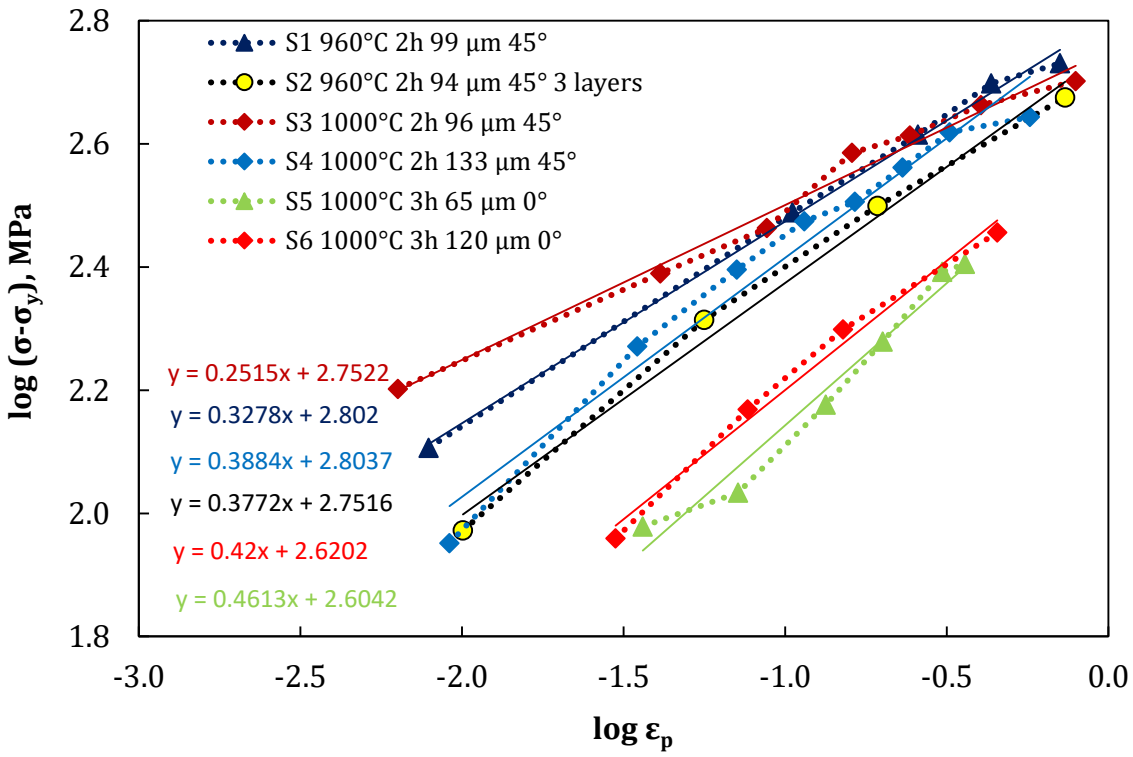

Figure 3.14: Log stress-log strain graph used in order to determine the hardening exponents.

3.2.3 X-RAY TOMOGRAMS

X-ray tomography allowed the visualization of void growth and coalescence in three dimensions. The visualization of voids in three-dimensions is possible because of the large differences in contrast between the matrix and the voids which allowed for a thresholding technique to be used where the voids can be separated from the rest of the material. Contrary to fractography which only provides information at fracture, tomographic reconstructions allow to follow the dimensions of voids during deformation in three-dimensions.

To visualize voids in three dimensions, the open source image analysis software ImageJ was used [196]. Void dimensions as a function of deformation were extracted manually. A typical example of tomograms is shown in Figure 3.15 (case of the S5 sample) where the evolution of void dimensions can be clearly observed. Voids first elongate in the tensile direction during the test and elongate in the transverse direction when coalescence starts.

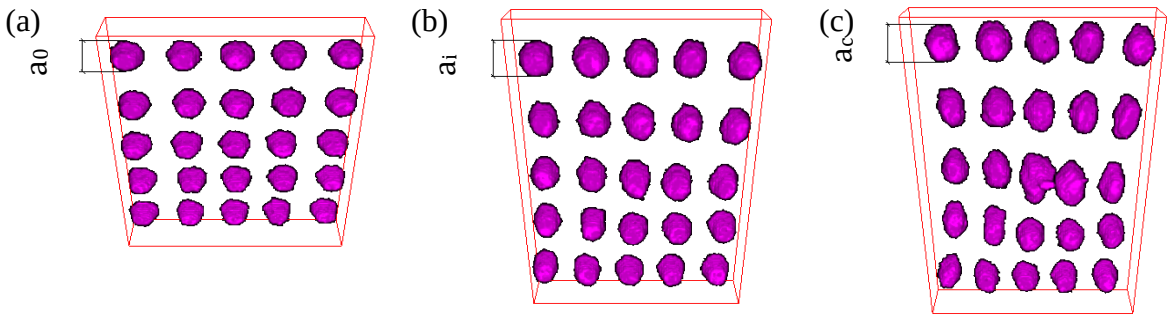

Figure 3.15. Tomographic reconstruction of a titanium sample containing one array of laser drilled holes. The example is for the S5 sample, that has been tested in-situ and the tomograms correspond to the following true strains (a) 0.00, (b) 0.16, (c) 0.30. The tensile direction is vertical. Initial void diameter a_0 is 35 μm.

Sequences of tomographic reconstructions are shown in Figure 3.16-Figure 3.21 for samples S1-S6. Void dimensions evolution can be clearly seen on this figure. Voids first elongate in the tensile direction during the test and elongate in the transverse direction when coalescence starts.

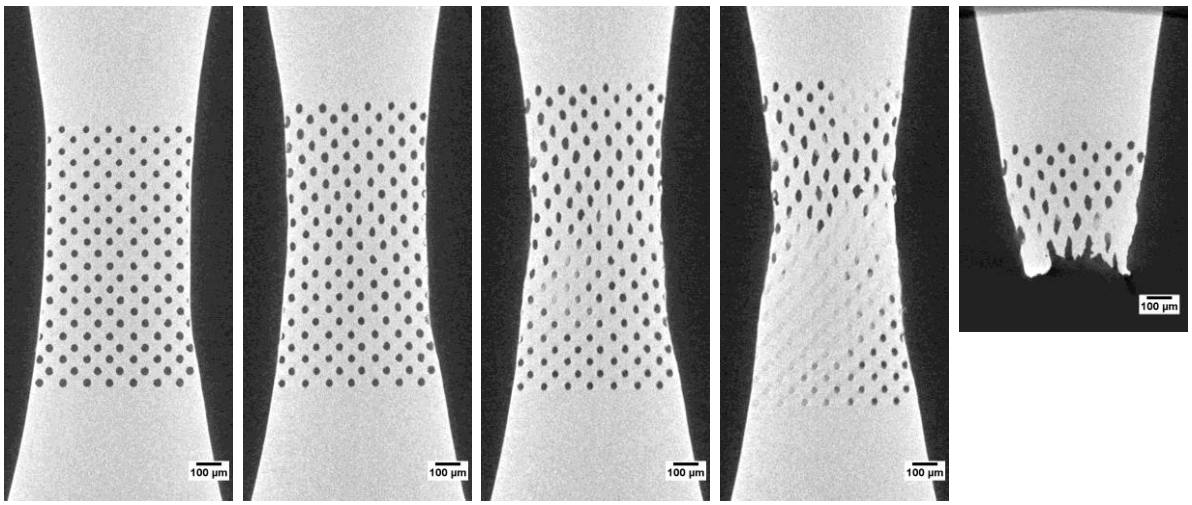

(a) (b) (c) (d) (e)

Figure 3.16: Sequence of tomographic reconstructions showing deformation for a titanium sample (S1) with a rectangular array of voids oriented at 45° with respect to the tensile axis at the following true strains: (a) 0, (b) 0.11, (c) 0.26, (d) 0.44 and (e) at fracture. Tensile axis is vertical.

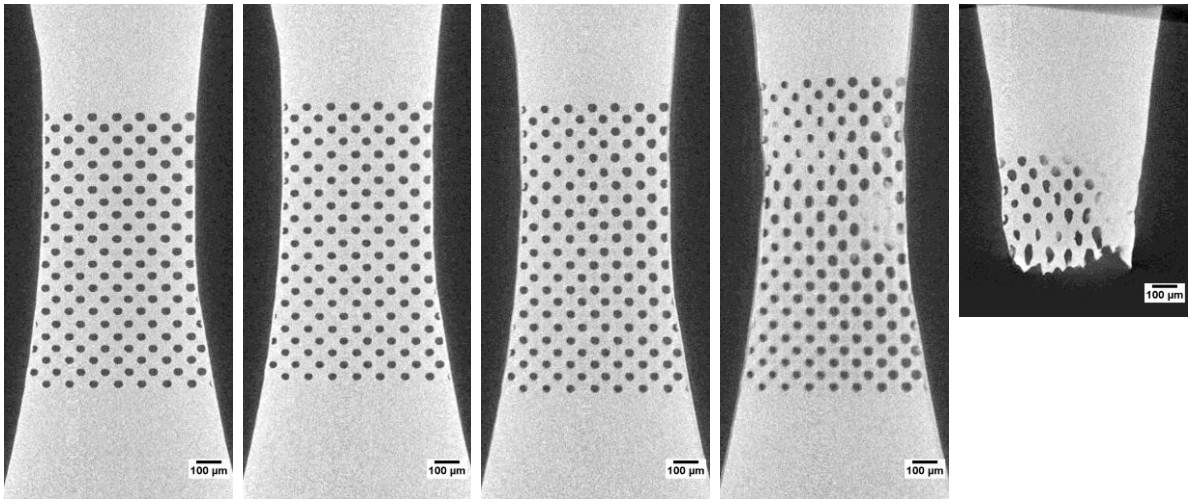

(a) (b) (c) (d) (e)

Figure 3.17: Sequence of tomographic reconstructions showing deformation for a titanium sample (S2) with a rectangular array of voids oriented at 0° with respect to the tensile axis at the following true strains: (a) 0, (b) 0.01, (c) 0.06, (d) 0.20 and (e) at fracture. Tensile axis is vertical.

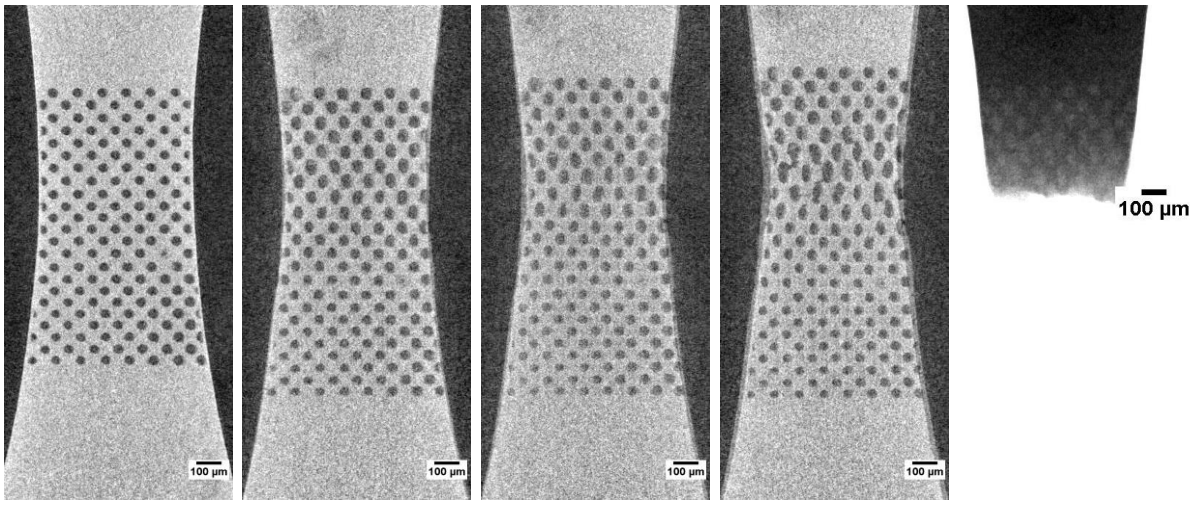

(a) (b) (c) (d) (e)

Figure 3.18: Sequence of tomographic reconstructions showing deformation for a titanium sample (S3) with a rectangular array of voids oriented at 0° with respect to the tensile axis at the following true strains: (a) 0, (b) 0.01, (c) 0.06, (d) 0.20 and (e) at fracture. Tensile axis is vertical.

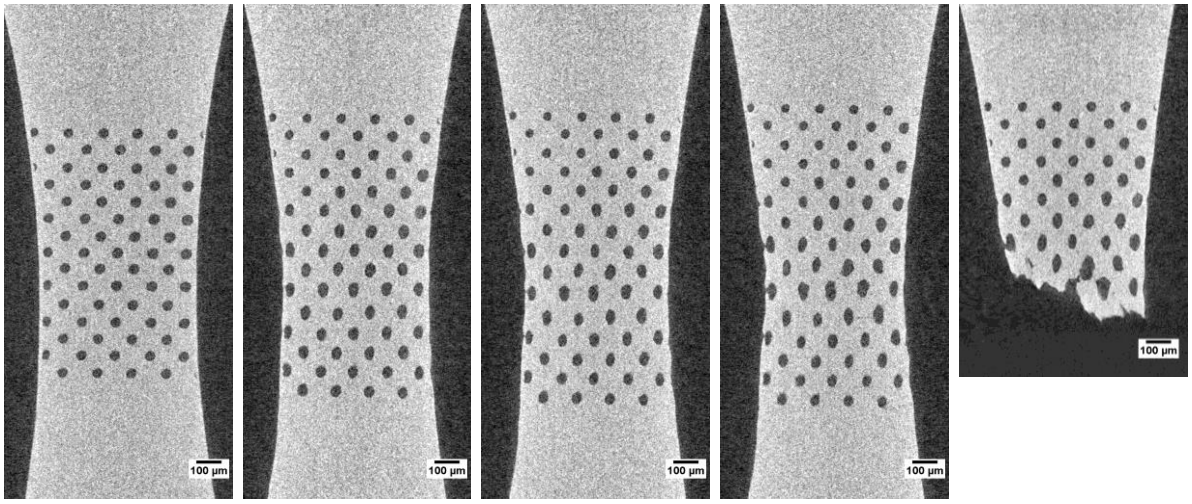

(a) (b) (c) (d) (e)

Figure 3.19: Sequence of tomographic reconstructions showing deformation for a titanium sample (S4) with a rectangular array of voids oriented at 0° with respect to the tensile axis at the following true strains: (a) 0, (b) 0.17, (c) 0.24, (d) 0.33 and (e) at fracture. Tensile axis is vertical.

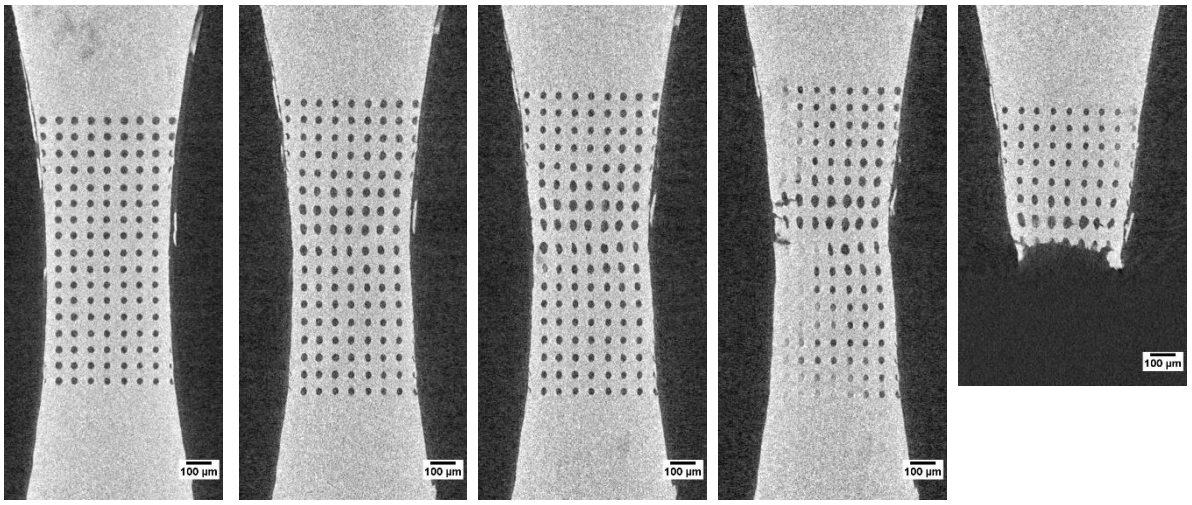

(a) (b) (c) (d) (e)

Figure 3.20: Sequence of tomographic reconstructions showing deformation for a titanium sample (S5) with a rectangular array of voids oriented at 0° with respect to the tensile axis at the following true strains: (a) 0, (b) 0.15, (c) 0.21, (d) 0.32 and (e) at fracture. Tensile axis is vertical.

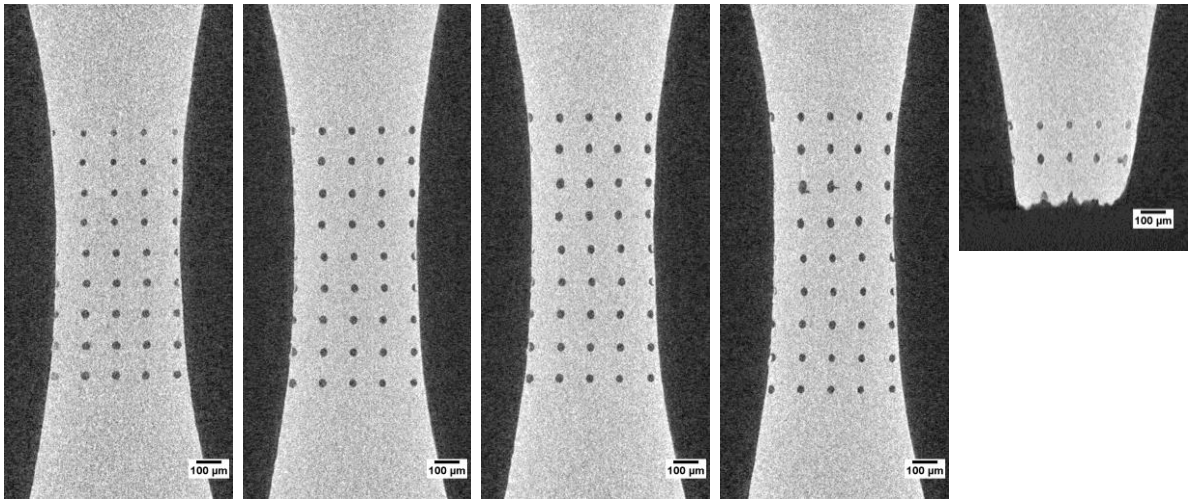

(a) (b) (c) (d) (e)

Figure 3.21: Sequence of tomographic reconstructions showing deformation for a titanium sample (S6) with a rectangular array of voids oriented at 0° with respect to the tensile axis at the following true strains: (a) 0, (b) 0.04, (c) 0.09, (d) 0.16 and (e) at fracture. Tensile axis is vertical.

3.2.4 Experimental void growth and comparison with Rice and Tracey model

Experimental results were compared to the Rice and Tracey model [142] for void growth. The Rice and Tracey equations give the principal radii R_1 and the radii in the transverse direction R_2 of the ellipsoidal void in the case of uniaxial tension in the tensile direction [107]:

$$R_1 = \left[\exp(D\varepsilon_1) + \frac{1+E}{D}\exp(D\varepsilon_1) - 1\right] R_0 \tag{3.4}$$

$$R_2 = \left[\exp(D\varepsilon_1) - \frac{1+E}{2D}\exp(D\varepsilon_1) - 1\right] R_0 \tag{3.5}$$

where

$$D = 0.558\sinh\left(\frac{3}{2}\frac{\sigma_m}{Y}\right) + 0.008\cosh\left(\frac{3}{2}\frac{\sigma_m}{Y}\right) \tag{3.6}$$

ε_1 is the total logarithmic strain integrated over the total strain path,

σ_m is the mean stress,

Y is the yield stress.

The parameters D and E are used in the Rice and Tracey model to vary the contribution of the volume and shape changing part to void growth, respectively. In the case of pure titanium, because the difference between the yield stress and the ultimate tensile stress (UTS) is high (more than a factor of 2), the material is assumed to be strongly hardening and the parameter $(1 + E)$ from equation 5 is equal to $5/3$ as proposed by Rice and Tracey [142].

The radius of curvature and the radius of the minimal section were measured in order to determine the average stress triaxiality T in the center of the minimum cross-section, using the Bridgman formula [201]:

$$\mathrm{T} = \frac{\sigma_m}{Y} = \frac{1}{3} + \ln\left(\frac{a + 2r}{2r}\right) \tag{3.7}$$

where a is radius of the smallest cross sectional area,

r is the neck radius.

Stress triaxiality does not evolve significantly in the samples and is equal to 0.37±0.003.

Void growth in the tensile direction was quantified in the different samples as a function of true strain (Figure 3.22(a)) and the following observations can be made: (i) when comparing samples S1 and S3, where the main difference between the two samples is the annealing temperature (i.e. material strength), it can be seen that void growth is similar in the harder material (1000 °C 2h) and the softer material (960 °C 2h) because the void growth curves overlap each other. This result indicates that the material strength does not significantly affect void growth or that another effect counterbalances its influence such as the grain orientation. (ii) Increasing the number of layers (see samples S1 and S2) leads to faster void growth as the volume fraction of voids increases significantly. (iii) Increasing the intervoid spacing for voids at both 45° and 0° leads to faster void growth (see samples S3 and S4, and S5 and S6

respectively) which seems counterintuitive. Again, this suggests that void growth may be more affected by the grain orientation in which voids are located rather than by the intervoid spacing. This effect is more evident in Figure 3.23 where the scatter in void growth for a given sample is large and is probably due to grain orientation effects.

Void growth in transverse direction was quantified in the different samples as a function of true strain (Figure 3.22(b)). However the changes in transverse direction are smaller compared to the changes in tensile direction and thus more noise can be seen in Figure 3.22(b). This effect is more evident in Figure 3.24 where the scatter in void growth for a given sample is large due to the small changes in transverse direction.

The growth curve for all voids that caused fracture is represented in Figure 3.25. The calculated exponential trendline for void growth in the tensile direction is close to Rice and Tracey model. This shows that on average void growth curves in the tensile direction follow the Rice and Tracey model. In the transverse direction the Rice and Tracey model does not predict void growth as it does not take into account void coalescence and interactions between voids.

When compared to the fastest growing void leading to fracture in all samples (Figure 3.22(a)), the Rice and Tracey model appears to provide a lower bound for void growth in the tensile direction. When compared to all voids in a given sample, the Rice and Tracey model also provides good overall void growth predictions in tensile direction (Figure 3.23 and Figure 3.25(a)). However, there is a large scatter in the experimental void growth results which means that different voids grow at different rates, possibly due to grain orientation effects. Similar scatter was observed in Ti-6Al-4V alloy [202]. A good fit is also observed between the experimental data and the Rice and Tracey model in the transverse direction at low strains (Figure 3.22(b), Figure 3.24, and Figure 3.25(b)). However the Rice and Tracey model significantly underestimates the void growth radius at higher strains because it does not take into account interactions between voids and void coalescence. To better understand and quantify grain orientation effects on void growth, crystal plasticity simulations were carried out (Chapter 4).

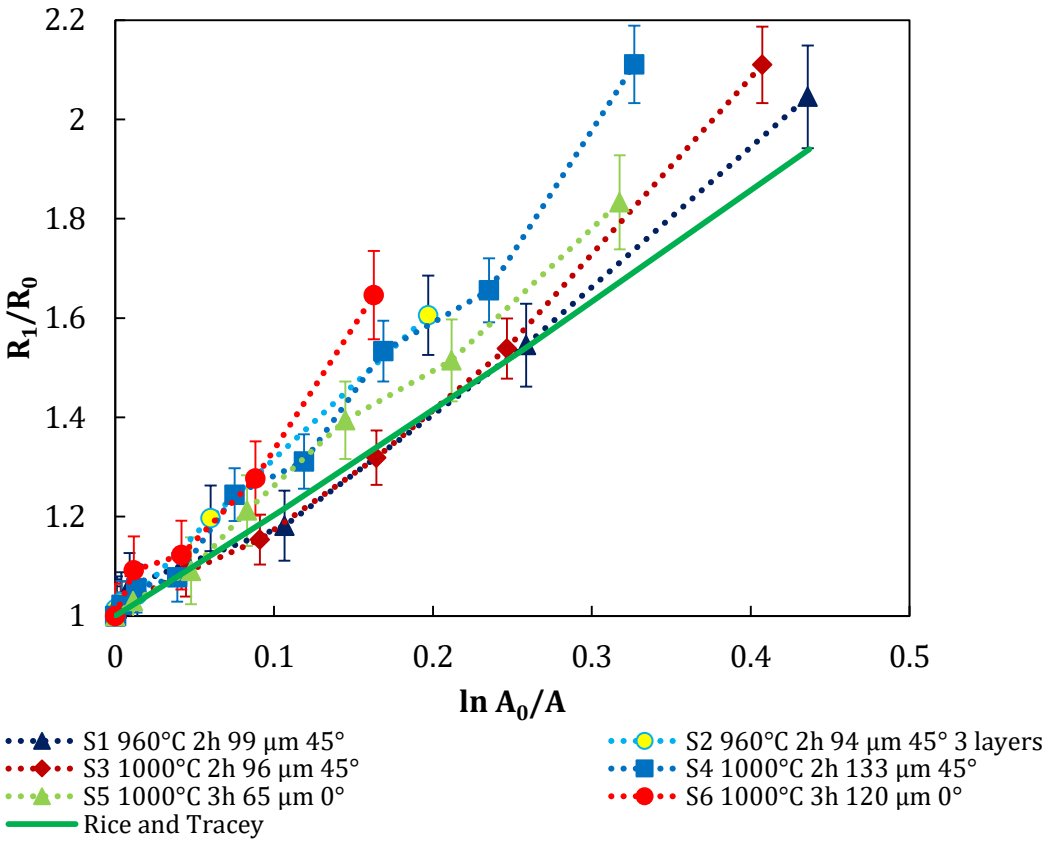
2.2
2
1.8
1.6
1.4
1.2
1
R1/R0
0
0.1
0.2
0.3
0.4
0.5
ln A0/A
S1 960°C 2h 99 µm 45°
S2 960°C 2h 94 µm 45° 3 layers
S3 1000°C 2h 96 µm 45°
S4 1000°C 2h 133 µm 45°
S5 1000°C 3h 65 µm 0°
S6 1000°C 3h 120 µm 0°
Rice and Tracey

(a)

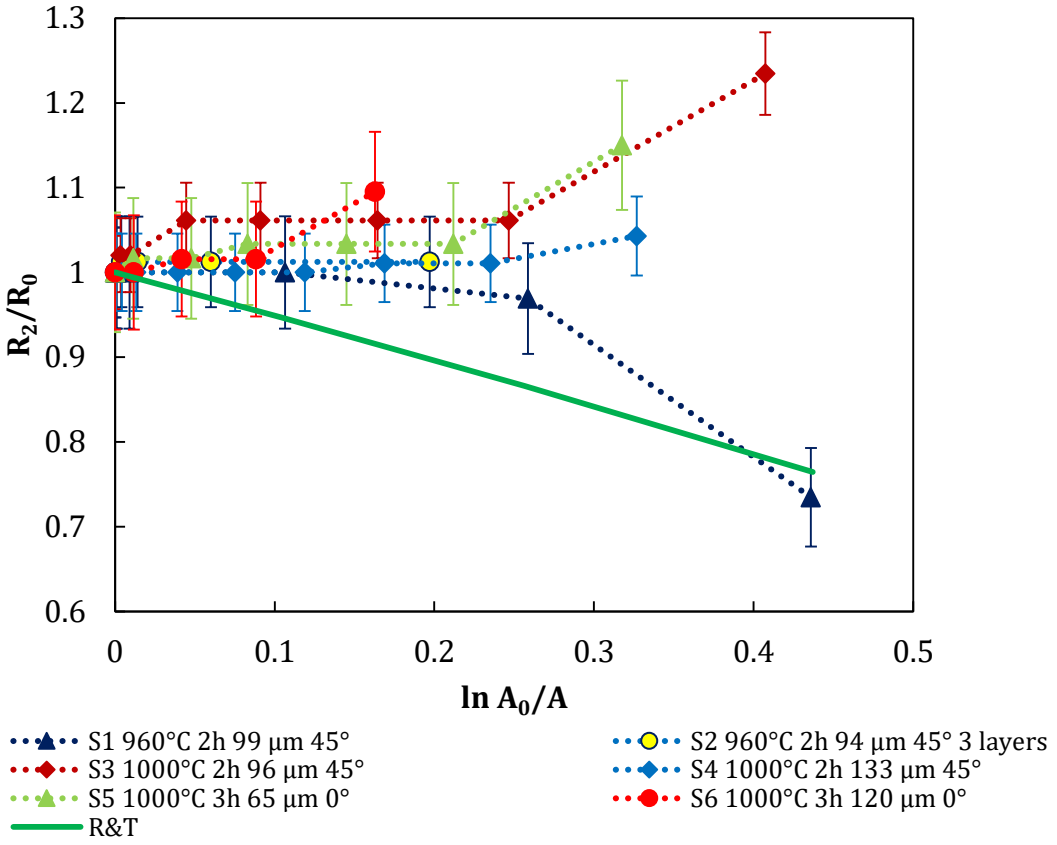

(b)

Figure 3.22: Void growth for the fastest growing void: (a) in the tensile direction, (b) in transverse direction.

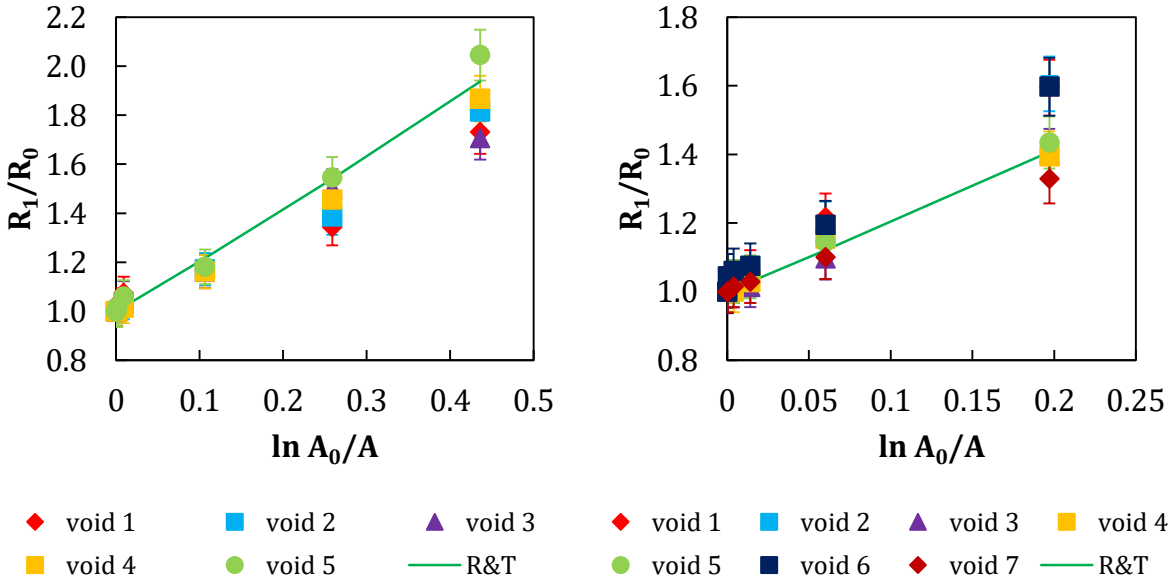

(a) (b)

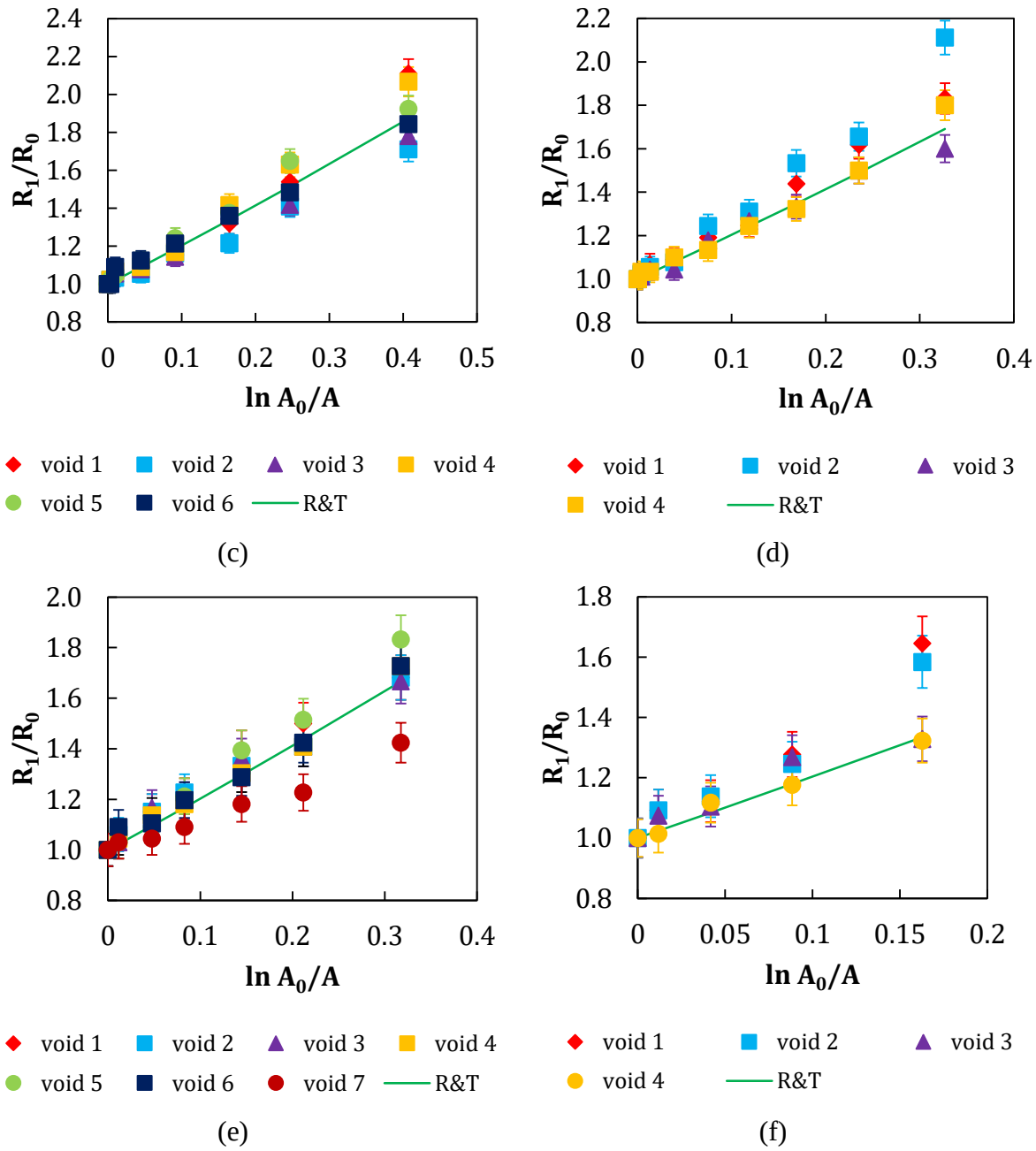

Figure 3.23: Comparison between experimental void growth (for voids in the fracture surface) and the Rice and Tracey model in tensile direction for samples (a) S1, (b) S2, (c) S3, (d) S4, (e) S5, (f) S6.

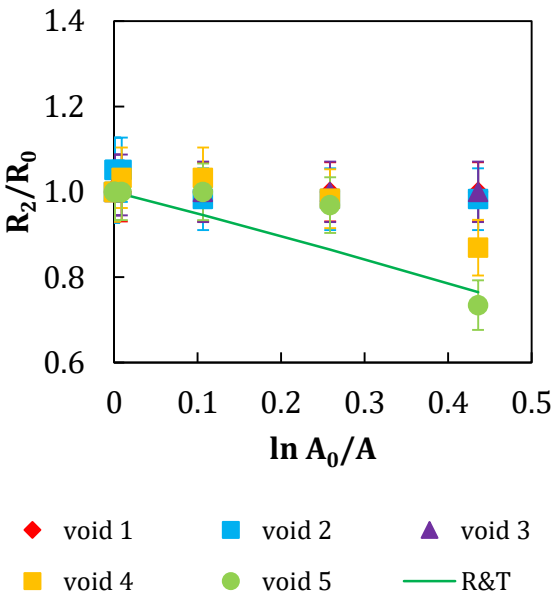
1.4
1.2
1.0
0.8
0.6
R_2/R_0
0
0.1
0.2
0.3
0.4
0.5
ln A_0/A
void 1
void 2
void 3
void 4
void 5
R&T

(a)

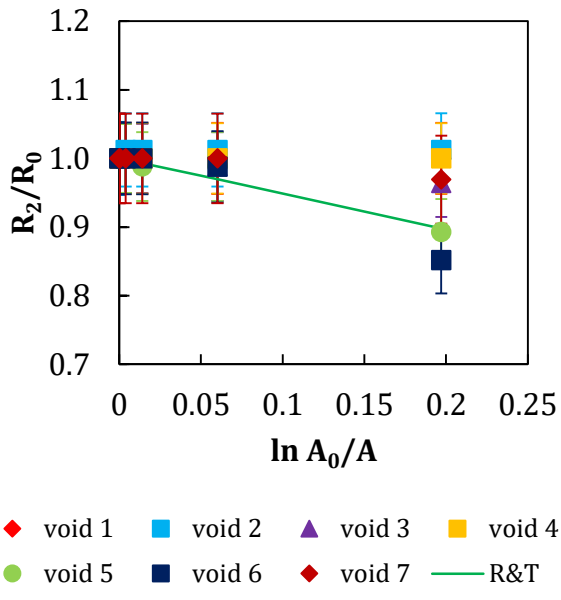
1.2
1.1
1.0
0.9
0.8
0.7
R_2/R_0
0
0.05
0.1
0.15
0.2
0.25
ln A_0/A
void 1
void 2
void 3
void 4
void 5
void 6
void 7
R&T

(b)

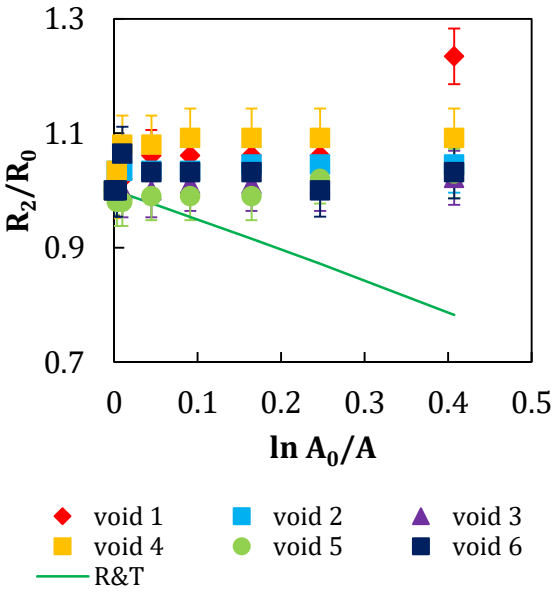
1.3
1.1
0.9
0.7
R_2/R_0
0
0.1
0.2
0.3
0.4
0.5
ln A_0/A
void 1
void 2
void 3
void 4
void 5
void 6
R&T

(c)

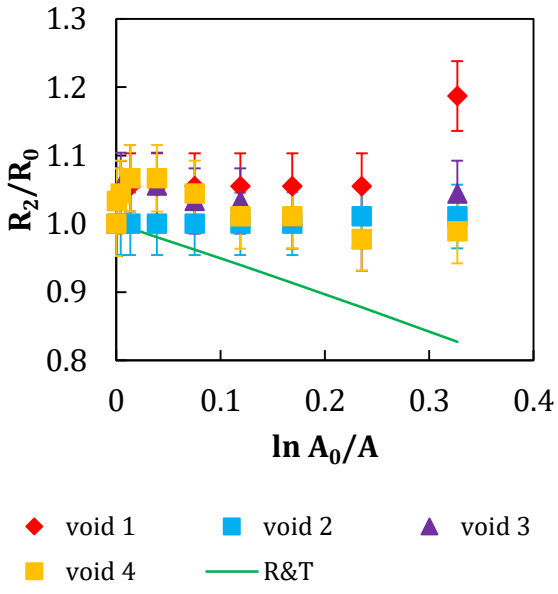
1.3
1.2
1.1
1.0
0.9
0.8
R_2/R_0
0
0.1
0.2
0.3
0.4
ln A_0/A
void 1
void 2
void 3
void 4
R&T

(d)

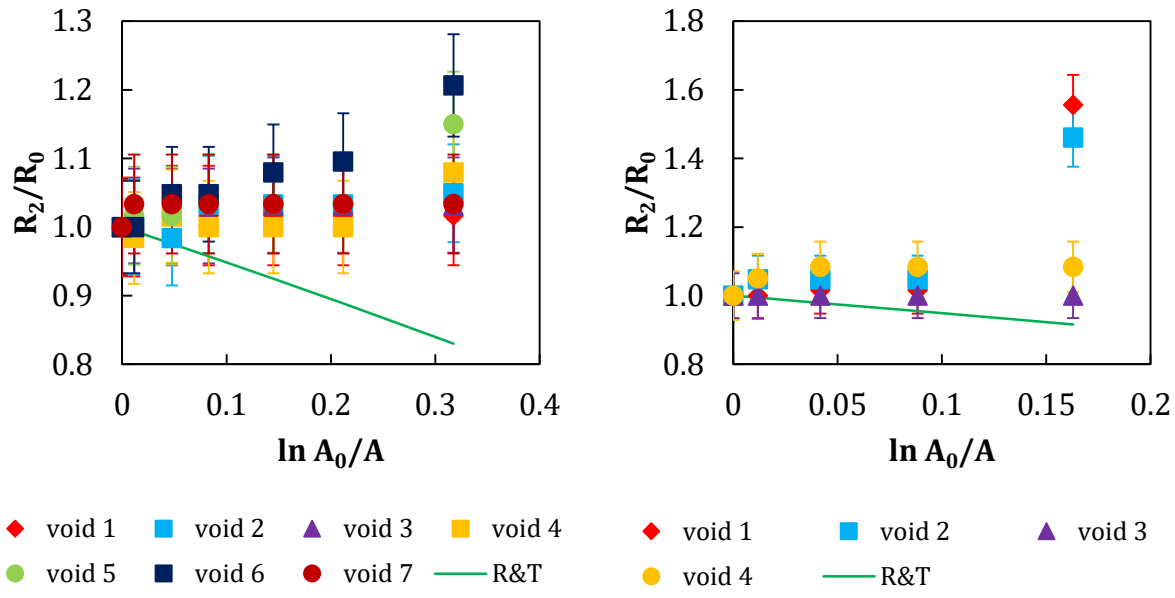

(e) (f)

Figure 3.24: Comparison between experimental void growth (for voids in the fracture surface) and the Rice and Tracey model in transverse direction for samples (a) S1, (b) S2, (c) S3, (d) S4, (e) S5, (f) S6.

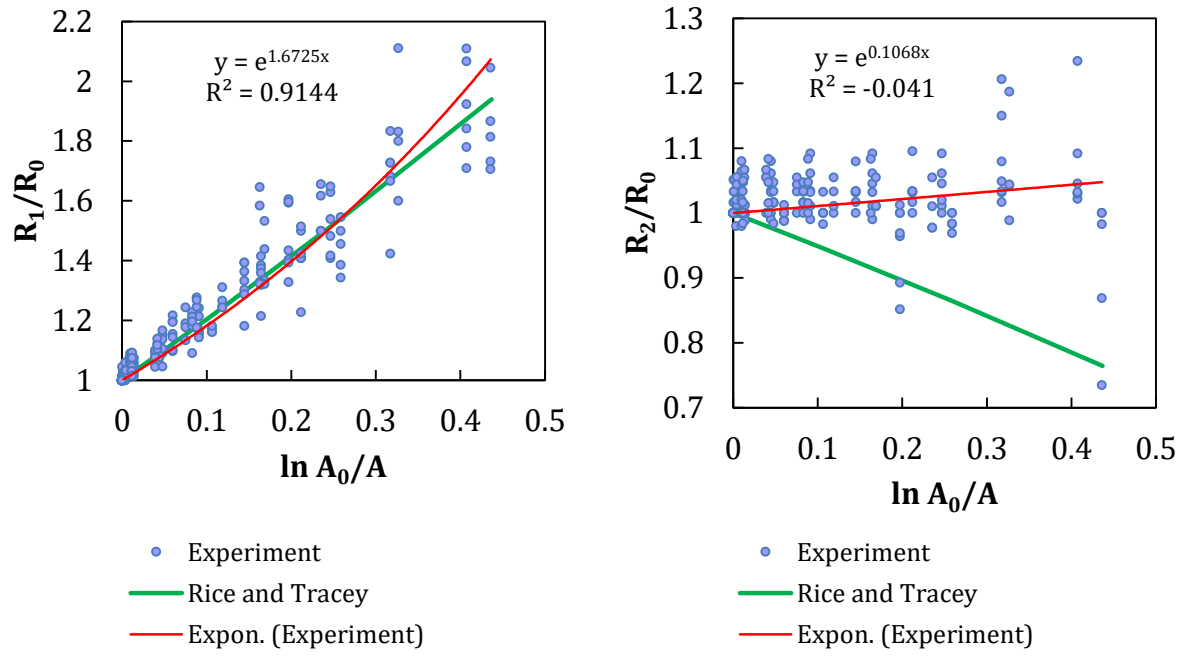

(a) (b)

Figure 3.25: Void growth of all voids that caused fracture in all samples: (a) in loading direction; (b) in transverse direction.

3.2.5 FRACTOGRAPHY

Fracture surfaces of titanium samples tested in tomography were observed in a scanning electron microscope (SEM) and are shown in Figure 3.26. Figure 3.26(d) and (f) show that the failure of the ligament between voids in samples S4 and S6 is largely ductile with the ligament necking down to a line. In samples S1, S2 and S3 (Figure 3.26(a)-(c)) one can see that the ligament between voids appears less uniform and contains more secondary voids. Sample S5 (Figure 3.26(e)) reveals an intervoid ligament failure with a brittle character as cleavage facets can be observed between most of the voids. One important difference between samples S4, S1 and S5 is their intervoid spacing. Based on the fracture analysis described above, a larger intervoid spacing (sample S4) results in a more ductile ligament failure while smaller intervoid spacing (sample S5) leads to a more brittle mode of ligament failure. When voids are close to each other there is a high probability for having only one grain in the intervoid ligament which would favor uninterrupted strain localization between voids and thus cleavage along a given slip system. If voids are further apart, more grains will be present in the intervoid ligament and the continuity of strain localization will be broken, making it more difficult for the grains to cleave. Furthermore, the closer the voids are, the less constraint the intervoid ligament will be, up to the point where localization bands can form freely from one void to the other if the voids are close enough (similar to reaching a Brown and Embury type criterion [167]). More work would need to be done in this direction to better understand the role on fracture of the intervoid spacing and number of grains in the ligament between voids.

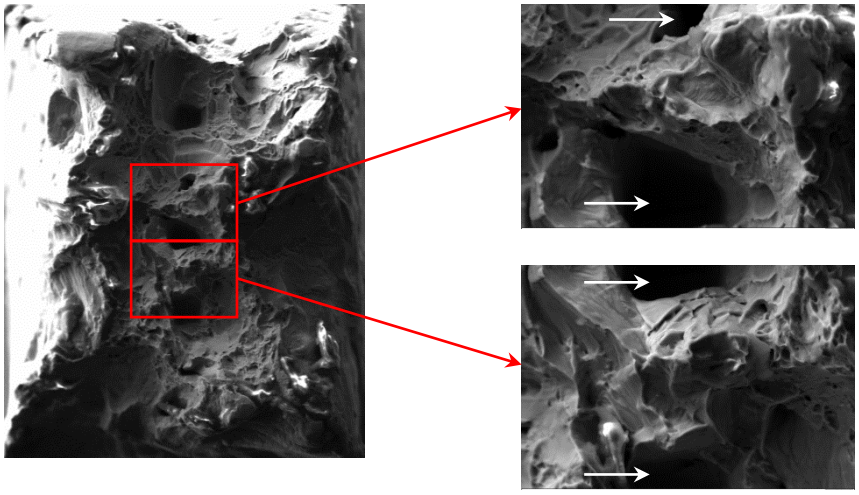

(a) sample S1

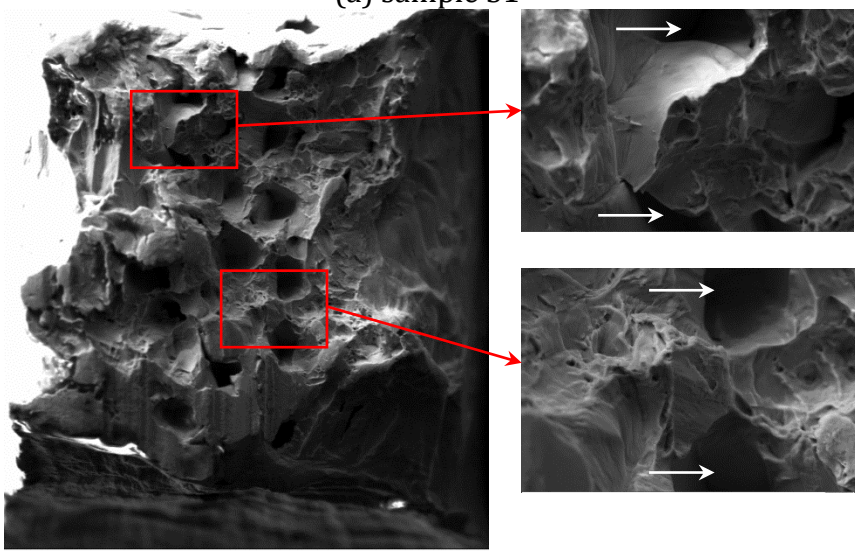

(b) sample S2

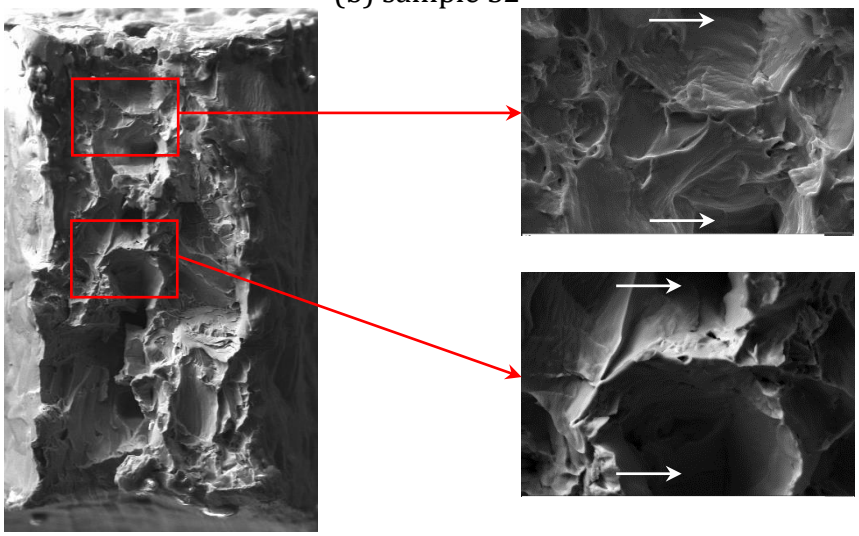

(c) sample S3

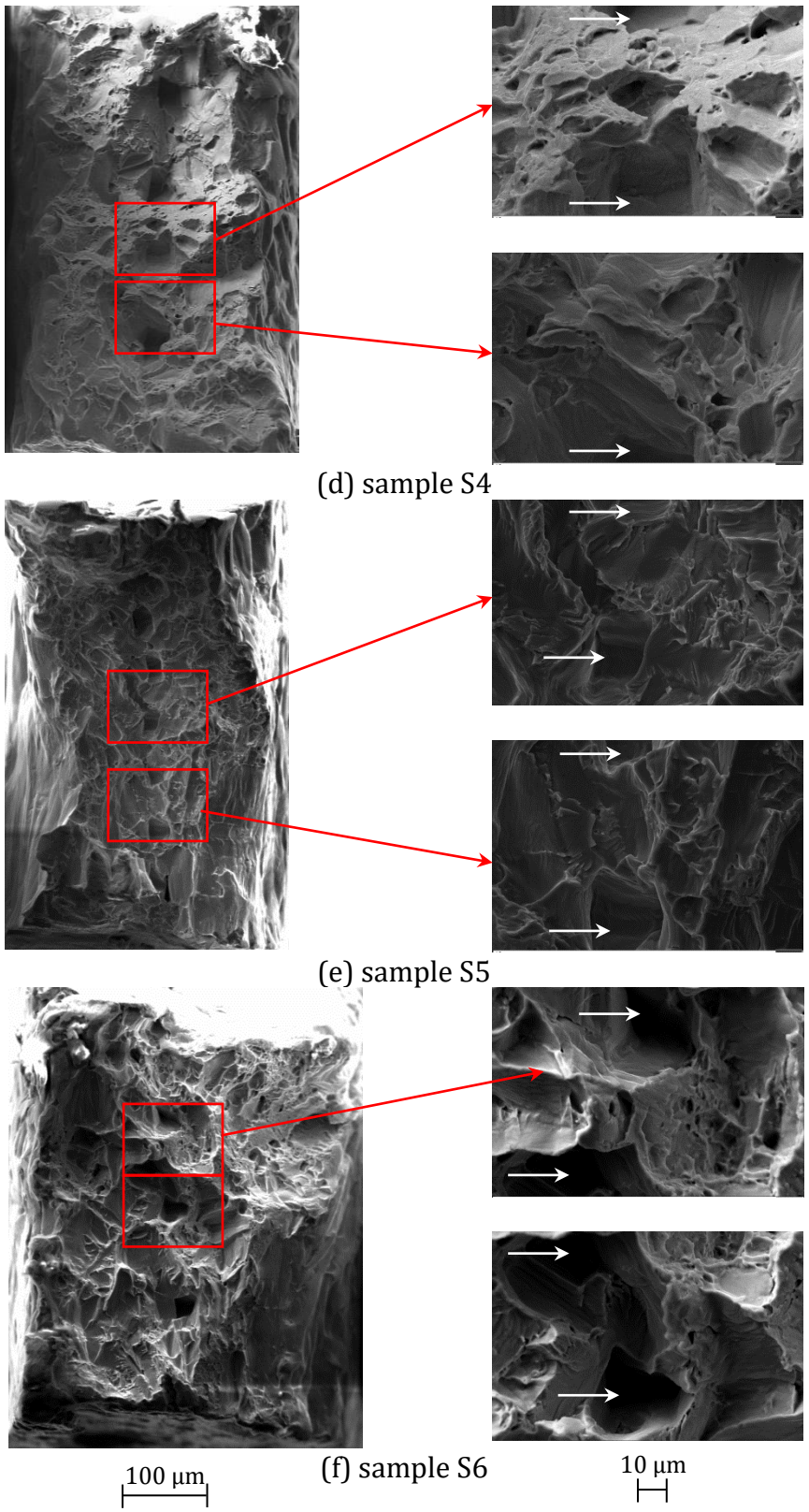

Figure 3.26: SEM images of the fracture surface of (a) sample S1, (b) sample S2, (c) sample S3, (d) sample S4, (e) sample S5, and (f) sample S6, with their respective close-ups of the ligament between two laser voids (indicated by the white arrows).

In summary, different behaviors in different samples may be attributed to different void interspacing and more so, to different grain orientations according to the present literature review (Subsection 2.3.2.3).

3.3 Discussion and conclusions

Model materials were fabricated by diffusion bonding CP Ti foils with and without prior laser drilling of voids, in order to obtain voids in the bulk of Ti samples. The annealing of CP Ti was carried out at temperatures of 960 °C to 1000 °C, which is higher than the phase transformation temperature (882 °C, Table 2.1, [1]). Samples were then cooled down with a cooling rate of 0.40-0.46 °C/s that resulted in a microstructure consisting of α lamella colonies which form grains. Inside each grain, α-plates have the same orientation [119]. It is important to note here that the microstructural unit of deformation is bigger than the voids drilled and thus it is possible to study the effect of grain orientation on void growth. This is consistent with literature [32], where it is claimed that cooling CP Ti with a cooling rate slower than 30°C/s [33] results in α lamella microstructure. This microstructure was characterised using the line-intercept method [194] and it was obtained that the width of α lamellae is 16-18 μm depending on the annealing temperature and time. Then the mechanical properties of the annealed samples were determined. The annealing at 1000 °C during 3 hours resulted in microhardness equal to 252 HV; the annealing at 1000 °C during 2 hours resulted in microhardness equal to 238 HV and finally the annealing at 960 °C during 2 hours resulted in microhardness equal to 228 HV. The changes in microhardness are not related to changes in microstructure but instead are due to the oxygen content in the samples. Indeed, it was demonstrated [199] that higher annealing temperature and time result in higher oxygen content in titanium, and thus higher microhardness because the oxygen addition leads to solid solution strengthening by asymmetric lattice distortion [200]. No twinning was seen in our CP Ti samples probably due to the presence of solute atoms (oxygen) as it was shown that solute atoms can suppress twinning [24]. The oxygen content of our samples was too low to be easily detectable using conventional techniques. The role of oxygen on slip behaviour is very complex: it was shown that oxygen content affects the magnitude and

the relative values of the critical resolved stress for three slip systems (basal, prismatic and pyramidal a) [203]. The higher oxygen and nitrogen content (0.1 wt. %) gave rise to the activation of three slip systems: basal, prismatic and pyramidal [203]. Slip was confined to prismatic slip and occasional activation of basal slip for the lower oxygen and nitrogen content (0.01 wt. %) [203]. In our samples the oxygen content was around 0.5-0.6 wt. % and three slip systems were activated (basal, prismatic and pyramidal c+a), which is consistent with [203].

Next, in-situ tensile tests were performed coupled with X-ray tomography in order to see the evolution of void growth inside Ti samples. Knowing the force applied and the instantaneous smallest cross sectional area, true stress-strain curves were calculated (Figure 3.13). Here again, the mechanical properties varied depending on the sample's annealing temperature and time. Higher annealing temperature and time resulted in higher yield stress and higher ultimate tensile strength due to the higher oxygen content.

X-ray tomography allowed visualizing and quantifying void growth inside Ti samples. After reconstructing the tomograms, the dimensions of the voids were measured using the open source image analysis software ImageJ [196]. The voids that lead to fracture in each sample were analysed. Void growth in the tensile direction is discussed first. From Figure 3.15 and Figure 3.22(a) it can be seen that the voids elongate in the tensile direction as the sample deforms. The fastest growing voids in each sample were compared and it was noted that there is a scatter in void growth (Figure 3.22(a)). First, it can be seen that samples with different material strength have similar void growth suggesting that the material strength does not significantly affect void growth or that another effect counterbalances its influence such as the grain orientation. In literature it was shown that the yield stress and the work hardening rate have an important effect on coalescence and that ductile fracture is favored by low yield stress, high work hardening rate [92]. It should be noted here that while the yield stresses in our work are significantly different, the work hardening rates of samples annealed under different conditions are fairly similar. Second, when the volume fraction of voids increases (this is achieved by increasing the number of layers

containing voids during diffusion bonding), void growth is faster. According to [92] high void volume fraction favours ductile fracture in FCC materials, however according to [204] the void fraction does not have a significant impact on the growth and linkage behavior of the voids in HCP material. This is because in contrast to FCC materials, the anisotropic deformation in HCP materials associated with the local microstructure outweighs the effects of the void fraction on the void growth [204]. These results are in agreement with our experimental observations. Third, increasing the intervoid spacing for voids at both 45° and 0° leads to faster void growth which is counterintuitive suggesting that void growth may be more affected by grain orientation rather than by the intervoid spacing which is in agreement with [204]. In order to confirm this statement, voids inside one sample (where the annealing conditions are the same) were compared to each other. Intuitively and according to the literature [92], the closer the voids in a FCC material are, the earlier the coalescence and the lower the final failure strain of the whole sample.

Void growth comparisons within a sample allows for isolating the effect of grain orientation on void growth as material strength and intervoid spacing remain the same. Figure 3.23 shows the scatter in void growth for voids leading to fracture in a given sample. The scatter in void growth for a given sample is large and is probably due to grain orientation effects because the other parameters are unchanged. This is consistent with [204] where it was shown that local microstructure of Mg affects void growth and coalescence. In the vast majority of cases the dominant fracture mechanisms involved twinning and grain boundary failure while failure of these boundaries lead to premature void coalescence. In agreement with our study, the large range of variability in void growth behavior in Ti-6Al-4V alloy was related to the effects of the local crystallographic orientation [202].

Void growth in the transverse direction was also extracted (Figure 3.22(b) and Figure 3.24). However the changes in void dimensions in the transverse direction are smaller compared to those in the tensile direction. Nevertheless it can be noted that first voids shrink in the transverse direction and then they grow once coalescence starts because interactions between voids forces them to growth towards each other.

Experimental void growths were compared to the Rice and Tracey model, developed for an isolated spherical void in an infinite media [142]. Equations (3.4) and (3.5) were used in order to evaluate void growth. Figure 3.22(a) shows that on average the Rice and Tracey model underestimates void growth for the fastest growing voids in the tensile direction. However on average the Rice and Tracey model predicts well the overall void growth (Figure 3.23, Figure 3.25(a)) in the tensile direction. This not unexpected as some voids will growth faster and some more slowly depending on the underlying grain orientation. The average can therefore be close to the behavior of a material not showing strong crystal plasticity effects. It is important to note that the Rice and Tracey model does not take into account the grain orientation, this is why crystal plasticity simulations were performed in order to predict grain orientation effects on void growth. This is in agreement with [205] where it was shown that the Rice and Tracey model provides a good prediction of the void growth behavior in copper during the early stages of deformation, before void interaction occurs. However, once the voids begin to interact with one another, void growth is amplified and the Rice and Tracey analysis no longer predicts void growth since it does not account for void interactions.

Main conclusions are presented next. Three main points were observed during the experiments. First, it was shown that the annealing temperature and time affect the oxygen content in CP titanium and thus affect the mechanical properties of the samples. Higher temperature and longer annealing time result in higher oxygen content in titanium thus higher microhardness and lower ultimate tensile strength due to solid solution strengthening by asymmetric lattice distortion [200].

The second point of interest was the evaluation of the effect of grain orientation on void growth. It was suggested that grain orientation affects void growth. It was found that the Rice and Tracey model predicts well the average void growth. However it was observed that void growth varies locally and this difference is potentially due to the underlying grains orientation. The effect of grain orientation on void growth will be discussed in Chapter 5.

Third, despite the different mechanical properties of samples subjected to different heat treatments, these differences did not affect void growth significantly. Differences in fracture modes were however observed between samples having different intervoid spacings: a larger intervoid spacing results in a more ductile ligament failure while smaller intervoid spacing leads to a more brittle mode of ligament failure. It is interesting to note that void growth is not strongly related to mechanical properties (strength).

Chapter 4 CRYSTAL PLASTICITY SIMULATIONS RESULTS ON THE INDIRECT OBSERVATIONS OF GRAIN ORIENTATION EFFECTS ON VOID GROWTH IN CP TITANIUM

This chapter describes crystal plasticity simulations results and presents their comparison to the experimental void growth results in CP titanium above the allotropic transition temperature.

4.1 CRYSTAL PLASTICITY SIMULATIONS

4.1.1 MODEL DEFINITION

The effect of grain orientation on void growth in titanium has been studied using a crystal plasticity finite element model developed by Prof. Javier Segurado and Prof. Javier Llorca (Department of Materials Science, Polytechnic University of Madrid and IMDEA Materiales) [206]. The subroutine code is written in Fortran. The behavior of Ti crystal is taken into account using an elasto-viscoplastic phenomenological crystal plasticity model which includes the microscopic mechanisms of plastic deformation by slip along basal, prismatic and pyramidal c + a systems [207]. The rate-sensitivity exponent was the same for all slip systems and was selected as m = 0.1, value obtained from [207]. The hardening is accounted for by a Voce-hardening law [208]:

$$h(\Gamma) = h_0 + \left(h_0 - h_s + \frac{h_0 h_s \Gamma}{\tau_s}\right) \exp^{-h_0 \Gamma / \tau_s} \tag{4.1}$$

where $h(\Gamma)$ is the hardening modulus, Γ is the accumulated shear strain in all slip systems, τ_0 is the initial critical resolved shear stress, τ_s is the saturation shear stress, h_0 is the initial hardening moduli, and h_s is the saturation hardening moduli.

These parameters were obtained combining literature values and inverse analysis of the experimental macroscopic tensile response (Figure 4.1). First, the following ratios of the CRSS between different slip systems were taken from microtests performed on crystalline pure Ti grains [7], $\tau^{basal} = 1.155\tau^{prismatic}$ and $\tau^{pyramidal} = 2.618\tau^{prismatic}$. Second, the ratio between τ_0 and τ_s were kept constant for all slip systems. Third, the

hardening moduli h_0 and h_s were identical for the three active slip systems. Finally, with these restrictions, the three parameters remaining (τ_0, h_0 and h_s) are searched imposing that the response of a polycrystalline crystal plasticity finite element model including the actual texture coincides with the corresponding experimental tensile curve (Figure 4.1). The experimental tensile curves of the three materials considered (samples S1, S3 and S6) are used to obtain the values of τ_0, h_0 and h_s for each material and the resulting parameters are shown in Table 4.1.

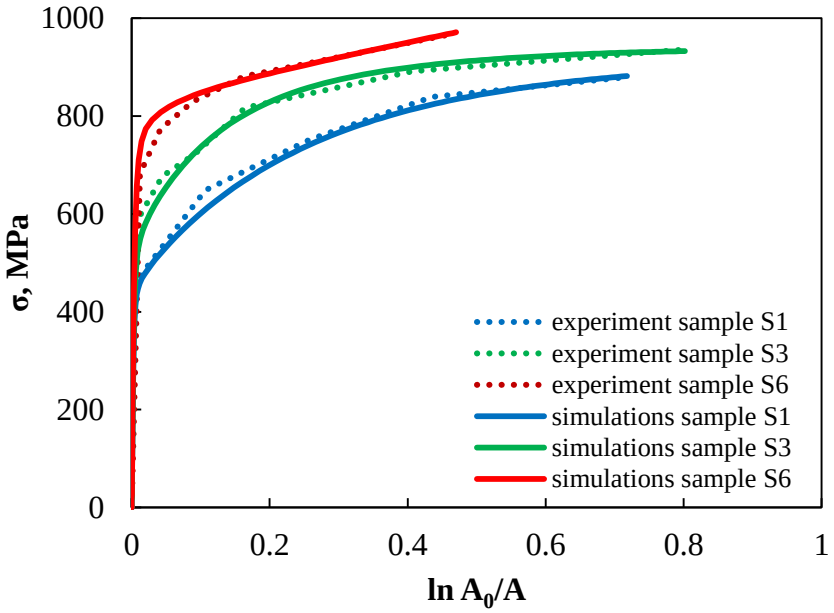

Figure 4.1: Tensile stress-strain curves: experimental and numerical simulations results.

Table 4.1: Parameters of Voce-hardening law for samples S1, S3 and S6.

Slip system	τ_0 (MPa)			τ_s (MPa)			h_0 (MPa)			h_s (MPa)		
	S1	S3	S6	S1	S3	S6	S1	S3	S6	S1	S3	S6
Prismatic	123	147	212	274	266	235	310	500	300	1	5	54
Basal	143	169	245	317	308	272	310	500	300	1	5	54
Pyramidal c+a	323	384	555	718	698	616	310	500	300	1	5	54

The procedure of running simulations with a crystal plasticity subroutine consists of several steps. First, the model is created through the Abaqus CAE. Then, the input file is

generated. Finally the input file is edited in order to incorporate the crystal plasticity subroutine. During this step crystal orientations are chosen and entered in the input file. When this procedure is done, the simulation is submitted using Abaqus Command program.

The subroutine used is a constitutive model of crystal plasticity for the implicit FE code ABAQUS. It is programmed in finite strains (using hyperelastic approach) and based on the multiplicative decomposition of plastic strain [206].

The decomposition of the deformation gradient, F, into its elastic $F^e$and plastic part F^p is assumed [209–213]:

$$F = F^e F^p \tag{4.2}$$

Using the definition of the velocity gradient, $L \equiv \nabla_x v = \dot{F}F^{-1}$, equation (4.1) leads to the additive decomposition of L as:

$$L = L^e + F^e L^p F^{e-1} \tag{4.3}$$

where L^e and L^p are the elastic and the plastic velocity gradients, respectively.

If plastic deformation takes place along multiple slip systems, L^p is defined as the sum of the shear rate, $\dot{\gamma}$, for each slip system α, according to:

$$L^p = \sum_\alpha \dot{\gamma}^\alpha (s^\alpha \otimes m^\alpha) \tag{4.4}$$

where s^α and m^α stand for the unit vectors in the slip direction and normal to the slip plane in the reference configuration, respectively.

The crystal is assumed to behave as an elasto-viscoplastic solid in which the plastic slip rate for a given slip system, follows a power-law dependency:

$$\dot{\gamma}^\alpha = \dot{\gamma}_0 \left(\frac{|\tau^\alpha|}{g^\alpha} \right)^{1/m} \operatorname{sgn}(\tau^\alpha) \tag{4.5}$$

where $\dot{\gamma}_0$ is a reference shear strain rate,
g^α is the critical shear stress on the slip system,
m is the rate-sensitivity exponent [214],

τ^{α} is the resolved shear stress on the α slip system.

τ^{α} is obtained as the projection of the Kirchoff stress on that α system:

$$\tau^{\alpha} = \mathbb{C}\left[(F^{eT}F^{e})^{1/2} - I\right] : s^{\alpha} \otimes m^{\alpha} \tag{4.6}$$

where $\mathbb{C}$ is the elastic stiffness tensor of the crystal.

The evolution of the critical shear stress, g^{α}, for a given slip system, α, is obtained using the classical hardening model of Asaro and Needleman, which defines the current slip resistance as:

$$\dot{g}^{\alpha} = \sum\nolimits_{\beta} q_{\alpha\beta} h(\Gamma) \dot{\gamma}_{\beta} \tag{4.7}$$

where $q_{\alpha\beta}$ with $\alpha = \beta$ and $\alpha \neq \beta$ are the self- and latent-hardening coefficients, respectively,
h is hardening modulus.

Voce-hardening law is used in order to determine h.

The accumulated shear strain in all slip systems, Γ, and is given by:

$$\Gamma = \int_{0}^{t} \sum\nolimits_{\alpha} \dot{\gamma}_{\alpha} dt \tag{4.8}$$

where t is time.

The orientation of the crystal (Figure 4.2) is entered to the subroutine in the following format: v1x, v1y, v1z, v2x, v2y, v2z, thetax. v_1 and v_2 correspond to vectors [100] and [001] expressed in the global system (e_x, e_y, e_z). thetax corresponds to an additional rotation around global x axis. Transformation matrix g used to transform Euler angles from the experiments into subroutine input parameters is given by the following equation:

$$g = \begin{bmatrix} cos\varphi_1 cos\varphi_2 - sin\varphi_1 sin\varphi_2 cos\Phi & sin\varphi_1 cos\varphi_2 + cos\varphi_1 sin\varphi_2 cos\Phi & sin\varphi_2 sin\Phi \\ -cos\varphi_1 sin\varphi_2 - sin\varphi_1 cos\varphi_2 cos\Phi & -sin\varphi_1 sin\varphi_2 + cos\varphi_1 cos\varphi_2 cos\Phi & cos\varphi_2 sin\Phi \\ sin\varphi_1 sin\Phi & -cos\varphi_1 sin\Phi & cos\Phi \end{bmatrix}$$

where φ1,Φ,φ2 are Euler angles.

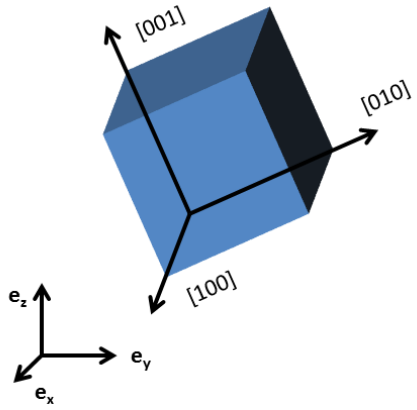

Figure 4.2: Orientation of single crystal respect to a global system [206].

Void growth simulations were run using a 3D finite element model in the shape of a cube (Figure 4.3(a)) consisting of grains (Figure 4.3(b)) with the grain in the middle containing a spherical void (Figure 4.3(c)). The grains were represented in the shape of a tetrakaidecahedron (Figure 4.3(b)) which is a reasonable approximation of grains in polycrystals [215]. A mesh dependence study was performed and appropriate mesh was selected (Figure 4.4). The grain in the middle, containing the spherical void, was modeled using the CP model previously described and using three different orientations of the crystal lattice with respect to the loading direction. The surrounding grains were modeled using standard isotropic J2 plasticity with yield stress and isotropic hardening evolution taken from tensile experiments (Figure 4.1). The size of the assembly was 80 μm, the grain size was 40 μm and the void size was 10 μm. For simulations with two voids the void size of 5 μm was selected so that two voids are completely embedded inside the grain having crystal plasticity properties. It was verified that the void diameter of 5 μm does not change the results compared to simulations with a 10 μm void diameter. Periodic boundary conditions were used, three faces (perpendicular to x, y and z axes) of the model had zero displacement and three opposite faces were linked to the deformation vector so that they could move could not bend.

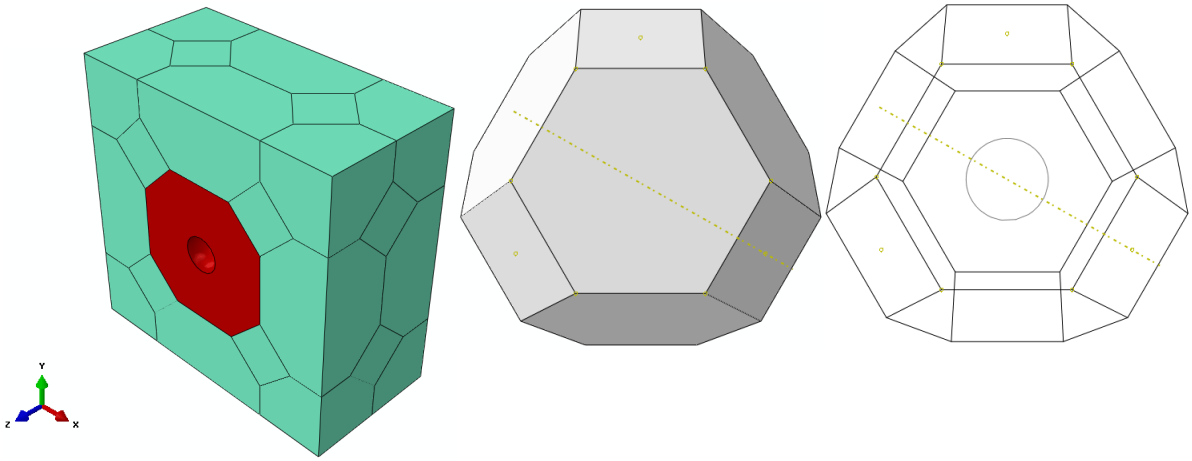

(a) (b) (c)

Figure 4.3: (a) 3D model. Half of the model is shown. Red color indicates crystal plasticity, green color indicates macroscopic properties of titanium; (b) tetrakaidecahedron used to construct the 3D model; (c) tetrakaidecahedron with the spherical void in the middle. Tensile direction coincides with the x axis.

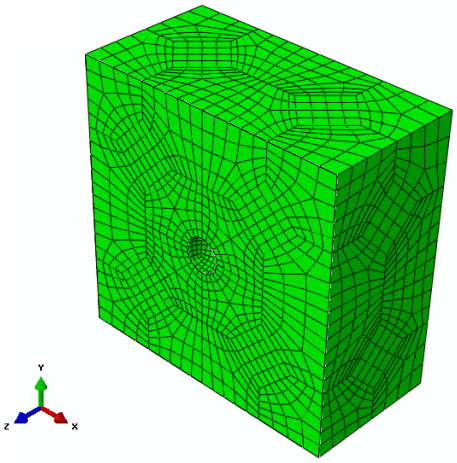

Figure 4.4: The mesh of 3D model. Half of the model is shown.

4.1.2 Simulations results

The results of the simulations show first that the evolution of void size with applied strain depends on the orientation of the grain in which the void is embedded (Figure 4.5 and Figure 4.6). While the simulation results do not match exactly the experiments, the range of scatter in the results is similar in both cases indicating that the scatter observed experimentally could indeed be due to grain orientation effects. Simulated void growth results for samples S1, S3, and S6 which were annealed at different temperatures, and thus have different strength levels, are compared in Figure 4.7. The

results show that material property (in this case the strength of the material) has a much smaller effect on voids growth than the orientation of the grains in these materials, which support the experimental observations.

In order to understand the effect of void interspacing on void growth, crystal plasticity simulations were performed using the material properties of sample S3 for two different intervoid spacings: 2d and 4d, where d is the void diameter (Figure 4.8). To achieve this, models with two voids spaced 2d and 4d were created. The results (Figure 4.9) show that increasing the intervoid spacing leads to a slight increase in void growth which is in agreement with the experimental results (Section 0) which initially seemed counterintuitive. For comparison purposes, Figure 4.9 also shows the results for a sample without crystal plasticity. While using isotropic hardening only, it can be seen that increasing void interspacing from 2d to 4d does not affect the void growth significantly (there is a slight increase in void growth with decreasing intervoid spacing which is expected). It is interesting to note that the results for isotropic plasticity are between the crystal plasticity results for different grain orientations, which is as expected. However, the orientation of the grain has a much stronger effect on void growth than the intervoid spacing as seen in Figure 4.9. Note that some void rotation with respect to the tensile axis can be observed in the simulation results (Figure 4.6, Figure 4.10 and Figure 4.11). Some void rotation can also be observed in the experimental results in Figure 3.16-Figure 3.21 but no direct comparison can be made with the simulation results as the grain orientation is not known in the experiments. Figure 4.12 and Figure 4.13 represent the zoomed version of experimental and simulation results with one void and a straight line as reference to better visualize void rotation.

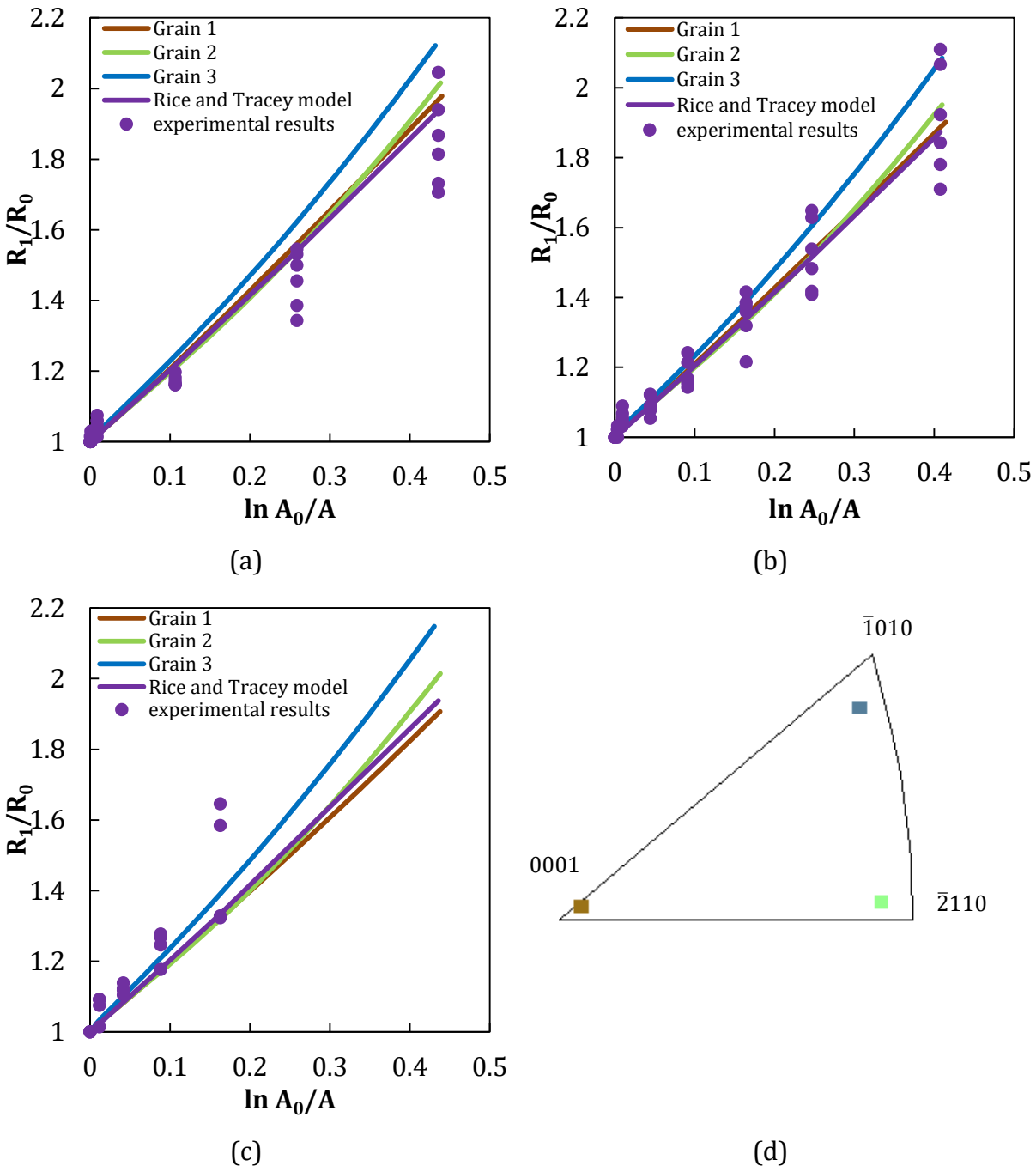

Figure 4.5: Experimental and simulation results of void growth in three samples: (a) S1, (b) S3 and (c) S6. (d) The inverse pole figure shows the three different grain orientations used in the simulations.

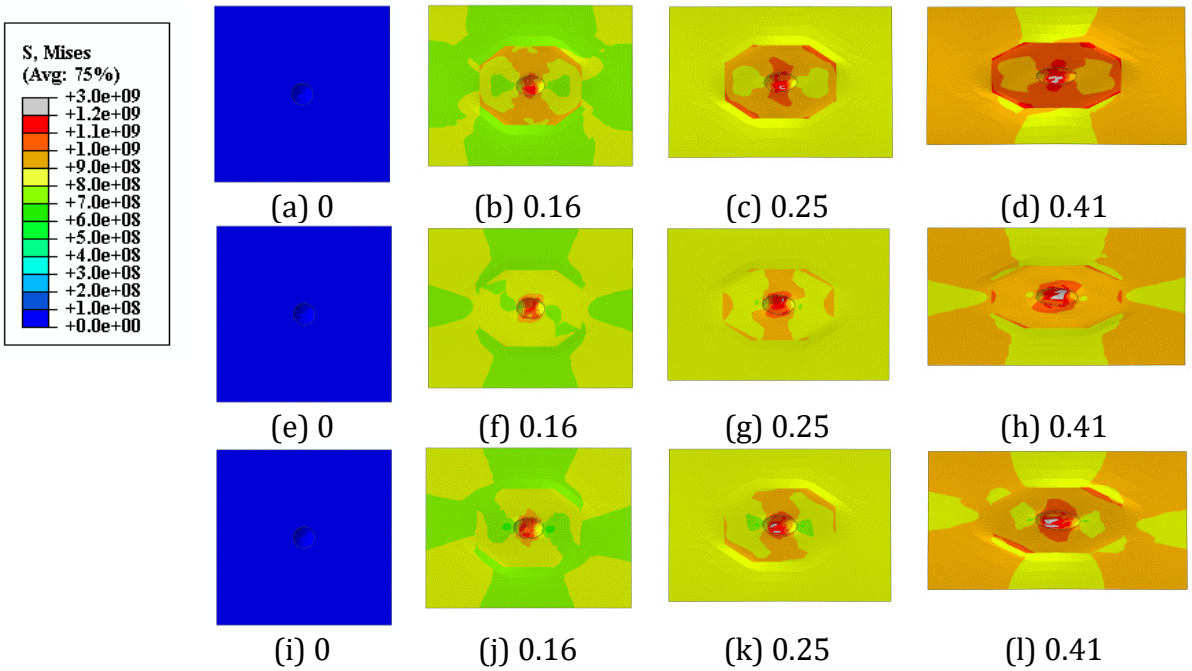

Figure 4.6: Visualization of void growth for sample S3 in grains with different orientation at different true strains: (a)-(d) Grain 1, (e)-(h) Grain 2, (i)-(l) Grain 3. Tensile direction is horizontal.

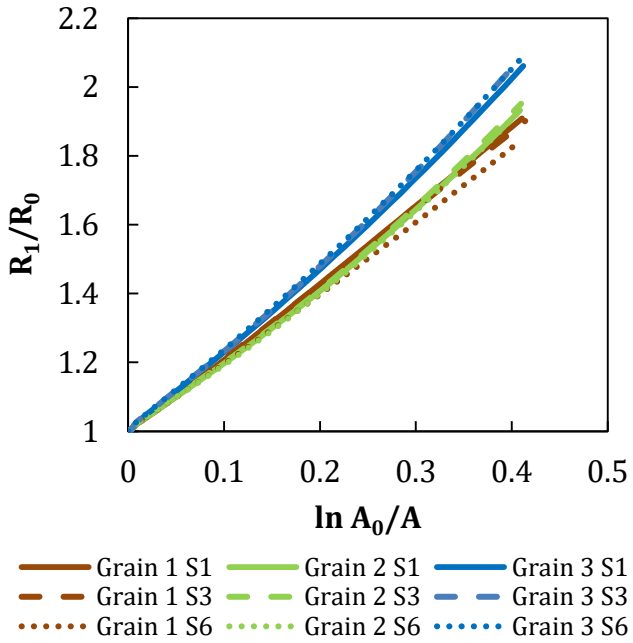

Figure 4.7: Comparison of void growth simulation results between different samples S1, S3 and S6.

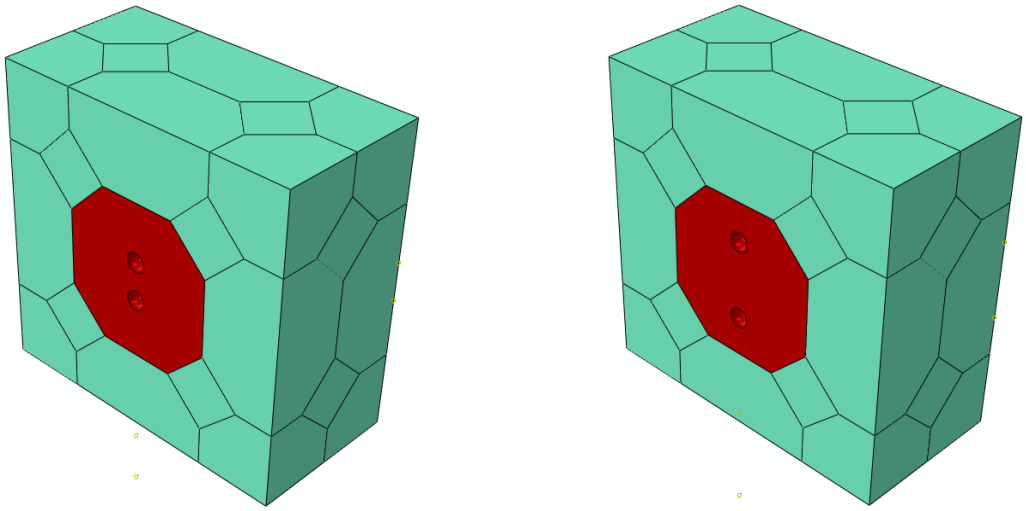

(a) (b)

Figure 4.8: 3D model with two voids interspaced at: (a) 2d, (b) 4d, where d is the void diameter. Half of the model is shown. Red color indicates crystal plasticity, green color indicates macroscopic properties of titanium. Tensile direction coincides with the x axis.

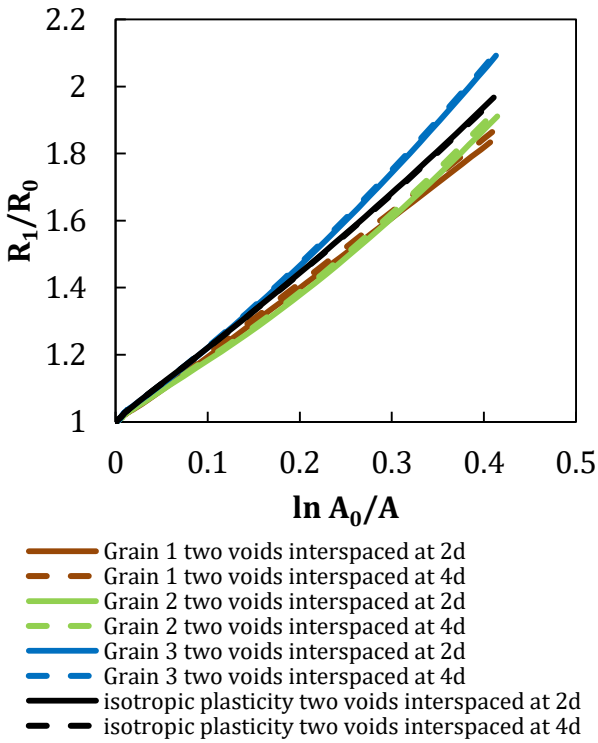

Figure 4.9: Comparison of void growth simulation results for sample S3 for two voids at different interspacings.

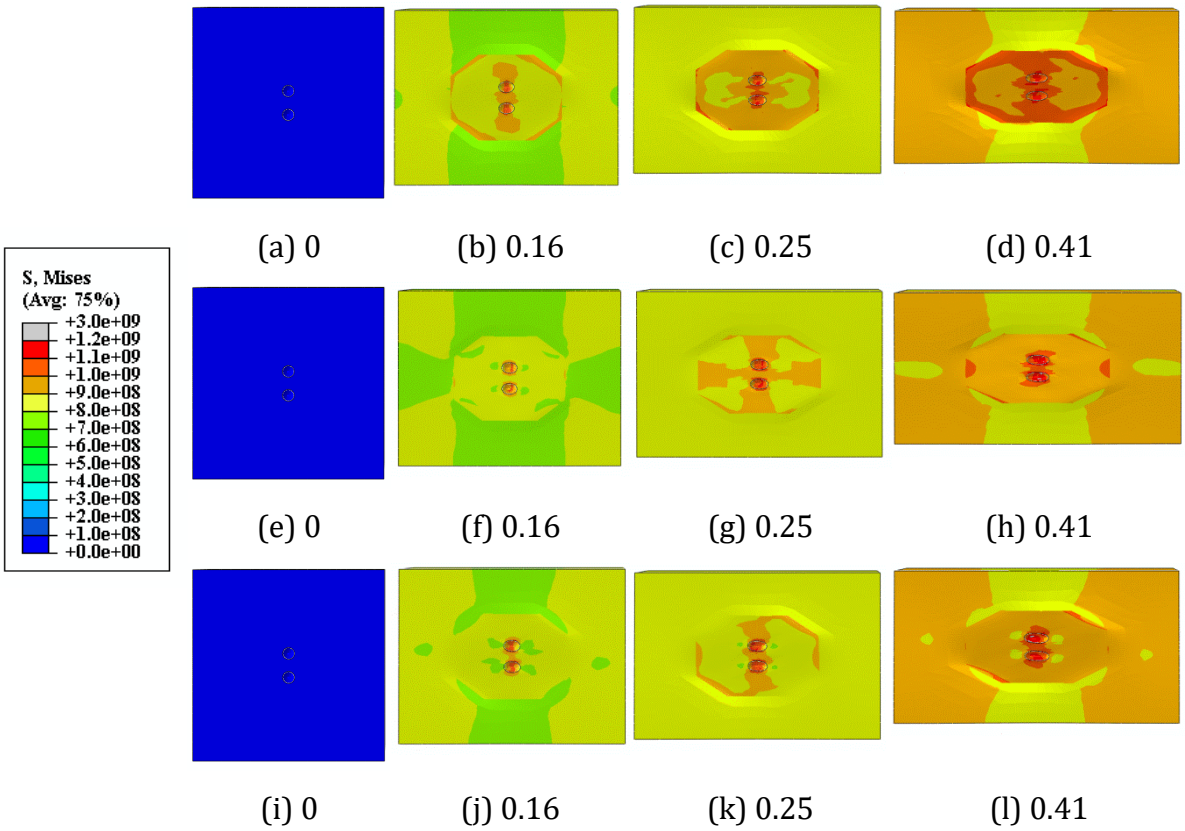

Figure 4.10: Visualization of void growth for two voids interspaced at 2d for sample S3 in grains with different orientation at different true strains: (a)-(d) Grain 1, (e)-(h) Grain 2, (i)-(l) Grain 3. Tensile direction is horizontal.

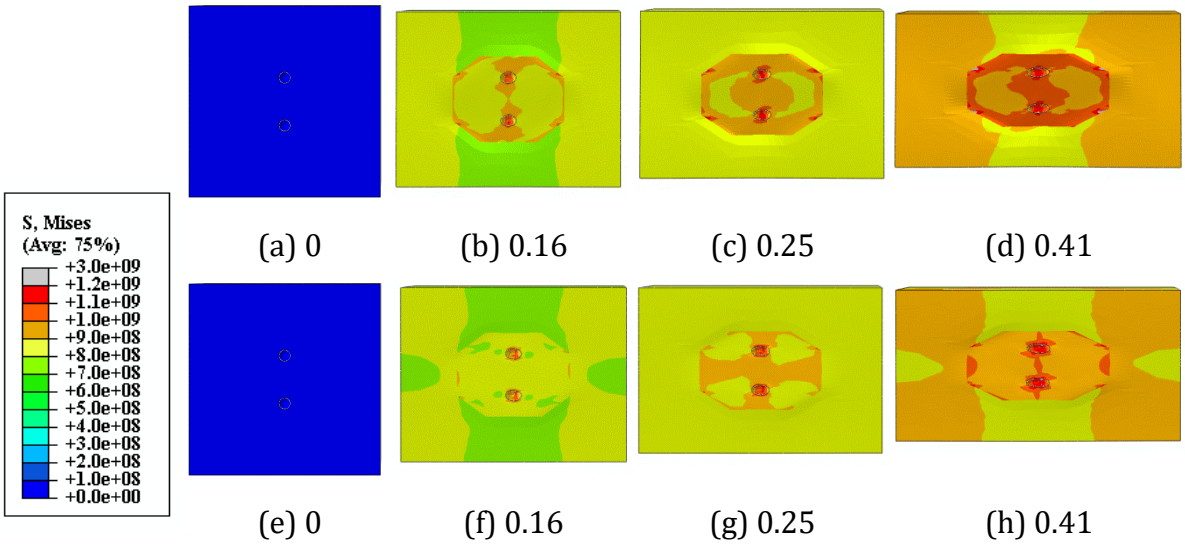

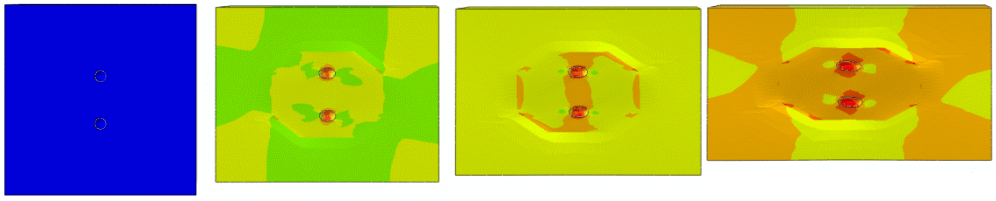

(i) 0 (j) 0.16 (k) 0.25 (l) 0.41

Figure 4.11: Visualization of void growth for two voids interspaced at 4d for sample S3 in grains with different orientation at different true strains: (a)-(d) Grain 1, (e)-(h) Grain 2, (i)-(l) Grain 3. Tensile direction is horizontal.

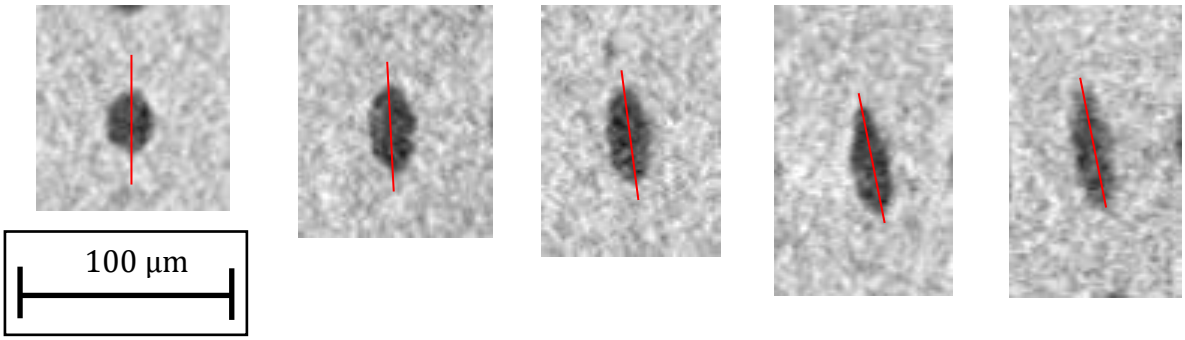

(a) (b) (c) (d) (e)

Figure 4.12: Zoomed version of experimental results for sample S5 showing one void and a straight line as reference to show the void rotation. Tensile direction is vertical.

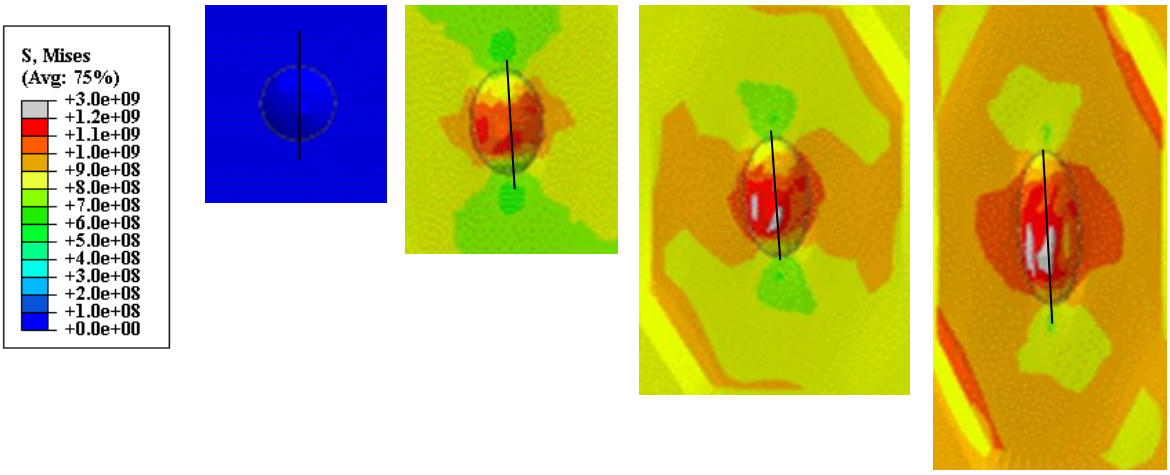

(a) 0 (b) 0.16 (c) 0.25 (d) 0.41

Figure 4.13: Zoomed version of simulation results for sample S3 for Grain 3 showing one void and a straight line as reference to show the void rotation. Tensile direction is vertical.

4.2 Discussion and conclusions

Crystal plasticity simulations were carried out using the software Abaqus v.6.11-1 and the user subroutine. The behavior of Ti crystal is taken into account using an elasto-viscoplastic phenomenological crystal plasticity model which includes the microscopic mechanisms of plastic deformation by slip along basal, prismatic and pyramidal c + a systems. The hardening is accounted for by a Voce-hardening law [49]. First the parameters of Voce-hardening law were determined by combining literature values [50] and inverse analysis of the experimental macroscopic tensile response for three samples (S1, S3 and S6).

A 3D finite element model was created in order to simulate void growth. The model consisted of 35 parts with the part in the middle containing a spherical void. The parts represent grains and were simulated in the shape of a tetrakaidecahedron (Figure 4.3) which is a reasonable approximation of grains in polycrystals [51]. A mesh study was performed and an appropriate mesh size was selected. The 8-linear node brick element (C3D8) was used.

The simulations were performed by taking into account the grain orientation. Three different grain orientations were analysed. The void growth showed the dependence on grain orientation (Figure 4.5). The crystal plasticity simulation results were compared to the experimental results. The scatter in the void growth (Figure 4.5) found in the simulations is similar to the experimental scatter which support the hypothesis that void growth depends on grain orientation.

The effect of material properties was studied using crystal plasticity simulations by performing simulations with different input parameters (Voce-hardening parameters). Figure 4.7 indicates that the material strength has a small effect on void growth as observed experimentally. Similar to [204] it can be concluded that local microstructure, in our case, grain orientations, have more effect on void growth than material strength.

3D crystal plasticity simulations with two voids located in one grain and spaced at two different distances (Figure 4.8) were performed in order to study the effect of intervoid spacing on void growth. Two intervoid spacings were analysed: 2d and 4d,

where d is the diameter of the void. Figure 4.9 shows that increasing the intervoid spacing leads to a slight increase in void growth which is in an agreement with the experimental results. It is important to note here that crystal plasticity simulations showed that grain orientation has a stonger effect on void growth than the intervoid spacing. This is in agreement with [204] where it was shown that local microstructure of Mg, in particular twins and grain boundaries, affects more void growth and coalescence than the void fraction.

The conclusions are presented next. The mechanical behaviour of Ti samples was modelled successfully by using crystal plasticity simulations. The models were created by taking into account the experimental stress-strain curves. The simulations allowed the analysis of void growth inside a grain of Ti with a given orientation. It was observed that void growth is affected by the orientation of the grain in which it is located. This explains the scatter in the experimental void growth curves observed in the previous chapter. In addition, the simulations confirmed that mechanical properties have a marginal influence on void growth which explains the behaviour observed experimentally in the samples subjected to different heat treatments. Finally, it was shown that the intervoid spacing does not affect the void growth significantly, in contrast to isotropic materials for which the closer the voids are, the earlier coalescence takes place which lowers the final failure strain of the whole sample [92].

Chapter 5 Direct comparison between effect of grain orientation on void growth in CP titanium alloy

5.1 New Heat Treatment procedure (below the transition temperature)

Diffusion bonding of CP titanium above the phase transition temperature led to microstructure that consists of colonies of α-plates (or α-lamellae) which form grains. Inside each grain, α-plates have the same orientation [121]. Even though the microstructural unit of deformation is the grain (which is larger than the void) it was not possible to determine grain orientation because it is challenging to obtain this information post mortem due to deformation in the sample. In order to make a one-to-one comparison between void growth and grain orientation, diffusion bonding was done below the phase transformation temperature to obtain lamella-free grains.

5.2 Experimental procedures

5.2.1 Material fabrication

Samples were fabricated in a two-step process. First, the samples were annealed (Figure 5.1(a)) to grow the grains close to their maximum size. EBSD was then used to obtain the grain orientation in the hole-containing sheet, and the diffusion bonding (Figure 5.1(b)) was then carried out. Different annealing and diffusion bonding temperatures and times were considered. The results which resulted in best bonding between Ti sheets were obtained using a diffusion bonding temperature of 870°C during 36 hours. As EBSD is done before diffusion bonding, it was verified that diffusion bonding heat treatment did not result in subsequent grain growth (Figure 5.2). After each heat treatment, the samples were polished and etched in order to ensure that no subsequent grain growth took place (Figure 5.2). Microhardness indents were done in order to compare the same region (Figure 5.2).

3D samples for in-situ testing in tomography were prepared as follows:

i) laser drilling of voids;

ii) annealing at 870°C during 36 hours to grow the grains close to their maximum size;

iii) EBSD to obtain grain orientation

iv) diffusion bonding at 870°C during 18 hours.

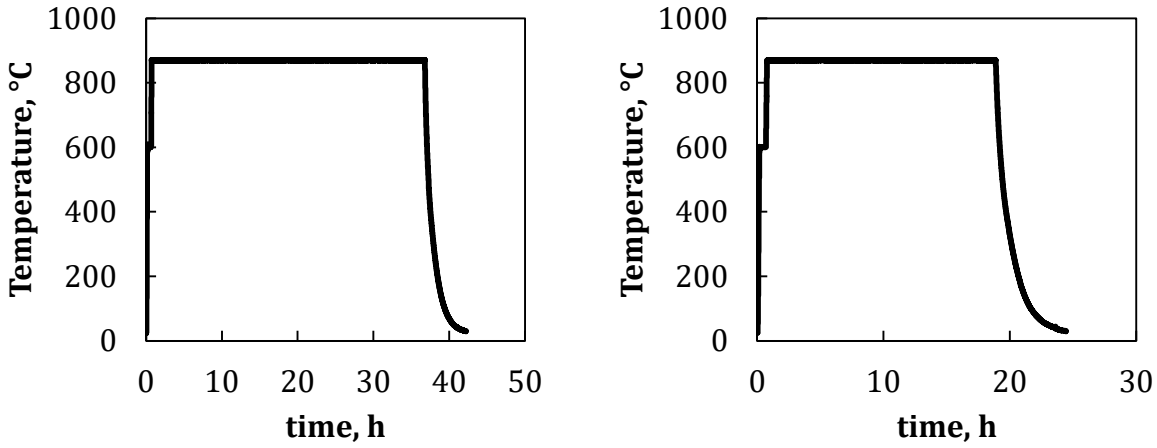

(a) (b)

Figure 5.1: (a) A typical thermal treatment curve obtained from annealing; (b) a typical thermal treatment curve obtained from diffusion bonding experiments.

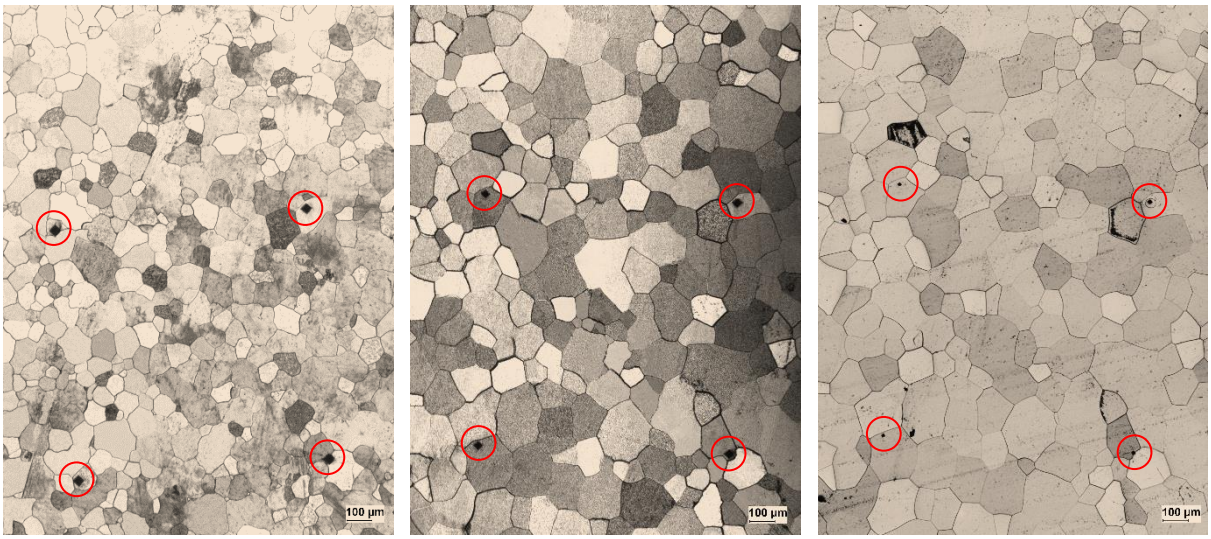

(a) (b) (c)

Figure 5.2: Optical micrographs of a sample annealed at 870 °C during various time: (a) 18 hours; (b) 36 hours; (c) 54 hours. The red circles indicate the hardness indents.

Samples were fabricated with a void diameter of 30 μm and an intervoid spacing of 70 μm (Table 5.1). Sample dimensions are indicated in Table 5.2.

Table 5.1: Samples prepared for testing.

Sample	void diameter (before polishing), μm	void interspacing, μm	void depth, μm
3D	30	70	32

Table 5.2. Sample dimensions.

sample	thickness, μm	width, μm
M1	280	550
M2	280	620
M3	350	530

5.2.2 Microstructural Characterization

Electron back scattered diffraction (EBSD) was performed using JEOL JSM-5300 SEM operating at 15 kV with a step size of 5 μm on all of the samples described above. Samples were then diffusion bonded and tested in tomography. Tomography reconstructions prior to deformation are superimposed with EBSD maps in Figure 5.3. Only voids that are completely within a grain, far from any debonding, and in the central section of the samples were analyzed. These voids, together with the names of the grains inside which they are located, are indicated in Figure 5.3. Figure 5.4 shows inverse pole figures for the samples M1, M2 and M3. Different colors indicate different grain orientation.

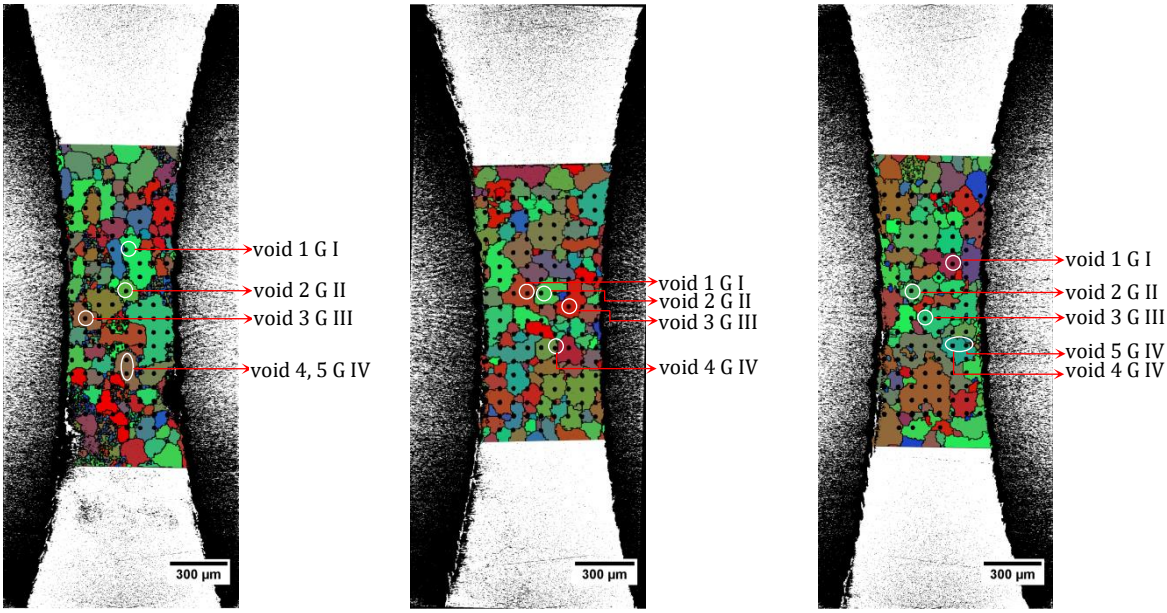

(a) (b) (c)

Figure 5.3: Initial tomography superimposed with EBSD for: (a) sample M1, (b) sample M2, (c) sample M3.

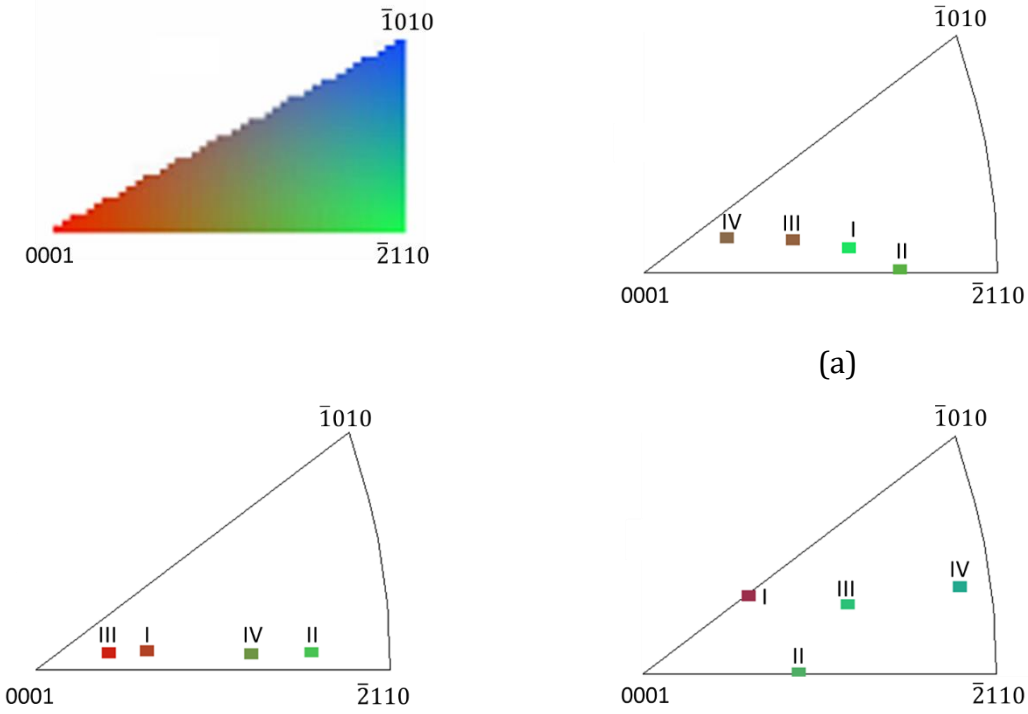

(a)

(b) (c)

Figure 5.4: Inverse pole figures for samples: (a) M1, (b) M2, (c) M3. The Greek numbers indicate the grain orientations indicated in Figure 5.3.

5.2.3 In-situ Tensile Testing (X-Ray tomograms)

The samples were tested in X-Ray tomography available at IMDEA Materiales in Spain. The tomograms were collected using a Nanotom 160NF (General Electric-Phoenix, Figure 5.5) at 90 kV and 170 µA using a tungsten target. For each tomogram, 500 radiographs were acquired with an exposure time of 750 ms. Tomogram voxel size was 1.35 µm. The tensile machine used to perform in-situ tensile tests are presented in Figure 5.6. Then true stress-strain curves were extracted and void growth curves were constructed.

Figure 5.5: Nanotom 160NF X-Ray tomography.

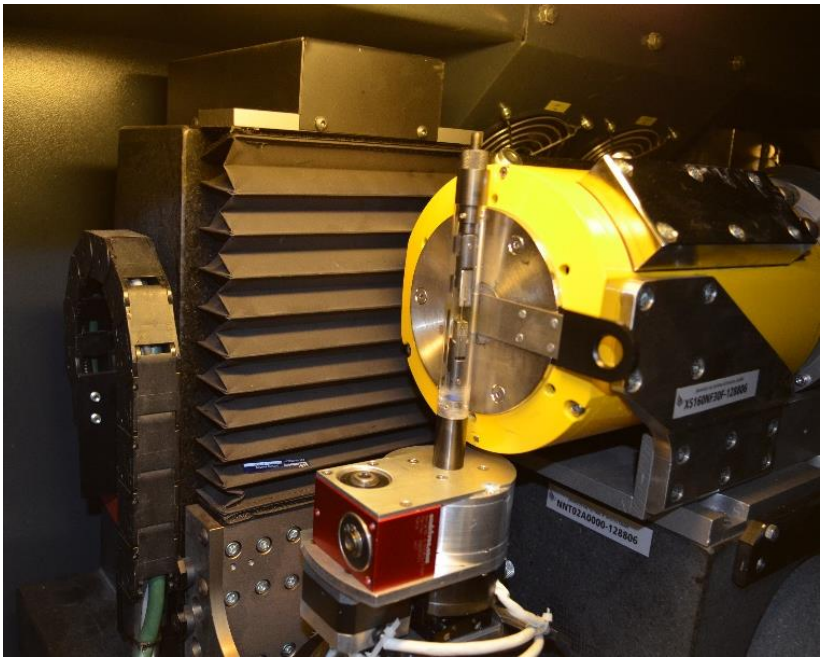

Figure 5.6: The tensile machine used to perform in-situ tensile tests.

5.3 Experimental results

5.3.1 Microstructural examination

The annealing of the CP titanium below the phase transition temperature resulted in equiaxed grains (Figure 5.2, Figure 5.3). The orientation of the grains was determined using EBSD.

5.3.2 In-situ Tensile Test Results

Similar to the procedure described in Section 3.2.2, true stress-strain curves were constructed for all samples. From Figure 5.7 it can be seen that the true stress-strain curves are superimposed which is as expected because all samples had the same heat treatment and had the same void configuration.

5.3.3 X-ray Tomograms

X-ray tomography allowed the visualization of void growth and coalescence in three dimensions. For example, growth of voids 4 and 5 in sample M1 are presented in Figure 5.8 where the evolution of void dimensions can be clearly observed. Voids first elongate in the tensile direction during the test and elongate in the transverse direction when coalescence starts.

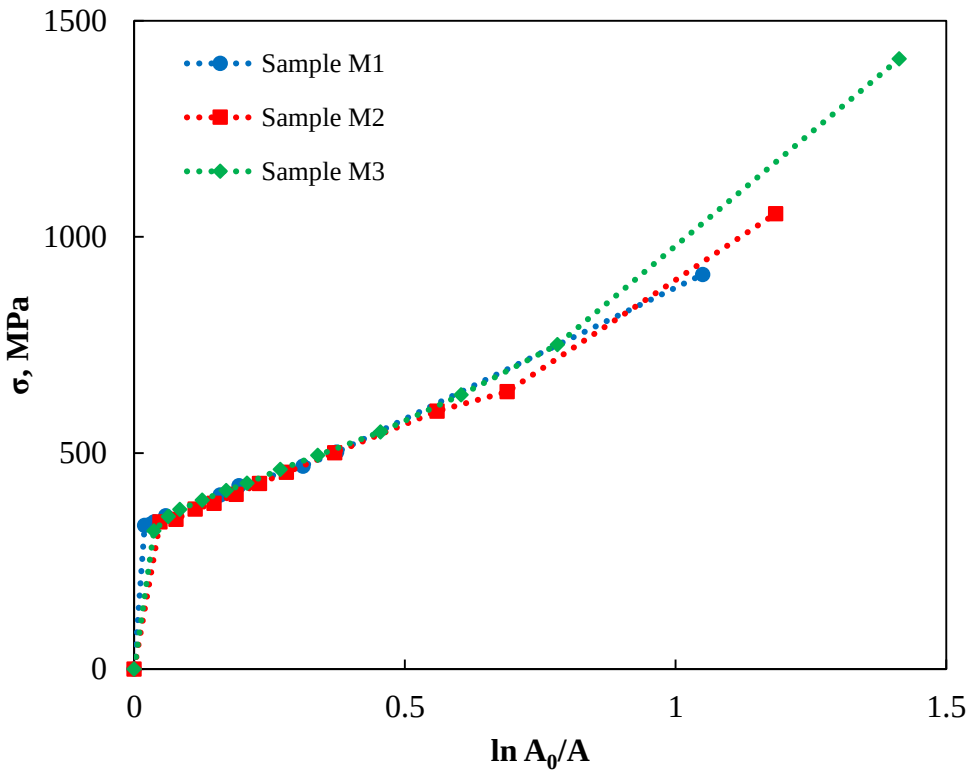

Figure 5.7: True stress-strain curves of CP titanium samples tested in tomography.

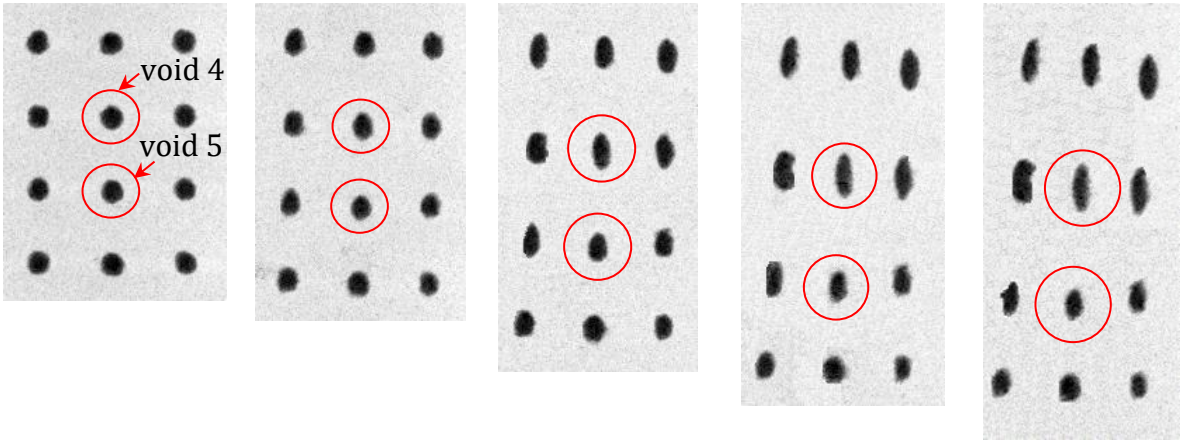

(a) 0 / 0 (b) 0.10 / 0.07 (c) 0.26 / 0.18 (d) 0.41 / 0.26 (e) 0.47 / 0.28

Figure 5.8: Tomography reconstructed void growth of voids 4 and 5 in sample M1. The numbers indicate the local strains for voids 4 and 5 respectively. The circles indicate the voids of interest.

5.3.4 Void Growth

Void growth was extracted from different grains and different samples. Normalized void diameter R_1/R_0 as a function of local strain is presented in Figure 5.9. It can be seen that void growth varies depending on the grain orientation. For sample M1 (Figure 5.9(a)) void 1 in grain I has the fastest void growth followed by void 3 in grain III, void 2 in grain II, void 4 in grain IV and finally void 5 in grain IV. Figure 5.10 presents transverse strain as a function of axial strain. It can be seen that the ratio between these strains stays more or less constant. These two strains define the strain state around the void which affects void growth. Depending on the grain orientation different slip systems tend to be activated (Figure 5.11).

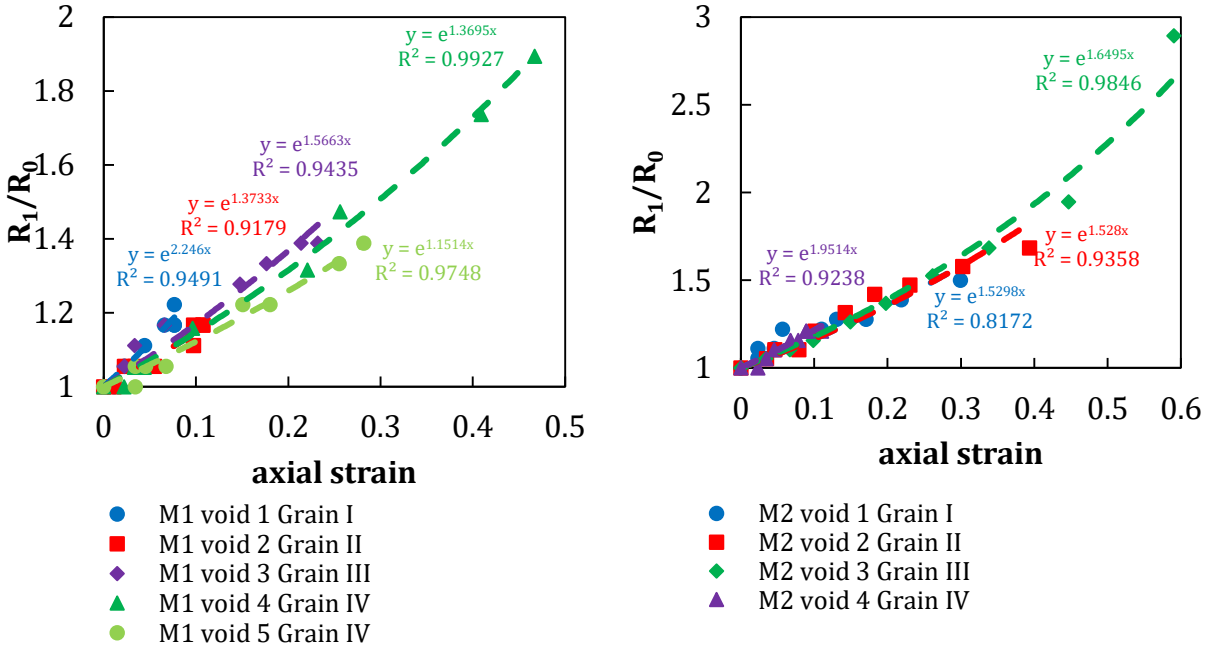

(a) (b)

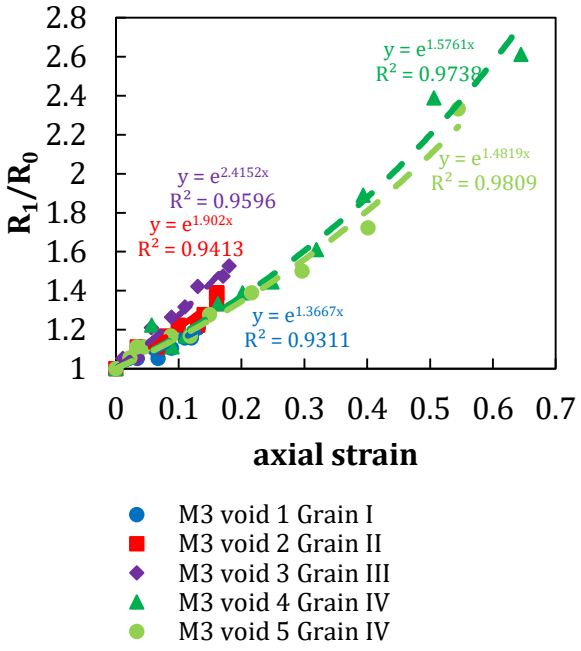

(c)

Figure 5.9: Void growth as a function of local strain in different samples: (a) sample M1, (b) sample M2, (c) sample M3. The experimental data is fitted with exponential curves.

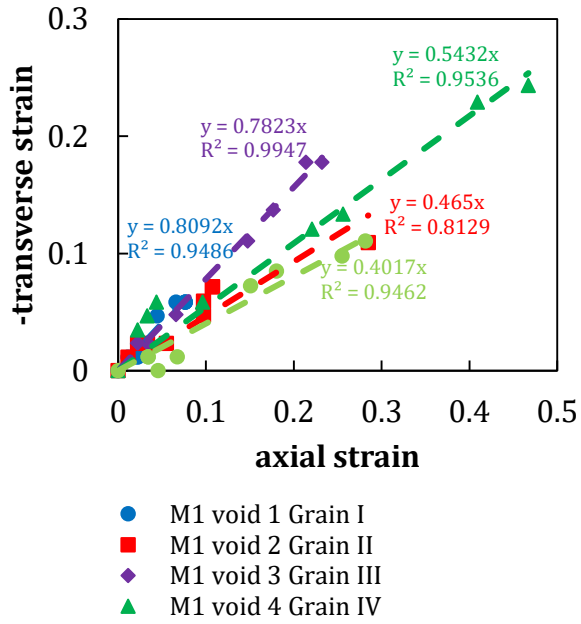

(a)

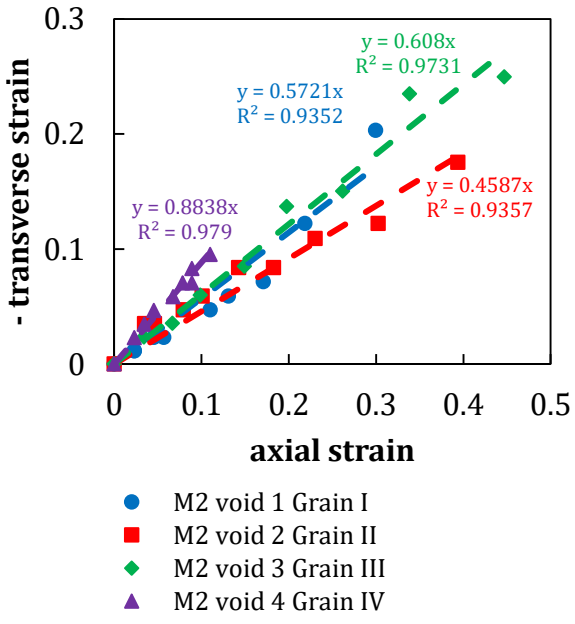

(b)

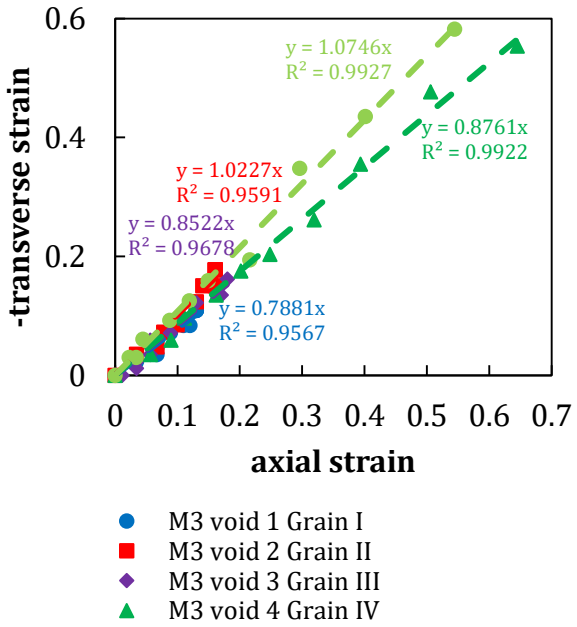

(c)

Figure 5.10: Transverse strain as a function of axial strain in different samples: (a) sample M1, (b) sample M2, (c) sample M3. The experimental data is fitted with linear curves.

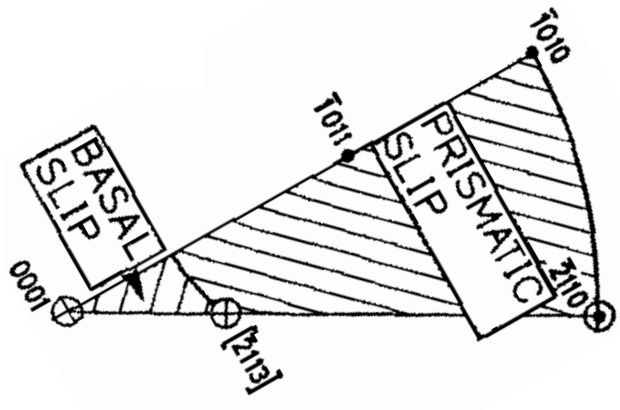

Figure 5.11: Predicted slip systems as a function of external load direction [4].

Void growth in the transverse direction was quantified in the different samples as a function of true strain (Figure 5.12). The changes in the transverse direction are small and within the noise as can be seen in Figure 5.12 which makes it difficult to draw any conclusions.

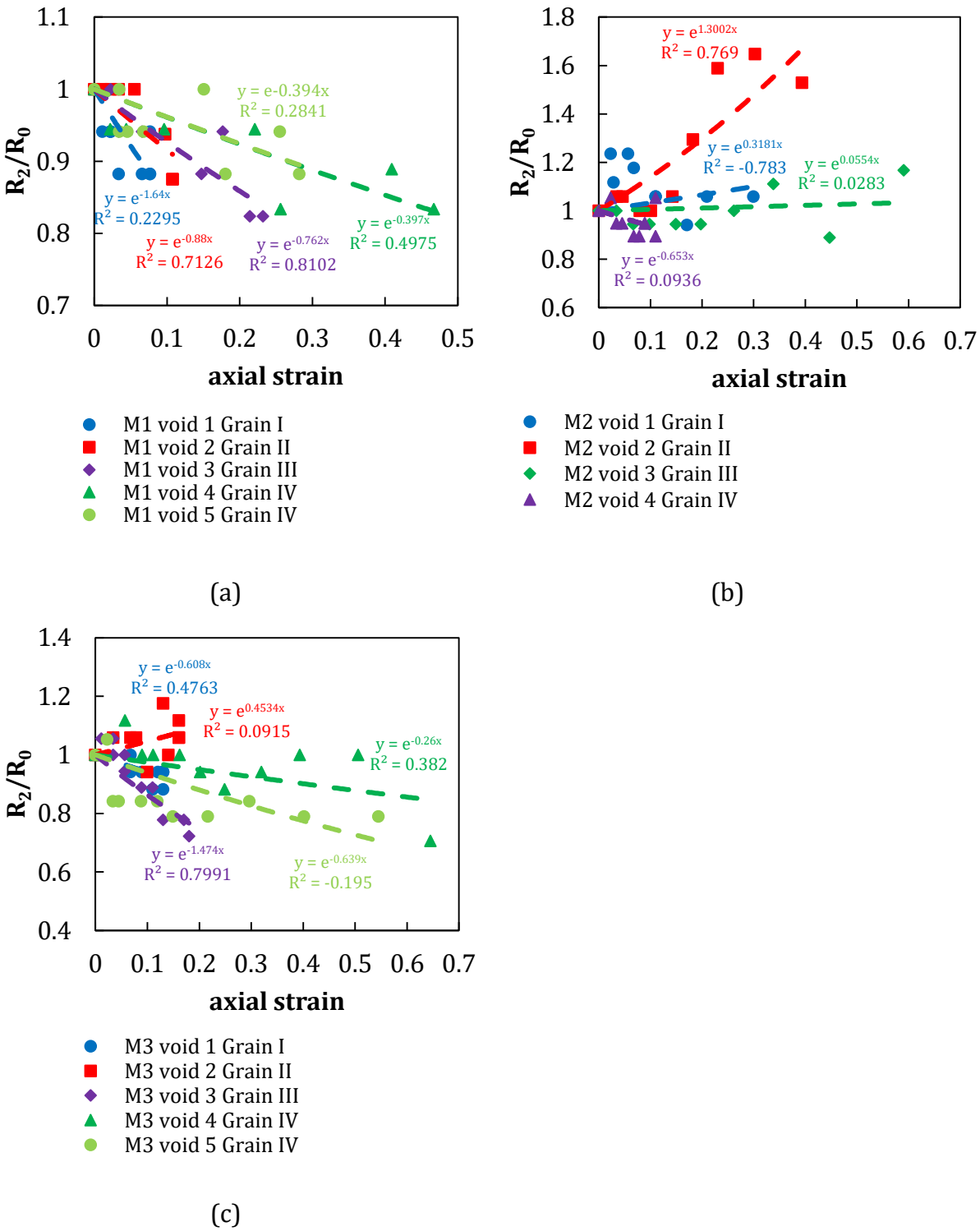

Figure 5.12: Void growth in transverse direction as a function of local strain in different samples: (a) sample M1, (b) sample M2, (c) sample M3. The experimental data is fitted with exponential curves.

5.4 FRACTOGRAPHY

Fracture surfaces of samples tested in-situ X-Ray tomography were studied using scanning electron microscope. Figure 5.13 shows the fracture surfaces of samples M1, M2 and M3. It can be seen that all three samples have ductile fracture which is indicated by the fibrous appearance.

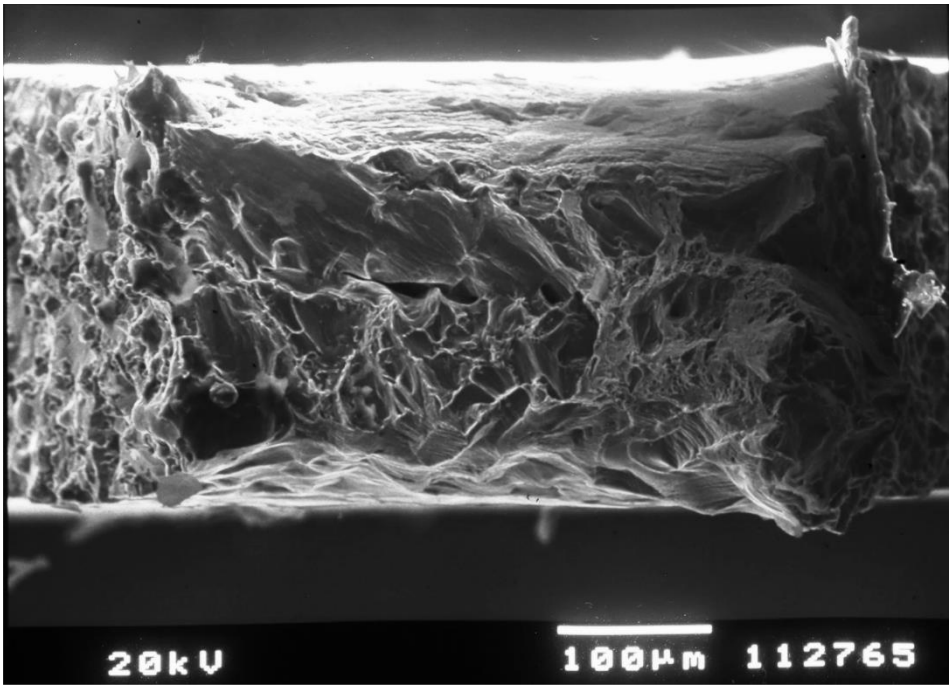

(a) M1

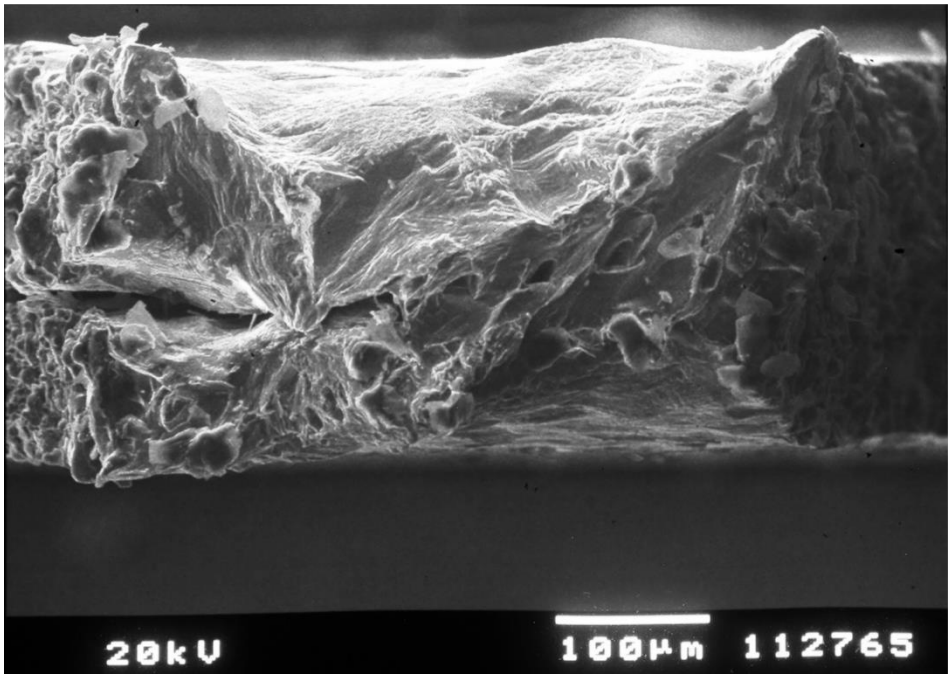

(b) M2

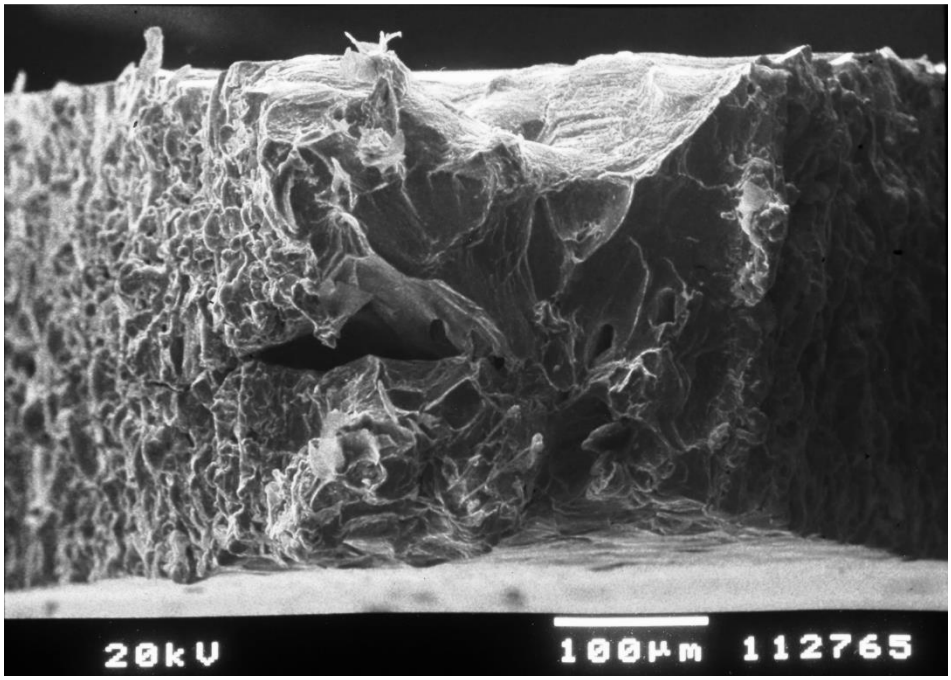

(c) M3

Figure 5.13: SEM images of the fracture surface of (a) sample M1 (b) sample M2, and (c) sample M3.

5.5 Discussion and conclusions

In Chapter 3 the effect of grain orientation on void growth was studied in an indirect way. In this Chapter 5 a one-to-one comparison between void growth and grain orientation was possible because the orientation of the grain in which the void is located is known. In order to achieve this, CP Ti samples were fabricated using the following approach: i) laser drilling of voids in the sample, ii) annealing at 870 °C (lower than the phase transformation temperature) during 36 hours, iii)EBSD analysis to obtain grain orientation information, and finally iv) diffusion bonding at 870 °C during 18 hours. Laser drilling parameters were selected so that the void diameter is equal to sheet thickness (32 μm) in order to obtain quasi-spherical voids. The void interspacing was kept constant and equal to 70 μm. By superimposing the EBSD map with the tomography reconstructions it was possible to make a one-to-one comparison between void growth and grain orientations.

In-situ tensile tests using X-Ray tomography provided the true stress-strain curves (Figure 5.7). All samples were subjected to the same heat treatment, and thus their true stress-strain curves were identical.

To simplify the void growth analyses, only voids completely located inside a grain were chosen. Voids near debonding events were not taken into account. From X-ray tomography reconstructions it can be seen that as the sample deforms, the voids first elongate in the tensile direction and shrink and in the transverse direction. When interactions between voids starts, voids grow towards each other in the transverse direction and coalescence occurs (Figure 5.8).

In order to construct void growth curves, the local axial strain was extracted from the tomography reconstructions. This local axial strain for each void was calculated based on the distance between two (upper and lower) neighbouring voids. Void growth in the tensile direction (Figure 5.9) showed that there is a scatter in void growth. This scatter is explained by the fact that the grains in which the different voids are located have different grain orientation. This is in the agreement with the literature because it was shown that grain orientation can significantly affect deformation and mechanical properties [8,9,11,26,112–115,117,118,216]. In particular, in Ti-6Al-4V

alloy the large range of variability in the void growth curves was attributed to the effects of the local crystallographic orientation [217]. In Mg void growth occurs rapidly in preferential directions due to the failure of twin and grain boundaries adjacent to pre-existing voids [218].

The void growth in the transverse direction (Figure 5.12) has more noise because the changes in void dimensions are smaller compared to the changes in the tensile direction. However, it can be noted that the void growth curves show evidence of void coalescence (when the transverse diameter of the voids increases). Similarly to the scatter in the void growth in the tensile direction, there is a scatter in the void growth curves in the transverse direction. This is also explained by the effect of grain orientation on void growth.

The main conclusions are presented next. Samples were prepared in order to confirm the effect of the grain orientation on void growth. This was realised by superimposing EBSD data and X-ray tomography data thanks to a new experimental method developed during this work where samples are first laser drilled to create voids and annealed to increase the grain size and, then EBSD was carried out to obtain grain orientations with respect to the voids location, and finally the samples were diffusion bonded. This enabled to extend the tomography data by taking into account grain orientation from the EBSD data.

This method allowed to confirm that void growth is indeed affected by grain orientations. This means that there are soft and hard orientations of the grains that contribute differently to void growth. Void growth was also analysed in the transverse direction but the changes were too small to draw any significant conlusions. Similarly, changes in the volume of the voids were investigated but again the changes were smaller compared to the amount of void growth in the tensile direction and were therefore not further analysed.

Chapter 6 CRYSTAL PLASTICITY RESULTS ON THE DIRECT COMPARISON BETWEEN THE EFFECT OF GRAIN ORIENTATION ON VOID GROWTH IN CP TITANIUM ALLOY

In order to study the effect of grain orientation on void growth in titanium, crystal plasticity finite element simulations were performed. The procedure and boundary conditions are described above (Section 4.1.1). Voce parameters were obtained combining literature values and inverse analysis of the experimental macroscopic tensile response (Table 6.1, Figure 6.1).

Table 6.1: Parameters of Voce-hardening law for samples M1, M2 and M3.

Slip system	τ_0 (MPa)	τ_s (MPa)	h_0 (MPa)	h_s (MPa)
Prismatic	86	95	2500	78
Basal	99	109	2500	78
Pyramidal c+a	225	248	2500	78

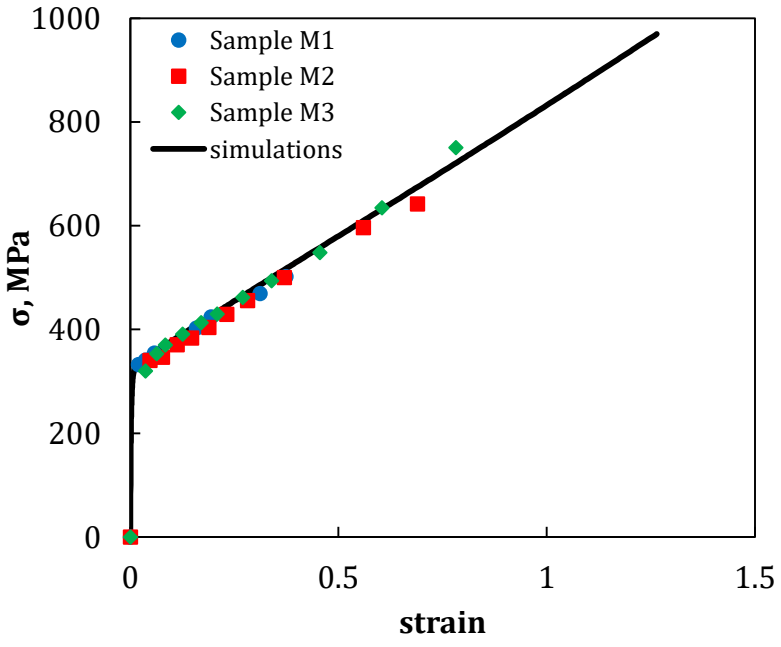

Figure 6.1: Tensile stress-strain curves: experimental results and numerical simulation.

6.1 Crystal plasticity results: one void in one grain.

6.1.1 Simulations Procedure

Void growth simulations were run using a 3D finite element model of a grain containing a spherical void (Figure 6.2), where the void diameter is 25 μm and grain size is 100 μm which is based on the experimental measurements. The mesh dependence study was performed and the appropriate mesh was selected (Figure A.1).

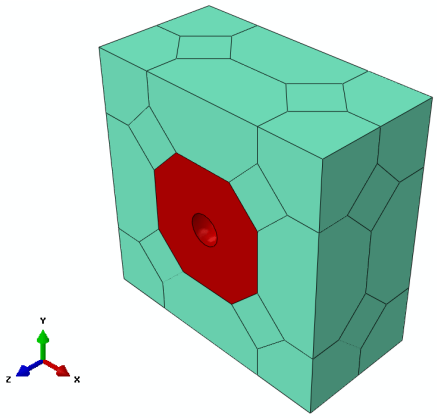

Figure 6.2: 3D model with one void located completely in one grain. Half of the model is shown. Red color indicates crystal plasticity; green color indicates macroscopic properties of titanium. Tensile direction coincides with the x axis.

Crystal plasticity simulations were run by taking into account the particular grain orientation and the local state of strain (ratio between transverse and axial local strains). This means that, for example, if the ratio between transverse and axial strain is equal to -0.8, then if the model is deformed by 100 μm in tensile direction, a displacement of -80 μm is imposed in the transverse direction.

6.1.2 Simulations results

Results of crystal plasticity simulations are presented in Figure 6.3.

Figure 6.3(b) shows the ratio between transverse and axial local strain for the voids in sample M1. These values were taken into account during crystal plasticity simulations. The fastest void growth in sample M1 (Figure 6.3(a)) is in void 1 followed by void 2, void 4, void 3 and void 5. Even though voids 4 and 5 are located inside the same grain IV, their void growth is different because of the different local strain state acting upon them. Thus, when simulating void growth, it is important to take into

account both the grain orientation and the local strain state. It can be seen that crystal plasticity simulations predict well experimental void growth.

Figure 6.3(c) shows void growth results for sample M2. Crystal plasticity simulations were based on the local strain states presented in Figure 6.3(d). It can be seen that the fastest growing void is void 4 followed by void 1, void 3 and void 2. Again, the crystal plasticity simulations predict well the experimental void growth. It is not clear why there are discrepancies between the two experimental points for void 1 and simulations.

Comparison between crystal plasticity simulations and experimental results for sample M3 is presented in Figure 6.3(e). Figure 6.3(f) shows the ration between the transverse and axial local strain that were taken into account during crystal plasticity simulations. It can be seen that the fastest growing void is void 4 followed by void 5, void 3, void 1 and void 2. One can note that in case of sample M3 the fit between crystal plasticity predictions and experimental results is not as good as for the other two samples. This can be explained by some other factors that were not taken into account in the simulations. By observing X-Ray tomography reconstructions (Figure 6.4) one can notice that there is more necking in sample M3 then in sample M1 and M2 and this might explain the discrepancies between experimental and simulation results. While in samples M1 and M2 stress triaxiality was 0.36 and did not change during the tensile test, in sample M3 stress triaxiality evolved from 0.36 to 0.56.

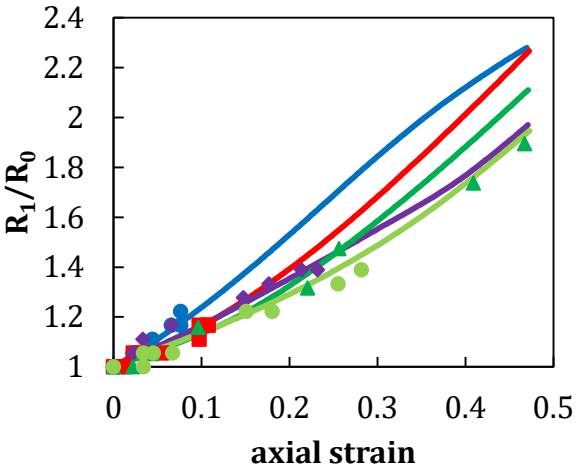

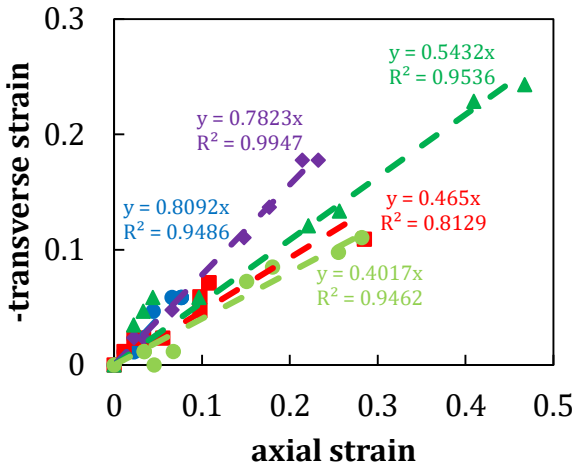

M1 void 1 Grain I
M1 void 2 Grain II
M1 void 3 Grain III
M1 void 4 Grain IV
M1 void 5 Grain IV
Crystal Plasticity M1 Grain I -0.81
Crystal Plasticity M1 Grain II -0.47
Crystal Plasticity M1 Grain III -0.78
Crystal Plasticity M1 Grain IV -0.54
Crystal Plasticity M1 Grain IV -0.40

(a)

(b)

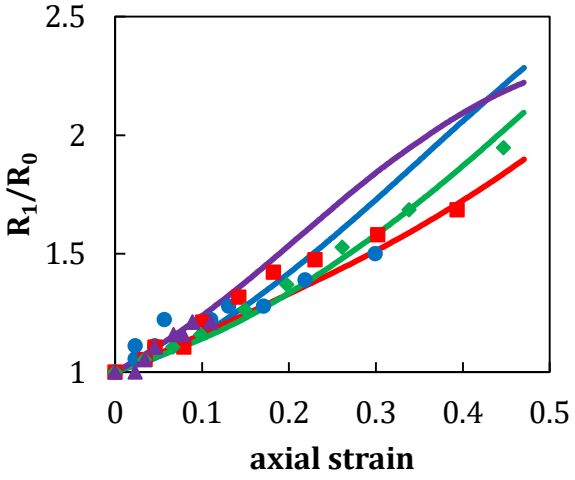

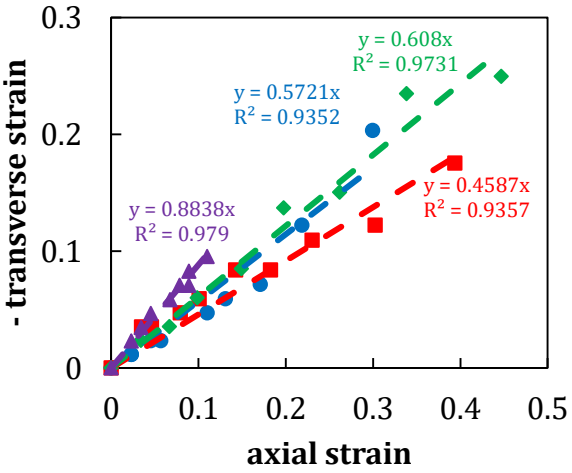

M2 void 1 Grain I
M2 void 2 Grain II
M2 void 3 Grain III
M2 void 4 Grain IV
Crystal Plasticity M2 Grain I -0.57
Crystal Plasticity M2 Grain II -0.46
Crystal Plasticity M2 Grain III -0.61
Crystal Plasticity M2 Grain IV -0.88

(c)

(d)

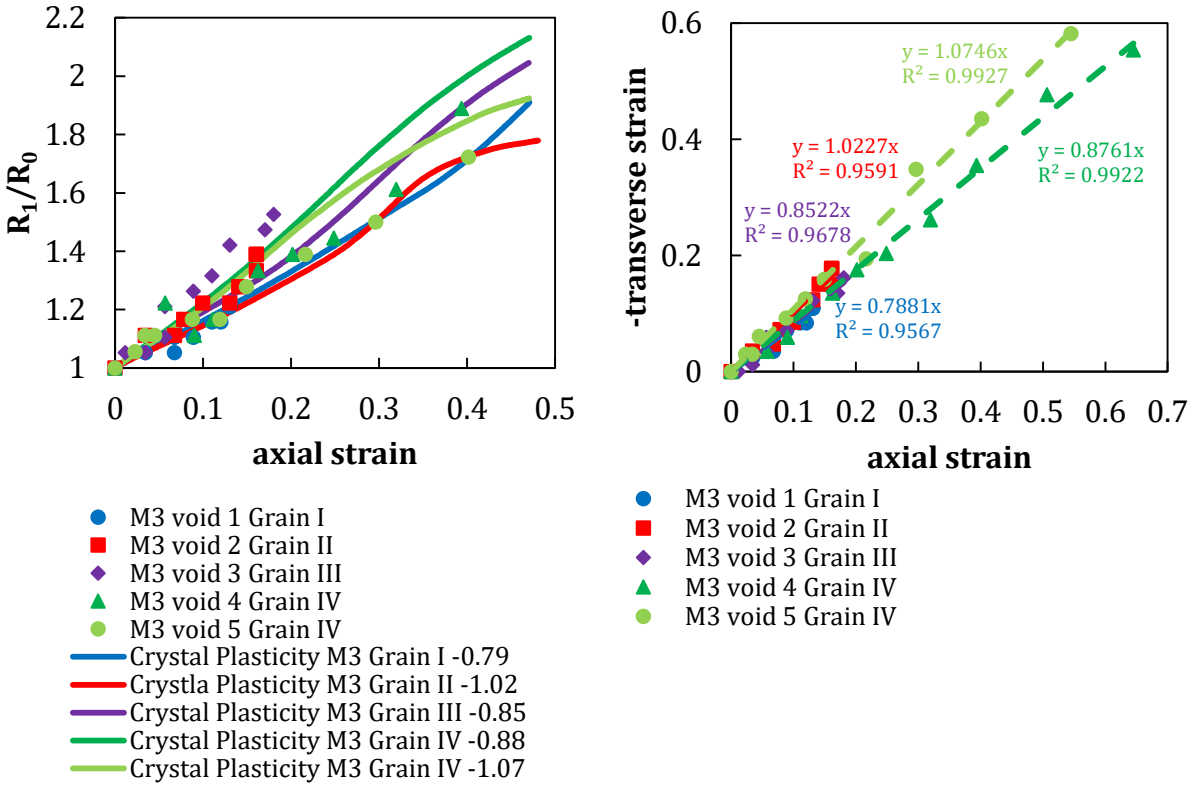

(e) (f)

Figure 6.3: Crystal plasticity results and experimental void growth as a function of local strain and transverse strain as a function of axial strain in different samples: (a), (b) sample M1, (c), (d) sample M2, (e), (f) sample M3.

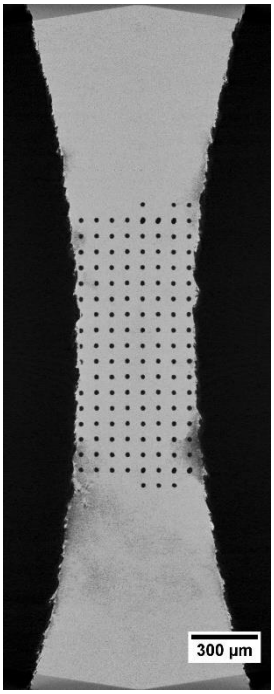

(a) sample M1

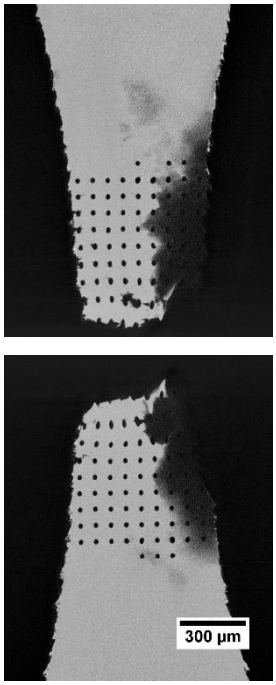

(b) sample M1

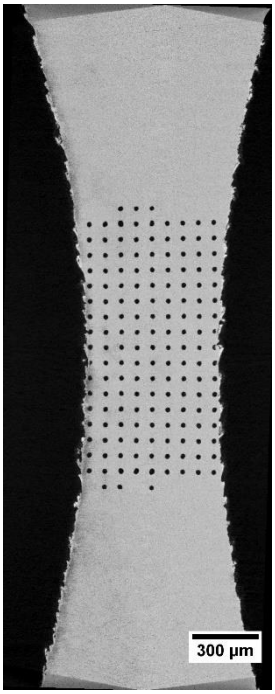

(c) sample M2

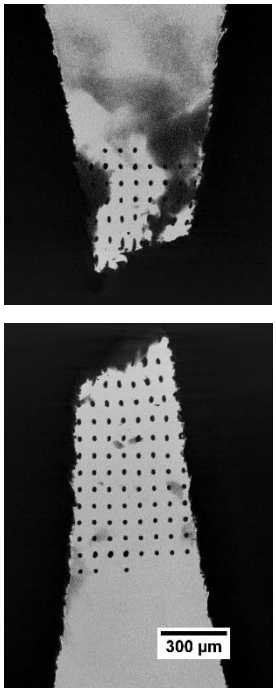

(d) sample M2

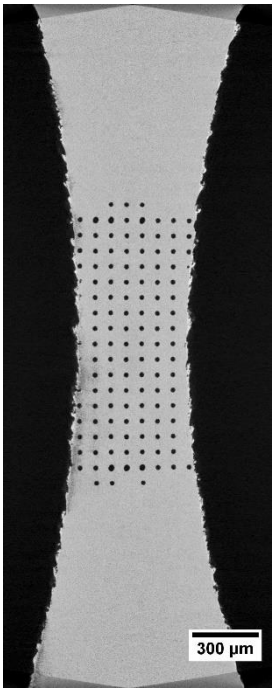

(e) sample M3

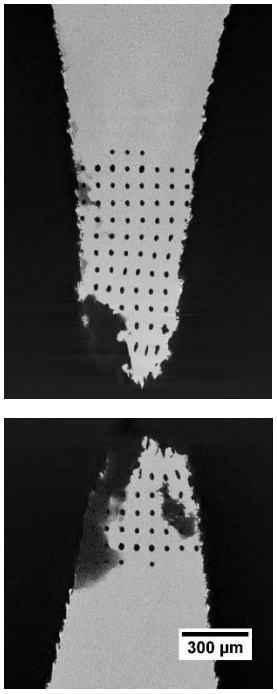

(f) sample M3

Figure 6.4: X-Ray tomography reconstructions of initial state and at fracture for different samples: (a)-(b) sample M1, (c)-(d) sample M2, (e)-(f) sample M3.

Activated slip systems were extracted for four grain orientations for samples M1, M2 and M3 at locations indicated in Figure 6.5. These three locations were chosen because they have different stress concentrations. Figure 6.6, Figure 6.7 and Figure 6.8 indicate that all three slip systems are activated in all cases. It can be noted that the fastest void growth is associated with activation of the basal slip system.

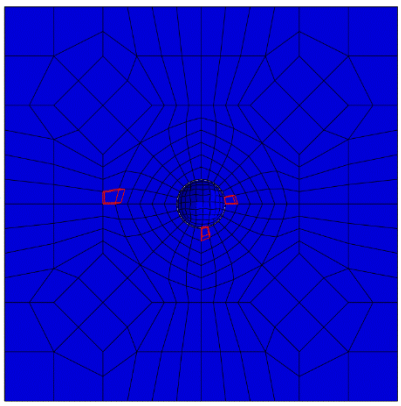

Figure 6.5: 3D model. Nodes in red indicate from where the parameters where extracted. Tensile direction is horizontal.

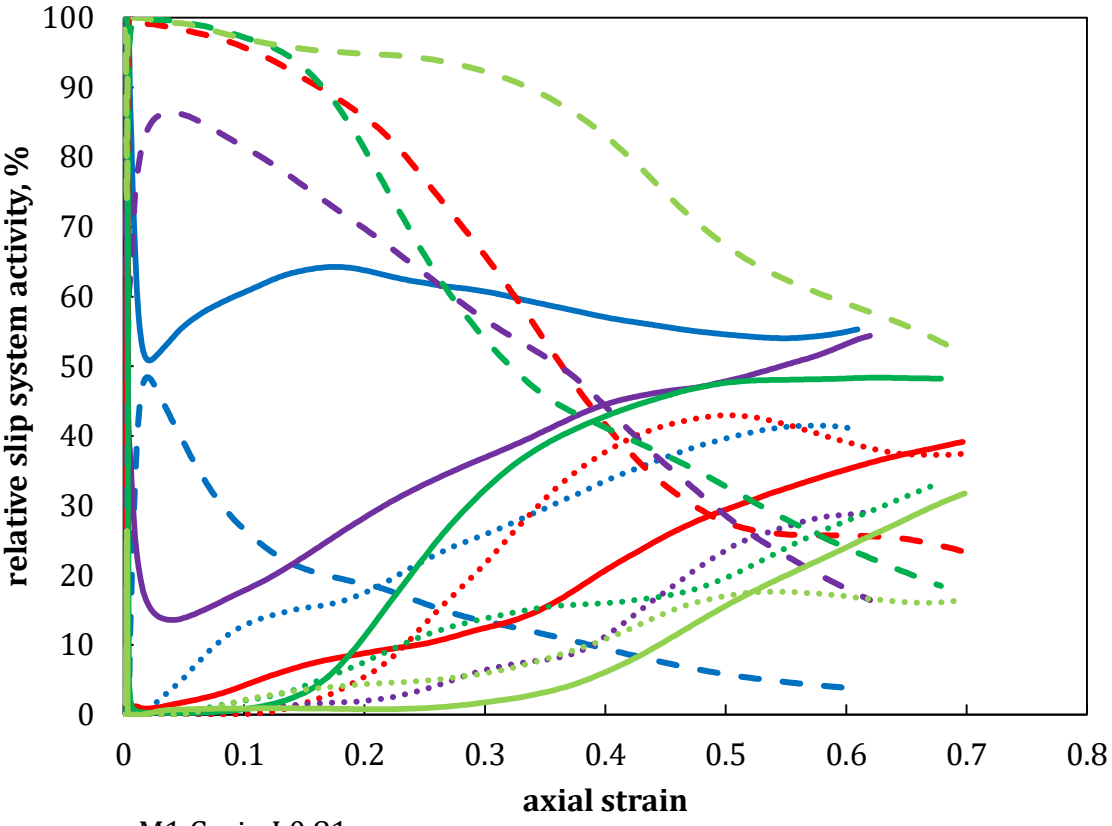
relative slip system activity, %
100
90
80
70
60
50
40
30
20
10
0
0
0.1
0.2
0.3
0.4
0.5
0.6
0.7
0.8
axial strain
M1 Grain I 0.81
M1 Grain II 0.47
M1 Grain III 0.78
M1 Grain IV 0.54
M1 Grain IV 0.40
Solid lines indicate basal slip
Dashed lines indicate prismatic slip
Dotted lines indicate pyramidal slip

(a) Sample M1

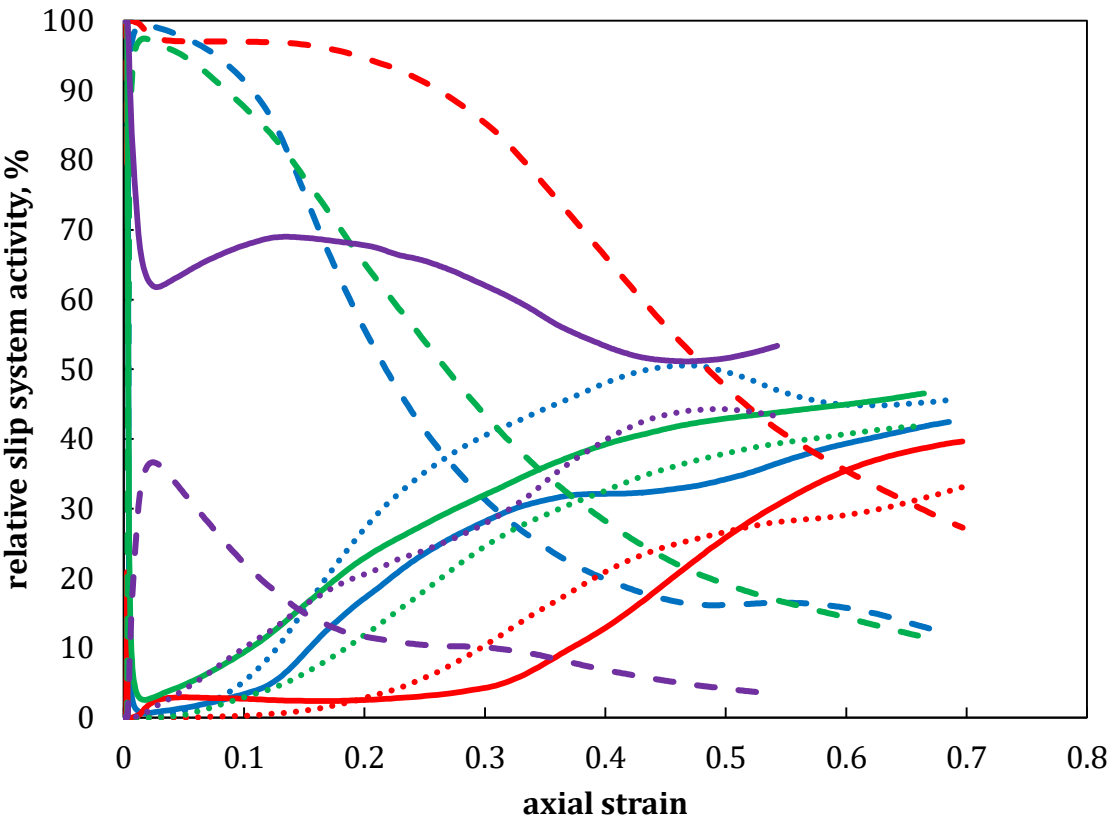
relative slip system activity, %
100
90
80
70
60
50
40
30
20
10
0
0
0.1
0.2
0.3
0.4
0.5
0.6
0.7
0.8
axial strain
M2 Grain I 0.57
M2 Grain II 0.46
M2 Grain III 0.61
M2 Grain IV 0.88
Solid lines indicate basal slip
Dashed lines indicate prismatic slip
Dotted lines indicate pyramidal slip

(b) Sample M2

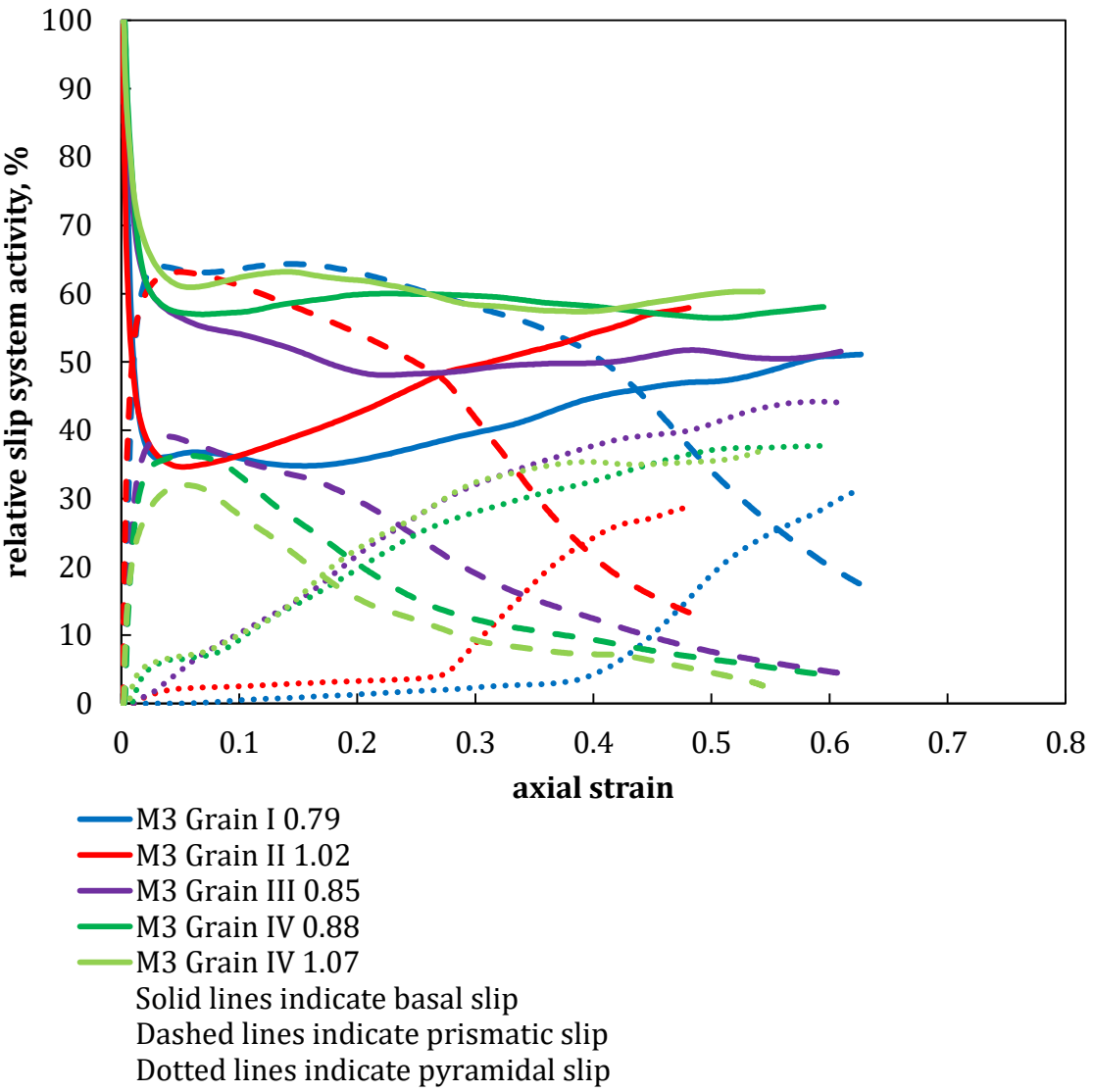

(c) Sample M3

Figure 6.6: Slip systems activated in the node right to the void in different grains in samples: (a) M1, (b) M2, (c) M3.

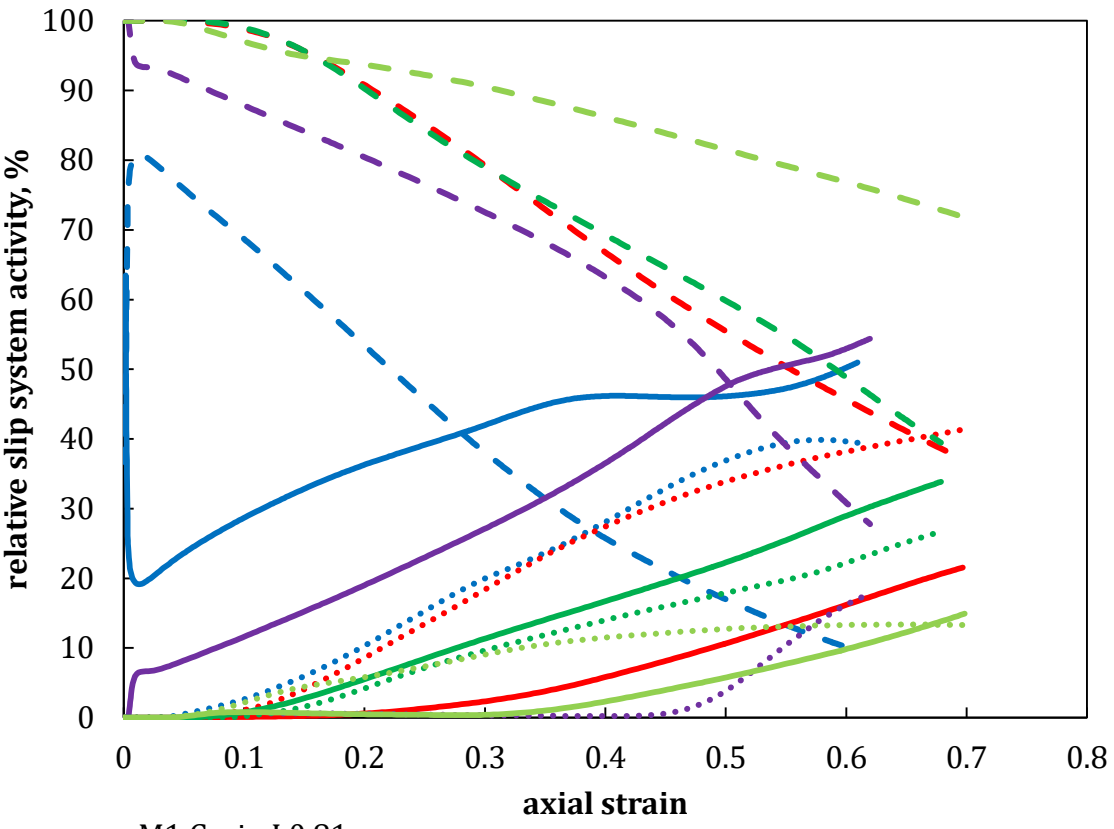
relative slip system activity, %
100
90
80
70
60
50
40
30
20
10
0
0
0.1
0.2
0.3
0.4
0.5
0.6
0.7
0.8
axial strain
M1 Grain I 0.81
M1 Grain II 0.47
M1 Grain III 0.78
M1 Grain IV 0.54
M1 Grain IV 0.40
Solid lines indicate basal slip
Dashed lines indicate prismatic slip
Dotted lines indicate pyramidal slip

(a) Sample M1

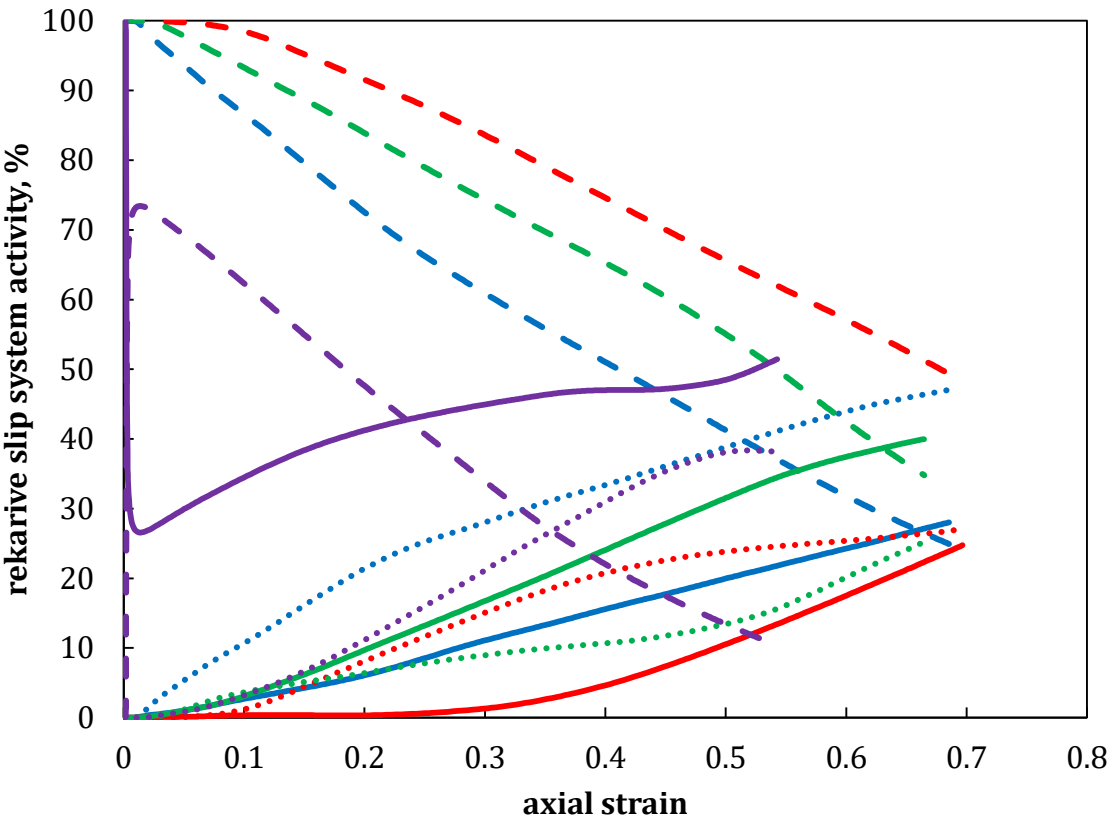
100
90
80
70
60
50
40
30
20
10
0
rekarive slip system activity, %
0
0.1
0.2
0.3
0.4
0.5
0.6
0.7
0.8
axial strain
M2 Grain I 0.57
M2 Grain II 0.46
M2 Grain III 0.61
M2 Grain IV 0.88
Solid lines indicate basal slip
Dashed lines indicate prismatic slip
Dotted lines indicate pyramidal slip

(b) Sample M2

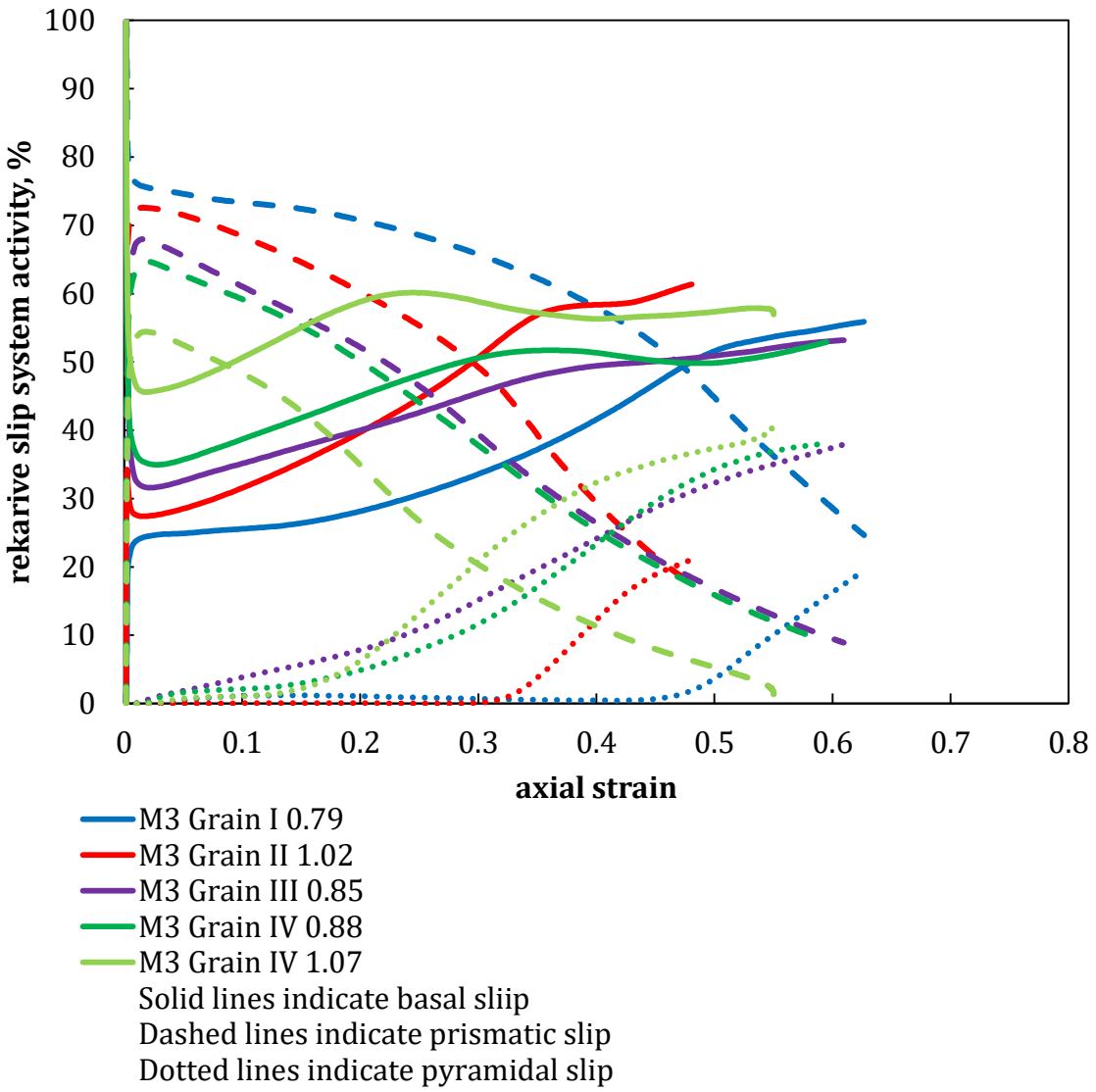

(c) Sample M3

Figure 6.7: Slip systems activated in the node far from the void in different grains in samples: (a) M1, (b) M2, (c) M3.

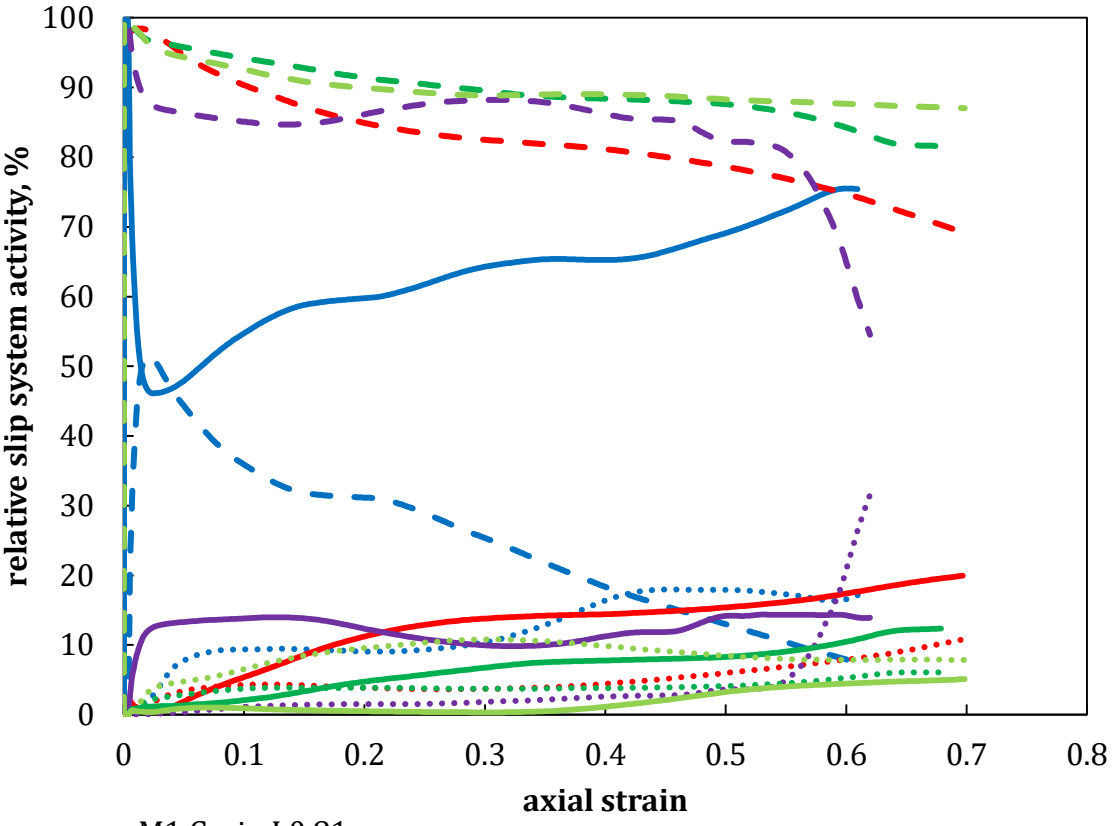
relative slip system activity, %
100
90
80
70
60
50
40
30
20
10
0
0
0.1
0.2
0.3
0.4
0.5
0.6
0.7
0.8
axial strain
M1 Grain I 0.81
M1 Grain II 0.47
M1 Grain III 0.78
M1 Grain IV 0.54
M1 Grain IV 0.40
Solid lines indicate basal slip
Dashed lines indicate prismatic slip
Dotted lines indicate pyramidal slip

(a) sample M1

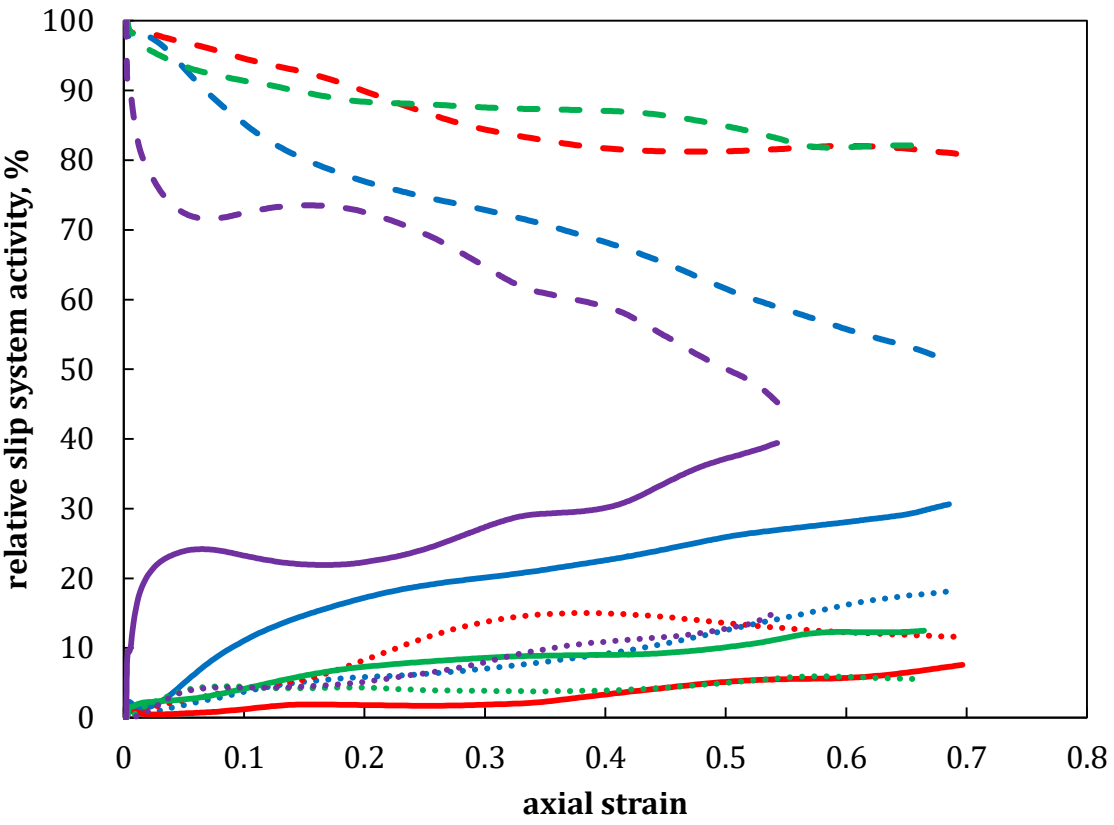
relative slip system activity, %
100
90
80
70
60
50
40
30
20
10
0
0
0.1
0.2
0.3
0.4
0.5
0.6
0.7
0.8
axial strain
M2 Grain I 0.57
M2 Grain II 0.46
M2 Grain III 0.61
M2 Grain IV 0.88
Solid lines indicate basal slip
Dashed lines indicate prismatic slip
Dotted lines indicate pyramidal slip

(b) sample M2

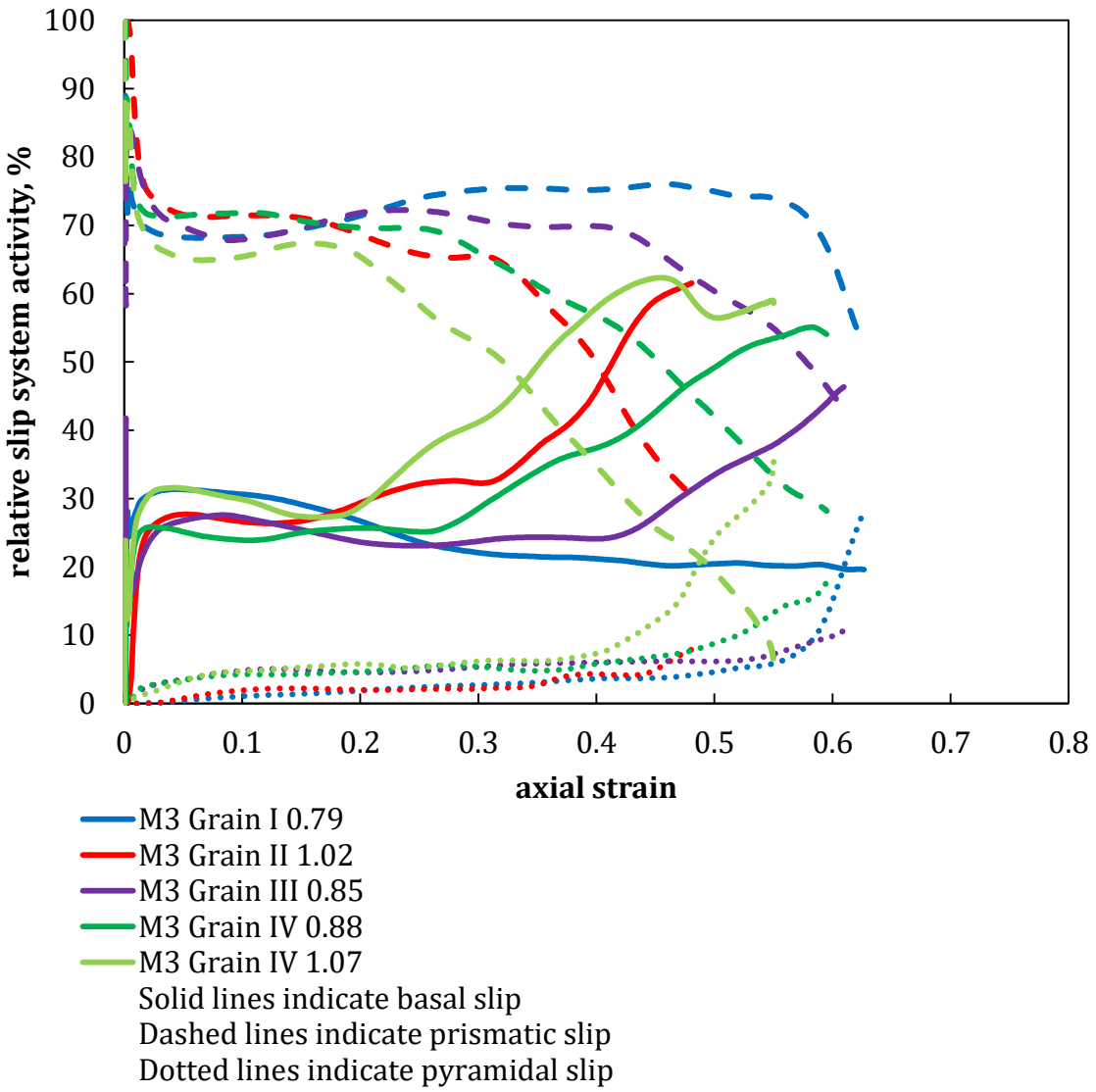

(c) sample M3

Figure 6.8: Slip systems activated in the node at the bottom of the void in different grains in samples: (a) M1, (b) M2, (c) M3.

It can be concluded that the crystal plasticity simulations predict well the experimental void growth and the differences between crystal plasticity. It is not clear why there are discrepancies between experimental and simulation results. In order to confirm the hypothesis that surrounding grains affect the void growth in a particular grain crystal plasticity simulations with two voids located in two adjacent grains are presented in Section 6.4.

6.2 Crystal plasticity: Changing the size of the box.

In order to see how the void volume fraction affects void growth, four models were created. In all four cases, the diameter of the voids is equal to 25 μm while the size of the box varies from 50 μm, 70 μm, 100 μm and 200 μm (Figure 6.9).

The void growth curves are shown in Figure 6.10. It can be seen that increasing the void fraction (which is equivalent to decreasing the size of the box from 200 μm to 50 μm) does not have a significant influence on void growth, as long as the local state of strain is taken into account.

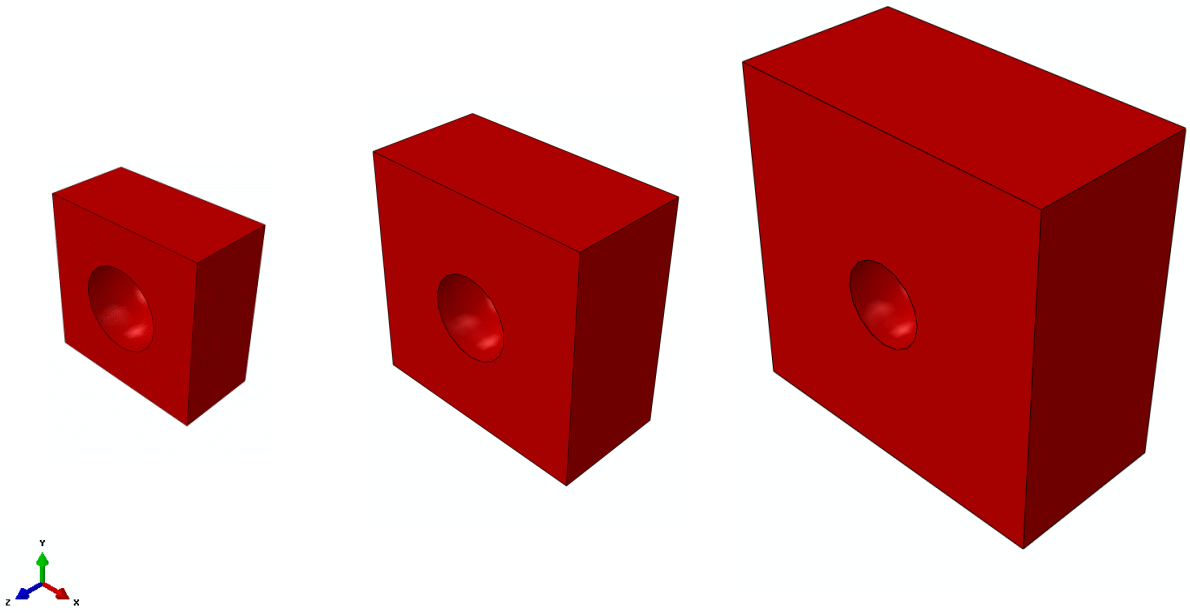

(a) box size 50 μm (b) box size 70 μm (c) box size 100 μm

Figure 6.9: 3D model with one grain in the shape of a cube containing one spherical void. Half of the model is shown. Red color indicates crystal plasticity. Tensile direction coincides with the x axis.

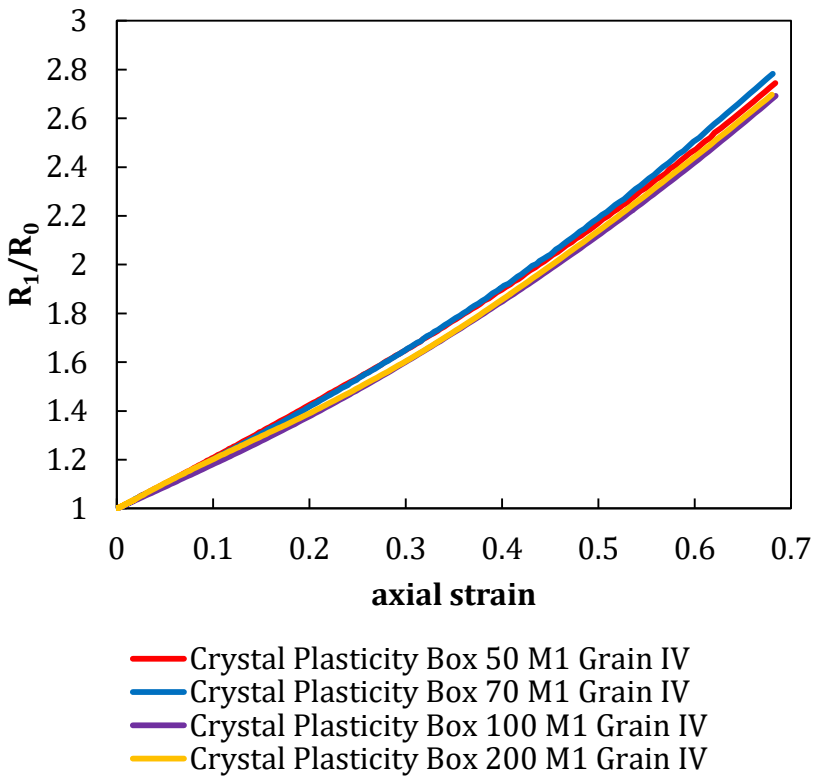

Figure 6.10: Void growth curves extracted from simulations in order to see the influence of void fraction on the void growth.

6.3 Crystal plasticity: the grain shape effect.

In order to investigate whether grain shape has any influence on void growth, two models were created: one as described above which contains a grain in the shape of a tetrakaidecahedron and the other one which contains a grain in the shape of a cube. The results are presented in Figure 6.11. It can be concluded that the shape of the grain does not have any significant influence on void growth.

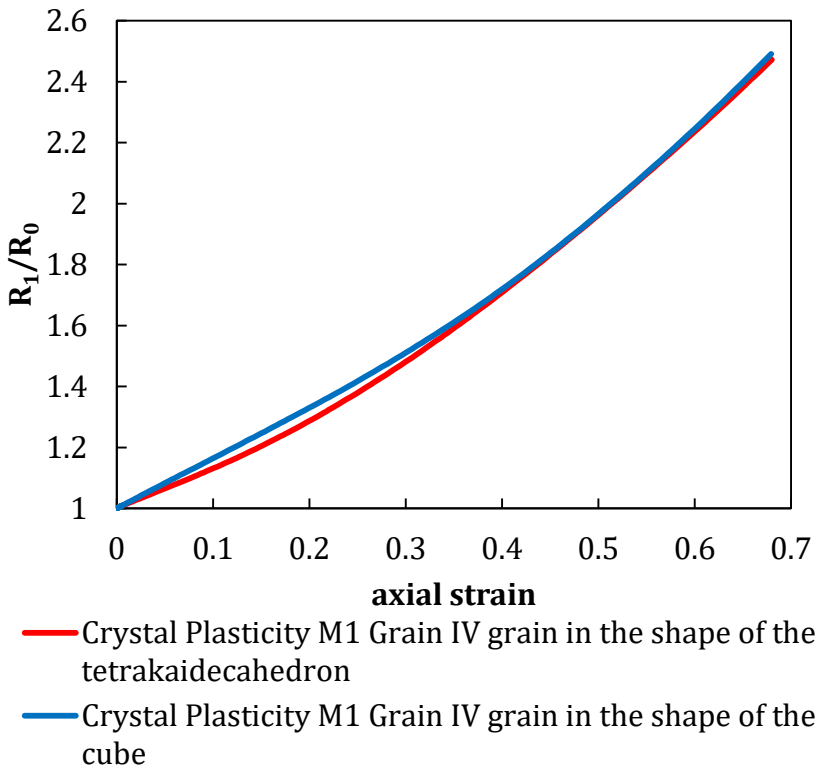

Figure 6.11: Void growth curves extracted from simulations in order to see the influence of the shape of the grain on the void growth.

6.4 Crystal plasticity: two voids in two adjacent grains.

In order to assess the hypothesis that the surrounding grains can affect void growth, crystal plasticity simulations were performed with the model shown in Figure 6.12. This model contains two voids which are located in two adjacent grains. To test this hypothesis, the upper and lower grains were first given the same orientation. The orientation of the upper grain was then changed while keeping the same orientation for the lower grain.

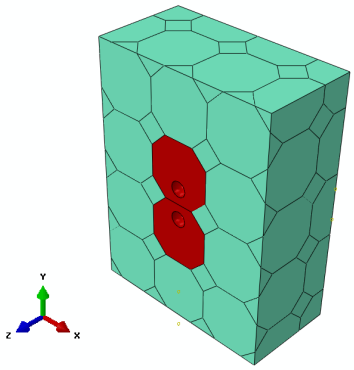

Figure 6.12: 3D model with two grains located in two adjacent grains. Half of the model is shown. Red color indicates crystal plasticity; green color indicates macroscopic properties of titanium. Tensile direction coincides with the x axis.

Results of crystal plasticity simulations are presented in Figure 6.13. It can be seen that the orientation of the surrounding grain affects the void growth in the particular grain.

The results of the simulations show that the evolution of void growth with applied strain depends on the orientation of the grain in which the void is embedded (Figure 6.14). However it is important to note that depending on the grain orientation the local strain state changes (Figure 6.15) and thus the results might be explained by the fact the local strain state changes the void growth.

In conclusion, the discrepancies between experimental results and the theory are indeed explained by the fact that void growth is a particular grain is not only affected by the grain orientation of this grain but also by the orientations of the surrounding grains.

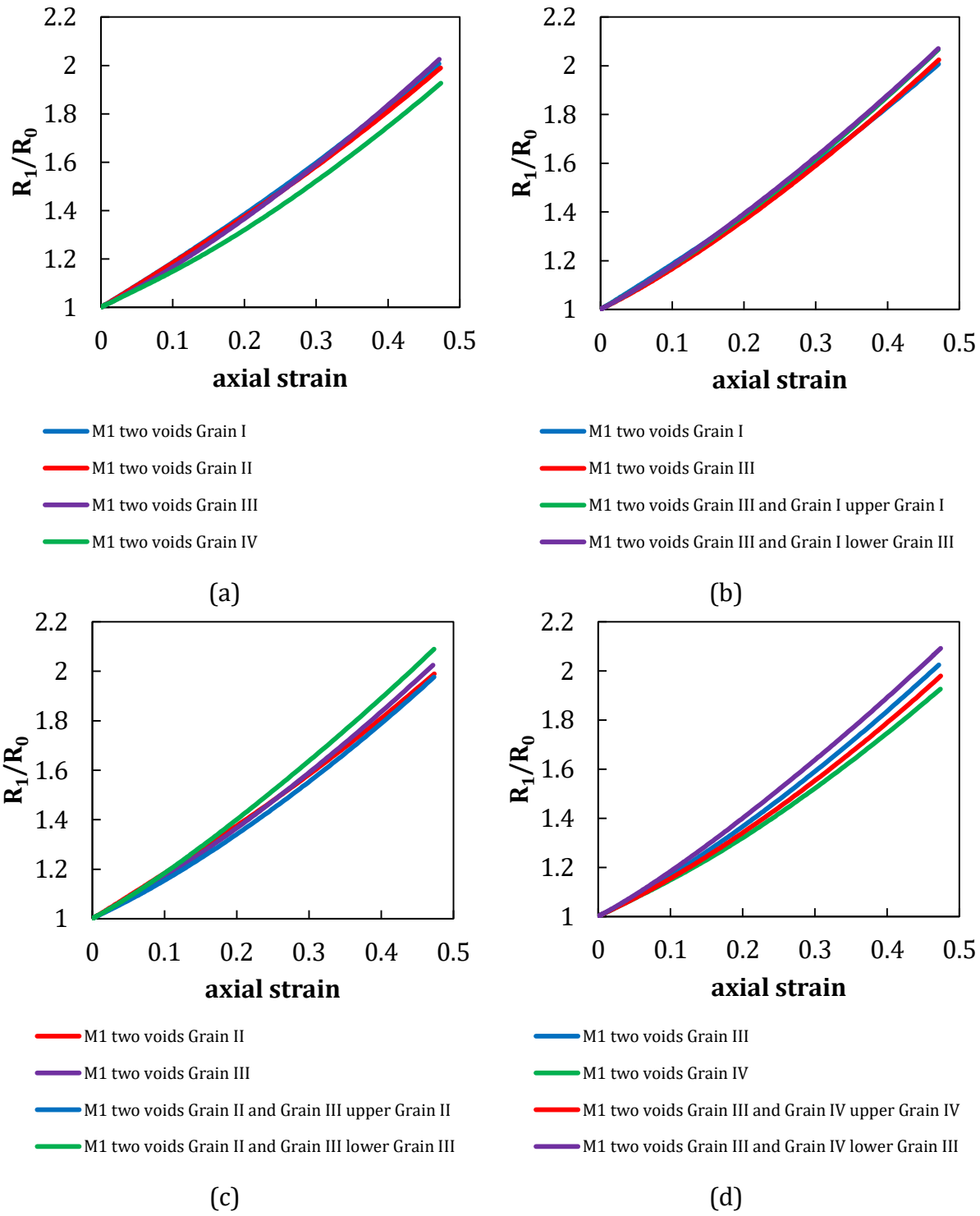

Figure 6.13: Crystal plasticity results strain for sample M1: (a) two voids that have the same orientation, (b) comparison between two voids having the same I and III orientations, and two voids having different orientations, (c) comparison between two voids having the same II and III orientations, and two voids having different orientations, (d) comparison between two voids having the same III and IV orientations, and two voids having different orientations.

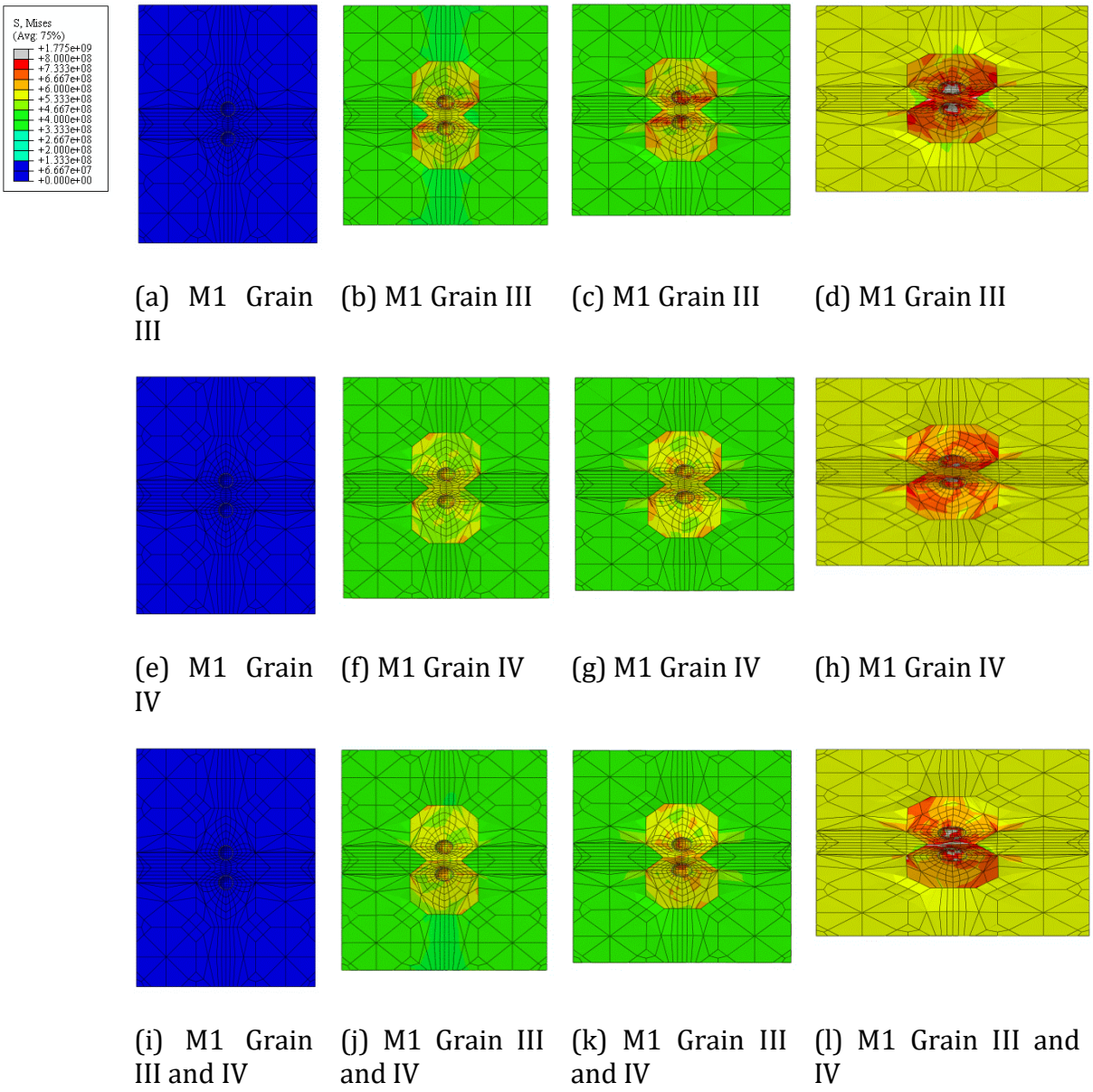

(a) M1 Grain III (b) M1 Grain III (c) M1 Grain III (d) M1 Grain III

(e) M1 Grain IV (f) M1 Grain IV (g) M1 Grain IV (h) M1 Grain IV

(i) M1 Grain III and IV (j) M1 Grain III and IV (k) M1 Grain III and IV (l) M1 Grain III and IV

Figure 6.14: Visualization of void growth at different true strains in sample M1 for two voids in two grains: (a)-(d) with the same orientation as Grain III, (e)-(h) with the same orientation as Grain IV, (i)-(l) with different orientations, where lower grain has orientation of Grain III and upper grain has the orientation of Grain IV. Tensile direction is horizontal.

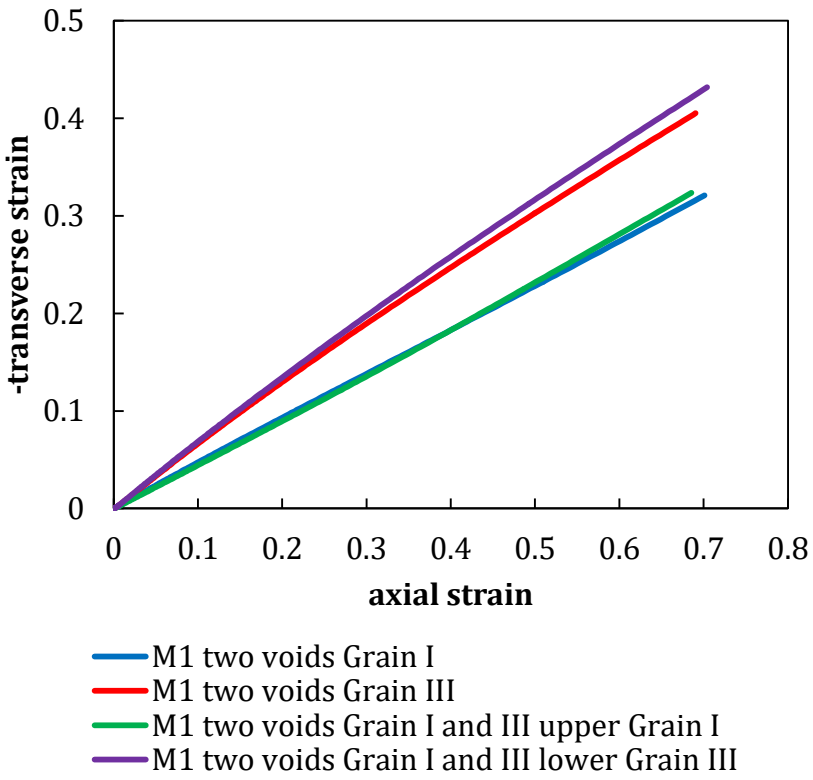

Figure 6.15: Transverse strain as a function of axial strain extracted from simulations.

6.5 Discussion and conclusions

The experimental results presented in Chapter 5 are compared to the simulation results in this Chapter. The crystal plasticity model described previously (Chapter 4) was used in order to predict the growth of voids located in grains with different orientations. First, the parameters of the Voce-hardening law were determined using the experimental true stress-strain curves. Then these parameters were used in order to predict void growth. A 3D model with one void located completely in one grain was used. It was shown that it is important to take into account the deformation state to which the grain is subjected. This is done by calculating the ratio between local transverse and axial strain and taking it into account in the model.

Figure 6.3 shows the comparison between experimental and simulated void growth in the tensile direction taking into account the ratio between local transverse and axial strains. This figure shows that void growth depends on grain orientation. It can be seen that there is a good agreement between experimental and simulation results. Thus it can be concluded that two main factors have to be taken into account in order to

predict void growth namely: the orientation of the grain in which the void is embedded and the local strain state around the void. This is in agreement with literature where the scatter in void growth curves in Ti-6Al-4V alloy is attributed to the effects of the local crystallographic orientation [202].

Figure 6.6-Figure 6.8 show the activity of the slip systems depending on the grain orientation. In all grain orientations studied in this Chapter, three slip systems are activated: basal, prismatic and pyramidal. Depending on the grain orientation the activity of each slip systems changes which explains why void growth changes depending on the grain orientation. From these figures it can be seen that simultaneous activation of basal slip systems results in the largest void growth rate. Basal slip is more active close to the voids, where stress concentration and triaxial stress states are more important compared to away from the void.

In order to study the effect of void volume fraction on void growth, four models were created which have different box sizes that surround the void (Figure 6.9). Figure 6.10 showed that the void volume fraction has a slight effect on void growth. This suggests that the grain orientation effect is more important than the void volume fraction effect, as long as local strains are considered. Similar conclusions were drawn in Chapter 3 where it was shown that the effect of grain orientation on void growth is more important than the intervoid spacing or the volume fraction of the voids.

As previously mentioned the grains were simulated in the shape of a tetrakaidecahedron which is a reasonable approximation of grains in polycrystals [215]. In order to see if the geometry of the grain affects void growth, the results of the original model having the grains in the shape of tetrakaidecahedrons were compared to a model having the grains in the shape of a cube. Figure 6.11 indicates that there is no significant difference between the results obtained with the model having the grains in the shape of a tetrakaidecahedron and the grains in the shape of a cube.

In order to study the effect of the surrounding grains on void growth, the model with two voids located inside two adjacent grains was created (Figure 6.12). Figure 6.13

indicates that the effect of grain orientation is more important than the effect of the surrounding grains as long as local strain are considered. Figure 6.14 shows that for the same strain level, the stress distribution around the void depends on the grain orientation. The effect of the surrounding grains was studied in the literature. It was shown that during fatigue testing, a crack nucleated at a hard grain – soft grain interface propagates through the hard-orientated grain, suggesting that the driving stress intensity depends on the local morphology and crystallographic orientations [219]. Furthermore, the plastic zone which develops at the tip of a crack in an hcp single crystal is strongly dependent on crystallographic orientation [219]. Even grains with similar orientations can follow different orientation trajectories depending on their misorientation with respect to neighboring grains [220]. The importance of neighboring grains can be understood in terms of the stress intensities resulting from grain misorientations [219].

The conclusions are presented next. Void growth was modelled by taking into account the grain orientation and the local strain state in the grain. Two different grain geometries were tested that both yielded similar results suggesting that grain geometry has limited effect on void growth.

In general these simulations showed that crystal plasticity models can predict effectively void growth in grains having different orientations. The activated slip systems in each particular grain were extracted from the model. In all cases the activation of three principal slip systems was observed: basal, prismatic and pyramidal.

The effect of the void volume fraction was modeled. It was observed that the void volume fraction does not significantly affect void growth.

The effect of the surrounding grains was simulated by creating a model with two adjacent grains and by varying the orientation of one with respect to the other grain. It was shown that void growth in a particular grain is only affected slightly by the surrounding grain orientation which is probably due to a change in local strain state.

Despite the fact that the parameters tested individually have a small influence on void growth, it is believed that the combined effect of these parameters could explain the discrepancies observed between experimental and simulated void growth curves.

Chapter 7 CONCLUSIONS AND FUTURE WORK

7.1 CONCLUSIONS

The scope of the present study can be phrased as a research question: what is the effect of grain orientation on void growth in annealed commercially pure titanium?

The fracture process of commercially pure titanium was visualized in model materials containing artificial holes. These model materials were fabricated using a femtosecond laser coupled with a diffusion bonding technique to obtain voids in the interior of titanium samples.

The main conclusions are as follows:

1. This thesis brings an important methodology to study the effect of grain orientation on void growth. New model materials were fabricated, where laser micromachining, diffusion bonding, EBSD and X-Ray tomography were used to visualize void growth in three-dimensions while knowing the grain orientation for each void. This allowed, for the first time, to directly couple void growth with grain orientation in three dimensions.

2. Intervoid spacing and material strength were found not to affect void growth significantly.

3. The Rice and Tracey model for void growth provided good predictions of average void growth rates.

4. Fracture surface analyses revealed different modes of intervoid ligament failure where smaller intervoid spacing leads to a more brittle failure. This effect was related to the number of grains in the intervoid ligament and to the ability of strain localization bands to form between voids.

5. A large scatter in void growth was observed experimentally and was hypothesized to be due to grain orientation effects. This hypothesis was supported by

crystal plasticity finite element simulations which showed a similar scatter in void growth results.

6. The importance of the local state of strain on void growth was demonstrated.

7. Crystal plasticity simulations that take into account the particular grain orientation and the local state of strain were found to predict well experimental void growth.

8. Crystal plasticity simulations confirmed that the orientation of the void-containing grain is more important than the orientation of grains surrounding it and more important than the void volume fraction in order to predict void growth.

This study and its findings are important not only for CP Ti used in aerospace and biomedical industries but also for other materials exhibiting properties which depend on the grain orientation and for the general understanding of the ductile fracture process.

7.2 FUTURE WORK

Future work may be done in the following directions:

1. Samples made from different materials (for example, magnesium or zirconium which also have an HCP structure but have different deformation behaviors) may be fabricated and tested using the same methodology.

2. The effect of void coalescence may be studied in more details. In this work the data on the coalescence event was difficult to obtain due to the limited number of tomograms acquired. However by using a different technique, for example, fast tomography, which allows to continuously visualize the sample during deformation, more details on void coalescence could be obtained.

3. The effect of positioning voids at grain boundaries or at triple joints on void growth may be studied because in real samples voids tend to appear at different locations and not only inside the grains.

4. Diffraction contrast tomography (DCT) may be used in order to see the grains including the surrounding grains in three dimensions. This will allow to study more in detail the effect of the surrounding grains on void growth and coalescence.

5. New materials with improved fracture properties may be designed using the knowledge that grain orientation affects void growth.

REFERENCES

[1] Lütjering G, Williams JC. Titanium. vol. 2nd ed. Berlin;New York: Springer; 2007.

[2] Yoo MH. Slip, twinning, and fracture in hexagonal close-packed metals. Metall Trans A 1981;12:409–18.

[3] Zarkades A, Larson R. F. The Science, Technology and Application of Titanium. Oxford, UK: Pergamon Press; 1970.

[4] Shechtman D, Brandon D. Orientation dependent slip in polycrystalline titanium. J Mater Sci 1973;8:1233–7. doi:10.1007/BF00549337.

[5] Banerjee D, Williams JC. Microstructure and slip character in titanium alloys. Def Sci J 1986;36:191–206.

[6] Partridge PG. The crystallography and deformation modes of hexagonal close-packed metals. Metall Rev 1967;12:169–94.

[7] Gong J, Wilkinson AJ. Anisotropy in the plastic flow properties of single-crystal α titanium determined from micro-cantilever beams. Acta Mater 2009;57:5693–705. doi:http://dx.doi.org/10.1016/j.actamat.2009.07.064.

[8] Viswanathan GB, Lee E, Maher DM, Banerjee S, Fraser HL. Direct observations and analyses of dislocation substructures in the α phase of an α/β Ti-alloy formed by nanoindentation. Acta Mater 2005;53:5101–15. doi:10.1016/j.actamat.2005.07.030.

[9] Merson E, Brydson R, Brown A. The effect of crystallographic orientation on the mechanical properties of titanium. J Phys Conf Ser 2008;126:12020. doi:10.1088/1742-6596/126/1/012020.

[10] Paton E. N, Baggerly G. R, Williams C. J. Rockwell Report. vol. SC 526.7FR. 1976.

[11] Britton TB, Liang H, Dunne FPE, Wilkinson AJ. The effect of crystal orientation on the indentation response of commercially pure titanium: experiments and simulations. Proc R Soc A Math Phys Eng Sci 2010;466:695–719.

[12] Fischer-Cripps AC. Nanoindentation. vol. 1. Springer; 2011.

[13] Dorn E. J, Mitchell B. J. High-Strength Materials . New York: John Wiley & Sons, Inc.; 1964.

[14] Callister WD, Rethwisch DG. Materials science and engineering: an introduction

2007.

[15] Bozzolo N, Chan L, Rollett AD. Misorientations induced by deformation twinning in titanium. J Appl Crystallogr 2010;43:596–602.

[16] Mahajan S, Williams DF. Deformation twinning in metals and alloys. Int Mater Rev 1973;18:43–61.

[17] Conrad H. Effect of interstitial solutes on the strength and ductility of titanium. Prog Mater Sci 1981;26:123–403. doi:10.1016/0079-6425(81)90001-3.

[18] Fundenberger JJ, Philippe MJ, Wagner F, Esling C. Modelling and prediction of mechanical properties for materials with hexagonal symmetry (zinc, titanium and zirconium alloys). Acta Mater 1997;45:4041–55. doi:10.1016/S1359-6454(97)00099-2.

[19] Singh AK, Schwarzer RA. Texture and anisotropy of mechanical properties in titanium and its alloys. Zeitschrift Fuer Met Res Adv Tech 2000;91:702–16.

[20] Zaefferer S. A study of active deformation systems in titanium alloys: dependence on alloy composition and correlation with deformation texture. Mater Sci Eng A 2003;344:20–30. doi:10.1016/S0921-5093(02)00421-5.

[21] Chun YB, Yu SH, Semiatin SL, Hwang SK. Effect of deformation twinning on microstructure and texture evolution during cold rolling of CP-titanium. Mater Sci Eng A 2005;398:209–19.

[22] Bozzolo N, Dewobroto N, Wenk HR, Wagner F. Microstructure and microtexture of highly cold-rolled commercially pure titanium. J Mater Sci 2007;42:2405–16. doi:10.1007/s10853-006-1302-2.

[23] Bozzolo N, Wagner F. Textures in HCP titanium and zirconium: Influence of twinning. Ceram Trans 2008;200:461–72.

[24] Paton E. N, Williams C. J, Rauscher P. G. Titanium Science and Technology. New York, USA: Plenum Press; 1973.

[25] Paton N, Backofen W. Plastic deformation of titanium at elevated temperatures. Metall Trans 1970;1:2839–47. doi:10.1007/BF03037822.

[26] Battaini M, Pereloma E V, Davies CHJ. Orientation effect on mechanical properties of commercially pure titanium at room temperature. Metall Mater Trans A Phys Metall Mater Sci 2007;38:276–85.

[27] Benmhenni N, Bouvier S, Brenner R, Chauveau T, Bacroix B. Micromechanical modelling of monotonic loading of CP α-Ti: Correlation between macroscopic and microscopic behaviour. Mater Sci Eng A 2013;573:222–33. doi:http://dx.doi.org/10.1016/j.msea.2013.02.022.

[28] Farrell K, Evans PR V. Some observations on mechanical twinning in polycrystalline niobium. J Less-Common Met 1965;8:222–34.

[29] Akhtar A. Basal slip and twinning in a-titanium single crystals. Metall Trans A 1975;6:1105–13.

[30] Burgers WG. On the process of transition of the cubic-body-centered modification into the hexagonal-close-packed modification of zirconium. Physica 1934;1:561–86. doi:10.1016/S0031-8914(34)80244-3.

[31] Newkirk JB, Geisler AH. Crystallographic aspects of the beta to alpha transformation in titanium. Acta Metall 1953;1:370–4. doi:10.1016/0001-6160(53)90113-8.

[32] Kim SK, Park JK. In-situ measurement of continuous cooling β → α transformation behavior of CP-Ti. Metall Mater Trans A 2002;33:1051–6. doi:10.1007/s11661-002-0206-2.

[33] Oh MS, Lee J-Y, Park JK. Continuous cooling Î²-to-Î± transformation behaviors of extra-pure and commercially pure Ti. Metall Mater Trans A 2004;35:3071–7. doi:10.1007/s11661-004-0052-5.

[34] Kofstad P, Anderson PB, Krudtaa OJ. Oxidation of titanium in the temperature range 800-1200°C. J Less-Common Met 1961;3:89–97.

[35] Williams J, Sommer A, Tung P. The influence of oxygen concentration on the internal stress and dislocation arrangements in a titanium. Metall Trans 1972;3:2979–84. doi:10.1007/BF02652870.

[36] Zwicker U. Titan and Titanlegierungen. Berlin, Germany: Springer-Verlag; 1974.

[37] Okamoto H. O-Ti (Oxygen-Titanium). J Phase Equilibria 2001;22:515. doi:10.1361/105497101770338635.

[38] Murray JL, Wriedt HA. The O–Ti (Oxygen-Titanium) system. J Phase Equilibria 1987;8:148–65. doi:10.1007/BF02873201.

[39] Enjo T, Ikeuchi K, Akikawa N. Effect of Oxide Film on the Early Process of

Diffusion Welding . Trans Join Weld Res Inst 1982;10:173–81.

[40] Enjo T, Ikeuchi K, Akikawa N, Maruyama T. Effect of α ↔ β on the Diffusion Welding of Titanium. Trans Join Weld Res Inst 1980;9:61–7.

[41] Enjo T, Ikeuchi K, Akikawa N. Effect of the Roughness of Faying Surface on the Early Process of Diffusion Welding. Trans Join Weld Res Inst 1982;11:49–56.

[42] Boyer R, Welsch G, Collings EW. Materials Properties Handbook - Titanium Alloys n.d.:1165.

[43] Mahoney W. M. Materials Properties Handbook: Titanium Alloys, Technical Note 5A: Superplastic Forming of Titanium Alloys. Materials Park, USA: ASM; 1994.

[44] King WH, Owczarski WA. Diffusion Welding of Commercially Pure Titanium. Weld J n.d.;Supp. 46:289–98.

[45] Conrad H, Keshavan MK, Sargent GA. No Title. Proc. 2nd Int. Conf. Mech. Behav. Mater., vol. Special Vo, Boston, Massachusetts; 1976, p. 538.

[46] Amateau MF, Burrier HI, Ebert LJ. Brittle Fracture in Alpha-Titanium. Trans Am Soc Met 1966;59:921.

[47] Salishchev GA, Mironov SY. Effect of grain size on mechanical properties of commercially pure titanium. Russ Phys J 2001;44:596–601.

[48] Krishnamohanrao Y, Kutumbarao V V, Rao PR. Fracture mechanism maps for titanium and its alloys. Acta Metall 1986;34:1783–806. doi:10.1016/0001-6160(86)90124-0.

[49] Conrad H, Doner M, de Meester B. Titanium Science and Technology, vol. 2. vol. 2. New York: R.I. Jaffee and H.M. Burte, eds.; Plenum Publ. Corp.; 1973.

[50] Pilchak AL, Porter WJ, John R. Room temperature fracture processes of a near-α titanium alloy following elevated temperature exposure. J Mater Sci 2012;47:7235–53.

[51] Hansen JO, Novotnak D. No Title. Heat Treat to Reduce Embrittlement Titan Alloy 1995.

[52] Tal-Gutelmacher E, Eliezer D. The hydrogen embrittlement of titanium-based alloys. JOM 2005;57:46–9.

[53] Gerard DA, Koss DA. The combined effect of stress state and grain size on hydrogen embrittlement of titanium. Scr Metall 1985;19:1521–4.

[54] Lentz CW, Koss DA, Stout MG, Hecker SS. The effect of hydrogen on the multiaxial stress-strain behavior of titanium tubing. Metall Trans A 1983;14:2527–33.

[55] Zhang Y, Wang Y-B, Qiao L-J, Chu W-Y, Hsiao C-M. Investigation of fractal dimensions of hydrogen-induced brittle fracture of titanium aluminide. Mater Sci Eng A 1994;177:L1–5. doi:10.1016/0921-5093(94)90501-0.

[56] Gandhi C, Ashby MF. Overview no. 5: Fracture-mechanism maps for materials which cleave: F.C.C., B.C.C. and H.C.P. metals and ceramics. Acta Metall 1979;27:1565–602. doi:10.1016/0001-6160(79)90042-7.

[57] Beevers CJ, Edmonds D V. Deformation and fracture of titanium/oxygen/hydrogen alloys. Met Soc AIME-Trans 1969;245:2391–8.

[58] Richardson LS, Grant NJ. No Title. Trans Am Inst Mining, Metall Pet Eng 1959;215:18.

[59] Rosi FD, Perkins FC. Mechanical properties and strain aging effects in titanium . Trans Am Soc Met 1953;45:972.

[60] Cuff TB, Grant NJ. No Title. Iron Age 1952;20:134.

[61] Rice JR, Thomson R. Ductile versus brittle behaviour of crystals. Philos Mag 1974;29:73–97.

[62] Stoloff NS, Gensamer M. No Title. Trans Metall Soc AIME 1963;227:70.

[63] Besson J. Continuum Models of Ductile Fracture: A Review. Int J Damage Mech 2010;19:3–52. doi:10.1177/1056789509103482.

[64] Benzerga AA, Leblond J-B. Ductile Fracture by Void Growth to Coalescence. Adv. Appl. Mech., vol. Volume 44, Elsevier; 2011, p. 169–305. doi:10.1016/S0065-2156(10)44003-X.

[65] Francois D, Pineau A, Zaoui A. Mechanical Behaviour of Materials. vol. 191. Springer Netherlands; 2013. doi:10.1007/978-94-007-4930-6_4.

[66] Argon AS, Im J. Separation of second phase particles in spheroidized 1045 steel, Cu-0.6pct Cr alloy, and maraging steel in plastic straining. Metall Trans A 1975;6:839–51.

[67] Beremin F. Cavity formation from inclusions in ductile fracture of A508 steel. Metall Trans A 1981;12:723–31. doi:10.1007/BF02648336.

[68] Le Roy G, Embury JD, Edwards G, Ashby MF. A model of ductile fracture based on

the nucleation and growth of voids. Acta Metall 1981;29:1509–22. doi:10.1016/0001-6160(81)90185-1.

[69] Bugat S. Comportement et endommagement des aciers austéno-ferritiques vieillis: une approche micromécanique. THES. 2000.

[70] Joly P, Cozar R, Pineau A. Effect of crystallographic orientation of austenite on the formation of cleavage cracks in ferrite in an aged duplex stainless steel. Scr Metall Mater 1990;24:2235–40. doi:10.1016/0956-716X(90)90071-N.

[71] Mahajan Y, Margolin H. Low Cycle Fatigue Behavior of Ti-6AI-2Sn-4Zr-6Mo: Part I. The Role of Microstructure in Low Cycle Crack Nucleation and Early Crack Growth. Metall Trans A 1982;13:257–68. doi:10.1007/BF02643316.

[72] Jago G, Bechet J, Bathis C. No Title. Titanium 1996;95:1203.

[73] Babout L, Brechet Y, Maire E, Fougères R. On the competition between particle fracture and particle decohesion in metal matrix composites. Acta Mater 2004;52:4517–25. doi:10.1016/j.actamat.2004.06.009.

[74] Benzerga AA. Rupture ductile des tôles anisotropes. . THES. 2000.

[75] Xue Q, Meyers MA, Nesterenko VF. Self-organization of shear bands in titanium and Ti–6Al–4V alloy. Acta Mater 2002;50:575–96. doi:10.1016/S1359-6454(01)00356-1.

[76] Kobayashi H, Dodd B. A numerical analysis for the formation of adiabatic shear bands including void nucleation and growth. Int J Impact Eng 1989;8:1–13. doi:10.1016/0734-743X(89)90027-4.

[77] Marini B, Mudry F, Pineau A. Experimental study of cavity growth in ductile rupture. Eng Fract Mech 1985;22:989–96.

[78] Garrison Jr. WM, Moody NR. Ductile fracture. J Phys Chem Solids 1987;48:1035–74.

[79] Mudry F. Etude de la rupture ductile et de la rupture par clivage d'aciers faiblement alliés. THES. 1982.

[80] Pardoen T, Delannay F. Assessment of void growth models from porosity measurements in cold-drawn copper bars. Metall Mater Trans A 1998;29:1895–909.

[81] Chae D, Koss DA. Damage accumulation and failure of HSLA-100 steel. Mater Sci

Eng A 2004;366:299–309. doi:10.1016/j.msea.2003.08.040.

[82] Jablokov V, Goto DM, Koss DA. Damage accumulation and failure of HY-100 steel. Metall Mater Trans A 2001;32:2985–94.

[83] Benzerga AA, Besson J, Pineau A. Anisotropic ductile fracture. Acta Mater 2004;52:4623–38.

[84] Margolin H, Mahajan Y. Void formation, void growth and tensile fracture in Ti-6AI-4V. Metall Trans A 1978;9:781–91. doi:10.1007/BF02649787.

[85] Greenfield M, Margolin H. The mechanism of void formation, void growth, and tensile fracture in an alloy consisting of two ductile phases. Metall Trans 1972;3:2649–59. doi:10.1007/BF02644241.

[86] Babout L, Maire E, Fougères R. Damage initiation in model metallic materials: X-ray tomography and modelling. Acta Mater 2004;52:2475–87.

[87] Weck A, Wilkinson DS, Maire E, Toda H. Visualization by X-ray tomography of void growth and coalescence leading to fracture in model materials. Acta Mater 2008;56:2919–28. doi:10.1016/j.actamat.2008.02.027.

[88] Maire E, Zhou S, Adrien J, Dimichiel M. Damage quantification in aluminium alloys using in situ tensile tests in X-ray tomography. Eng Fract Mech 2011;78:2679–90. doi:10.1016/j.engfracmech.2011.07.004.

[89] Argon AS, Im J, Safoglu R. Cavity formation from inclusions in ductile fracture. Metall Trans A 1975;6:825–37.

[90] Cox T, Low J. An investigation of the plastic fracture of AISI 4340 and 18 Nickel-200 grade maraging steels. Metall Trans 1974;5:1457–70. doi:10.1007/BF02646633.

[91] Benzerga AA. No Title. Unpubl Res 1999.

[92] Weck A, Wilkinson DS. Experimental investigation of void coalescence in metallic sheets containing laser drilled holes. Acta Mater 2008;56:1774–84. doi:10.1016/j.actamat.2007.12.035.

[93] Weck AG. The role of coalescence on ductile fracture. THES. McMaster University (Canada), 2007.

[94] Hosokawa A, Wilkinson DS, Kang J, Maire E. Onset of void coalescence in uniaxial tension studied by continuous X-ray tomography. Acta Mater 2013;61:1021–36.

[95] French I, Weinrich P, Weaver C. Tensile fracture of free machining brass as a function of hydrostatic pressure. Acta Metall 1973;21:1045–9. doi:10.1016/0001-6160(73)90020-5.

[96] French IE, Weinrich PF. The effect of hydrostatic pressure on the tensile fracture of α-brass. Acta Metall 1973;21:1533–7. doi:10.1016/0001-6160(73)90183-1.

[97] French I, Weinrich P. The influence of hydrostatic pressure on the tensile deformation and fracture of copper. Metall Trans A 1975;6:785–90. doi:10.1007/BF02672300.

[98] Pugh HLID, Green D. No Title. Proc Inst Mech Eng n.d.;179:417.

[99] Yajima M, Ishii M, Kobayashi M. The effects of hydrostatic pressure on the ductility of metals and alloys. Int J Fract Mech 1970;6:139–50. doi:10.1007/BF00189821.

[100] French IE, Weinrich PF. The influence of hydrostatic pressure on the tensile deformation of a spheroidised 0.5% steel. Scr Metall 1974;8:87–90. doi:10.1016/0036-9748(74)90449-9.

[101] Work CE, Dolan TJ. No Title. Proc ASTM 1953;53:611.

[102] Dieter GE. Ductility, Chapter 1. ASM Semin Am Soc Met Ohio, 1968 1967:1.

[103] Nadai A, Manjoine MJ. No Title. J Appl Mech 1941;8:77.

[104] Brown LM, Stobbs WM. The work-hardening of copper-silica v. equilibrium plastic relaxation by secondary dislocations. Philos Mag 1976;34:351–72. doi:10.1080/14786437608222028.

[105] Ashby MF, Gandhi C, Taplin DMR. Overview No. 3 Fracture-mechanism maps and their construction for f.c.c. metals and alloys. Acta Metall 1979;27:699–729. doi:10.1016/0001-6160(79)90105-6.

[106] Brindley B. The mechanism of ductile fracture in an Fe-21 %Cr-0.05 % C alloy. Acta Metall 1968;16:587–95. doi:10.1016/0001-6160(68)90133-8.

[107] Thomason PF. Ductile fracture of metals. Pergamon Press; 1990.

[108] Nasiri-Abarbekoh H, Ekrami A, Ziaei-Moayyed AA, Shohani M. Effects of rolling reduction on mechanical properties anisotropy of commercially pure titanium. Mater Des 2012;34:268–74. doi:10.1016/j.matdes.2011.06.024.

[109] Elsayed A, Umeda J, Kondoh K. The texture and anisotropy of hot extruded

magnesium alloys fabricated via rapid solidification powder metallurgy. Mater Des 2011;32:4590–7. doi:10.1016/j.matdes.2011.03.066.

[110] Tajally M, Emadoddin E. Mechanical and anisotropic behaviors of 7075 aluminum alloy sheets. Mater Des 2011;32:1594–9. doi:10.1016/j.matdes.2010.09.001.

[111] Jaffee RI, Promisel NE. No Title. Am. Soc. Met. Inst. Met. Metall. Soc. Aime. Sci. Technol. Appl. Titan. proceedings., Oxford, UK, Pergamon Press; 1970.

[112] Rugg D, Dixon M, Dunne FPE. Effective structural unit size in titanium alloys. J Strain Anal Eng Des 2007;42:269–79.

[113] Buckley DH. No Title. Influ Cryst Orientat Frict Charact Titan Single Cryst Vac 1965.

[114] Vanstone RH, Low JR. The effect of microstructure on the fracture toughness of titanium alloys 1973.

[115] Bathini U, Srivatsan TS, Patnaik A, Quick T. A study of the tensile deformation and fracture behavior of commercially pure titanium and titanium alloy: Influence of orientation and microstructure. J Mater Eng Perform 2010;19:1172–82.

[116] Nasiri-Abarbekoh H, Ekrami A, Ziaei-Moayyed AA. Impact of phase transformation on mechanical properties anisotropy of commercially pure titanium. Mater Des 2012;37:223–7. doi:10.1016/j.matdes.2011.12.040.

[117] Bantounas I, Dye D, Lindley TC. The effect of grain orientation on fracture morphology during high-cycle fatigue of Ti–6Al–4V. Acta Mater 2009;57:3584–95. doi:10.1016/j.actamat.2009.04.018.

[118] Bantounas I, Dye D, Lindley TC. The role of microtexture on the faceted fracture morphology in Ti–6Al–4V subjected to high-cycle fatigue. Acta Mater 2010;58:3908–18. doi:10.1016/j.actamat.2010.03.036.

[119] Nixon ME, Cazacu O, Lebensohn RA. Anisotropic response of high-purity a-titanium: Experimental characterization and constitutive modeling. Int J Plast 2010;26:516–32.

[120] Herbig M, King A, Reischig P, Proudhon H, Lauridsen EM, Marrow J, et al. 3-D growth of a short fatigue crack within a polycrystalline microstructure studied using combined diffraction and phase-contrast X-ray tomography. Acta Mater

2011;59:590–601.

[121] Bieler TR, Glavicic MG, Semiatin SL. Using OIM to investigate the microstructural evolution of Ti-6Ai-4V. JOM 2002;54:31–6. doi:10.1007/BF02822602.

[122] Khasegava A, Khisumura T, Fukuda M. Effect of Texture on the Deep-Drawing Ability of Sheets of Commercial-Purity Titanium. Proc. 3d Int. Conf. Titan., vol. 3, VILS, Moscow, Russia; 1978, p. 151–164.

[123] Betsofen SY, Ilyin AA, Plikhunov V V, Plotnikov AD, Filatov AA. Texture and anisotropy in the mechanical properties of titanium alloys caused by the mechanism of plastic deformation. Russ Metall 2007;2007:387–93.

[124] Bieler TR, Crimp MA, Yang Y, Wang L, Eisenlohr P, Mason DE, et al. Strain heterogeneity and damage nucleation at grain boundaries during monotonic deformation in commercial purity titanium. JOM 2009;61:45–52.

[125] Umakoshi Y, Nakano T, Ogawa B. Orientation dependence of fracture behavior of Ti3Al single crystals with D019 structure. Scr Mater 1996;34:1161–9.

[126] Minonishi Y. Plastic deformation of single crystals of Ti3Al with D019 structure. Philos Mag A Phys Condens Matter, Struct Defects Mech Prop 1991;63:1085–93.

[127] Umakoshi Y, Nakano T, Takenaka T, Sumimoto K, Yamane T. Orientation and temperature dependence of yield stress and slip geometry of Ti3Al and Ti3Al-V single crystals. Acta Metall Mater 1993;41:1149–54.

[128] Inui H, Toda Y, Shirai Y, Yamaguchi M. Low-temperature deformation of single crystals of a DO19 compound with an off-stoichiometric composition (Ti-36·5 at.% Al). Philos Mag A 1994;69:1161–77. doi:10.1080/01418619408242246.

[129] McDowell DL. A perspective on trends in multiscale plasticity. Int J Plast 2010;26:1280–309.

[130] Tanaka K, Mori T, Nakamura T. Cavity formation at the interface of a apherical inclusion in a plastically deformed matrix. Phil Mag 1970;21:267–79.

[131] Goods SH, Brown LM. Nucleation of cavities by plastic deformation. Acta Met 1979;27:1–15.

[132] Helbert AL, Feaugas X, Clavel M. Effects of microstructural parameters and back stress on damage mechanisms in a/ß titanium alloys. Acta Mater 1998;46:939–51.

[133] Needleman A. Continuum model for void nucleation by inclusion debonding. J Appl Mech Trans ASME 1987;54:525–31.

[134] Needleman A, Tvergaard V. An analysis of ductile rupture modes at a crack tip. J Mech Phys Solids 1987;35:151–83. doi:10.1016/0022-5096(87)90034-2.

[135] Nutt SR, Needleman A. Void nucleation at fiber ends in Al&z.sbnd;SiC composites. Scr Metall 1987;21:705–10. doi:10.1016/0036-9748(87)90389-9.

[136] Segurado J, LLorca J. A new three-dimensional interface finite element to simulate fracture in composites. Int J Solids Struct 2004;41:2977–93. doi:10.1016/j.ijsolstr.2004.01.007.

[137] Katani S, Madadi F, Atapour M, Ziaei Rad S. Micromechanical modelling of damage behaviour of Ti–6Al–4V. Mater Des 2013;49:1016–21. doi:10.1016/j.matdes.2013.02.021.

[138] Kumar J, Srivathsa B, Kumar V. Stress triaxiality effect on fracture behavior of IMI-834 titanium alloy: A micromechanics approach. Mater Des 2009;30:1118–23. doi:10.1016/j.matdes.2008.06.044.

[139] Helbert AL, Feaugas X, Clavel M. Influence of stress triaxiality on the damage mechanisms in an equiaxed a/ß Ti-6Al-4V alloy. Metall Mater Trans A Phys Metall Mater Sci 1996;27 A:3043–58.

[140] Vadillo G, Zaera R, Fernandez-Saez J. Consistent integration of the constitutive equations of Gurson materials under adiabatic conditions. Comput Methods Appl Mech Eng 2008;197:1280–95. doi:10.1016/j.cma.2007.11.008.

[141] Dunne FPE, Katramados I. Micro-mechanical modelling of strain induced porosity under generally compressive stress states. Int J Plast 1998;14:577–95. doi:10.1016/S0749-6419(99)80001-1.

[142] Rice JR, Tracey DM. On the ductile enlargement of voids in triaxial stress fields∗. J Mech Phys Solids 1969;17:201–17. doi:10.1016/0022-5096(69)90033-7.

[143] Gurson AL. Continuum theory of ductile rupture by void nucleation and growth: part 1 - yield criteria and flow rules for porous ductile media. J Eng Mater Technol Trans ASME 1977;99 Ser H:2–15.

[144] McClintock FA. A Criterion for Ductile Fracture by the Growth of Holes. J Appl Mech 1968;35:363–71.

[145] Atkinson JD. No Title. THES. 1973.

[146] Brown LM. No Title. Cambridge Fract. Conf. Churchill Coll. Inst. Phys., 1974.

[147] Marini B. Croissance des Cavites en Plasticite. Rupture sous Chargements Non-Radiaux et en Mode Mixte. THES. 1984.

[148] Budiansky B, Hutchinson JW, Slutsky S. Void growth and collapse in viscous solids. . Oxford: Hopkins HG, Sewell MJ (eds) Mechanics of solids. The Rodney Hill 60th anniversary volume. Pergamon; 1982.

[149] Tracey DM. Strain-hardening and interaction effects on the growth of voids in ductile fracture. Eng Fract Mech 1971;3:301–15. doi:10.1016/0013-7944(71)90040-3.

[150] Huang Y. Accurate dilatation rates for spherical voids in triaxial stress fields. J Appl Mech 1991;58:1084.

[151] Tvergaard V. Influence of voids on shear band instabilities under plane strain conditions. Int J Fract 1981;17:389–407. doi:10.1007/BF00036191.

[152] Leblond J-B, Perrin G, Devaux J. An improved Gurson-type model for hardenable ductile metals. Eur J Mech 1995;14:499–527.

[153] Besson J, Guillemer-Neel C. An extension of the Green and Gurson models to kinematic hardening. Mech Mater 2003;35:1–18. doi:10.1016/S0167-6636(02)00169-2.

[154] Pardoen T, Hutchinson JW. An extended model for void growth and coalescence. J Mech Phys Solids 2000;48:2467–512. doi:10.1016/S0022-5096(00)00019-3.

[155] Gologanu M, Leblond JB, Devaux J. Approximate models for ductile metals containing non-spherical voids-Case of axisymmetric prolate ellipsoidal cavities. J Mech Phys Solids 1993;41:1723–54. doi:10.1016/0022-5096(93)90029-F.

[156] Perrin G, Leblond J-B. Accelerated void growth in porous ductile solids containing two populations of cavities. Int J Plast 2000;16:91–120. doi:10.1016/S0749-6419(99)00049-2.

[157] Berg C. Inelastic behaviour of solids. McGraw-Hill; 1970.

[158] Yamamoto H. Conditions for shear localization in the ductile fracture of void-containing materials. Int J Fract 1978;14:347–65. doi:10.1007/BF00015989.

[159] Tvergaard V, Needleman A. Analysis of the cup-cone fracture in a round tensile

bar. Acta Metall 1984;32:157–69. doi:10.1016/0001-6160(84)90213-X.

[160] Pineau A, Pardoen T. Failure of metals. Amsterdam: In: Milne I, Ritchie RO, Karihaloo B (eds) Comprehensive structural integrity, vol 2. Elsevier; 2007.

[161] Benzerga AA, Besson J. Plastic potentials for anisotropic porous solids. Eur J Mech A/Solids 2001;20:397–434.

[162] O'Regan TL, Quinn DF, Howe MA, McHugh PE. Void growth simulations in single crystals. Comput Mech 1997;20:115–21.

[163] Potirniche GP, Hearndon JL, Horstemeyer MF, Ling XW. Lattice orientation effects on void growth and coalescence in fcc single crystals. Int J Plast 2006;22:921–42. doi:10.1016/j.ijplas.2005.06.003.

[164] Yerra SK, Tekog˜lu C, Scheyvaerts F, Delannay L, Van Houtte P, Pardoen T. Void growth and coalescence in single crystals. Int J Solids Struct 2010;47:1016–29. doi:10.1016/j.ijsolstr.2009.12.019.

[165] Crépin J, Bretheau T, Caldemaison D. Cavity growth and rupture of ß-treated zirconium: A crystallographic model. Acta Mater 1996;44:4927–35.

[166] Keralavarma SM, Hoelscher S, Benzerga AA. Void growth and coalescence in anisotropic plastic solids. Int J Solids Struct 2011;48:1696–710. doi:10.1016/j.ijsolstr.2011.02.020.

[167] Brown LM, Embury JD. Initiation and growth of voids at second phase particles. Inst Met Monogr Rep Ser 1973;1:164–9.

[168] Besson J. Local approach to fracture . Paris: Presses Ecole des Mines de Paris; 2004.

[169] Needleman A, Tvergaard V. An analysis of ductile rupture in notched bars. J Mech Phys Solids 1984;32:461–90. doi:10.1016/0022-5096(84)90031-0.

[170] Benzerga AA, Besson J, Pineau A. Coalescence-controlled anisotropic ductile fracture. J Eng Mater Technol Trans ASME 1999;121:221–9.

[171] Gao X, Kim J. Modeling of ductile fracture: Significance of void coalescence. Int J Solids Struct 2006;43:6277–93. doi:10.1016/j.ijsolstr.2005.08.008.

[172] Zhang ZL, Thaulow C, Odegard J. Complete Gurson model approach for ductile fracture. Eng Fract Mech 2000;67:155–68.

[173] Kim J, Gao X, Srivatsan TS. Modeling of void growth in ductile solids: Effects of

stress triaxiality and initial porosity. Eng Fract Mech 2004;71:379–400.

[174] Thomason PF. A theory for ductile fracture by internal necking of cavities. , , 360. J Inst Met 1968;96:360–5.

[175] Ma D, Chen D, Wu S, Wang H, Cai C, Deng G. Dynamic experimental verification of void coalescence criteria. Mater Sci Eng A 2012;533:96–106. doi:10.1016/j.msea.2011.11.041.

[176] Benzerga AA. Micromechanics of coalescence in ductile fracture. J Mech Phys Solids 2002;50:1331–62. doi:10.1016/S0022-5096(01)00125-9.

[177] Fabregue D, Pardoen T. A constitutive model for elastoplastic solids containing primary and secondary voids. J Mech Phys Solids 2008;56:719–41. doi:10.1016/j.jmps.2007.07.008.

[178] Tang T, Kim S, Horstemeyer MF. Molecular dynamics simulations of void growth and coalescence in single crystal magnesium. Acta Mater 2010;58:4742–59. doi:10.1016/j.actamat.2010.05.011.

[179] Pineau A. Development of the Local Approach to Fracture over the Past 25 years: Theory and Applications. Int J Fract 2006;138:139–66. doi:10.1007/s10704-006-0035-1.

[180] Crocker AG, Flewitt PEJ, Smith GE. Computational Modelling of Fracture in Polycrystalline Materials. Int Mater Rev 2005;50:99–125. doi:10.1179/174328005X14285.

[181] Hughes GM, Smith GE, Flewitt PEJ, Crocker AG. The brittle fracture of polycrystalline zinc. Proc R Soc A Math Phys Eng Sci 2007;463:2129–51.

[182] Cottrell AH. Theory of brittle fracture in steel and similar metals. TransMetSocAIME 1958;212.

[183] Hall EO. The Deformation and Ageing of Mild Steel: III Discussion of Results. Proc Phys Soc B 1951;64:747.

[184] Petch NJ. The Cleavage Strength of Polycrystals . J Iron Steel Inst 1953;174:25–8.

[185] Rosenfield AR, Shetty DK, Skidmore AJ. Fractographic observations of cleavage initiation in the ductile-brittle transition region of a reactor-pressure vessel steel. Metall Trans A, Phys Metall Mater Sci 1983;14 A:1934–7.

[186] Lambert-Perlade A, Sturel T, Gourgues AF, Besson J, Pineau A. Mechanisms and

modeling of cleavage fracture in simulated heat-affected zone microstructures of a high-strength low alloy steel. Metall Mater Trans A 2004;35:1039–53. doi:10.1007/s11661-004-0030-y.

[187] Martín-Meizoso A, Ocaña-Arizcorreta I, Gil-Sevillano J, Fuentes-Pérez M. Modelling cleavage fracture of bainitic steels. Acta Metall Mater 1994;42:2057–68.

[188] Beremin F, Pineau A, Mudry F, Devaux J-C, D'Escatha Y, Ledermann P. A local criterion for cleavage fracture of a nuclear pressure vessel steel. Metall Trans A 1983;14:2277–87. doi:10.1007/BF02663302.

[189] Bakker A, Koers RWI. Prediction of cleavage fracture events in the brittle-ductile transition region of a ferritic steel. In: pp . Blauel,JG;Schwalbe,K-H Defect Assess Components – Fundam Appl ESIS/EG 9 Mech Eng Publ London 1991:613–32.

[190] Xia L, Cheng L. Transition from ductile tearing to cleavage fracture: A cell-model approach. Int J Fract 1997;87:289–305. doi:10.1023/A:1007434828898.

[191] Gao, Faleskog, Fong S. Analysis of ductile to cleavage transition in part-through cracks using a cell model incorporating statistics. Fatigue Fract Eng Mater Struct 1999;22:239–50. doi:10.1046/j.1460-2695.1999.00151.x.

[192] Batdorf SB, Crose JG. A statistical theory for the fracture of brittle structures subjected to nonuniform polyaxial stresses. J Appl Mech 1974;41:459–64.

[193] Weck A, Crawford THR, Borowiec A, Wilkinson DS, Preston JS. Femtosecond laser-based fabrication of a new model material to study fracture. Appl Phys A 2007;86:55–61. doi:10.1007/s00339-006-3730-x.

[194] E112-10 AS. Test methods for determining average grain size. ASTM Annu B Stand 2010;2012:03.01.

[195] E384-11e1 A. Standard Test Method for Knoop and Vickers Hardness of Materials 2011;2012.

[196] Rasband WS. ImageJ. U S Natl Institutes Heal Bethesda, Maryland, USA n.d.;http://ima.

[197] E8/E8M-11 A. Standard Test Methods for Tension Testing of Metallic Materials 2012.

[198] Buffiere J, Maire E, Adrien J, Masse J, Boller E. In Situ Experiments with X ray Tomography: an Attractive Tool for Experimental Mechanics. Exp Mech 2010;50:289–305. doi:10.1007/s11340-010-9333-7.

[199] Kang D-S, Lee K-J, Kwon E-P, Tsuchiyama T, Takaki S. Variation of work hardening rate by oxygen contents in pure titanium alloy. Mater Sci Eng A 2015;632:120–6.

[200] Wei Q, Wang L, Fu Y, Qin J, Lu W, Zhang D. Influence of oxygen content on microstructure and mechanical properties of Ti–Nb–Ta–Zr alloy. Mater Des 2011;32:2934–9. doi:http://dx.doi.org.proxy.bib.uottawa.ca/10.1016/j.matdes.2010.11.049.

[201] Bridgman PW. Studies in large plastic flow and fracture. New York: McGraw-Hill; 1952.

[202] Lecarme L, Maire E, Kumar K.C. A, De Vleeschouwer C, Jacques L, Simar A, et al. Heterogenous void growth revealed by in situ 3-D X-ray microtomography using automatic cavity tracking. Acta Mater 2014;63:130–9. doi:10.1016/j.actamat.2013.10.014.

[203] Churchman AT. The Slip Modes of Titanium and the Effect of Purity on their Occurrence during Tensile Deformation of Single Crystals. Proc R Soc Lond A Math Phys Sci 1954;226:216–26.

[204] Nemcko MJ, Qiao H, Wu P, Wilkinson DS. Effects of void fraction on void growth and linkage in commercially pure magnesium. Acta Mater 2016;113:68–80. doi:10.1016/j.actamat.2016.04.008.

[205] Hosokawa A, Wilkinson DS, Kang J, Maire E. Onset of void coalescence in uniaxial tension studied by continuous X-ray tomography 2013;61:1021–36. doi:10.1016/j.actamat.2012.08.002.

[206] Segurado J. Crystal Plasticity Subroutine 2012.

[207] Segurado J, Llorca J. Simulation of the deformation of polycrystalline nanostructured Ti by computational homogenization. Sel Publ EU FP7 Proj VIRTUAL NANOTITANIUM (VINAT)"Theoretical Anal Virtual Test Titanium-Based Nanomater 2013;76:3–11. doi:http://dx.doi.org/10.1016/j.commatsci.2013.03.008.

[208] Tome C, Canova GR, Kocks UF, Christodoulou N, Jonas JJ. The relation between macroscopic and microscopic strain hardening in F.C.C. polycrystals. Acta Metall 1984;32:1637–53. doi:http://dx.doi.org/10.1016/0001-6160(84)90222-0.

[209] Asaro RJ. Micromechanics of Crystals and Polycrystals. Adv Appl Mech 1983;23:1–115. doi:http://dx.doi.org/10.1016/S0065-2156(08)70242-4.

[210] Asaro RJ, Needleman A. Overview no. 42 Texture development and strain hardening in rate dependent polycrystals. Acta Metall 1985;33:923–53. doi:http://dx.doi.org/10.1016/0001-6160(85)90188-9.

[211] Peirce D, Asaro RJ, Needleman A. An analysis of nonuniform and localized deformation in ductile single crystals. Acta Metall 1982;30:1087–119. doi:http://dx.doi.org/10.1016/0001-6160(82)90005-0.

[212] Peirce D, Asaro RJ, Needleman A. Material rate dependence and localized deformation in crystalline solids. Acta Metall 1983;31:1951–76. doi:http://dx.doi.org/10.1016/0001-6160(83)90014-7.

[213] Rice JR. Inelastic constitutive relations for solids: An internal-variable theory and its application to metal plasticity. J Mech Phys Solids 1971;19:433–55. doi:http://dx.doi.org/10.1016/0022-5096(71)90010-X.

[214] Hutchinson JW. Bounds and Self-Consistent Estimates for Creep of Polycrystalline Materials. Proc R Soc LondonSeries A, Math Phys Sci 1976;348:101–27. doi:10.2307/79120.

[215] Hosford WF. Materials Science: An Intermediate Text. Http://ebooks.cambridge.org/: Cambridge University Press; 2006.

[216] Salishchev G, Mironov S, Zherebtsov S, Belyakov A. Changes in misorientations of grain boundaries in titanium during deformation. Mater Charact 2010;61:732–9.

[217] Lecarme L, Tekoğlu C, Pardoen T. Void growth and coalescence in ductile solids with stage III and stage IV strain hardening. Int J Plast 2011;27:1203–23.

[218] Nemcko MJ, Wilkinson DS. On the damage and fracture of commercially pure magnesium using x-ray microtomography. Mater Sci Eng A 2016;676:146–55. doi:10.1016/j.msea.2016.08.095.

[219] Kartal ME, Cuddihy MA, Dunne FPE. Effects of crystallographic orientation and grain morphology on crack tip stress state and plasticity. Int J Fatigue

2014;61:46–58. doi:http://dx.doi.org/10.1016/j.ijfatigue.2013.11.022.

[220] Saxena AK, Tewari A, Pant P. Quantitative analysis of orientation and near neighbor interaction effects during deformation of polycrystalline Ti6Al4V. Mater Sci Eng A 2015;648:1–8. doi:http://dx.doi.org/10.1016/j.msea.2015.09.013.

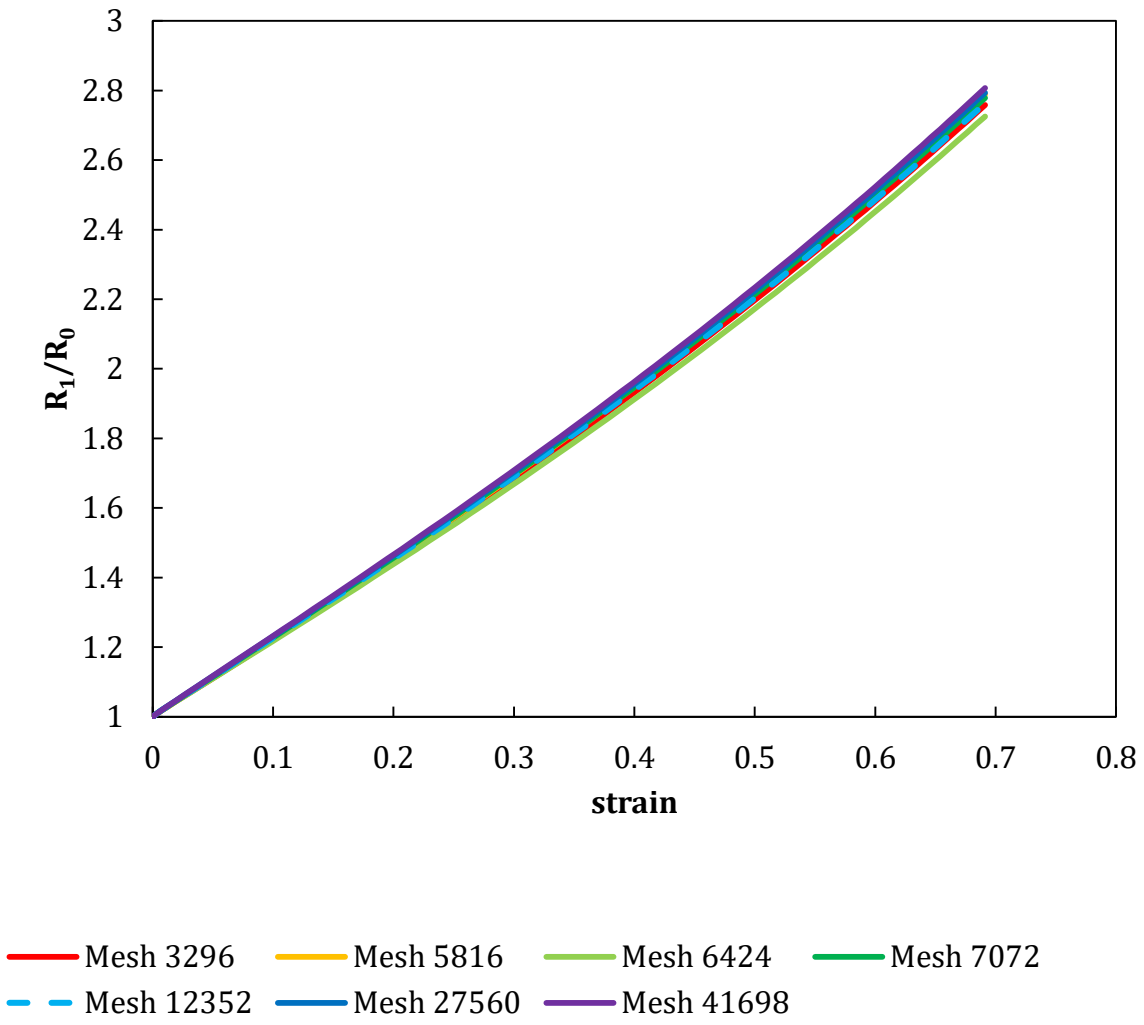

Figure A.1: Mesh dependence study for simulations with one void for samples M1, M2 and M3.